Enhanced Gas Path Modelling for Condition Monitoring

Thesis Report

Mohamed Yaakoub

Delft University of Technology

TU Delft

KLM

Enhanced Gas Path Modelling for Condition Monitoring

Thesis Report

by

Mohamed Yaakoub

Institution:	Delft University of Technology
Company:	KLM Engine Services
Submission date:	Thursday 23rd November, 2023

The cover photo is courtesy of KLM (Image taken by Mark Wagtendonk).

TU Delft

Preface

This thesis marks the end of a 5-year long educational journey at the Aerospace faculty in the Delft University of Technology. I am grateful to have had the opportunity to conduct my thesis at KLM Engine Services, where I gained a lot of knowledge and insights into the MRO industry.

I would like to thank my supervisors at KLM Ir. Juan Regueiro and Ir. Tim Rootliep for the constant help they offered during the project's duration. I would like to extend my gratitude to my university supervisor, Dr. Ir. Wilfried Visser, for his immense guidance and help. I would also like to thank Prof. dr. ir. Piero Colonna and Ir. Paul Roling for being part of my graduation committee.

During my time at KLM, I was lucky to meet some amazing colleagues in the data team who made my time there delightful. I would love to express my gratitude to Albert Timmer, Antonis Paradeisanos, Yaïr Brouwer, and Leandro Rodrigues. Thank you all for the amazing time and the coffee addiction. I would also like to thank my friends Walid and Daniel for sharing the frustration of doing the thesis alongside me and driving me to Schiphol many times. I will remember my time at KLM with all the nice moments and laughs I spent with all of you.

This master's journey would not have been complete without the presence of the two amazing smart people, Javier and Elena, in my life. Thank you for making the past 2 years fun. I would have lost my mind by now if it were not for you. Also thanks for proofreading this report!

I would also like to mention my parents who stood by my side since the first day and are the source of my motivation, Elsayed and Jehan. And I cannot forget my amazing sisters, Nada, Hanin, and Youmna, who are my greatest beloved supporters. Thank you all for your continuous support and love.

I would like to thank all the friends I made here and my friends back home in Egypt, for continuously believing in me. I dearly appreciate your presence in my life.

When I first arrived in Delft, I was a young aspiring high-school graduate. Today, I am on the verge of concluding with my Master's studies. This journey was tough and challenging. I am very content with what I have achieved and am looking forward to more challenges in life.

Mohamed Yaakoub
Delft, November 2023

Executive Summary

Aero engines are pivotal components in aviation, driving aircraft forward through their efficiency, power-to-weight ratio, and reliability. These engines rely on principles of thermodynamics to convert fuel energy into thrust. Aero engines are essential assets in aviation, with maintenance constituting a substantial portion of the operational costs. Maintenance, repair, and overhaul (MRO) shops use gas path analysis (GPA) for engine health management, employing gas performance modeling tools to simulate engine performance. The accuracy of these models significantly impacts engine health indications, making it crucial to refine the underlying reference model.

This report presents the work conducted in a thesis study, part of an Aerospace engineering Master's degree conducted in collaboration with KLM Engine Services (ES) to enhance gas path modeling systematically. The primary objective of the research is to produce a highly accurate model for simulating aero engines in operation. This model is intended for condition monitoring utilizing a GPA tool to enhance maintenance efficiency at KLM ES. KLM ES's wealth of operational data provides a unique advantage in this modeling challenge. This project is a continuation of a series of projects carried out at KLM ES. The most relevant project is a systematic approach that modelled turbofan steady-state test cell data with high accuracy. This project aims to push the model further by enhancing its accuracy in simulating on-wing steady-state flight data measured by the engine's data acquisition system in service.

The contents of the reports portray the steps taken to conduct the thesis study. This includes a solid introduction of the project and the purpose of conducting it. The research question and objective are outlined in order to lay the foundation for what the reader expects in the report. As part of the thesis, a literature is conducted to gather the relevant material surrounding turbofan modelling. The most pertinent material is presented as background information. Additionally, as a large part of the project focused on modelling losses in turbofans, a complementary overview of a fluid dynamic review on modelling losses in jet engines specifically in turbomachinery and nozzles is provided.

The study conducted is on the GEnx-1b turbofan model created at a preceding project at KLM ES. The engine is part of the fleet at KLM and an abundance of flight data is available. The model is thus discussed in more detail with a focus on the flaws in the current modelling approach specifically with regards to correcting Reynolds effects. Moreover, the work here presents a novel method that utilizes the so-called "Off design (OD) functions" that are input parameters in the steady-state simulations. These OD functions are then introduced in order to provide context into how the physical models are altered in order to improve the model's accuracy.

Furthermore, the model enhancement methodology is presented. This includes motivation for the flight selection and data filtering approach used to enhance the model. Due to the model mismatch at take-off conditions as a result of test-cell/on-wing data and engine-to-engine difference a model take-off calibration step is presented. The methodology then extends to include the correction of the turbomachinery components and specifically how the maps are reverse-engineered. Adjoined to that method, the nozzle losses corrections are also introduced. The outcome of the methodological framework is a series of OD scaling factors that are able to increase the model's accuracy in take-off, climb, and cruise.

To check the outcome of the approach employed, the gas path simulation using the newly corrected model is dissected. The results of the simulation indicate alterations in the gas path parameters. The changes are a result of the model reverse engineering and are in line with the physical theory of aero engines. Finally, to fully examine the extent to which the newly obtained model can used, a validation analysis is conducted. The model was validated using a month of operational flights of the same engine. The simulated results match the measured flight data with high accuracy. The average model error reduction in simulating the on-wing measurement parameters in the take-off, climb, and cruise phases are 0.84%, 0.30%, and 1.7%, respectively.

Contents

Nomenclature

Acronyms

AM	Adaptive Modelling
amb	Ambient
CBM	Condition-based monitoring
CFD	Computational Fluid Dynamics
CRZ	Cruise
DP	Design Point
EGT	Gravitational constant
ES	Engine Services
ETA	Efficiency
FOD	Foreign Object Damage
FPR	Fan Pressure Ratio
GA	Genetic Algorithm
GPA	Gas Path Analysis
HPC	High Pressure Compressor
HPT	High Pressure Turbine
IGV	Inlet Guide Vane
LES	Large Eddy Simulations
LPC	Low Pressure Compressor
LPT	Low Pressure Turbine
MDP	Multi Design Point
MRO	Maintenance, Repair, & Overhaul
OD	Off Design
OEM	Original Equipment Manufacturer
OF	Objective Function
OPR	Overall Pressure Ratio
PR	Pressure Ratio
RANS	Reynolds Averaged Navier-Stokes
Re	Reynolds number
ref	reference

RMSE	Root Mean Squared Error	
RNI	Reynolds Number Index	
RTO	Rolling Take Off	
SF	Scaling Factor	
SLS	Sea Level Static	
SM	Surge Margin	
TIT	Turbine Inlet Temperature	
TO	Take Off	
TOC	Top Of Climb	
WAC	Corrected mass flow rate	

Greek symbols Sets

η	Efficiency	
π	Pressure Ratio	

Roman symbols

$\dot{m}_c$	Corrected Mass Flow	
μ	Dynamic Viscosity	$\mathrm{Pa \cdot s}$
μ	Dynamic Viscosity	Pas
ρ	Density	$\mathrm{kg\,m^{-3}}$
A	Area	$\mathrm{m^2}$
B	Characteristic Length	m
F	Force	N
L	Non-dimensional Speed	
N	Shaft speed	rpm
P	pressure	$\mathrm{N/m^2}$
Q	Mass Flow Rate	$\mathrm{kg\,s^{-1}}$
R	Specific Gas Constant	J/kg/K
T	Temperature	K
V	Velocity	$\mathrm{m\,s^{-1}}$
W	Mass Flow Rate	$\mathrm{kg\,s^{-1}}$

List of Figures

List of Tables

1. Introduction

Gas turbines play a crucial role in aviation, providing the power necessary for aircraft propulsion. These exceptional engines referred to as aero engines have revolutionized air travel and are the primary choice for aircraft propulsion in the industry due to their efficiency, power-to-weight ratio, and high reliability.

Aero engines make use of principles of thermodynamics in order to convert energy in fuels into propulsive energy in the form of thrust in a continuous air-breathing flow [26]. The general components of aero engines include the fan, low-speed compressor, high-speed compressor, combustion chamber, low-speed turbine, high-speed turbine, core nozzle, and duct nozzle. As the aircraft is propelled forward, the flow goes through the fan and then separates into a bypass and core flow. The bypass flow immediately produces propulsive thrust. Meanwhile, the core flow is further compressed in the compressors, then mixed with fuel and ignited in the combustion chamber. This results in a gas expansion that drives the turbine that supplies the needed energy partially for the compressors, which are connected to the turbine through a shaft and partially for propelling the aircraft. The exhaust gas then leaves the core nozzle producing propulsive thrust.

Aero engines are valuable assets in the aviation industry. Maintaining, repairing, and continuously checking for faults is a key objective for aviation operators. Maintenance support of an aero engine accounts for 24% of the overall costs [39]. Due to this driving factor, maintenance, repair, and overhaul (MRO) shops employ different strategies in order to reduce operational costs as much as possible. A key concept that is used in engine health management is gas path analyses (GPA). GPA provides health indications of the engine's components and measures of deterioration. This is done with the aid of gas performance modeling tools that simulate engine performance in flight.

The quality of the GPA's engine health indications is highly reliant on the accuracy of the underlying reference model. Therefore, at KLM Engine Services several projects have been undergone to produce state-of-the-art models for their fleet's engines. The most recent project was performed by Ramdin [40], where a systematic approach for modelling modern turbofan engines was created. The approach utilized the classical on-design/off-design modelling method. Additionally, the model's component maps were actively tuned and adapted using a second-order polynomial function. The approach simulated the engine test-cell data with high accuracy. Further validation, was performed using GEnx-1B Continuous Engine Operating Data (CEOD) and indicated several key improvements. Most deviations were noticed in the cruise phase of the dataset. It was concluded that the major underlying reason for the deviations is an error in the Reynolds effect implementation and representation of the nozzle coefficients. Other ambiguities and concerns are raised considering the approach: the separation of the on-design/off-design model matching and the underlying component maps adaptation method.

The aim of this project is to conduct a thesis study to further enhance the systematic approach. The end goal is to produce a framework that is able to produce a model that simulates aero-engines in operation accurately and reliably. At KLM ES, this can be conveniently tested due to the abundance of operational data, a major advantage in the modelling challenge. The study is conducted using the Genx-1b continuous engine flight data (CEOD). Due to the lack of full sensor measurements along the engine gas path, a major obstacle in the modelling problem is the under-determined system of equations. Moreover, the study attempts to motivate all the choices in the systematic approach and provide evidence for the superiority of a specific method over other alternatives. Additionally, the work presented utilizes novel methods; therefore, supplementary discussions such as sensitivity analyses are provided to clarify any ambiguity.

1.1. Research question and objective

In this section, the research question and objective are presented.

1.1.1. Research questions

The following main research question has been formulated in order to fulfill the goal of this project:

How can an enhanced gas path modelling strategy be developed for the new generation of turbofan engines for condition monitoring purposes by utilizing on-wing measurements, and general physical relations?

In order to answer this main question systematically, sub-questions are mapped out below.

1. How can the on-wing engine measured operational data be utilized to improve the model's accuracy?
2. How can on-wing gas path predictions at take-off be improved using a test-cell fitted model?
3. Can the model be correlated with the simulated gas path Reynolds numbers to improve the model's accuracy?
4. How can the nozzle losses be modelled to improve the model's accuracy?
5. Can the enhanced model be utilized for different flights?

1.1.2. Research objective

The main research objective of this thesis project is defined as follows:

The objective of this research project is to investigate methods that can improve Gas Path Analysis for the new generation of turbofan engines at KLM Engine Services by developing an enhanced modelling approach using test-cell and on-wing data.

The main research objective can be further divided into sub-objectives. The first sub-objective is to check the reduced data measurement points along the gas path in the GEnx-1b CEOD and how it can best be utilized to investigate the research questions. The next objective is to attempt to improve the model at the design point (take-off conditions) and then further implement the Reynolds effect and nozzle losses corrections. The results of the model could then be validated using different on-wing data sets on the same engine the model is fitted to. If the methodology is proven to be valid, building accurate models can be performed more efficiently and accurately in the future allowing for better health assessment and maintenance at KLM ES.

The report is structured as follows. Firstly, general background information is presented in Chapter 2. Then the origins of the model inaccuracy, the loss mechanisms, and the methods to correct for Reynolds-related errors are discussed in Chapter 3. In Chapter 4, the GEnx-1b turbofan model is analyzed. The means of components performance models scaling is discussed in Chapter 5. Model enhancements using OD scaling functions are discussed in Chapter 6. Then, the system performance simulations are analyzed in Chapter 7. The enhanced model validation is discussed in Chapter 8. Finally, the conclusions are presented in Chapter 9 and the recommendations for further improvements are suggested in Chapter 10.

2. Background information

This chapter provides background information on general aero engine health monitoring practices in the maintenance, repair, and overhaul (MRO) industry. The chapter aims to guide the reader by introducing the main driving motives behind the gas turbine modeling problem and an overview of the challenges in the field. Section 2.1 provides an overview of health monitoring practices and includes an introduction to gas path analyses. Section 2.2 discusses gas path analyses in more detail with emphasis on the practices at KLM Engine Services. Then, component maps representation and adaptation using advanced techniques in literature are discussed in Section 2.3. Finally, the chapter spotlights the importance of data availability, its usage in performance matching, and model validation in Section 2.4.

2.1. Aero engine health monitoring

Aero engines are machines widely used in the aerospace sector. Civil and military aircraft, helicopters, and drones all make use of the gas turbine technology. Aero engines are unsteady and non-linear in nature. The generic main structure of twin-spool aero engines comprises an air intake, low and high-pressure compressors, combustion chamber, low and high-pressure turbines, bypass nozzle, and core nozzle. More complex ones also contain additional accessories and systems such as a gearbox, engine starting system, fuel system, lubrication system, air bleed, variable guide vane (vgv), anti-icing, etc. Additionally, an aero engine undergoes a considerate temperature and pressure variation during a cycle. For instance, the turbine inlet temperature (TIT) could go higher than 1800 K. The overall pressure ratio of modern civil engines could exceed 50 [41].

For airliners and civil operators, aero engines are valuable assets. Maintenance support for the entire life cycle of the engine account for 24% of the overall cost [67]. This makes the role of engine manufacturers and MRO shops very crucial. Nowadays, they adopt condition monitoring techniques in order to make decisions for aero engine maintenance and overhaul. These health monitoring methods ensure that the aero engine is functioning safely and cost-effectively [41].

2.1.1. Engine performance deterioration

During a typical flight, the engine encounters sand, dust, smog, etc. that causes deviations in the gas path causing performance deterioration. In general aero engines deterioration can be categorized as recoverable, non-recoverable, or permanent deterioration [41]. These deteriorations can cause changes in performance parameters such as compressor and turbine flow capacity and isentropic efficiencies. These deviations would subsequently lead to deviations in pressure, temperature, fuel flow, and shaft speed measurements. Faults in aero engines could occur due to several causes:

- **Fouling** - Fouling is caused by attached particles on engine blade airfoils and the annulus surfaces. Adhered particles could include smoke, oil mists, carbon, or sea salts. Usually fouling is controlled by a proper air filtration system or in severe cases through washing in maintenance shops. The built-up material then changes the shape of the surface it is attached to. For instance, that could be an airfoil that would then have some degree of surface roughness decreasing the efficiency of the component [25].
- **Erosion** - Erosion is the removal of flow path component material due to abrasive particles such as sand, salt, hydrocarbons, etc.[19]. Similar to fouling, erosion causes surface roughness to increase, changing the airfoil profile, incidence angle, blade tips, and seal clearances. In very unfavorable conditions erosion can lead to complete rotor blades reduction up to the root in very short periods of time. Additionally, erosion damage can be severe in regions operating in sandy deserts [22].

- **Foreign object damage (FOD)** - FOD could result in an immediate catastrophic failure or non-recoverable deterioration. This includes direct destruction to the aircraft like an engine failure [21].
- **Blade tip clearance and rubbing** - In aero engines the use of abradable seals is common. It is used to limit the risk of damage due to the rotating and stationary elements if rubbing occurs [14]. Rubbing could occur in non-favorable conditions such as in-flight turbulence or heaving landing. The induced vibration of the engine could cause axial movements of the rotating elements allowing for contact with the stationary parts. Rubbing wear is a major part of engine deterioration [41]. A 1% blade tip clearance increase could result in over 1% decrease in the total thrust and efficiency of the engine [9].
- **Thermal distortion** - Thermal distortion occurs in components that deal with high temperatures in the gas path. The highest temperature is usually at the exit of the combustion chamber and the components that are most susceptible to thermal stresses are the high-speed turbine and the nozzle. Turbine blades and nozzle guide vanes are components that are immersed in the hot gas flow and can suffer from thermal-mechanical fatigue [36].

2.1.2. Engine health management

Continuous identification of air engine malfunctions and faults has been in demand due to the safety standards increase in aviation. Currently, most of the mechanical failures are detected prior to occurring [41]. This necessitates advanced health monitoring strategies such as condition-based monitoring (CBM). CBM involves continuously assessing a machine's condition to determine whether it needs maintenance or repairs. Numerous metrics are collected and analyzed, including vibration, temperature, pressure, oil parameters, and other pertinent indicators unique to the equipment. Through CBM, potential problems or abnormalities may be detected early, enabling preventative maintenance, and reducing unanticipated failures and downtime.

CBM encompasses two principal aspects: diagnostics and prognostics. Diagnostics of engines entail identifying and diagnosing the underlying causes of problems occurring within them, using various techniques and tools. In this procedure, the specific faults, failures, or malfunctions that are affecting the engine's performance are identified. Analysis of sensor data, performance tests, inspection of components, and use of specialized equipment are all possible diagnostic techniques. As a result of diagnosing underlying problems, repair or maintenance actions can be guided accordingly. Prognostics, on the other hand, aims to predict future engine health. The process involves analyzing engine data, such as sensor readings, performance trends, or historical maintenance records, to predict when specific components will fail or degrade. Maintenance teams use prognostics to make informed decisions on timing repairs to prevent unforeseen failures in an effort to optimize the engine's availability.

In practice, applying prognostic health management is challenging [41]. The description of the physical problem is not straightforward. Engine manufacturers tend to keep crucial engine performance metrics as company secrets or proprietary. Moreover, modelling the engine's behavior accurately is not so trivial as modern aero engines are complex with multiple subsystems affecting each other. The data available for creating a prognostic health management model is another issue. Fundamentally, the requirements needed for finding a solution are the challenge. For decades, researchers attempted several methods in order to find a sufficiently accurate answer [45].

One important aspect of engine maintenance that aids in both prognostic and diagnostic health management is gas path analysis (GPA). GPA uses real gas path measurements to determine the engine's health by estimating the changes in the engine's performance. This provides an indication of the engine's health degradation [27]. GPA can be utilized to optimize predictive maintenance optimizing the engine's availability, reducing downtime and overall costs.

2.1.3. Gas Path Analysis

As discussed, GPA is a method that uses measured performance parameters to provide a health indication for the engine's components. It is a powerful tool for engine maintenance and overhaul service providers. It enables component condition monitoring providing valuable diagnostics information without the need for engine disassembly [56]. From an economic and industrial point of view, this leads to a large decrease in maintenance costs.

Applying GPA has the potential of being useful for the engine maintenance provider, isolating and pinpointing the faulty component as well as the customer, reducing downtime and cost. However, the quality of the method is reliant on the underlying modelling technique. Engine modelling as a process is highly reliant on the available data. And that is the OEM'S proprietary in many cases [52]. Not being able to model the engine with sufficient accuracy would directly lead to incorrect estimations of the engine's health conditions. Additionally, in practice GPA cannot be generically applicable. Often maintenance and overhaul shops provide services for a few different engine types. Each engine has a separately defined modelling problem due to different engine configurations or measured data sets. Additionally, engine-to-engine differences exist adding a challenge even for applications within the same engine family.

The data required for GPA could also be acquired from multiple sources (e.g. in-flight or test cell). This adds additional uncertainty due to the different data formats and sets of measured parameters. The manual interference of an end user discourages the usability of the method leading to maintenance shops' reluctance in investing resources in GPA. Moreover, engine maintenance can be triggered by problems other than not up to par engine performance. For instance, some engine parts have limited lifetime usage or might need a complete replacement for mechanical issues.

In general, GPA usage for engine maintenance has limitations but at the same time has great potential if made use of correctly and effectively. Therefore, there has been vast research attempting to improve and generalize the applicability of GPA [55, 47, 54, 65, 70].

2.2. Gas path analyses at KLM Engine Services

Engines undergo several maintenance shop visits in their operative lifetimes as part of the engine's health monitoring. KLM engine services (ES) is one such MRO shop that provides services for a number of aero engines. The maintenance strategy at KLM is based on preventive and corrective maintenance. Preventive maintenance is applied based on a fixed schedule. Corrective maintenance is based on the engine failing to meet performance requirements. Recently, the addition of diagnostic maintenance was implemented. The method is based on making use of datasets of the sensors onboard engines during flights typically referred to as on-wing data. The health of the engine is determined then based on GPA. The software used to model the engines is the Gas Path Simulation program (GSP) [58]. GSP is an object-oriented component-based simulation tool program that allows users to perform steady-state and transient simulations of any gas turbine configuration. Additionally, GSP allows the user to perform design point calculations and off-design calculations.

In general, the trend at KLM ES is targeted at conducting maintenance efficiently and reliably. This objective is possibly achieved by enhancing the implemented GPA methodology. As technology advances, new complex engines are developed inherently producing more challenges. As a result, the cost-driven industry encourages more research to keep pace with the advancements. The following is a rundown of the recent projects conducted at KLM ES.

The diagnostic method at KLM first employed by Verbist [56] assesses health conditions using a model-based GPA (alternative methods exist, see for instance the study by the same author). Furthermore, the model results are obtained using adaptive modelling (AM). AM is a procedure where component maps

are adapted using a map modification approach that captures the engine's non-linear deviation. Since the process adapts the engine's gas path to the measured dataset, the adaptation in itself is a measure of the engine's health deviation. The model-based approach depends heavily on the measured data, which usually comprises of missing data points along the gas path. This leads to high uncertainty for some component condition estimations. Additionally, the method depends on the available component maps used for the reference model. Engine-to-engine differences do exist and can be significant. Using a single reference model for a single engine type has the potential to lead to further errors.

The aforementioned setbacks provoked the need for a different approach. An evolutionary algorithm-based multi-operating point gas path analysis (MOPE-EA GPA) method was developed by Rootliep [43]. Modern turbofans have fewer sensors on board compared to their predecessors [62], creating more unknowns in the GPA method. The developed MOPA-EA GPA approach deals with under-determined systems meanwhile utilizing genetic algorithms. The method is still based on AM modifying the reference component maps using measurement data. The results of the approach were promising yet some inconsistencies were present for the GEnx-1b engine. This was due to incorrect modelling of the engine (wrong design point and reference maps). GPA errors increase with inaccurate reference models.

The MOPA-EA GPA tool was further improved by Otten [38]. The new model attempted to integrate secondary performance parameters into AM by correlating them to map modifiers. The secondary performance effects were then modeled as an additional step on the reference models. This means that the method did not improve the model itself (design point and reference maps).

Other projects at KLM ES were focused on enhancing the performance models. A model for the Genx-1B was created by Van Moorselaar [35] that included design point and off-design modelling. The design point was obtained by manually calibrating the model against a chosen point iteratively. The off-design performance was captured by tuning reference maps. Map tuning was performed using a basic approach of map speed line re-labeling and relocation. The method is further discussed in Section 2.3.4.

Den Haan [17] also created a model for the CF6-80 engine. The design point was manually established iteratively. The off-design performance was captured by tuning standard GSP maps by relabelling speed lines and relocating design points similarly to the model by Van Moorselaar. El Bouazzaoui [12] created a model for the CFM56-7B using a similar approach used by Den Haan. Additionally, a project by Roell [42] was conducted to research the discrepancy between on-wing and test-cell corrected turbofan performance indicators.

Finally, a systematic approach for modelling modern turbofan engines was developed by Ramdin [40]. The design point was computed by defining an optimization problem in order to overcome the under-determined problem. The off-design conditions were calibrated in an optimization problem that adapted the component maps until satisfactory results were achieved.

2.3. Component maps representation and adaptation

Reverse engineering and fine-tuning of component maps is an important area of research for modelling aero engines' performance. The component maps provide valuable insight into the behavior of engine components (e.g., fans, compressors, or turbines) under different operating conditions. In general, component maps of modern aero engines are manufacturer's proprietary [52]. This is a challenge in the context of accurately understanding and modelling engine performance. This stirred the motivation to research reverse engineering techniques. Reverse engineering is key to extracting and deciphering the component maps, allowing researchers to accurately depict the engine's behavior [63]. Generally, aero engines of similar technology and complexity tend to have similar characteristic behavior [52]. Therefore for modelling tasks, using similar maps to the engine at hand could possibly be obtained from the public domain or literature. However, in the context of accurately modelling an aero engine for purposes that requires great accuracy in order to deliver satisfactory results, one may not just depend on

generic component maps. For example, using a generic component map for GPA, where the method is even sensitive to engine-to-engine differences [55], would quickly lead to inaccurate results. Fortunately, fine tuning techniques do exist [63, 51, 64, 62, 29, 23, 34, 46, 24, 66] to allow for component maps refinement. By leveraging advanced fine-tuning methods, researchers have the potential to significant performance-matching improvements. If the model's component maps are different from the real ones, a prediction error is inevitable [29]. Figure 2.1 depicts an exemplary performance deviation in off-design conditions. Moreover, engine performance is non-linear in off-design conditions, which makes modelling the actual performance challenging.

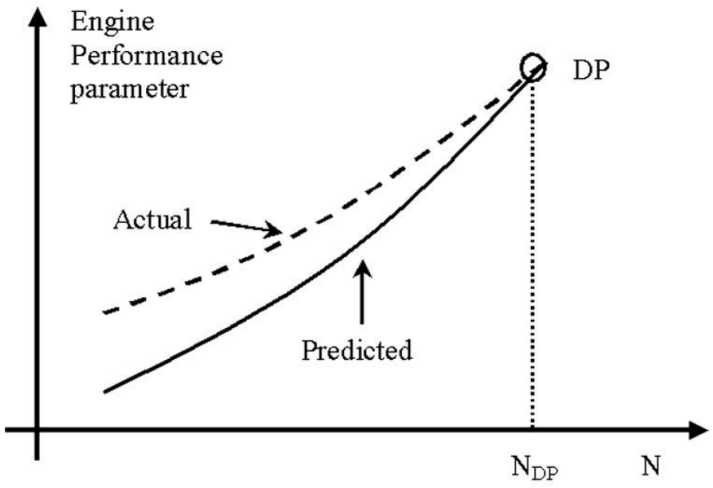

Figure 2.1: Off-design engine performance mismatch [29]

Some researchers make use of methods that depend on performing CFD simulation [1, 49, 39]. These require knowledge of the geometry of the turbomachines, good definitions of the boundary conditions, and estimation of the heat transfer effects. Other researchers employed scaling and shifting techniques [29, 24]. These depend on assuming a map from open literature and further iteratively employing adaptation scaling factors for the map characteristic parameters in order to capture the non-linear behavior of gas turbines. Other researchers came up with a method that depends on generating the component maps either by analytical solutions or assuming a regression model [46, 52, 64, 63]. The adaptation of the map is a procedure that enhances the quality of the imposed model using scaling factors. The scaling factors then change the underlying equations that attempt to capture the map behaviour rather than scaling the design points themselves.

Due to the natural sequence of events, some methods are successors of others making the previous ones less and less relevant. Some other methods such as those that depend on CFD simulations can be infeasible in many cases for the lack of accurate geometric parameterization of the gas turbine being used or due to the lack of accurate temperature measurements. Also, some researchers present models that are case-specific and cannot be easily generalized such as the ones presented in [69]. This section, therefore, aims to provide a detailed description of the most relevant methods that are characterized by sufficient generality for the purposes of modeling the problem at hand.

2.3.1. Li et al.'s scaling and shifting method

Li et al. [29, 28] introduced a non-linear adaptation method utilizing a genetic algorithm. The method uses a quadratic form of scaling factor functions to come up with scaling factors for the different non-dimensional speeds. The optimum scaling factors are then produced via a minimization problem utilizing genetic algorithms.

The adaption strategy focuses on modifying the component maps by applying scaling factors to the maps' characteristic parameters. This could be for instance the correct mass flow rate, pressure ratio, isentropic efficiency, enthalpy drop ratio, or non-dimensional rotational speed. eqs. (2.1) to (2.4) defines the scaling factors, with A and A^* representing the original and adapted parameters. Additionally, a starting component map is required for this method. This could be a map from the literature that captures the same technology-level performance of the component that is of interest.

$$SF_{WAC,\mathrm{OD}} = \frac{WAC_{A*}}{WAC_A} \tag{2.1}$$

$$SF_{PR,\mathrm{OD}} = \frac{PR_{A*}}{PR_A} \tag{2.2}$$

$$SF_{ETA,\mathrm{OD}} = \frac{ETA_{A*}}{ETA_A} \tag{2.3}$$

$$SF_{DH,\mathrm{OD}} = \frac{DH_{A*}}{DH_A} \tag{2.4}$$

The map scaling factors are then calculated using the quadratic scaling factor function shown in Equation 2.5, where a, b, and c represent the scaling function coefficients. SF_X represents a scaling factor for any of the characteristic performance parameters. L_{DP} and L_{OD} denote the non-dimensional speed at the design point (map scaling point) and operating off-design points respectively.

$$SF_X = a + b\left(\left|\frac{L_{\mathrm{DP}} - L_{\mathrm{OD}}}{L_{\mathrm{DP}}}\right|\right) + c\left(\left|\frac{L_{\mathrm{DP}} - L_{\mathrm{OD}}}{L_{\mathrm{DP}}}\right|\right)^2 \tag{2.5}$$

Coefficients a, b, and c are then determined by the solver in an optimization framework based on the objective function shown in Equation 2.6 that is based on the average difference between the predicted value and the actual value. σ_i is a weighting factor that is assumed to be 1, meaning all measurements are expected to have an equal contribution. m is the number of measurements and n is the number of off-design points.

$$\mathrm{OF} = \frac{1}{n}\frac{1}{m}\left[\sum_{j=1}^{n}\sum_{i=1}^{m}\sigma_i\left|\frac{P_{(\mathrm{predicted})i,j} - P_{(\mathrm{actual})i,j}}{P_{(\mathrm{actual})i,j}}\right|\right] \times 100 \tag{2.6}$$

On one hand, using a scaling factor for each characteristic performance parameter rather than a single scaling factor for the entire map ensures capturing the non-linear behavior of the gas turbine. On the other hand, using a quadratic function for obtaining the scaling function increases the fidelity of the adaption model. This obviously comes at an increased computational cost, but it is a choice to be made for the specific project's application and the expected results. Figure 2.2 depicts the effect of changing the scaling factor coefficients b and c on the scaling factor lines. In this case, the design point is chosen as a reference point for adaption. Meaning that at the design point, the value is fixed. This implies that $a = 1$. Setting c to zero changes the scaling function to be linear simplifying the approach. Setting b to zero still produces a nonlinear function with less freedom for adaptation. It should be also obvious that if both coefficients are set to zero no map scaling would occur.

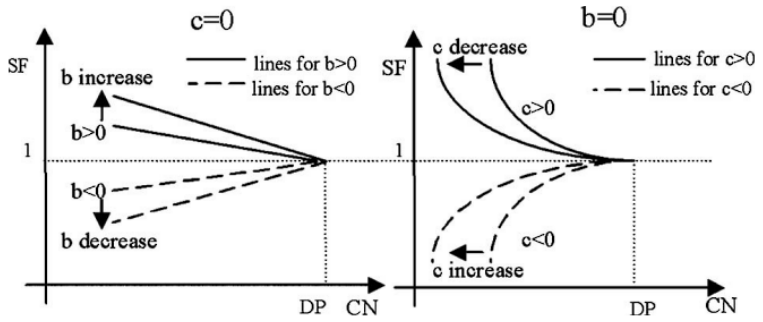

Figure 2.2: SF coefficients. variations on the scaling factor lines [29]

2.3.2. Tsoutsanis et al. fitting method

Tsoutsanis et al. [50, 51] developed a method to adapt component maps, where the shape of the map is mathematically represented by ellipses. The model is then numerically adapted by rotating and translating the ellipses until sufficient convergence is met. The map fitting process employed starts by choosing a reference map. This could be a map that is available in open literature in digital form. The objective is to fit the digitized map data by a single mathematical expression for every single non-dimensional speed line. The authors claim that using ellipse expressions for map fitting is the most robust mathematical approach (i.e. compared to neural networks [66] or polynomials).

The representation choice adopted relates the corrected mass flow rate m_c and the isentropic efficiency η to the pressure ratio π and the non-dimensional speed line N. Thus, the mathematical representation of the pressure ratio vs corrected mass flow function is given by Equation 2.7 and Equation 2.8, respectively. The coefficients a and b are the semi-minor and the semi-major axes of the ellipse, respectively. x_o and y_0 are the ellipse's center coordinates.

$$\left(\frac{m_0 - x_0}{a_\pi}\right)^2 + \left(\frac{\pi_0 - y_0}{b_\pi}\right)^2 = 1 \tag{2.7}$$

$$\left(\frac{m_0 - x_0}{a_\eta}\right)^2 + \left(\frac{\eta_0 - y_0}{b_\eta}\right)^2 = 1 \tag{2.8}$$

Adding the rotational degree of freedom for the ellipses by defining the rotation angle θ results in eqs. (2.9) to (2.11)

$$m = m_0 \cos(\theta_\pi) - \pi_0 \sin(\theta_\pi) \tag{2.9}$$

$$\pi = m_0 \sin(\theta_\pi) + \pi_0 \cos(\theta_\pi) \tag{2.10}$$

$$\eta = m_0 \sin(\theta_\eta) + \eta_0 \cos(\theta_\eta) \tag{2.11}$$

Furthermore, the surge line is expressed as a second-order polynomial by defining the pressure ratio as a function of the non-dimensional corrected speed as in Equation 2.12. Here, i indicates the index of the speed line and a, b, and c are the polynomial's coefficients. Also a surge margin sm is defined to impose a maximum pressure ratio in Equation 2.13

$$\pi_{\text{surge}} = aN_i^2 + bN_i + c \tag{2.12}$$

$$\pi_{\text{max}_i} = \left(\frac{\pi_{\text{surge}_i}}{(1+sm)} \right) \tag{2.13}$$

Three different approaches with varying complexity are then considered for adaptation. A representation of the fitting approaches is depicted in Figure 2.3. The three approaches are listed as follows:

- **Approach 1** Centering the map at the origin for the π vs. m curve and at a translated point in x for η vs. m curve. Rotation is completely constrained.
- **Approach 2** Centering the map at the origin and allowing for rotation
- **Approach 3** Centering the map at a translated point in x and y and allowing for rotation

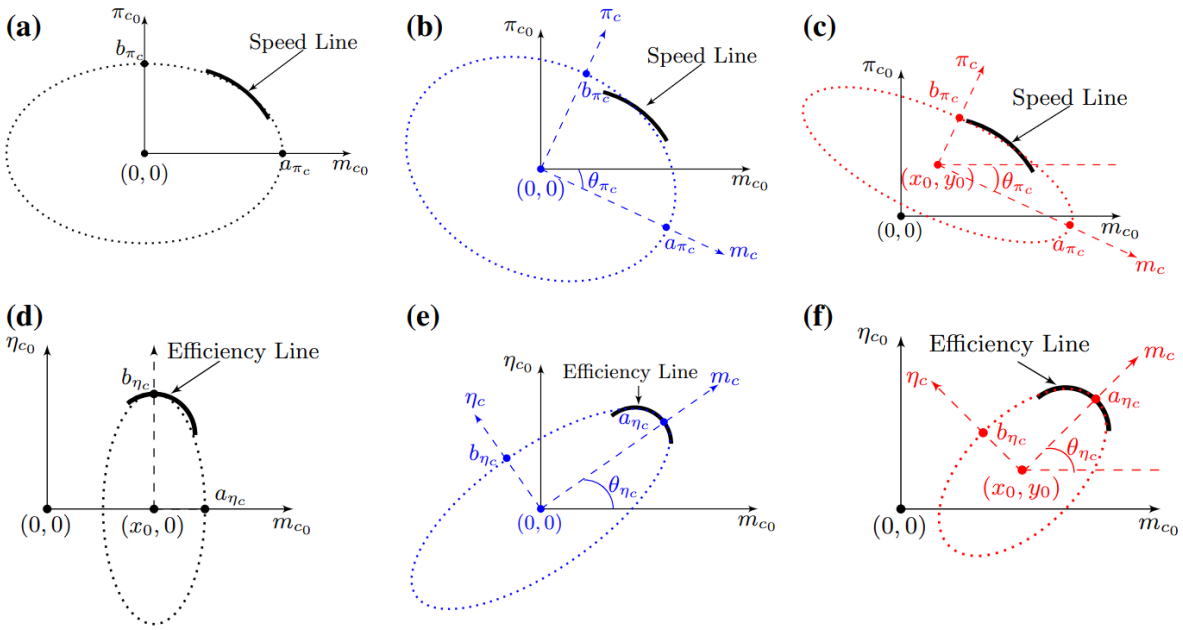

Figure 2.3: Adaptation approach for (a) π vs. m - Approach 1. (b) π vs. m - Approach 2. (c) π vs. m - Approach 3. (d) η vs. m - Approach 1. (e) η vs. m - Approach 2. (f) η vs. m - Approach 3 [51]

The complexity of the adaptation method increases with the order of the approach. This is due to the increased degrees of freedom that are introduced. Each coefficient is an addition to the design vector input for the optimizer. The needed coefficients to be computed are tabulated in Table 2.1. Furthermore, each coefficient needs to be expressed as a function of the non-dimensional rotational speed as there exists an ellipse for each speed line. This is done using a polynomial function that is robust enough to be smooth and allow for extrapolation. A generic form of such function is given in Equation 2.14. Every single coefficient then will consist of a set of sub-coefficients. The order of the polynomial is then chosen accordingly to capture a smooth curve that would lead to a sufficiently accurate model. An obvious trade-off to the increased complexity is the computational time, especially in gas turbines that have multiple components (turbomachines) that require adaptation.

$$g(N) = g_1 N^i + \cdots + g_i N + g_{i+1} \tag{2.14}$$

Table 2.1: Adaptation coefficients for each approach.

Method	Coefficient
Approach 1	$a_\pi, b_\pi, a_\eta, b_\eta, x_{0_\eta}$
Approach 2	$a_\pi, b_\pi, \theta_\pi, a_\eta, b_{\eta_c}, \theta_\eta$
Approach 3	$a_\pi, b_\pi, \theta_\pi, x_{0_\pi}, y_{0_\pi}, a_\eta, b_\eta, \theta_\eta, x_{0_\eta}, y_{0_\eta}$

The sub-coefficients were then computed in a minimization problem implementing Nelder Mead algorithm [37] with a similar objective function to the one described in Section 2.3.1. The model was tested on a compressor performance map. The fitting error of approach 1 is worse than the one resulting from using neural network methods and is therefore ignored. Approach 2 results in an accumulated fitting error of 2.9% and 0.54% for corrected mass flow rate and isentropic efficiency, respectively. Approach 3 results in an accumulated fitting error of 2.2% and 0.41% for corrected mass flow rate and isentropic efficiency, respectively. The authors conclude that approach 2 leads to the best trade-off between the model's accuracy and complexity.

2.3.3. Yang et al.'s fitting method

Yang et al. [64] developed a new adaption method that builds on the work of Tsoutsanis et.al [51]. The authors claim that their new method is not only as robust or even more robust in capturing the engine's off-design performance accuracy as the approach 3 discussed in Section 2.3.2 but also less computationally demanding. Moreover, their method does not require a reference map as a generic map is constructed.

The map is first generated by assuming circles with radii equal to the distance between every operating point and the origin. So in the case of having 9 operating points, 9 concentric circles around the origin are formed like the one shown in Figure 2.4. Then map tuning is performed using scaling, translation, and rotation. The final equations for the corrected mass flow M_c, pressure ratio Π_c, isentropic efficiency H_c are presented by eqs. (2.15) to (2.17).

$$\begin{aligned} M_c = {} & a\cos\left(SF_{\pi\varphi}\right)\cos\left(\theta_{\pi c}\right) - b\sin\left(SF_{\pi\varphi}\right)\sin\left(\theta_{\pi c}\right) - \\ & a\cos\left(SF_{\pi\theta}\right)\cos\left(SF_{\pi\varphi}\right) + b\sin\left(SF_{\pi\theta}\right)\sin\left(SF_{\pi\varphi}\right) + \\ & m_{c0} \end{aligned} \tag{2.15}$$

$$\begin{aligned} \Pi_c = {} & a\cos\left(SF_{\pi\varphi}\right)\cos\left(\theta_{\pi c}\right) + b\sin\left(SF_{\pi\varphi}\right)\sin\left(\theta_{\pi c}\right) - \\ & a\cos\left(SF_{\pi\theta}\right)\sin\left(SF_{\pi\varphi}\right) + b\sin\left(SF_{\pi\theta}\right)\cos\left(SF_{\pi\varphi}\right) + \\ & \pi_{c0}. \end{aligned} \tag{2.16}$$

$$\begin{aligned} \mathrm{H}_c = {} & a\cos\left(SF_{\eta\varphi}\right)\cos\left(\theta_{\eta c}\right) + b\sin\left(SF_{\eta\varphi}\right)\sin\left(\theta_{\eta c}\right) - \\ & a\cos\left(SF_{\eta\theta}\right)\sin\left(SF_{\eta\varphi}\right) + b\sin\left(SF_{\eta\theta}\right)\cos\left(SF_{\eta\varphi}\right) + \\ & \eta_{c0}. \end{aligned} \tag{2.17}$$

with $a = R(1 + SF_{\pi m})$ and $b = R(1 + SF_{\pi\pi})$ for corrected mass flow and pressure ratio equations. Coefficients a and b are not explicitly defined for the $m_c - \eta_c$ map; however, it is implied through logic: $a = R\left(1 + SF_{\eta m}\right)$ $b = R(1 + SF_{\pi\pi})$. The subscript 0 indicates the operating points. $\theta_{\pi c}$ and $\theta_{\eta c}$ are the angles of the parameter equations. The Adaptation factors are defined as follows:

- **Scaling** - $SF_{\pi m}, SF_{\pi\pi}, SF_{\eta m}, SF_{\eta\eta}$
- **Translation** - $SF_{\pi\theta}, SF_{\eta\theta}$

- **Rotation** - $SF_{\pi\varphi}, SF_{\eta\varphi}$

$$SF_i = \sum_{k=1}^{n} SF_{i_k} N^{k-1} \tag{2.18}$$

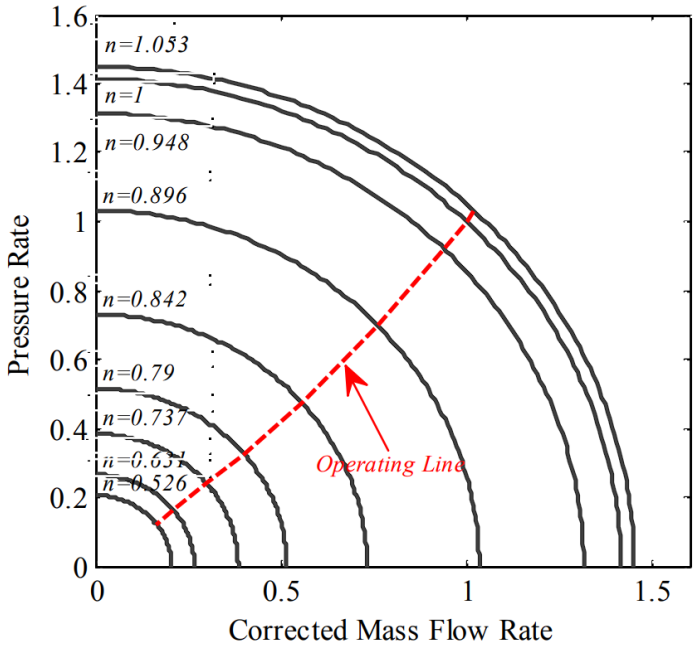

Figure 2.4: Compressor map initialization using concentric circles at the operating points [64].

The surge boundary and margins are defined as in Equation 2.12 and Equation 2.13 respectively. Each adaptation coefficient is then defined as a polynomial function of the rotating speed N in the form shown in Equation 2.18.

The method is then compared to the three approaches discussed in Section 2.3.2 in predicting the compressor map of GE LM2500 [31]. The total errors of approaches 1 and 2 are not reported here because the new method discussed here significantly outperforms them. For the $m_c - \pi_c$ map, approach 3 consists of 45 tuning sub-coefficients with a total error of 5.2%. The new method consists of 12 tuning sub-coefficients with a total error of 3.95%. For the $m_c - \eta_c$ map, approach 3 consists of 38 tuning sub-coefficients with a total error of 4.56%. The new method consists of 12 tuning sub-coefficients with a total error of 4.46%

2.3.4. Artificial neural network (ANN)

A different approach that captures the performance of turbomachinery by means of an artificial neural network (ANN) has been growing in the scientific community. This is due to their fast and computationally inexpensive response [15]. Researchers like Yu [66], Ghorbanian [15], and Zhou et al. [71] all utilize variations of ANNs to generate components maps (the latter includes several other references). The method is reported to be able to capture the non-linearity of the maps with great accuracy. However, the quality of the maps is then highly based on the abundance of the available data [71]. ANNs are also fully data-driven, meaning that it is prone to producing nonphysical maps. Also, the complexity of implementing the method is the highest compared to the other methods [62] and a lot of specific types of ANNs are reported for different types of applications. This is unfavorable for its generic use, causing the method to be only reliable for certain types of gas turbines and therefore application in industry.

2.4. Data availability and model validation

In order to accomplish a reliable numerical model for engine performance a concert validation method needs to be established. Validating the model will guarantee a level of compliance in real physical applications (e.g. GPA). A challenge in engine performance matching is data availability. This is especially true in modern complex engines. In the aviation industry, OEM usually do not allow airliners to access engine sensor reading datasets below certain flight hours. This means that the usable data from engines that have been in service for a long duration can be the only option. At that point, the engine will have experienced deterioration from the out-of-factory conditions.

Typically engine datasets are provided based on test cell runs in static sea-level atmospheric conditions or on-wing data. Generally, the test cell datasets are higher in fidelity due to the controlled physical conditions, the addition of gas path sensors, and the operational stability of the engine. A challenge in engine performance matching is the choice of datasets for the matching procedure and for validation. The easier choice from a numerical modelling point of view is to match based on test cell data as the problem becomes less under-defined due to the additional sensor readings. One then would validate the model using the on-wing data. However, the model needs to take into account the atmospheric conditions variations (such as the aforementioned Reynolds effect) and consequent performance change, that in some cases could only be accomplished by the inclusion of on-wing data into the modelling problem itself. Then the challenge is extended to potentially validating the model using different operational engines. One then needs to be careful in considering the engine deterioration and engine-to-engine differences. Another option is to do engine performance matching using on-wing data. However, the under-determined modelling problem might produce non-physical results. Overall, data availability in this research field is a challenge. One needs to be aware at an early stage prior to setting up model matching frameworks of how the model validation methodology will be executed in order to produce sufficiently reliable results for engineering purposes.

3. Improving gas turbine modelling accuracy

The Reynolds number effect can be observed in aero engine turbomachinery at high altitudes [60]. This is mainly due to the low dense air, which lowers the Reynolds number over the surfaces. Upon this decrease, boundary layers thicken and viscous losses are augmented. In severe cases, separation off surfaces could occur substantially increasing losses. This phenomenon has an adverse effect on engine performance as it directly affects the overall pressure ratios achieved in components, mass flow, and efficiency. This chapter provides a review on the Reynolds number effects in turbomachines starting from a theoretical overview with a brief introduction on boundary layer viscous losses in Section 3.1. The loss mechanisms due to low Reynolds numbers are discussed in Section 3.2. Then finally, the effect of the Reynolds number on Engine performance from a system modelling point of view is discussed in Section 3.3.

3.1. Origins of model inaccuracy: viscous effects

The Reynolds number is a dimensionless parameter that is important to the understanding of fluid flow and its impact on turbomachinery performance. It is defined as [2]

$$Re = \frac{\rho \cdot V \cdot L}{\mu} \tag{3.1}$$

where ρ represents the density of the fluid, V denotes the velocity of the fluid relative to the object or surface L is a characteristic length such as the chord length of an airfoil, and represents the dynamic viscosity of the fluid. As can be seen in Equation 3.1, several parameters affect the Reynolds number. As altitude increases, the air density drops due to a decrease in atmospheric pressure. This directly decreases the Reynolds number. The key effect is that the Reynolds number change is associated with alterations in the flow. The large decrease in Reynolds number can result in a flow transition from turbulent to laminar affecting flow separation, boundary layer, and the turbomachine's efficiency.

The Reynolds number is a measure of inertial forces to viscous forces. Low Reynolds losses over the turbomachinery blades are due to flow interactions in the viscous region. This viscous region is characterized by high shear forces that are present in the boundary layer thickness. The thickness of the boundary layer is directly related to the Reynolds number. For instance, the boundary layer thickness over a flat plate can be described by the so-called Blasius boundary layer solution shown in Equation 3.2. The relation defines how for small Reynolds numbers the boundary layer is thicker, containing more viscous interactions. The physical correlation between the Reynolds number and the boundary layer thickness in turbomachinery is similarly present as experimental data suggests [60, 4, 59].

$$\delta_{99}(x) \approx 5.0\sqrt{\frac{\nu x}{u_0}} = 5.0\frac{x}{\sqrt{\mathrm{Re}_x}} \tag{3.2}$$

At low Reynolds numbers, the flow over the blade can potentially separate from the blade surface creating a laminar separation bubble which subsequently forms the free shear layer that transitions into turbulence. The high turbulent energy in the flow could lead to turbulent reattachment decreasing the laminar separation bubble. In Figure 3.1, CFD DNS simulation shows a laminar separation bubble emerging near (X_1) followed by flow turbulent transition near (X_2) which consequently leads to reattachment.

In turbomachines, viscous effects influence performance in a number of ways [6]. Firstly, viscous effects limit the pressure rise. Secondly, viscous effects lead to flow blockage. Blade surfaces and the end-wall

regions have the main growth of boundary layers that could create a flow blockage. Blockage reduces the effective area for which the flow passes. The reduced area ultimately leads to a decrease in the mass flow rate. Lastly, viscous effects directly lead to losses decreasing the overall efficiency of the turbomachine. The viscous boundary layer increases shear interactions between the layers, especially in turbulent flow, near the blade surfaces, hub, and casing causing viscous dissipation. Viscous dissipation leads to a direct loss of energy as well as a decrease in the mean flow velocity.

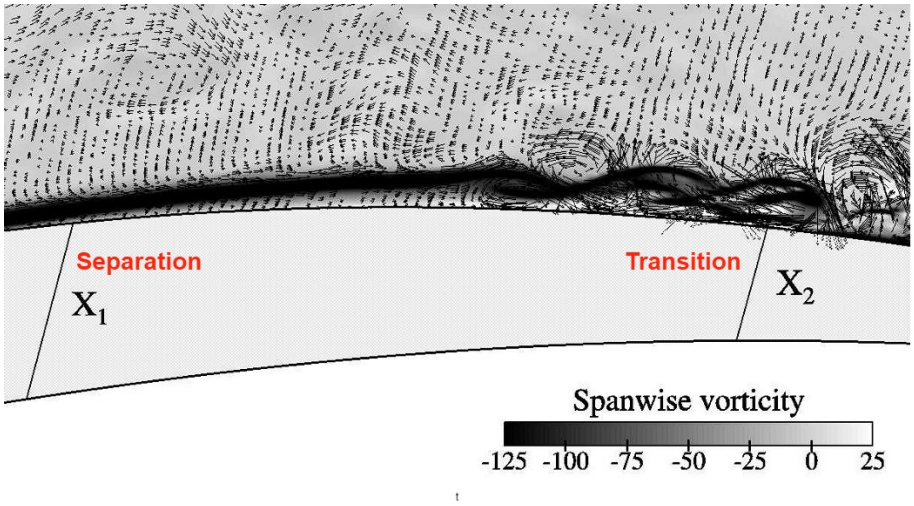

Figure 3.1: DNS side view of the suction side of a compressor blade showing the laminar separation bubble and flow transition at Re = 138,500. Image adpated from [68]

The model for viscous losses in the boundary layer can be quantified using a total loss coefficient. The model assumes that total pressure outside the boundary layer is constant, the working fluid is incompressible, and the static pressure and flow angles at the exit plane are constant. The total loss is a quantification of pressure loss due to viscosity. As shown in Equation 3.3 [44], the total loss coefficient ζ is inversely proportional to the Reynolds number. For laminar flow, typically m is 0.5, and between 0.2 to 0.25 for turbulent flow [4].

$$\zeta \sim \frac{1}{\mathrm{Re}^m} \tag{3.3}$$

Blade surfaces are not the only viscous regions where losses occur. As the flow passes through the turbomachinery cascade contact is made with walls (hub and casing). This gives rise to another viscous region called the end-walls. The end-wall viscous region is depicted in Figure 3.2. The dominant regions where losses are present limiting the pressure rise and inducing blockage are the corners near the suction surface in the end-walls. Figure 3.3 depicts normalized stagnation pressure downstream of a third-stage stator in a compressor. It can be seen that near the corner region on the suction side, the pressure losses are more pronounced due to the growth of the boundary layer. Flows in those regions are highly three-dimensional and are prone to separation. Additionally, modeling this region is further complicated by the presence of tip vortices due to tip secondary flows.

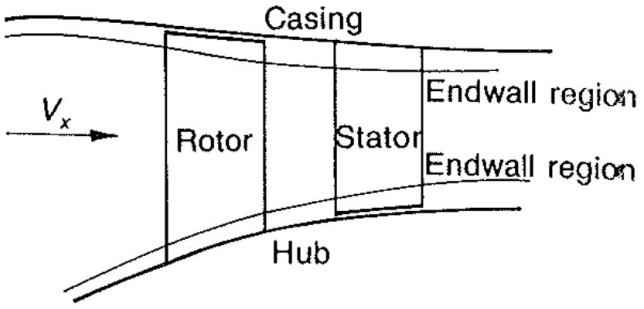

Figure 3.2: End-wall boundary layer in the meridional plane [6].

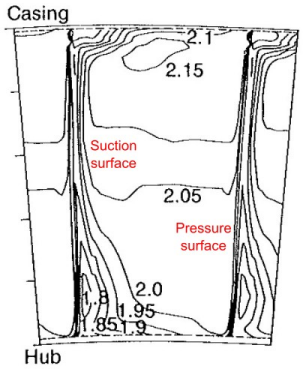

Figure 3.3: Contours of normalized stagnation pressure from a very efficient compressor downstream of a stage. Image adapted from [6].

3.2. Loss mechanisms

Losses in turbomachine cascades are mainly split into 3 parts: profile losses, end-wall losses, and tip leakage losses. In the past, researchers widely used these 3 categories for loss accounting as a means of quantifying the type of loss independently to a certain degree. It is now recognized and accepted that the loss mechanisms are "seldom really independent" [7]. Nonetheless, understanding the physical loss generation mechanisms allows one to correctly assess the degree to which a certain machine can be made efficient. Ideally, one is able to quantify losses and directly able to calculate them. In reality, this is not the case as the general physical understanding of turbomachines losses is still inadequate. That's why researchers and designers rely on experimental and simulated (e.g. CFD Direct Numerical Simulations) results in order to fit a model, which is then extrapolated to produce satisfactory results.

3.2.1. Profile losses

Profile losses refer to the loss generated in the boundary layer near the blades' surfaces far enough from the end walls. This is similar to what is depicted in Figure 3.1. The loss is assumed to be 2-two-dimensional (no secondary flow effects are accounted for) with the addition of losses occurring in the trailing edge, typically referred to as "trailing edge mixing losses". Profile losses are caused due to Reynolds number effects, Mach number effects, geometric parameters, and surface roughness [44]. Some researchers provide quantified models for profile losses, such as the one in [44] which accounts for profile loss using a single coefficient. Denton [7] quantified profile loss using 2 coefficients: boundary layer loss and trailing edge mixing loss. Numerical results show that trailing edge mixing loss is the main cause of profile loss in compressor cascades [59].

Trailing edge mixing

Any fluid that encounters a rate of shear strain results in entropy generation due to viscous shear. Very high rates of shearing occur in blade wakes. This is especially true in turbulent wakes where the viscosity is large. Vortices, leakage jets, and separation all contribute to mixing losses.

Low Reynolds numbers give rise to flow separation and subsequent turbulent mixing in the blade wake as depicted in Figure 3.1. In the wake of the trailing edge, the separated region will give rise to large vortices and lead to increased levels of dissipation and lost work. Test results show that trailing edge losses could reach 1/3 of the total two-dimensional losses in subsonic flows. In supersonic flows, the figure reached 50 percent [33].

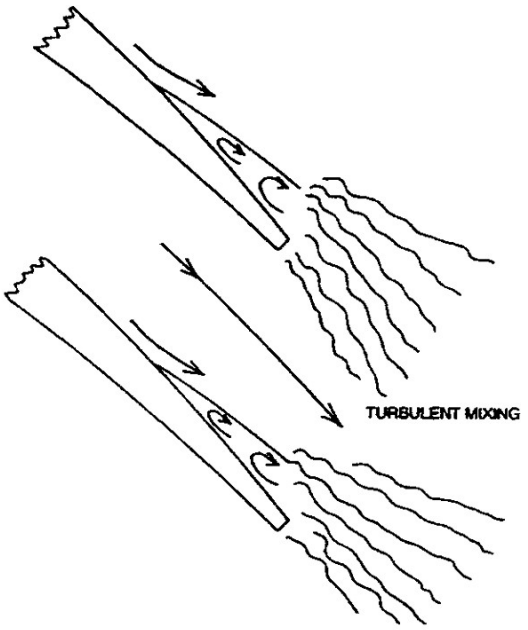

Figure 3.4: Turbulent wake mixing at trailing edge due to separated boundary layer [7].

3.2.2. End-wall losses

The regions that limit the pressure rise, create blockage and generate losses the most are the corner regions between the suction surfaces of the blades and the end wall. Losses in those regions are referred to as end-wall losses. The flows in the end-wall regions are highly complex and three-dimensional. Figure 3.3 depicts stagnation pressure losses near those corner regions. The loss mechanism in those regions is due to the growth of the boundary layer on the casing and their interactions with secondary flows due to tip clearances [44].

The effect is quite major in compressors as they exhibit continuously decelerating flow axially. Throughout the compressor, the boundary layers on the end-walls start to thicken quite rapidly in the first few stages, and the flow becomes less and less uniform. This results in low axial velocities near the hub and tip regions as shown in Figure 3.5. Stalling in those regions becomes more prone and the total work output is reduced.

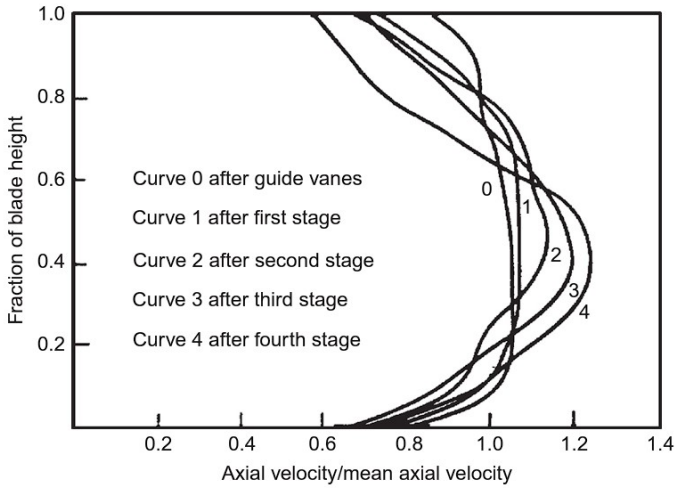

Figure 3.5: Axial velocity profiles in compressor illustrating end-wall boundary layer effect [10].

Cumpsty [6] concludes that in order to quantify end-wall losses one should look for methods involving the full three-dimensional Navier-stokes (i.e. CFD methods) as the fluid interactions are too complex. However, recent efforts in [44] show total loss coefficient estimates for end-wall losses due to friction and secondary flow interactions. The result indicates dependence on momentum boundary layer thickness for both terms which can then be related to the Reynolds number. For instance, the authors provide an estimate that correlates with $Re^{-0.2}$ (a clear inverse dependence, i.e. low Reynolds number correlates with high losses).

3.2.3. Tip leakage losses

Tip leakage occurs as the name suggests in the tips part of rotors. Due to the difference in pressures between the suction and pressure side of the blade, the flow tends to escape through the tip clearances and form a system of bound vortices. Tip vortices induce drag forces and thus, directly result in an efficiency decrease. Additionally, in turbines, the mass flow that escapes the tip clearance does not contribute to power generation. In compressors, the flow that escapes results in a total pressure loss at the end of the stage.

The primary source of tip leakage losses and entropy generation is a result of mixing. Treatment could be expanded for both thin and thick blades as depicted in Figure 3.6. Tip leakage vortices are typically formed on the suction side of the blade and directly cause viscous dissipation. Between the casing and the tip of the blade, an adverse pressure gradient can cause separation on the blade's tip surface. The separation bubble is a region of reversed flow i.e. further viscous dissipation. Moreover, the flow could potentially transition if not already inherently turbulent and cause further losses. However, the mass flow in the tip gap is relatively small and the losses in that gap are likely insignificant [7].

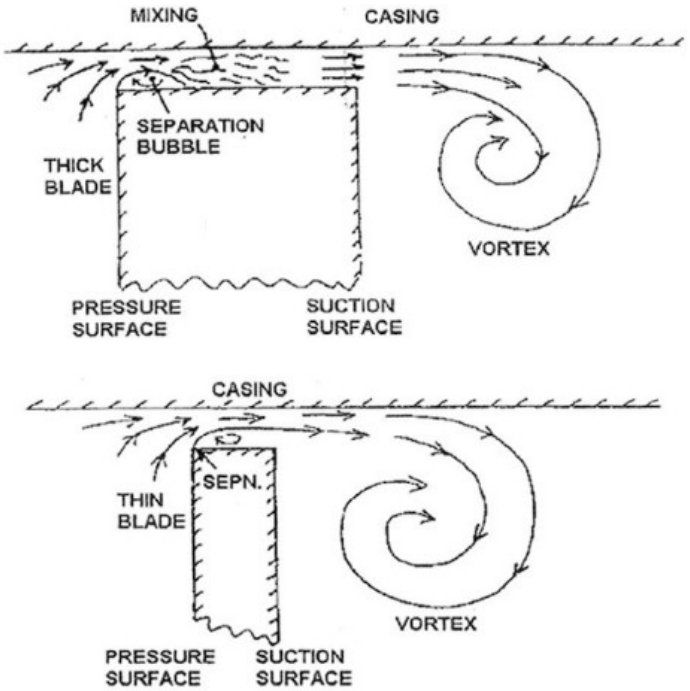

Figure 3.6: Tip leakage flow over the tip of an unshrouded blade. [7]

3.3. Effect of Reynolds number on engine performance

As discussed low Reynolds are associated with losses in turbomachines. This infact will lower the overall engine performance. For instance, the efficient performance of compressors is limited by the growth and separation of the boundary layer over the cascade blades' surfaces [10]. Based on the numerical study by Wang et. al [59], the main cause of performance deterioration due to low Reynolds numbers is the laminar separation bubble occurring at the trailing edge of the rotating blades. This subsequently causes the flows on most of the trailing engine blade surfaces to be in a laminar state [48], which is prone to separation more than in a turbulent state. Severe laminar separation can directly cause rotational stalls greatly affecting the entire engine's performance. In such cases, the engine flow capacity as well as the efficiency drops. The performance deterioration is depicted in Figure 3.7. Additionally, the surge lines of the affected components move downwards affecting the stability of components at normally operable points. In general, low Reynolds numbers have unfavorable effects on engine performance. It is then the engineer's job to understand and quantify those effects to a sufficient level in order to predict the engine's overall behavior.

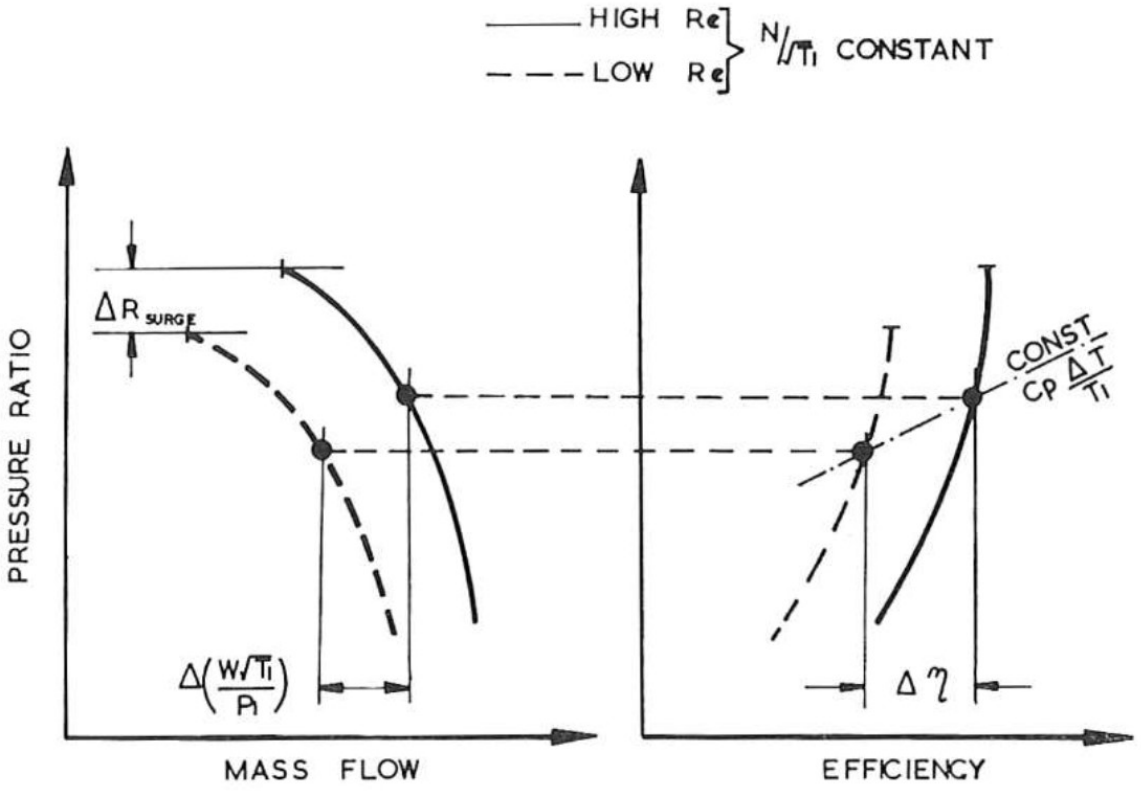

Figure 3.7: Sketch showing the effect of Reynolds number in compressor performance [60]

3.3.1. Flow behaviour in axial compressors and turbines

There is a fundamental difference between the behavior of the boundary layer over the blade surface of a compressor and that of a turbine. The difference is a result of the levels of acceleration and diffusion between the two types of turbomachines. This essentially indicates the need for a separate modeling approach in the treatment of losses due to Reynolds numbers for compressors and turbines.

As the flow passes through the compressor, the static pressure increases between the inlet and outlet. The change is a result of added energy increasing total pressure and diffusion increasing static pressure in the compressor cascade. What particularly affects the boundary layer growth over the blades is the amount of diffusion which tends to produce thick boundary layers and could possibly lead to flow

separation. This observation is for instance the basis on which the Lieblein diffusion factors are based [30][1]. The analysis concluded by Lieblein showed that in minimum loss regions over blade surfaces, the total loss in pressure is mainly attributed to velocity diffusion on the suction side, where the boundary layer thickens [10]. Therefore, the amount of diffusion over a stage possible is limited. High values of diffusion can lead to flow separation causing compressor surge.

Compared to compressors, the boundary layers in axial turbine cascades are more stable and the risk of separation is much lower. This is because the flow within the turbine stage is accelerating. The diffusion factors on the suction surfaces are typically small and the risk of boundary layer separation is low. These characteristics give turbine cascade designs a wide range for low loss performance. Therefore, turbine blades can have a higher loading compared to compressor blades without running the risk of boundary layer separation. Moreover, in modern turbofans, turbine blades are typically cooled through tabs on the blade surfaces. This increases the surface roughness on the blade, which affects the growth of the boundary layer. Increased surface roughness lowers the Reynolds number at which flow transitions and reduces the chances of flow separation [8].

The Reynolds number effect is therefore much more pronounced in compressors than in turbines. Typically the correction for the Reynolds number in turbines is based on the friction loss correlation introduced earlier to calculate inefficiency (i.e. $\left(1-\eta_{\text{tt}}\right) \propto Re^{m}$) for very low Reynolds numbers (values in the ranges $10^4 - 10^5$) [10]. As the boundary layer is not expected to thicken considerably in turbine cascades, no blockage effects are assumed and thus, the mass flow is unaffected.

3.3.2. Reynolds number performance correlations

The relationship between turbomachinery performance and Reynolds number is not theoretically formulated. It is hardly so that the Reynolds number is the sole reason for performance deviation. The arguments presented in this chapter related the losses in turbomachines to the phenomena of boundary layer growth as a result of low Reynolds numbers. However, boundary layer thickness over a surface is a property that could be defined in terms of Reynold's number and other factors such as surface velocity distributions, inlet Mach numbers, free-stream turbulence, flow unsteadiness, and surface roughness also influence boundary layer growth. In order to provide engineering solutions for practical reasons, assumptions are made given the current knowledge and understanding. In certain cases where the Reynolds number changes are quite significant, it can be valid to assume that Reynolds number effects are dominant and shall be correlated with losses [32].

Moreover, the lack of knowledge to establish a formulation of the losses in turbomachines due to low Reynolds numbers requires the use of empirical models. The accuracy of the model is then a question of how reliable the test data is and over what ranges of Reynolds numbers. The correlation of the losses is then presented in terms of efficiency, mass flow, and surge pressure ratio corrections. Correlating pressure ratio is also a possibility and a choice but it is implicitly defined and corrected by correcting efficiency and mass flow. Additionally, occasionally researchers provide two models depending on whether the operating condition is above or below a specific predetermined critical Reynolds number, where flow transitions (see Carter et al. [5]). This is because significant losses are present in the laminar region, especially at the flow separation point.

One note-worthy correlation that is presented here is the Wassel correlation which is based on experiments involving 20 compressors with stage numbers varying between 3 up to 16. The correlation provides corrections for efficiency, mass flow, and surge pressure ratio. Additionally, the effect of the Mach number is also accounted for in the correlation. In general, Reynolds number correlations are based on compressor experiments rather than turbines as the effect is much more pronounced in the former. In any case, if a turbine is operating at very low speeds, it is expected that the effect is not very dramatic and

[1] The Lieblein diffusion factor is a parameter used in compressor cascades preliminary designs in order to account for stage loss and blade loading. High values of diffusion factor around 0.6 and higher run the risk of flow separation.

a correction for efficiency can be done as discussed. In Appendix A, the Wassel correlation application along with another empirical method called the Livinov method [53] are discussed in more detail.

3.3.3. Reynolds corrections in gas turbine simulation tools

Kurzke [26] mentions a Reynolds effect correction method based on various sources. The discussion is also extended for application in performance programs. The method starts by establishing the definition for the Reynolds Number Index (RNI), which is the ratio of the true Reynolds number to a reference Reynolds number typically defined at sea level conditions. Using some clever derivations, the author presents the final form for the RNI in Equation 3.4.

$$RNI = \frac{P}{P_{ref}} \sqrt{\frac{R_{ref} T_{ref}}{RT}} \frac{\mu_{ref}}{\mu} \tag{3.4}$$

The method then depends on a pipe flow analogy established by the author in order to describe the Reynolds number effect on the performance of turbomachinery. The pressure loss in pipes is described by a Moody chart [20]. The analogy then quantifies the turbomachinery losses with varying Reynolds numbers. The Moody chart for estimating the Reynolds effect is shown in Figure 3.8. Equation 3.5 presents the underlying equation used. The value for n is not well defined and is dependent on the component being used. According to Kurzke [26], the variation of the reported figures for n in literature should not be shocking, as they are based on different engines that are also from different generations. Nevertheless, general remarks could be made. From Figure 3.8, a steeper slope for losses is associated with the low Reynolds number region compared to the middle region (i.e. $n = 0.5$ and $n = 0.2$ lines). The reason for the high losses in the low Reynolds numbers region is that the flows associated with them are mainly laminar with a larger boundary layer more prone to separation and higher losses. Moreover, the losses beyond a certain Reynolds number seem to be constant. This is the point where the flow is highly turbulent and laminar separation is improbable.

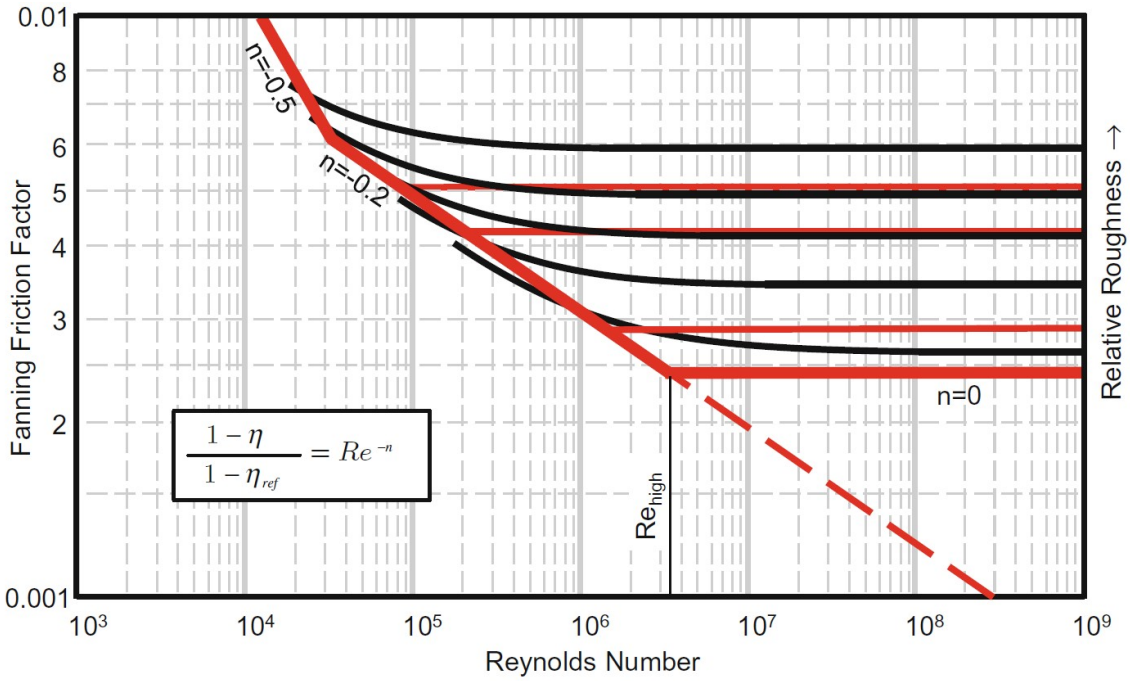

Figure 3.8: Moody chart relating turbomachinery losses to Reynolds number [26]

$$\frac{1-\eta}{1-\eta_{ref}} = \left(\frac{Re_{ref}}{Re}\right)^{n} = \text{Loss factor} + 1 \tag{3.5}$$

The efficiency correction $f_{1-\eta}$ at a certain point is defined in Equation 3.6. The ratio of loss factor represents the change with respect to the loss factor at RE_{high} (point beyond which profile losses variation is negligible). The value a stands for the percentage of loss due to friction.

$$f_{1-\eta} = 1 + \frac{a}{100} * \left(\frac{\text{friction factor @ Correction point}}{\text{friction factor @}RE_{High}} - 1\right) \tag{3.6}$$

In performance programs, the Reynolds effect correction is then directly implemented to the component maps parameters. In Equation 3.7, the efficiency correction for a value η_{map} is defined. For the mass flow correction, kurzke suggests using a fixed factor based on the efficiency correction. The ratio $f_{massflow}/f_{efficiency}$ is between 0.4 and 0.6.

$$\eta = \eta_{map}\left(1 - f_{1-\eta}(1-\eta)\right) \tag{3.7}$$

3.3.4. 0D/3D correction method

A novel method for Reynolds number correction is presented by Tang et. al [48]. The method is based on 0D/3D iteration simulations. The 0D engine performance simulation is used to provide the component's inlet and outlet boundary conditions, which are in turn needed for the 3D simulation. The 3D simulation is CFD based and provides high-fidelity results, which are passed to the 0D model to modify the component maps. The Reynolds effect is then quantified by iterating a loop with the two simulation models until satisfactory results are reached. The results shown indicate agreement with high-altitude experimental data. From an end goal standpoint, this method seems to be full-proof. However, creating accurate CFD simulations for modern complex engines with multi-stage components is a very complicated task. Precise geometric descriptions of the turbomachinery profiles are not readily available. Engine deterioration, surface roughness, cooling, and bleed valves all need to be taken into account in order to create a reliable enough model. Additionally, new engine performance matching methods are computationally heavy (e.g. Neural networks, genetic algorithms, particle swarm optimization, etc.). Incorporating CFD simulations as an addition to the performance matching problem will increase the computational time significantly. Moreover, an extra layer of uncertainty in the overall procedure is added. Additional complications can quickly emerge regarding issues such as mesh refinement, simulation fidelity (i.e. RANS or LES), turbulence model, or convergence criteria.

3.3.5. Performance matching

In the context of performance matching using numerical gas turbine system simulation (0D modeling), the Reynolds number effect can be ambiguous due to the underlying methodology. Independently defining the Reynolds number effect and isolating it depends on the approach chosen for the matching problem. Typically, in performance matching, an on-design point is matched by solving an aerothermodynamic problem based on a single operating point that is then used for component maps scaling [45]. Component maps are then adapted in an iterative process to meet a number of off-design operating points. A key element in the matching process is the data used and it is what causes this ambiguity. For instance, a great match can be achieved using a state-of-the-art method such as the one presented by [28], given that the problem is well-defined and the dataset is reliable. Basically, such an employed method will attempt to match the data regardless of the underlying effects. For example, assume that the data set used is based on flight data recorded for cruise conditions. Additionally, assume that the

data set is completely reliable and all the key parameters (e.g. temperature and pressures along the gas path) are readily available such that the component matching problem is well-defined. The resulting numerical model will be based on maps that carry the underlying effect of Reynold's number inherently. Model errors are then only present (assuming that the Reynolds effect correction is not taken into account) at different operating Reynolds numbers (i.e. different altitudes or flight speeds). This poses a definitive challenge in processes where performance matching is based on for instance test cell data in static sea level conditions and attempting to validate results based on operating on-wing data for the entire flight envelope (which includes high altitude data points). In order to systematically obtain valuable and satisfactory results for the entire operating envelope, the Reynolds number effect should be systematically isolated and accounted for.

3.4. Nozzle losses

Nozzles are the last components in the gas flow paths of aero-engines. Typically two separate nozzles exist for turbofans: the core nozzle and the bypass nozzle. As with any non-ideal component, nozzles are not fully efficient in converting the available energy into actual work or thrust. Nozzle losses are generally due to many factors. Some of these factors are listed below.

- **Friction losses** - As the gas flows through the nozzle, friction is encountered with other fluid particles and the nozzle walls. This friction leads to heat energy dissipation which reduces the kinetic energy. Thus surface roughness and viscosity are major contributors to friction losses.
- **Shock losses** - In flights that reach the supersonic flow regimes, shock waves may occur within the nozzle [2]. Shock waves are generally characterized by reductions in kinetic energy and pressure, adversely affecting the nozzle performance.
- **Heat transfer losses** - High temperatures in nozzles can be reduced as a result of heat transfer to the surroundings or cooling systems [11]. The heat loss can be attributed to thermal energy that could have been converted to useful thrust.
- **Flow separation and boundary layer effects** - In adverse conditions flow separation could occur, detaching the flow from the nozzle walls. This quickly leads to very unfavorable conditions with increased levels of friction and viscous losses [18]. Additionally, a boundary layer can form on the nozzle walls, creating drag and reducing performance.

Typically in performance matching several assumptions are made with regard to some of the loss types due to insufficient information and in order to simplify the problem. Generally, the nozzle performance is depicted by characteristic parameters that capture the non-ideal expansion such as thrust coefficient (C_T), discharge coefficient (C_D), or Velocity coefficients (C_V). A description of the coefficients along with their quantification method is discussed in Section 3.5.

3.5. Nozzle coefficients correction

Nozzle losses in gas performance programs are typically represented by a coefficient of discharge (CD), thrust (CT), or velocity (CV) in Equation 3.8, Equation 3.9, and Equation 3.10, respectively [13].

$$\text{CD} = A9_{\text{effective}} / A9_{\text{geometric}} \tag{3.8}$$

$$\text{CT} = \text{FG} / FG_{\text{ideal}} \tag{3.9}$$

$$CV = V9/V9_{ideal} \tag{3.10}$$

CD represents the effective area that is available for the mainstream flow to pass through, which directly affects the mass flow. The coefficient quantifies the effect of blockage due to aerodynamic separation on the nozzle walls. CV represents the total pressure loss upstream of the nozzle exit, and the effects of nonuniform temperature, pressure, or velocity in the nozzle exit plane [26]. According to some definitions such as the one presented in [13, 16], CV is equivalent in definition to CT. Meaning that the accounting for the loss mechanisms is the same for both cases. However, this is all dependent on how the correction is applied in practice and the expansion mechanism in the nozzle. Kurkze [26] makes the distinction between CT and CV very clear, at least for application purposes. The correction for CV and CT are exactly equivalent under the assumption that the flow at the nozzle exit is subsonic. If the pressure ratio is beyond the critical value (around 1.86) a pressure term in the thrust equation needs to be accounted for. In this case, the thrust coefficient correction will take into account the deviation of the nozzle geometry for a non-ideal process (the second term in Equation 3.11). Kurkze recommends avoiding this type of correction as it is a different loss mechanism that should be corrected separately. Then, the correction for CV (which Kurkze calls Thrust coefficient C_{FG}) can be applied using Equation 3.11 (CT as defined in Equation 3.9 is referred to $C_{FG_i deal}$).

$$F_{G8} = W_8 V_8 C_{FG} + A_8 (P_{s8} - P_{amb}) \tag{3.11}$$

Kruzke [26] provides the correction relation for CD and CV (C_{FG}) which is adopted from Grey and Wilsted [16] shown in Figure 3.9 and Figure 3.10, respectively.

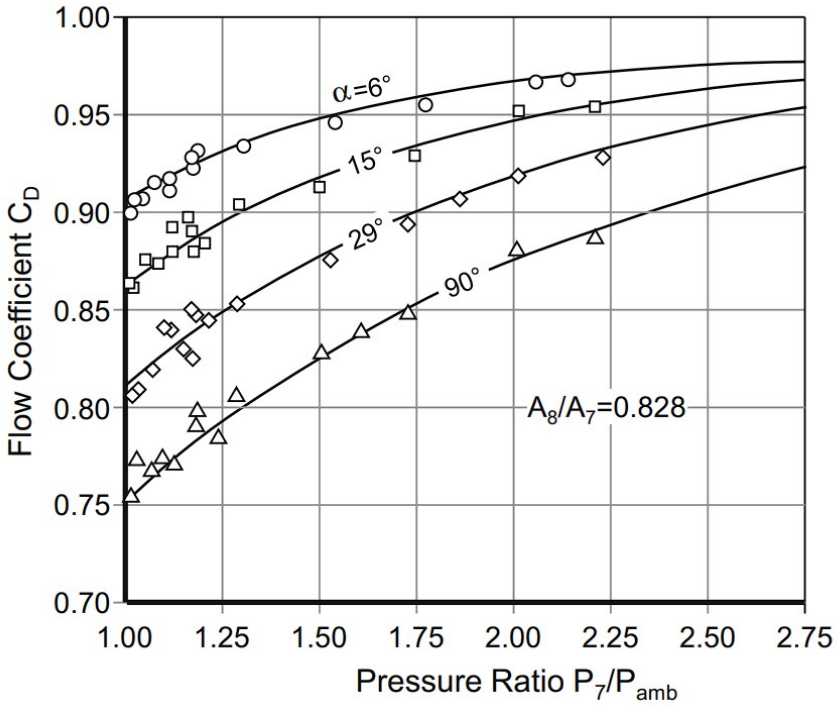

Figure 3.9: Discharge coefficient correction for convergent nozzles [16]

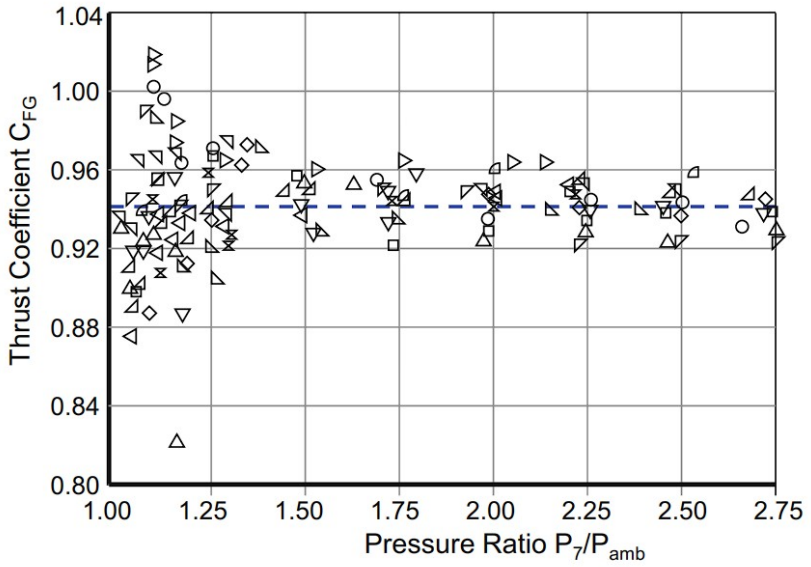

Figure 3.10: Velocity coefficient correction for convergent nozzles [16]

Walsh and Fletcher [13] provide another correction relation for the CD correction shown in Figure 3.11. The difference between the CV and CT corrections are not distinctly presented and therefore is assumed that the authors are only considering the nozzle thrust to have no pressure term. The correction relation is shown in Figure 3.12

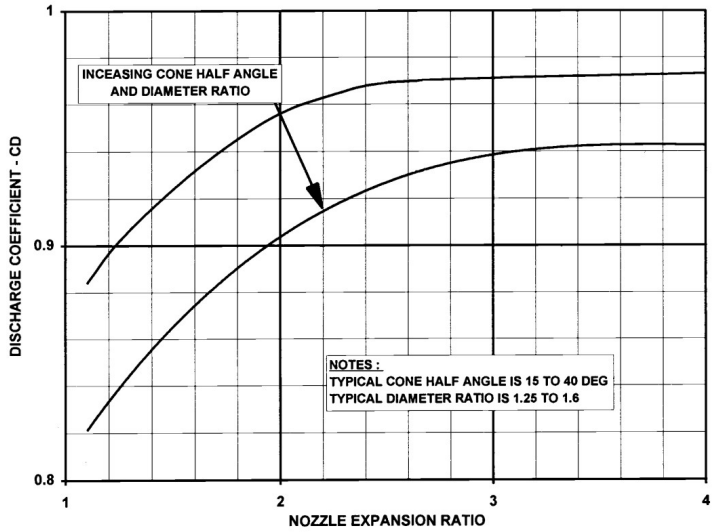

Figure 3.11: Discharge coefficient correction for convergent nozzles [13]

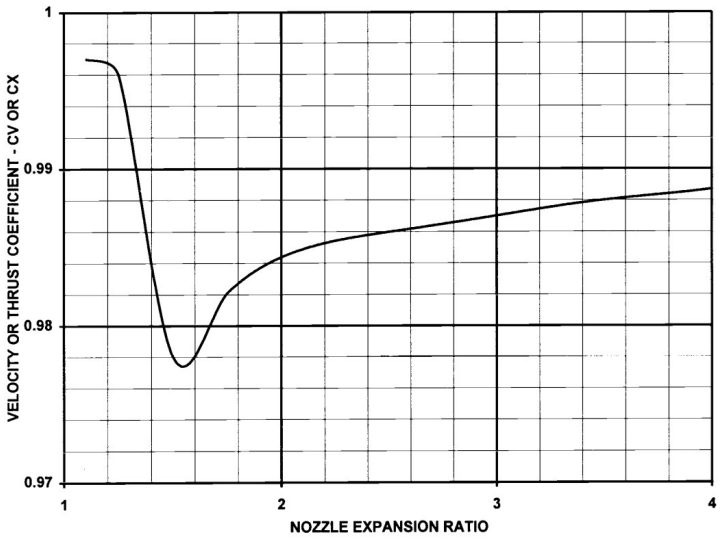

Figure 3.12: Velocity coefficient correction for convergent nozzles [13]

The difference between the reported corrections relations is not explicitly mentioned. It is assumed that it is due to differences in the types of engines used or testing conditions for the correlation data.

4. GEnx-1b turbofan engine model

The main analyses outlined in this project are conducted on the Genx-1b turbofan model. The model is used to form the basis of the study for establishing the "proof of method". The methodology discussed in the work presented is generalizable. However, the model itself is a specific element of the problem. It is important to identify the unique specifications of an engine. A turbofan model can have a unique architecture and a set of assumptions that influence the outcomes of the conducted study. This chapter focuses on the Genx-1b model in order to lay a foundation for the enhanced modeling methodology. First, the systematic approach used to build the model is discussed in Section 4.1. Then, an overview of the GSP model is outlined in Section 4.2. The current Reynolds correction method employed in the model is discussed in Section 4.4. Finally, the model deviation at off-design in simulating on-wing data is discussed in Section 4.5.

4.1. Systematic modelling approach

The current modelling approach is based on a multi-step systematic method mainly constructed using the classical on-design/off-design modelling approach (see [61]) using test cell data with an additional step of model matching using on-wing data.

The first step in the process is to determine the design point. Due to the nature of the under-determined problem, having too many unknowns for the number of equations, due to the lack of all the gas path measurements (i.e. temperatures, pressures, etc.) in the engine, multiple solutions exist for the design problem. In the current approach, this is dealt with by employing an optimization framework that attempts to minimize an objective function to produce a solution for a chosen design vector meanwhile violating the problem constraints as little as possible. The additional set of constraints imposed is the key to solving the under-determined problem. Additionally, the design vector solutions are bounded in order to avoid unrealistic solutions for the specific engine model. The objective function is the root mean square (RMS) error function that uses the model's simulated performance parameters and the test-cell target parameters. The minimization problem utilizing genetic algorithms (GA) is then attempted until satisfactory results are achieved. In the cases where non-satisfactory results are reached, bounds are adjusted or the GA optimizer settings are changed.

The second part of the process is the off-design modelling. This is done by tuning or adapting the component maps in an optimization framework employing GA. The design vector in this case is composed of the scaling polynomials coefficients (see Section 2.3, Li et al.'s method) for every component map. No constraints are required for the map adaptation but several bounds are imposed to avoid non-physical maps. The objective function was once again based on the RMS error function using the available test cell data points. The key challenge in off-design modelling setup is the requirement for good reference maps for adaptation. The quality of the map and its similarity to the actual map in terms of technological level is of crucial importance to guarantee a good solver convergence with a possible physical solution. The component maps are then adapted until satisfactory results are achieved. In the cases where non-satisfactory results are reached, bounds are adjusted, GA optimizer settings are changed, or the map design point is replaced.

The outcome of this systematic approach is a model that represents test cell data with high accuracy. For instance, the maximum mean error of gas path calculation of the developed GEnx-1B model at the design point is around 0.45% and at the off-design conditions is around 1%. However, the model accuracy starts to drop when flight conditions are simulated and on-wing data is compared. In the end, the purpose of the model is to simulate the fleet's trajectories with high accuracy. Therefore, a logical continuation of the project is to develop an enhanced method that improves the model's accuracy in operational flight conditions.

4.2. GSP model

The GSP model for the project's investigation is based on the work done by Ramdin [40], where the model was created and verified using test-cell data of the GEnx-1b. The model's off-design calculations were matched through reverse engineering of the maps. The model is shown in Figure 4.1. In terms of the model architecture, the main components of the actual engine resemble the model, except for the fan core and booster stages, which are combined. This treatment is the recommendation by Kurzke [26] when the sensor data between the fan core and booster are missing. Work in the past [17, 35] has shown that this indeed improves the model's accuracy.

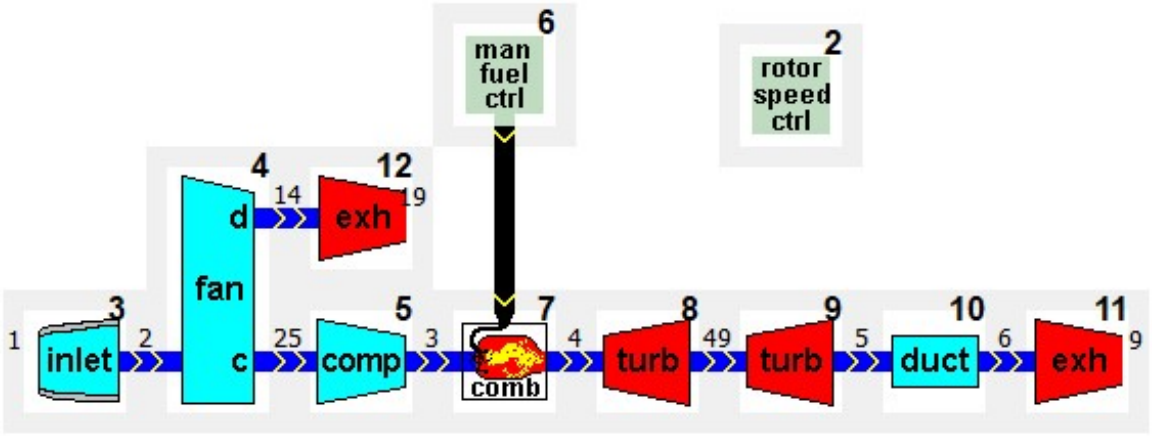

Figure 4.1: GEnx-1b turbofan numerical model in GSP.

The model also makes use of the rotor speed control block. In this case, the engine performance is controlled through the N1 shaft. This consequently makes the fuel flow a free state that is solved implicitly to maintain the power needed to achieve the N1 rotational speed. The model is then used externally through the GSP API. The model simulation inputs are shown in Table 4.1. The inputs are used to simulate off-design steady-state points, which are described by the ambient conditions and the N1 corrected speed. Additionally, the extracted power from the HPT for auxiliary use is indicated. Using these parameters is sufficient to simulate all the gas path variables from the model. However, for model matching, only specific parameters that are specified in Table 4.2 along the gas path of the actual engine, are available from the GEnx-1b CEOD. These parameters are used as *target* parameters, which is the basis of the model-matching procedure. The lack of all gas path parameters is ultimately the reason why model matching is challenging, that is the problem is mathematically under-determined.

Table 4.1: Input parameters used for the steady-state OD simulations.

Simulation input parameter
T0
P0
Mach
N1c
Extracted power

Table 4.2: Simulation output target parameters used to compute model error.

Target parameters
TT25
TT3
Ps3
TT49
Wf
N2

4.3. Model assumptions

The section provides a list of the assumptions made to create the GEnx-1b model adapted from [40].

- The model merges the fan core and booster into one module in GSP. This has been reported in the past to increase accuracy due to the missing data measurements between the two models.
- The effects of variable geometry, which are the Inlet Guide Vanes (IGV) and the Variable Stator Vanes (VSV), are assumed to be captured by the performance maps.
- The effect of the variable bleed valve (VBV) and transient bleed valve (TBV) are neglected in the analyses. Their positions are assumed to be very close to the high power settings [40].
- The model generated using the data of one reference engine is representative of the entire pool of engines.
- The model's design point is fitted to take-off conditions. This was done using test cell sea level static conditions. The Off-design fitting was also based on test cell sea level static conditions.
- The combustor pressure loss, the combustion efficiency, and the mechanical efficiencies in the model are assumed to be constant.
- The chosen design point on the component maps is assumed to resemble the true design point with high accuracy. On this basis, the off-design fitted map built using the scaling procedure is valid at any operable off-design point.

4.4. Current Reynolds correction method

The Reynolds effect implementation in GSP is based on the implementation provided by Kurzke discussed in Section 3.3.3, which is also implemented in GasTurb [1]. The method works by specifying loss factors at RNI (check the definition in Section 3.3.3) values. The loss factors are applied directly to the efficiency and mass flow values of the component. Moreover, the losses at different Reynolds numbers are based on a linear interpolation between both values. Clearly, the method has limitations. Firstly, the accuracy of the method is heavily limited by the number of RNI/loss factor data points available, if any are available in the first place. Secondly, as established in Chapter 3, the Reynolds number correction is different for a compressor and a turbine (i.e. mass flow losses and efficiency due to low Reynolds numbers are not as significant in turbines compared to compressors). Thus, the method does not offer flexibility for component type-specific corrections. Lastly, the method lies heavily on correlations that can be based on different types of turbofans, with different ratings and number of stages.

This current Reynolds number implementation calls for the urge to investigate a more engine-specific method, that offers sufficient flexibility to take into account different turbomachine types. Additionally, the method should consider corrections per turbomachine component (e.g. corrections for the LPC should be different than the HPC for the difference in the number of stages, and position in the gas path that influence inlet temperatures and pressures.) Finally, the method should also offer higher fidelity (accuracy) by basing the corrections on higher-order functions.

4.5. On wing / off-design model deviation

As discussed, the model was originally fitted on test-cell data, and a good match was achieved. Now considering simulating on-wing data, a singular flight is first chosen for analysis. The chosen flight and the motivation behind the flight choice are discussed in more detail in Section 6.1. First simulating the original model without any modification (i.e. calibrated on static test cell conditions), it can be seen in Figure 4.2, that the model error can be as significant as 5% in fuel flow. More importantly, the error at take-off is higher than expected, as the model is supposedly fitted to take-off conditions and is highly accurate at test cell conditions. This discrepancy can be attributed to engine-to-engine differences, installation effects, or data acquisition system errors. In order to correct this difference, a calibration step (discussed in Section 6.3) is needed such that the model represents take-off conditions correctly.

[1] https://www.gasturb.com/

The result is shown in Figure 4.3. It can be seen that by calibrating the model to take-off conditions, the model error of further points in the climb and cruise deviates. The error trend is similar to what Ramdin [40] reached in the validation step with the on-wing data of the same engine used for fitting the model. Thus, a new methodology is required as an additional step that accurately simulates on-wing flight conditions away from take-off conditions.

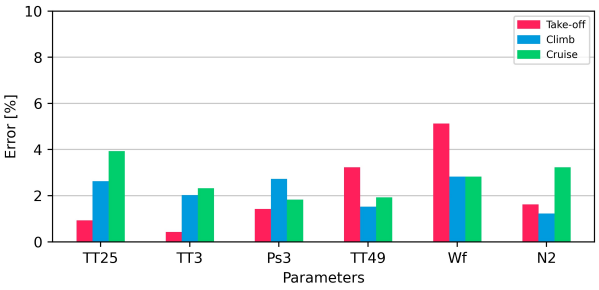

Figure 4.2: On-wing simulated flight error without take-off conditions calibration.

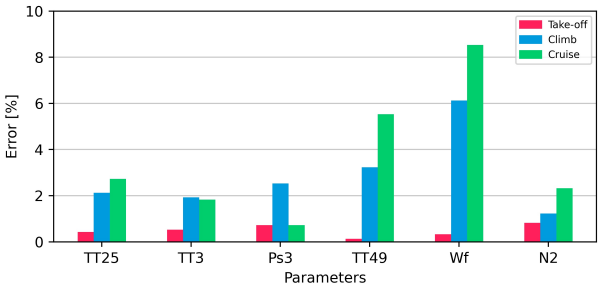

Figure 4.3: On-wing simulated flight error with take-off conditions calibration.

5. Component performance models scaling

In order to represent components in off-design conditions, models rely on component maps or auxiliary functions. In the case of turbomachinery components, maps are used to depict the engine performance. In the case of propelling nozzles, loss coefficients can be utilized. This chapter overviews the methods, and models that simulate off-design conditions for turbomachines and propelling nozzles. The discussions presented are limited to turbomachinery and nozzles due to the potential model accuracy gain in utilizing the correct methodology in modelling their performance. Moreover, the chapter discusses the methods used in order to tweak the components' performance in off-design, a major tool in the off-design matching procedure. The discussions for turbomachinery and propelling nozzles are presented in Section 5.1 and Section 5.2, respectively.

5.1. Turbomachinery

Turbomachinery performance is quite complex with many underlying effects [10]. In modelling problems, their performance is depicted by specific component maps. These maps are largely the backbone of the off-design simulation and influence the outcome significantly. This section overviews how the component maps are represented in numerical solvers as well as how the design point and off-design scaling are applied.

5.1.1. Map representation

During the off-design cycle calculation components performance are represented by maps. In high-speed spool speed regions of the compressor maps, the lines are nearly vertical. This means multiple solutions for the pressure ratio exist for the same corrected mass flow and spool speed. Additionally, the surge region creates problems in the matrix representation of the maps. A lot of entries would be "not a number". Therefore, the beta lines (an auxiliary parameter) are introduced and used to represent the maps such that performance parameters are uniquely represented and all the map matrix entries are valid values.

What is of importance in the off-design analysis is realizing that pressure ratios, mass flow, and efficiencies are all functions of the beta value and the spool speed (i.e $\pi, \dot{m}_c, \eta = f(\beta, n_c)$). The representation of the performance parameters as functions of beta and corrected spool speed is shown in Figure 5.1, Figure 5.2, and Figure 5.3, for a generic compressor and in Figure 5.4, Figure 5.5, and Figure 5.6 for a generic turbine.

In off-design conditions, the numerical simulator needs to find a set of off-design state variables. From these state variables, all other parameters can be solved. The flight conditions and the map performance values are then used as boundary conditions and source terms in the equations. The state variables are then solved iteratively to satisfy the conservation laws. The conservation laws are represented in error functions, which are part of the off-design iteration loop. The loop is depicted in Figure 5.7. In case the error function accuracy is not satisfied the state variables are altered in the next iteration until the simulation converges.

In the off-design process, the state variables of the component maps are β and N_c. This means in order to satisfy the conservation laws appropriate (β, N_c) are needed. This means that the pressure ratio, mass flow, and efficiencies are in fact part of the loop and multiple combinations are tested until the solver converges.

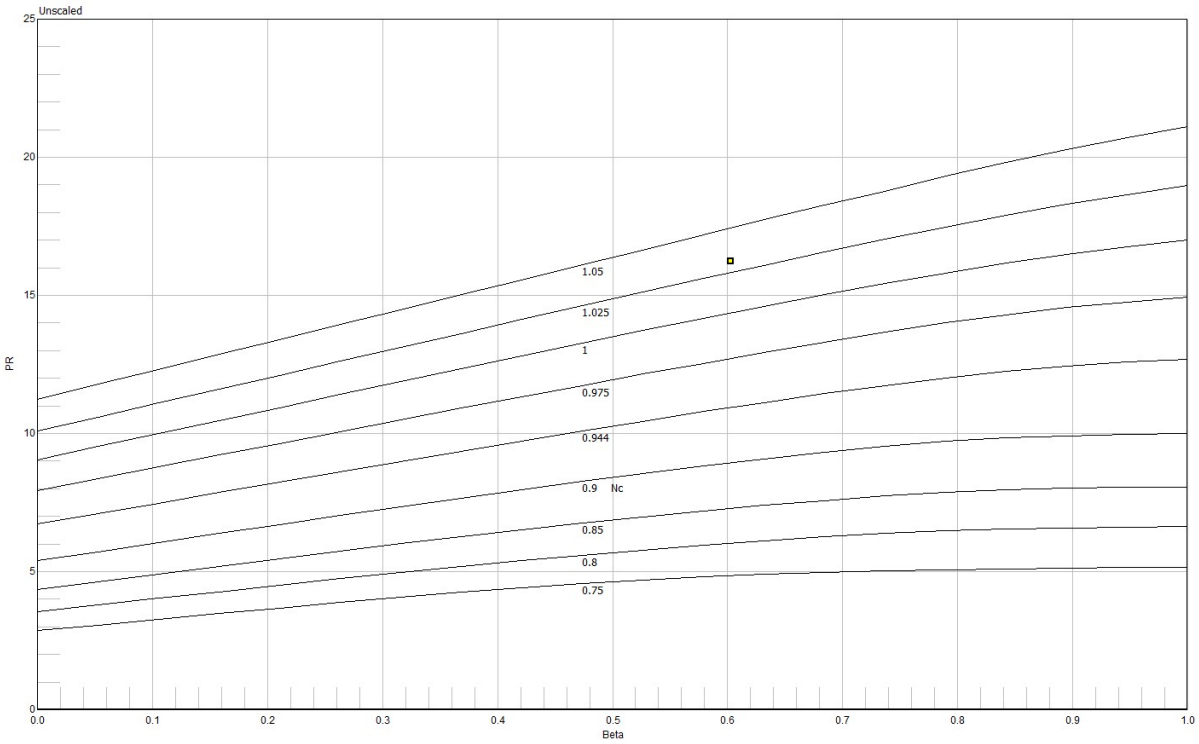

Figure 5.1: Generic compressor pressure ratio vs Beta lines variation with Nc. y-axis: PR [-], x-axis: Beta [-].

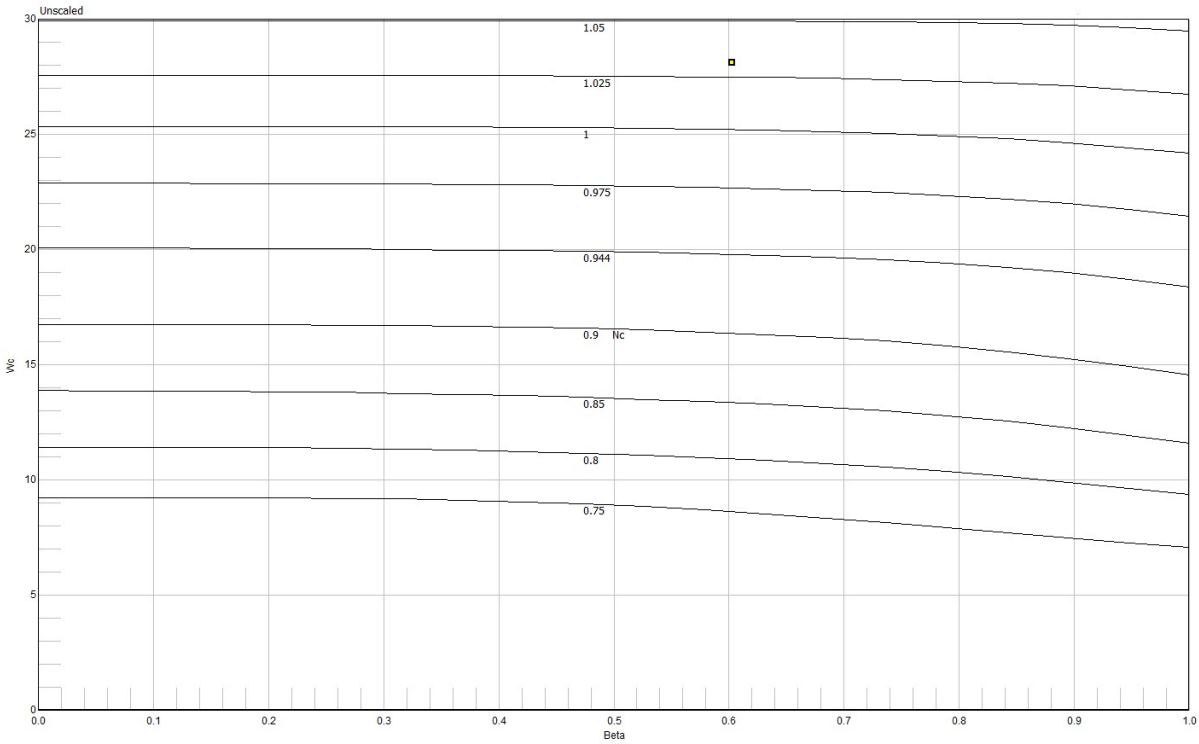

Figure 5.2: Generic compressor corrected mass flow vs Beta lines variation with Nc. y-axis: Wc [kg/s], x-axis: Beta [-].

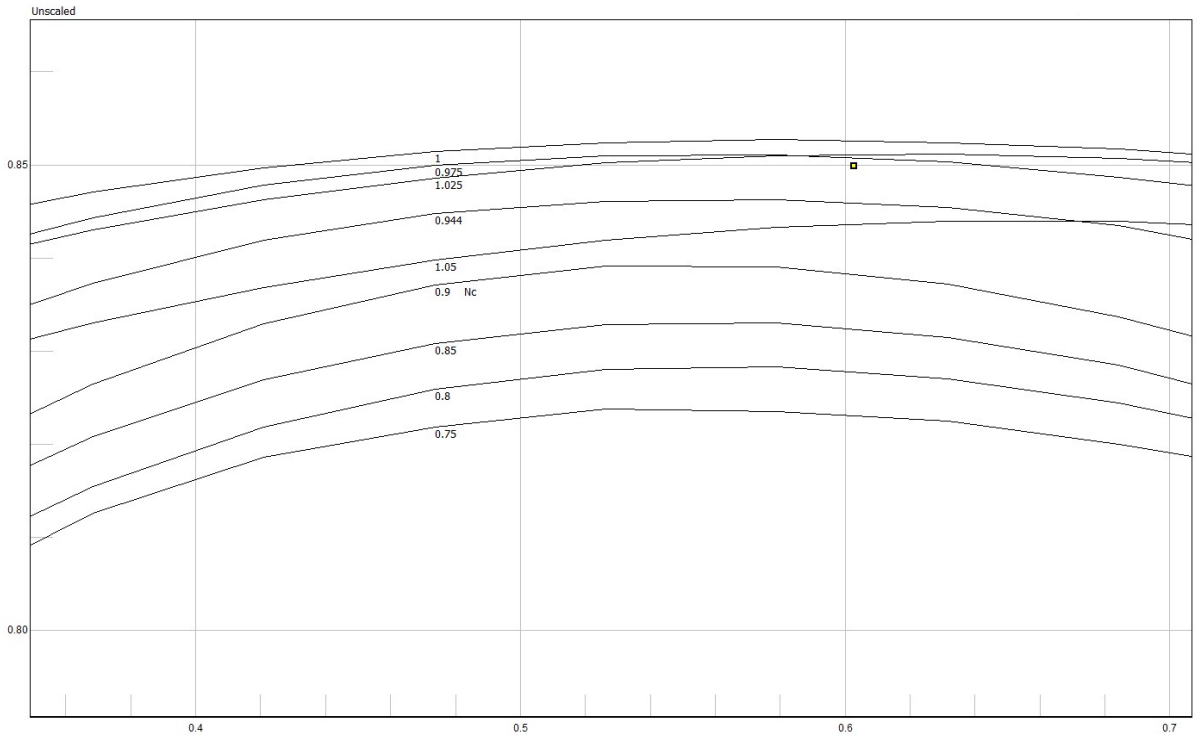

Figure 5.3: Generic compressor efficiency vs Beta lines variation with Nc. y-axis: Efficiency [-], x-axis: Beta [-].

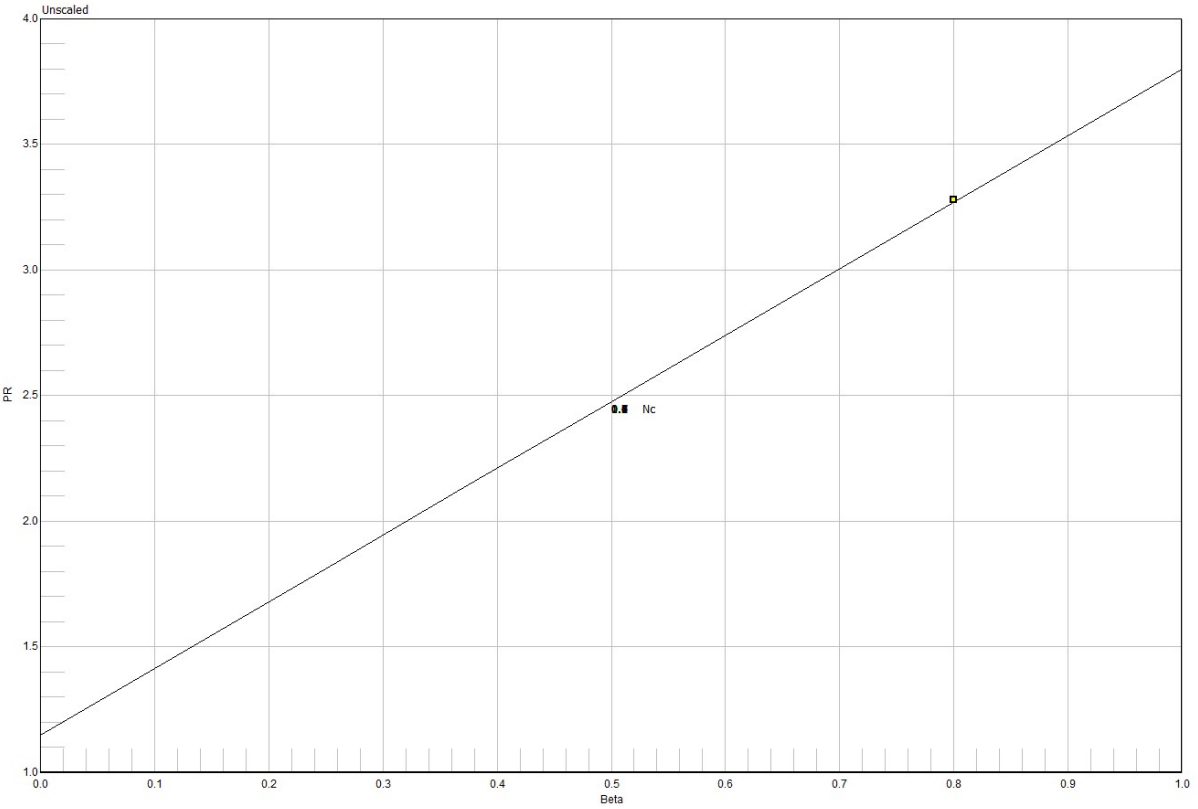

Figure 5.4: Generic turbine pressure ratio vs Beta lines variation with Nc. y-axis: PR [-], x-axis: Beta [-].[1]

[1]The pressure ratio can be seen to be independent of the spool speed. This is because the beta lines in the generic turbine map (y-axis: $\dot{(}m_c$) vs x-axis: π) are all vertical.

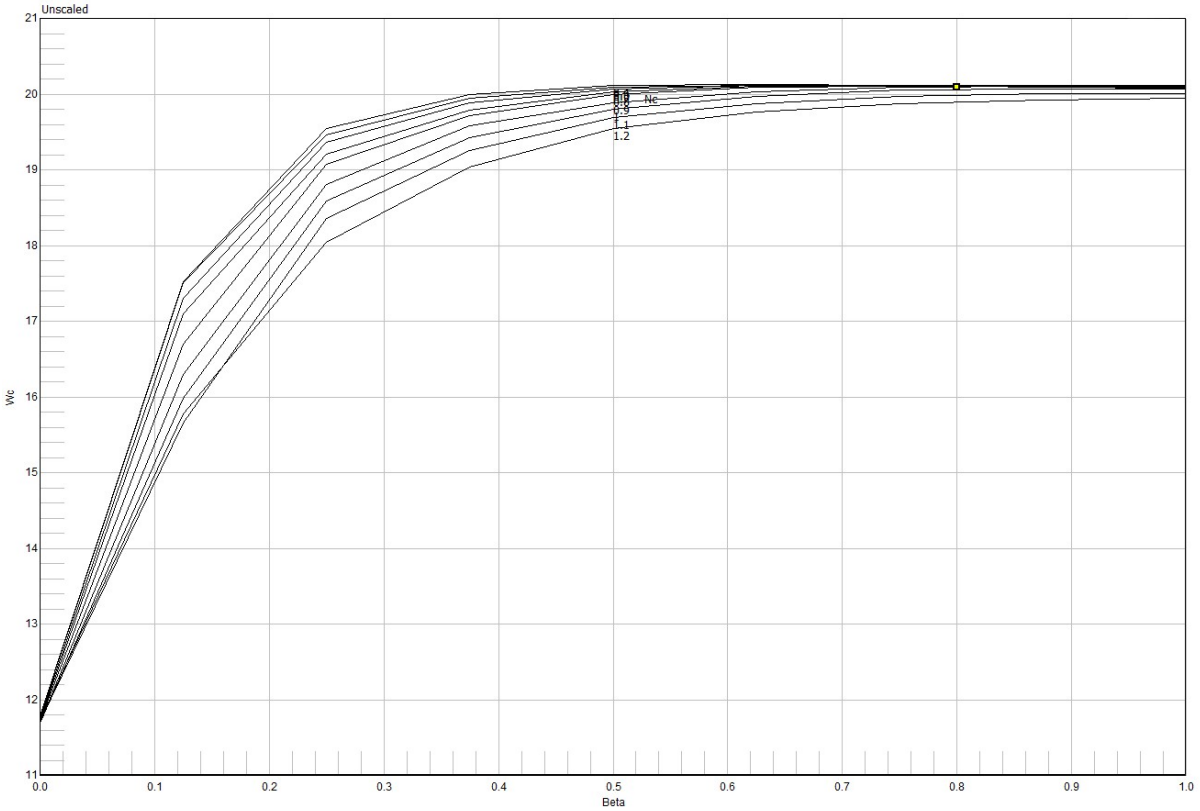

Figure 5.5: Generic turbine corrected mass flow vs Beta lines variation with Nc. y-axis: Wc [kg/s], x-axis: Beta [-].

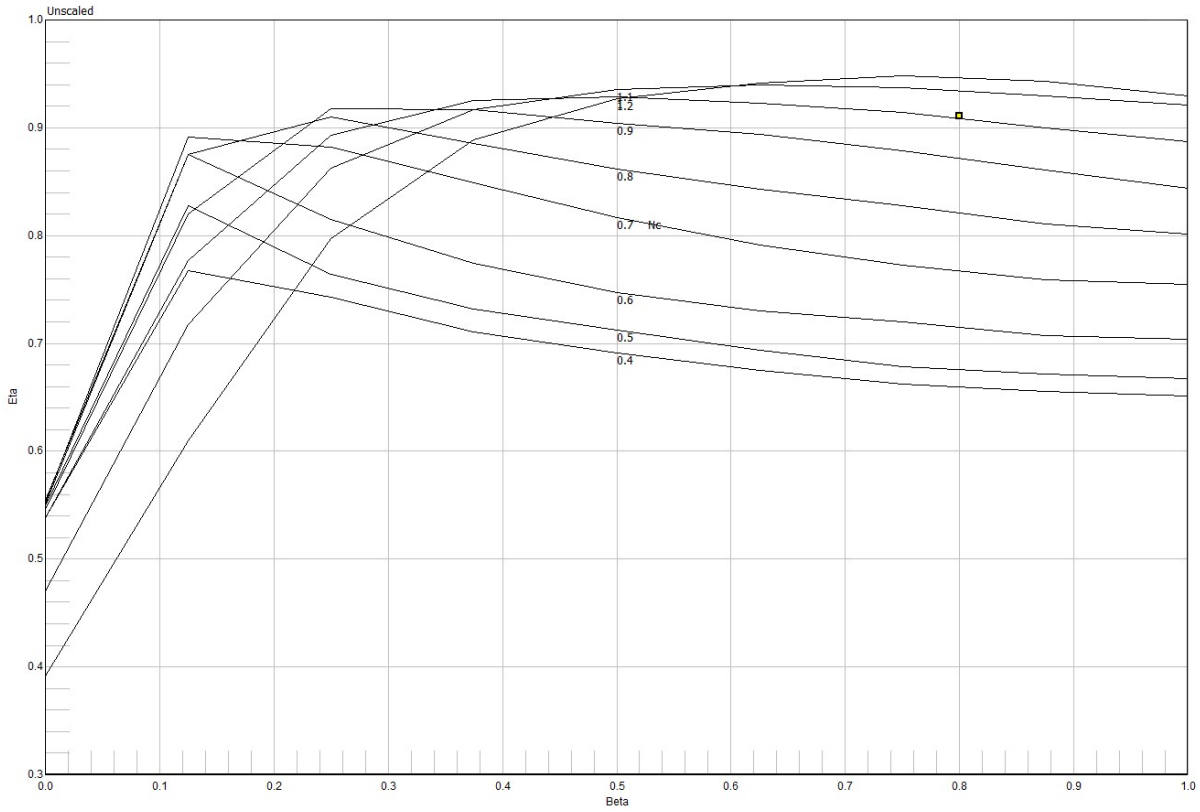

Figure 5.6: Generic turbine efficiency vs Beta lines variation with Nc. y-axis: Efficiency [-], x-axis: Beta [-].

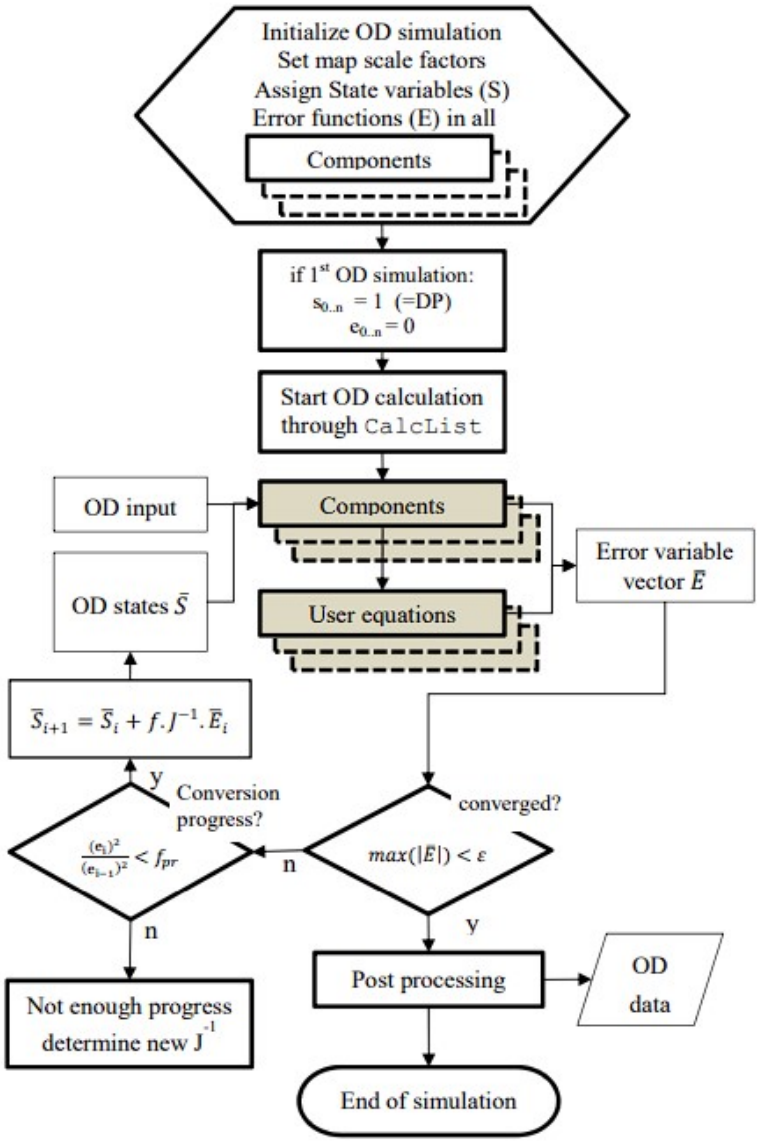

Figure 5.7: Generic GSP Off-Design calculation procedure [57].

5.1.2. Design point map scaling

The performance of turbomachines at off-design operation points is depicted by component maps. These maps are guides for relating the component's pressure ratio, and efficiency, to the mass flow and spool speed. In system modeling, the cycle reference point is first calculated prior to any off-design calculations. This point is also typically referred to as the design point. The design point is crucial for off-design design calculations as it is used to scale the "unscaled" map. This type of scaling is referred to as *design point scaling* and is useful for generically obtaining engine performance independent of the engine's size.

Take for example the unscaled map of the GEnx-1B model HPC shown in Figure 5.8. In order to obtain the scaled version shown in Figure 5.9, design rotor speed, pressure ratio, efficiency, and mass flow need to be set. Additionally, the design point on the unscaled map needs to be specified. In GSP, this is done by specifying a design beta value and design rotor speed [2]. The obtained map is a scaled version that is applicable for off-design performance calculations.

[2] See [40] for a detailed review on map beta lines representation.

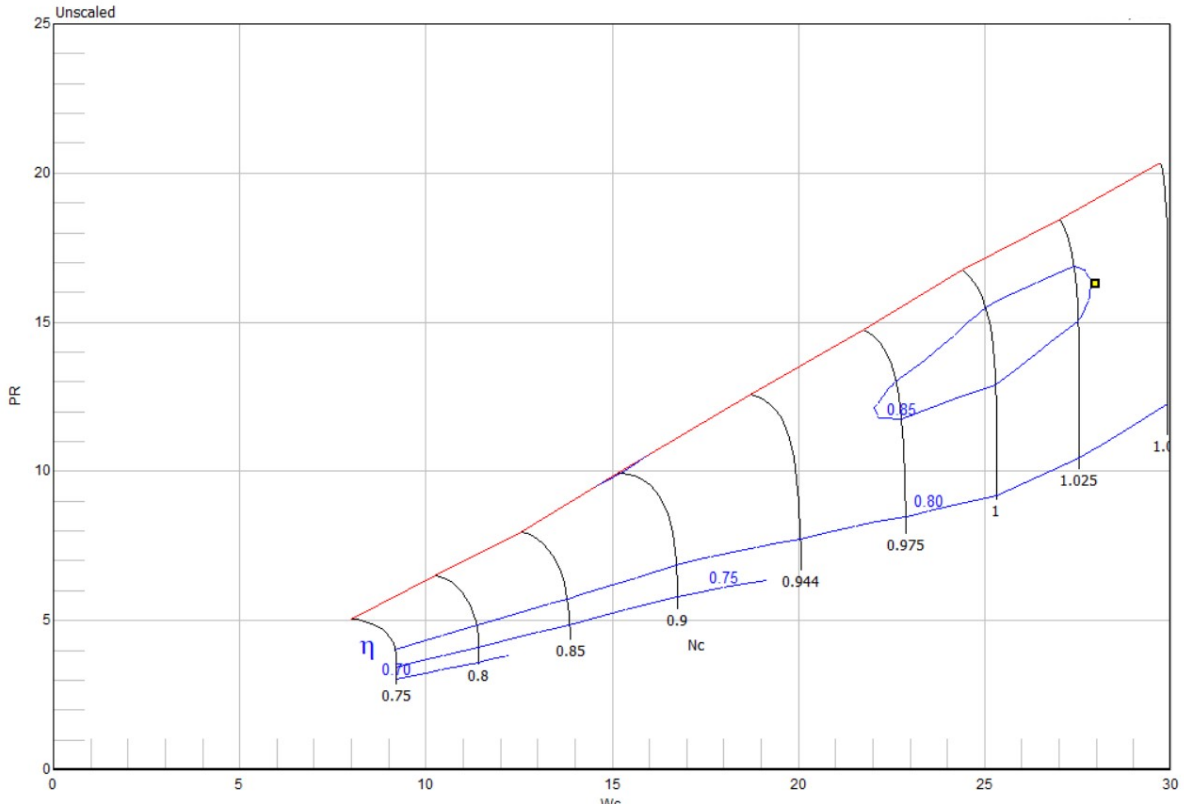

Figure 5.8: Unscaled HPC component map. Image obtained from GSP GEnx-1B model.

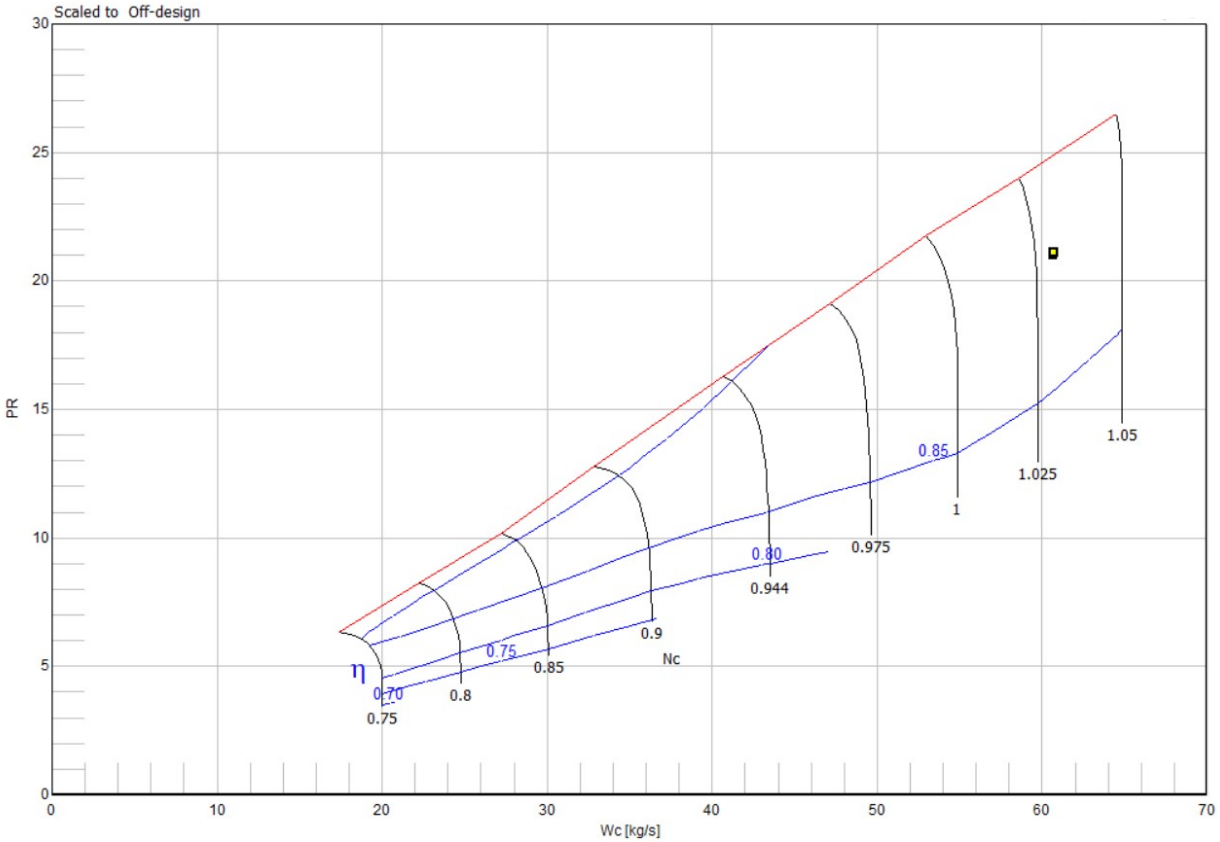

Figure 5.9: Scaled HPC component map. Image obtained from GSP GEnx-1B model.

5.1.3. Off-design maps scaling

An important outcome of the previously mentioned design point scaling is a limitation in off-design modelling. The limitation is present when a certain engine performance is required in the off-design calculation that is without altering the design point. Achieving the latter can be done through two methods: by specifying a different design reference point or by modifying the component map itself. Specifying different design reference points by iterating until a certain performance is obtained in off-design is a way to achieve a match at a single off-design point. However, this method fails when multiple off-design matches are required simultaneously as only one off-design condition can be solved at a time.

On the other hand, modifying the map that is inputted into the simulation is another way to obtain a performance requirement at off-design points. Typically, the maps are modified by scaling them prior to being input into the simulation. The issue however lies in the *design-point scaling* step that scales the map a second time. The result is a down-scaled or up-scaled version of the intended modification. The map parameters manipulations through scaling then are not straightforward as it would also be dependent on the design parameters (e.g. scaling the map pressure ratio by a certain factor would not result in a scaled version of that map with that same factor).

A workaround for this limitation is the introduction of *off-design scaling factors* in the simulation tool. The off-design scaling factors are introduced as a secondary step on top of design point scaling for any off-design point independently of one another. This ensures a performance-matching methodology that offers the flexibility of altering the performance maps for each off-design point. Additionally, the effect of scaling is directly apparent on the final scaled map. The off-design scaling factors definitions for pressure ratio, corrected mass flow, and efficiency are shown shown in Equation 5.1, Equation 5.2, and Equation 5.3, respectively. The pressure ratio scaling factors terms are subtracted by 1, as no compressor ideally would have a pressure ratio lower than 1; otherwise, it is windmilling a turbine.

$$SF_{\pi} = \frac{\pi_{sacled} - 1}{\pi_{unscaled} - 1} \tag{5.1}$$

$$SF_{\dot{m}_c} = \frac{\dot{m}_{cscaled}}{\dot{m}_{cunscaled}} \tag{5.2}$$

$$SF_{\eta} = \frac{eta_{scaled}}{eta_{unscaled}} \tag{5.3}$$

5.1.4. OD caling factor sensitivity

In order to use OD scaling factors to further enhance the model, their effects on the engine performance need to be understood. The discussions presented here provide the sensitivity analyses conducted for each turbomachinery component to understand how the scaling factors affect the target parameters. The underlying effects of using the OD scaling factors in steady-state simulation due to the shift in the turbomachinery components' equilibrium are presented in Appendix B. The scaling factors were altered by a 5% change both positive and negative individually (i.e. the pressure ratio, corrected mass flow, and efficiency once at a time). The chosen point for the analysis is a steady-state take-off point, and all the simulations are based on individual steady-state simulations with the chosen take-off condition.

As the scaling factors directly alter the operating point of the respective components, the equilibrium point of the entire engine shifts to satisfy the new conditions. These conditions in the numerical solver are represented as error equations that impose the conservation laws. The direct consequence is an alteration in the gas path simulated variables. The sensitivity analyses point to the magnitude of such change with respect to the on-wing sensor measured parameters. The focus is to provide connection

for a how each scaling factor for each component affects the target parameters, which is a valuable tool in the fitting process.

The sensitivity results are presented in Figure 5.10 to Figure 5.24. The results are limited to the on-wing sensor measured parameters that are used as target parameters in the fitting problem as introduced in Section 4.2. The results shown here will be used as guidelines for interpreting the usage of the turbomachinery scaling factors in the OD fitting of the model. They will serve as the baseline for examining the physical phenomena as discussed in Chapter 7.

Prior to exploring the usage of the scaling factors in the fitting problem, certain phenomena are readily clear from the results. For instance, scaling the fan bypass parameters mainly affects the fuel flow. The target parameters lack bypass gas path measurements. This consequently reflects on the results. The fuel flow, however, is greatly related to the performance of the entire engine. The bypass section contributes to most of the thrust and if the bypass performance increases or decreases, the fuel flow shall greatly deviate. Additionally, the fuel flow parameter is generally mostly affected by the efficiency of the components. This follows as the efficiencies determine how much energy supplied to or extracted from the working fluid is useful. As a secondary effect, altering the component's efficiencies directly affects the fuel flow and consequently affects the TT49 parameters. This is because the fluid temperature aft of the combustor is directly related to the amount of fuel used in the combustion. Moreover, it can be seen that the scaling of the efficiency of the turbines shows the largest alterations in the target parameters. This is useful in determining the degrees of freedom that shall be used in the fitting problem.

Fan bypass

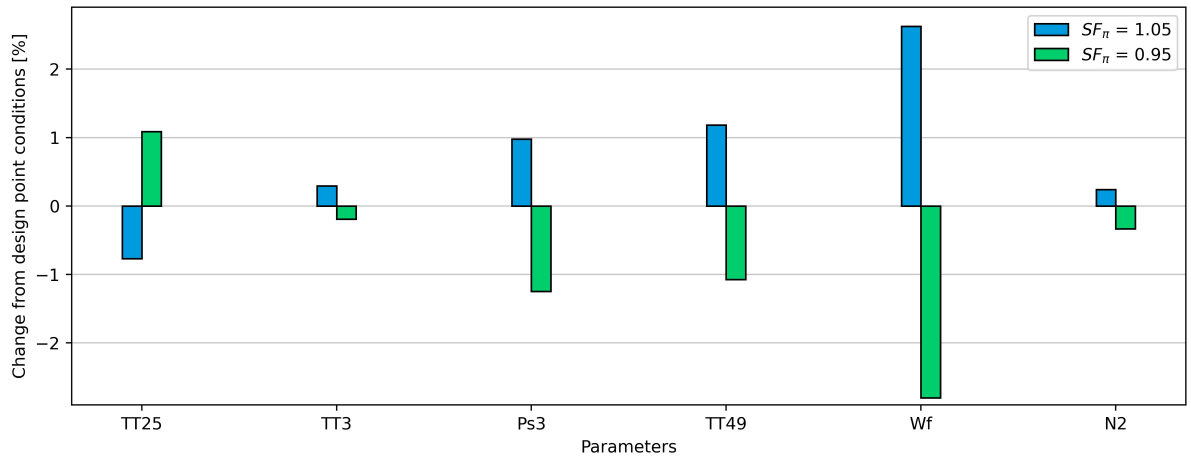

Figure 5.10: Effect of changing fan bypass pressure ratio OD scaling factor on the target parameters. Changes are computed based on the reference value ($SF_\pi = 1$)

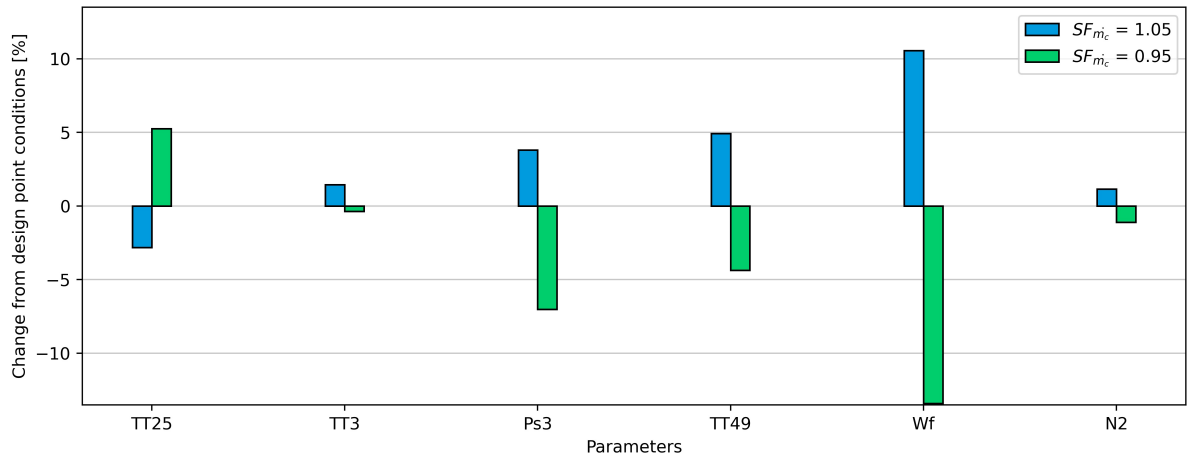

Figure 5.11: Effect of changing fan bypass mass flow OD scaling factor on the target parameters. Changes are computed based on the reference value ($SF_{\dot{m}_c} = 1$)

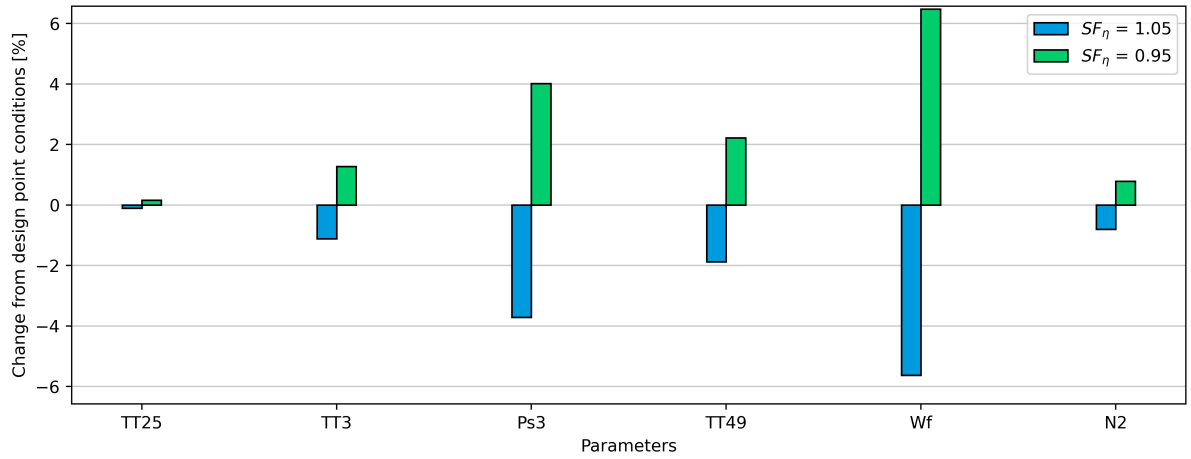

Figure 5.12: Effect of changing fan bypass efficiency OD scaling factor on the target parameters. Changes are computed based on the reference value ($SF_{\eta} = 1$)

Fan core

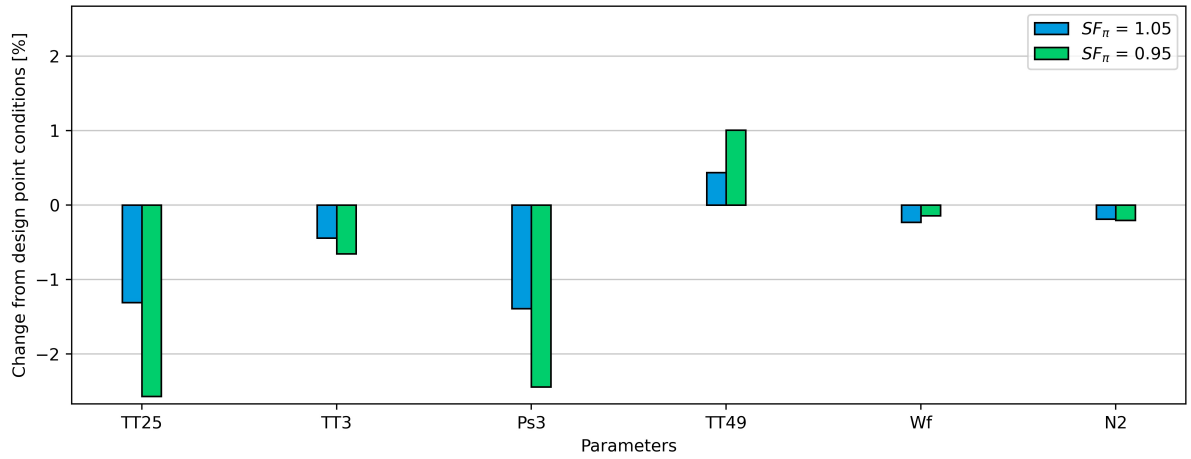

Figure 5.13: Effect of changing fan core pressure ratio OD scaling factor on the target parameters. Changes are computed based on the reference value ($SF_{\pi} = 1$)

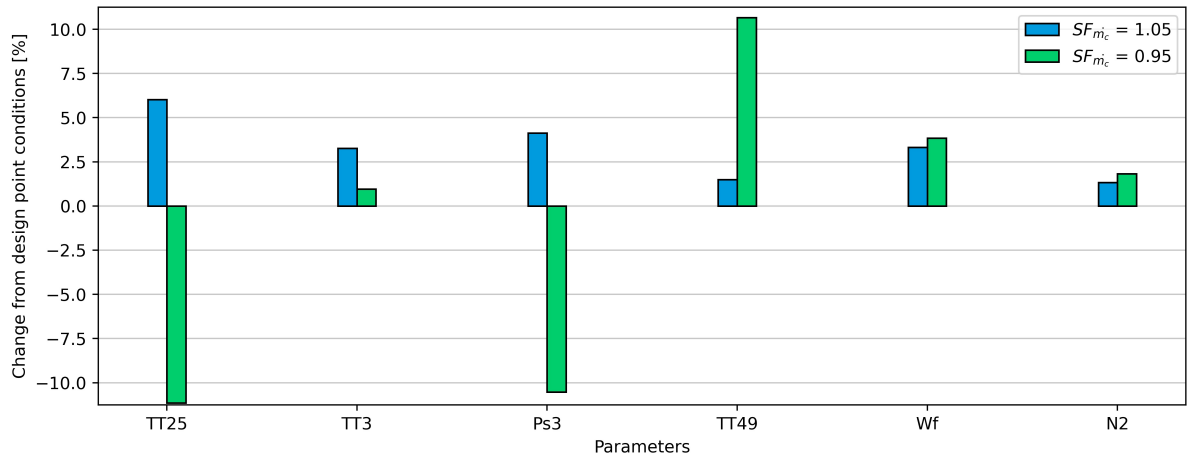

Figure 5.14: Effect of changing fan core mass flow OD scaling factor on the target parameters. Changes are computed based on the reference value ($SF_{\dot{m}_c} = 1$)

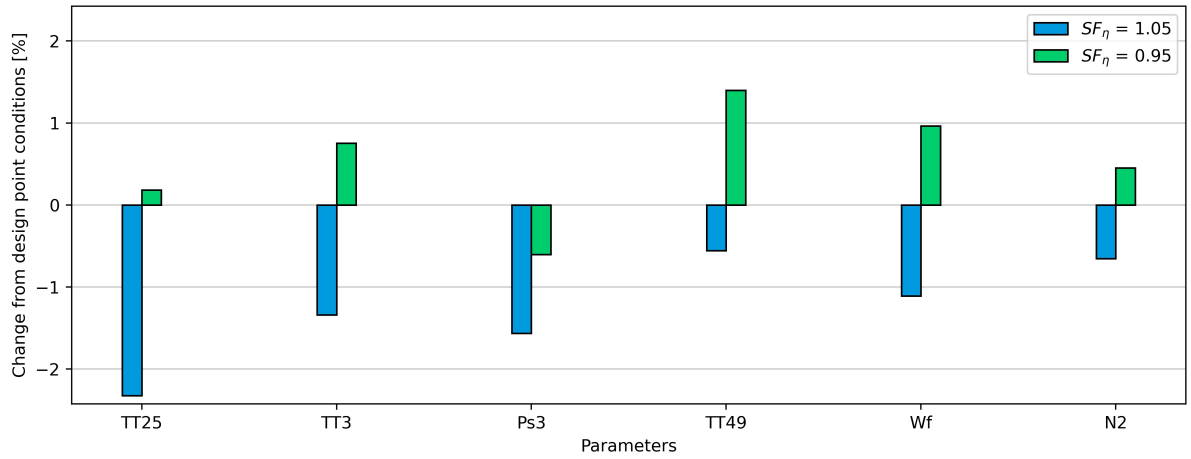

Figure 5.15: Effect of changing fan core efficiency OD scaling factor on the target parameters. Changes are computed based on the reference value ($SF_\eta = 1$)

HPC

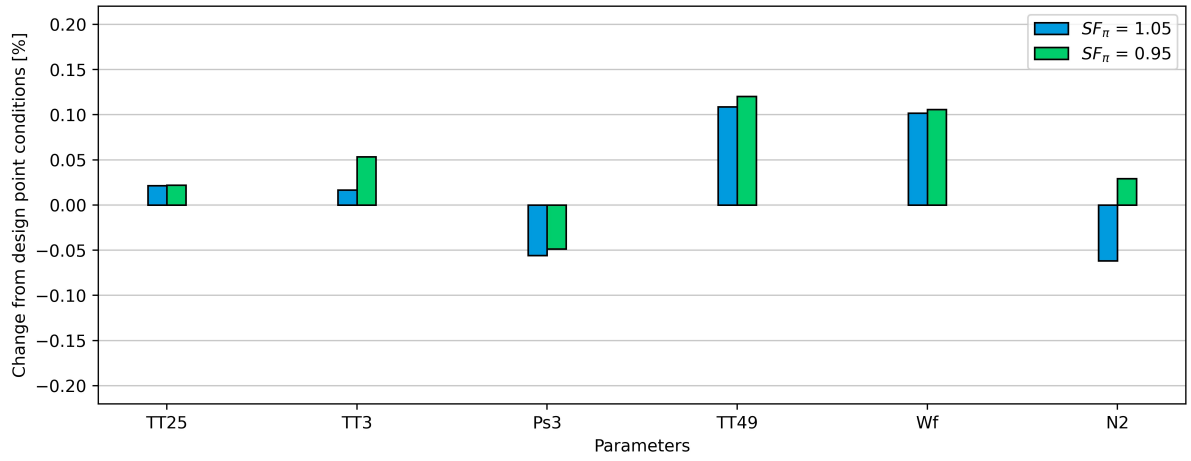

Figure 5.16: Effect of changing HPC pressure ratio OD scaling factor on the target parameters. Changes are computed based on the reference value ($SF_\pi = 1$)

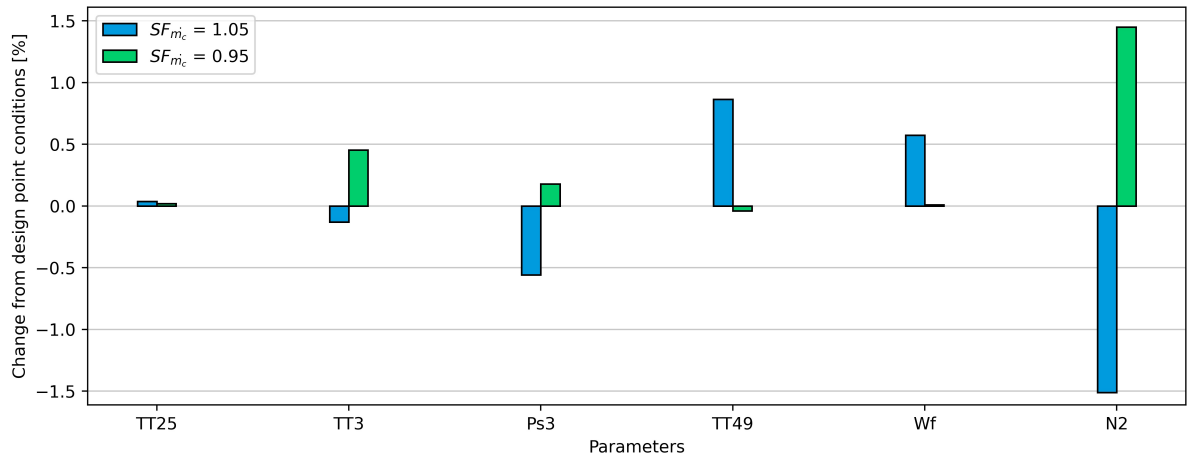

Figure 5.17: Effect of changing HPC mass flow OD scaling factor on the target parameters. Changes are computed based on the reference value ($SF_{\dot{m}_c} = 1$)

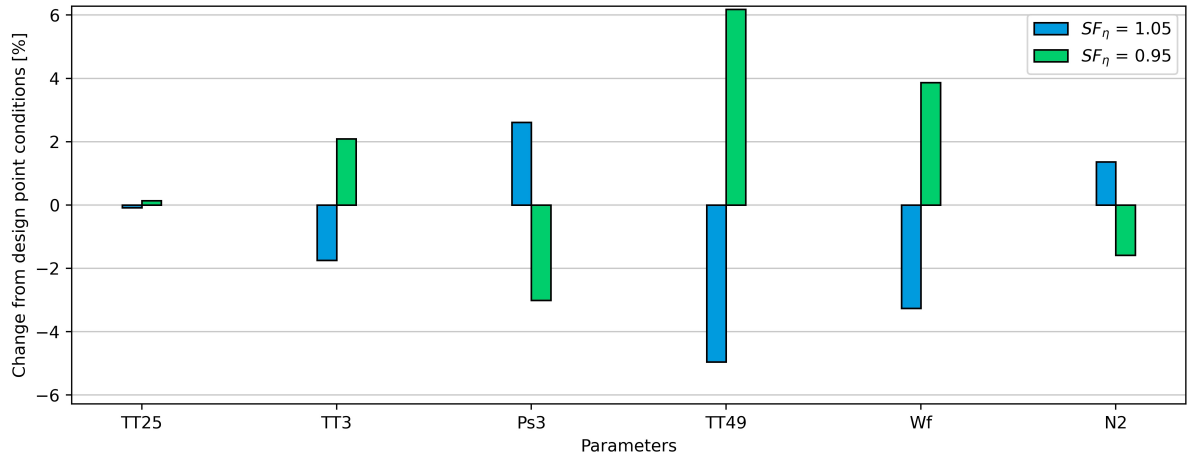

Figure 5.18: Effect of changing HPC efficiency OD scaling factor on the target parameters. Changes are computed based on the reference value ($SF_\eta = 1$)

HPT

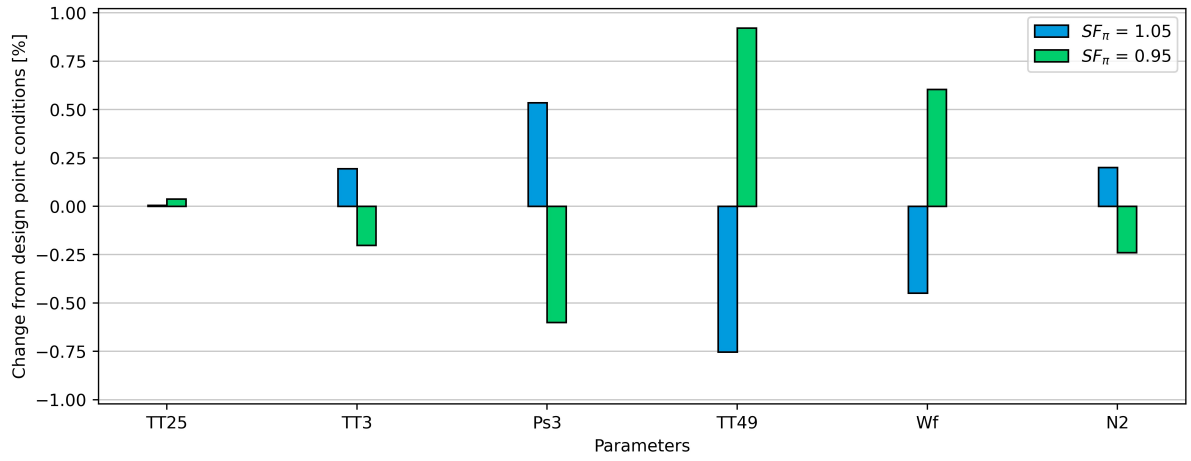

Figure 5.19: Effect of changing HPT pressure ratio OD scaling factor on the target parameters. Changes are computed based on the reference value ($SF_\pi = 1$)

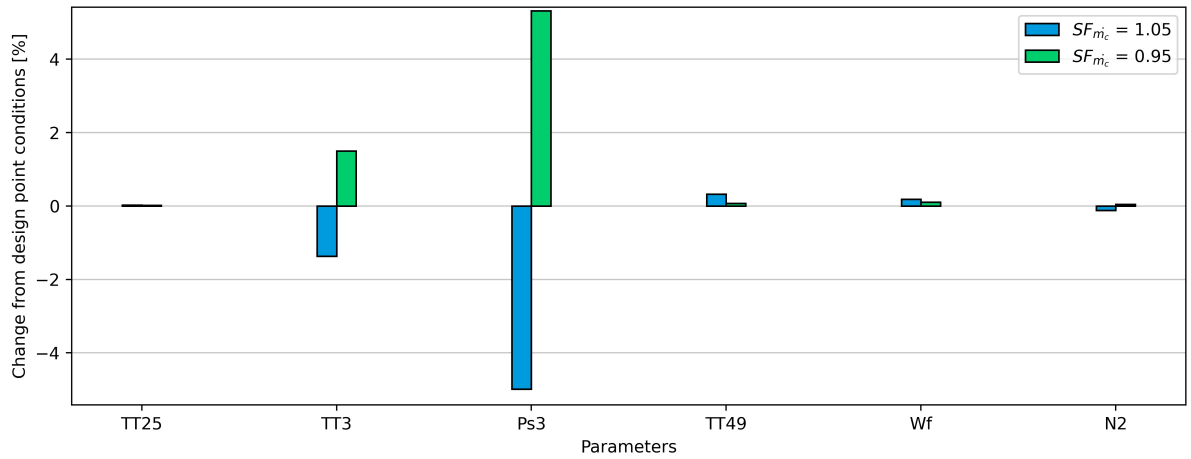

Figure 5.20: Effect of changing HPT mass flow OD scaling factor on the target parameters. Changes are computed based on the reference value ($SF_{\dot{m}_c} = 1$)

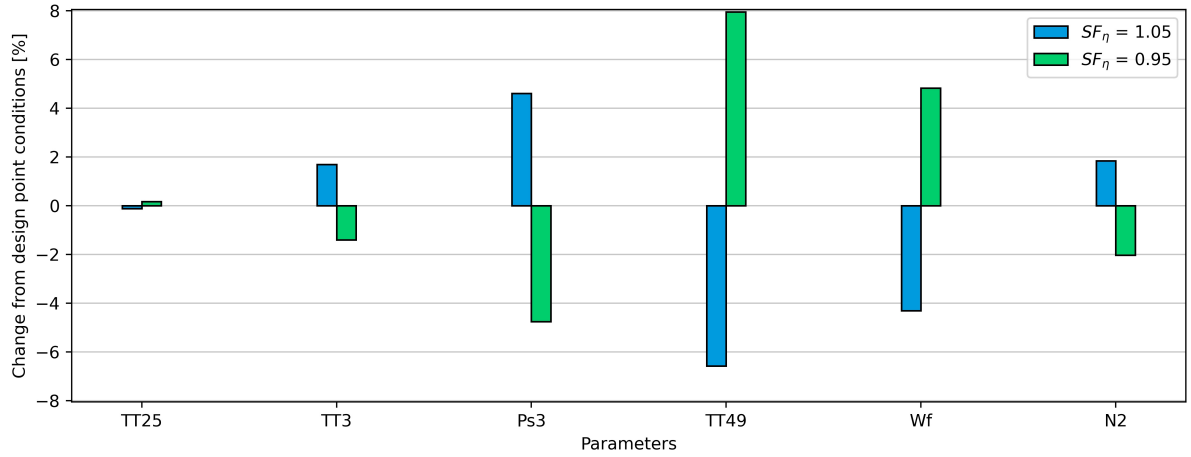

Figure 5.21: Effect of changing HPT efficiency OD scaling factor on the target parameters. Changes are computed based on the reference value ($SF_\eta = 1$)

LPT

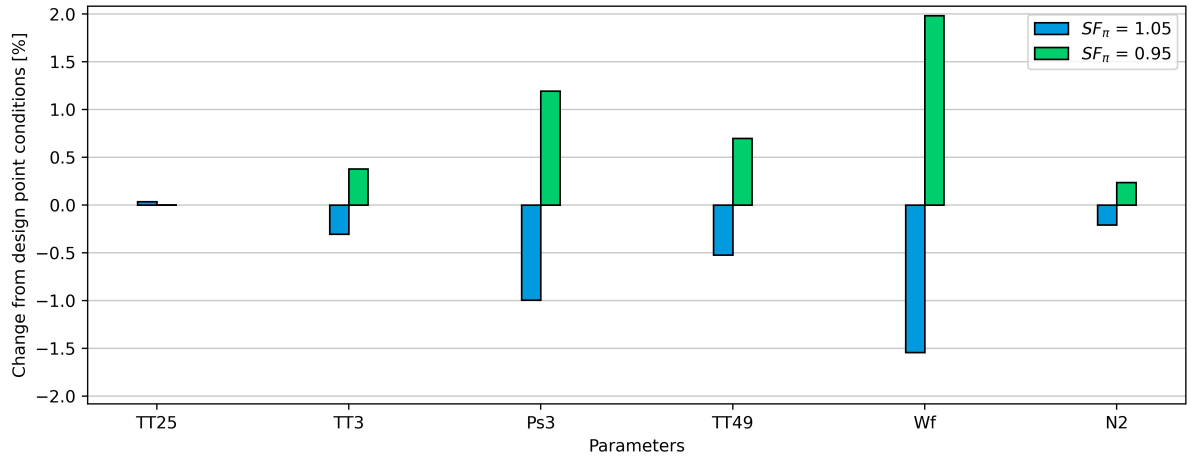

Figure 5.22: Effect of changing LPT pressure ratio OD scaling factor on the target parameters. Changes are computed based on the reference value ($SF_\pi = 1$)

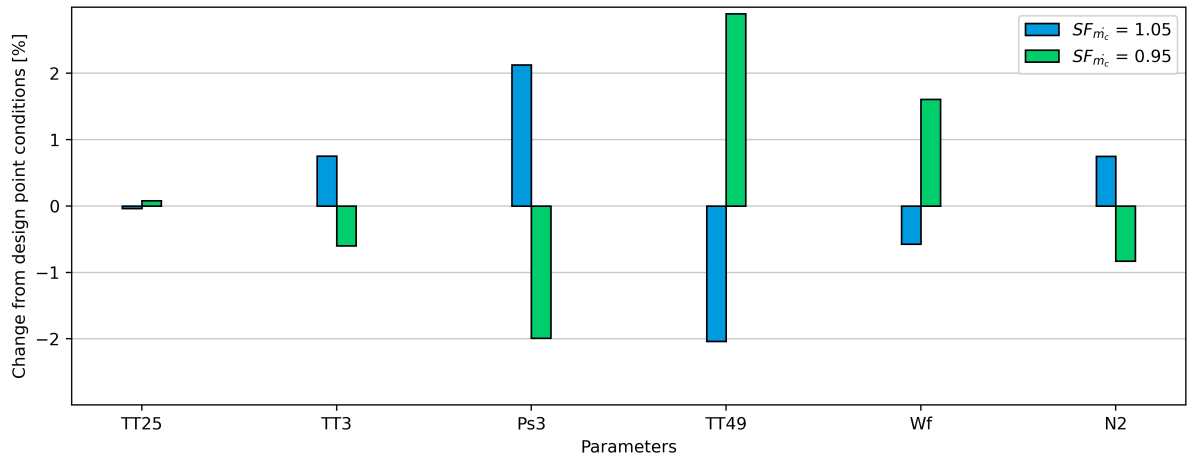

Figure 5.23: Effect of changing LPT mass flow OD scaling factor on the target parameters. Changes are computed based on the reference value ($SF_{\dot{m}_c} = 1$)

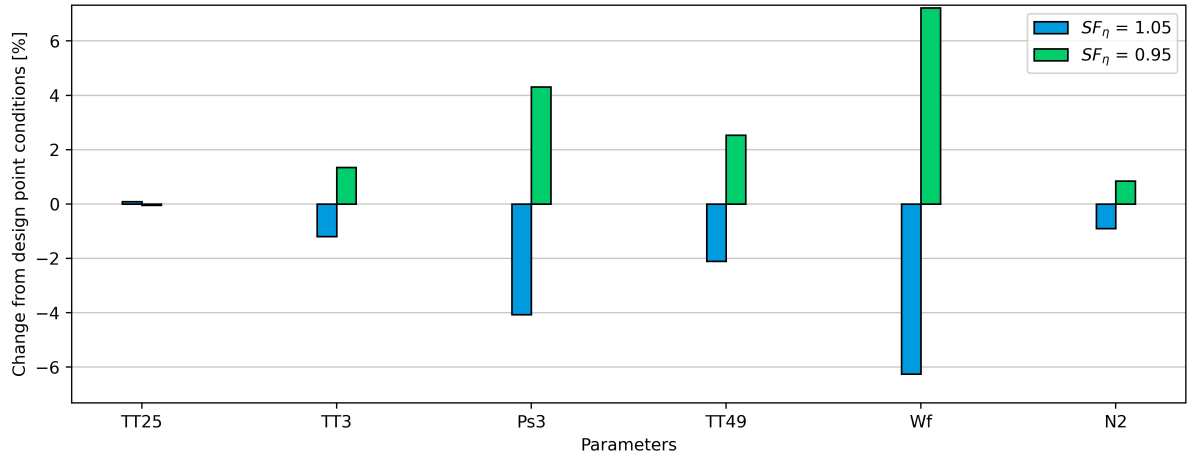

Figure 5.24: Effect of changing LPT efficiency OD scaling factor on the target parameters. Changes are computed based on the reference value ($SF_\eta = 1$)

5.2. Propelling nozzles

This section overviews how the nozzle losses are represented in numerical solvers as well as how the off-design scaling is applied.

5.2.1. Losses representation in GSP

Nozzle loss representation in GSP is depicted using the thrust, velocity, and discharge coefficients. Their definitions are similar to the ones discussed in the equations shown in Section 3.5. The coefficient values can be altered at the design point in order to match a certain nozzle performance. In off-design scaling, only the thrust and velocity coefficients can be altered. However, nozzle variable geometries can be imposed to alter the flow areas.

5.2.2. Nozzle coefficients sensitivity

The nozzle thrust and mass flow rate are controlled through the usage of the nozzles coefficients. The OD scaling functions in GSP allow for analysis through the use of the thrust or velocity coefficients. The

discharge area could technically be altered by varying the nozzle area (geometry); however, the implementation is a workaround that is unneeded. It is important to comprehend how the nozzle coefficients affect the target parameters. This is because the values are chosen by the optimizer that determines them based on fitting the model to meet the target parameters.

The thrust coefficients do not affect any of the gas path parameters except the thrust. It is simply a correction for the final thrust values. Therefore, the target parameters are not affected by the coefficient of thrust. The sensitivity analysis presented here is based on a -+5% change for the velocity coefficients of the bypass and core nozzles. The change is based on the design point value ($C_V = 1$). The analyses for the bypass and core nozzles are shown in Figure 5.25 and Figure 5.26, respectively.

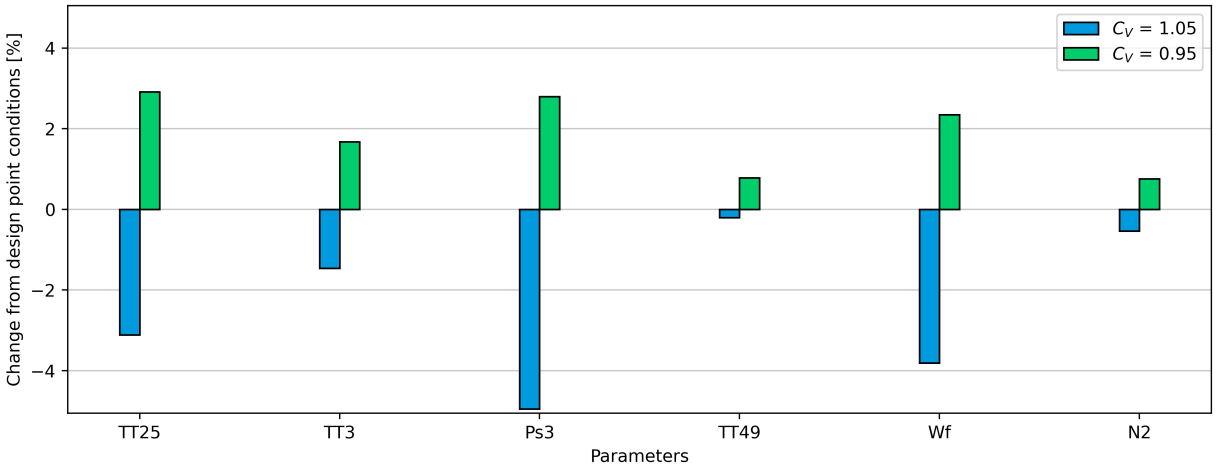

Figure 5.25: Effect of changing bypass nozzle coefficient of velocity on the target parameters. Changes are computed based on the reference value ($C_V = 1$)

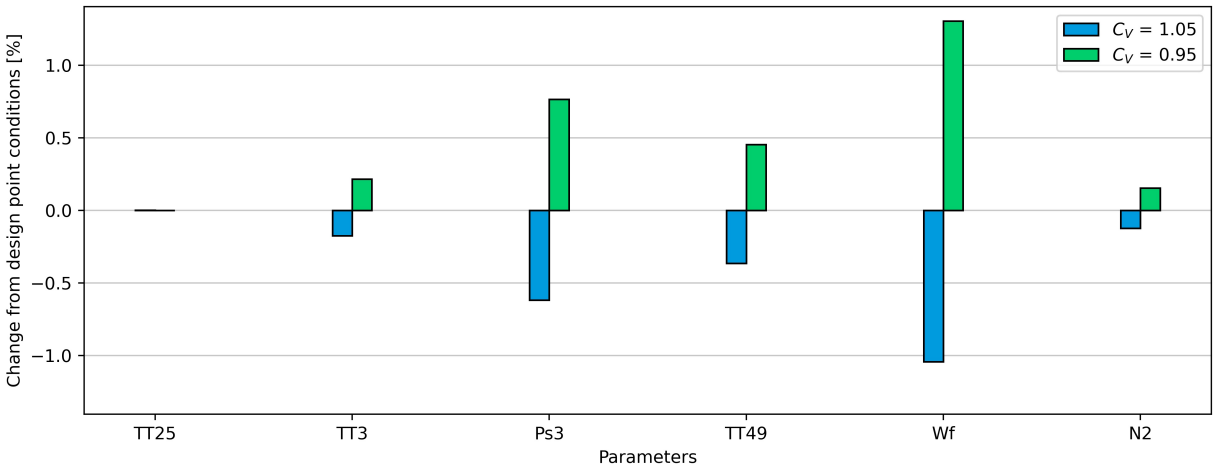

Figure 5.26: Effect of changing core nozzle coefficient of velocity on the target parameters. Changes are computed based on the reference value ($C_V = 1$)

Bypass nozzle C_V sensitivity

The effect of changing CV directly changes the axial velocity leaving the nozzle. This way the momentum is also changed altering the net force of the engine. The change in axial velocity has another peripheral yet integral effect, that is a change in the mass flow. This results in a change in the engine equilibrium and a shift in the operating point.

The effect of increasing the bypass C_V increases the mass flow rate of the bypass and decreases the mass flow rate of the core. The total mass flow, however, also increases. It can be seen that an increase in C_V results in a decrease in all the target parameters. The operating points on the Fan core map can be seen in Figure 5.27. The increase in C_V results in an increase in the corrected mass flow rate due to the total increase of the mass flow rate (note that inlet conditions are constant). As the $N1$ shaft speed is the input condition, which acts as a boundary condition in the system of equations the operating line has to move on the same corrected spool speed. Therefore, the increase in the corrected mass flow rate results in a decrease in the pressure ratio. This decrease subsequently leads to a decrease in total temperature aft of the LPC core (TT25). This decrease in total temperature is also reflected in TT3. Static pressure aft of the HPC also decreases. This can be attributed to the decrease in total pressure. It can also be attributed to the increase in the axial velocity component, which increases the dynamic term of the pressure leading to a lower static term. The effect on TT49 is, however, not significant. This is mainly because the total mass flow through the core is reduced, which means the flow leaving the combustor mixes at a higher fuel-to-air ratio. Therefore, the effects on gas path temperatures aft of the combustor are not significant. The fuel flow decreases meanwhile the thrust increases due to the increased bypass momentum, which results in a higher-performing engine[3]. The decrease in N2 can be attributed to the lower energy that could be extracted in the HPT due to the decrease in the fuel flow. The same arguments hold for the decrease in C_V, with differences in magnitude being attributed to the non-linearity of the turbo-fan.

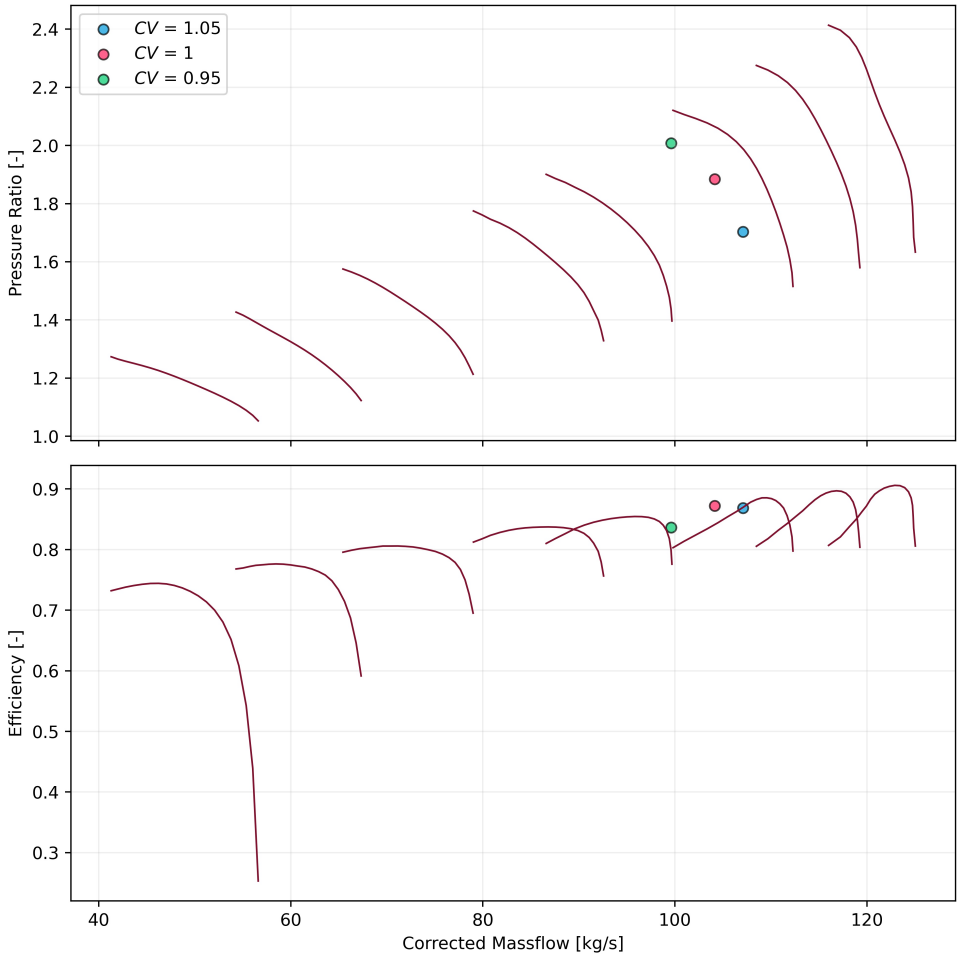

Figure 5.27: Steady-state operating points for the different CV values plotted on the fan core map.

[3]This finding here that the increase in C_V results in higher performance is crucial in interpreting the content of the results chapter.

Core nozzle C_V sensitivity

The effect of altering core C_V on the engine performance in general is smaller than changing the bypass C_V. The effects are mainly attributed to the total mass flow rate change, which is higher in the bypass than in the nozzle. Unlike in the bypass, the effect of increasing the core C_V decreases the mass flow rate (slightly!). The differences could be attributed to the difference in the bypass gas path compared to the nozzle, which has multiple components with complex energy balances and potential choking in the turbines. Due to the slight mass flow rate change, the components' operating points do not shift significantly, which is reflected in the slight change of TT25 and TT3. Ps3 is mainly reduced due to the increase in the axial velocity component. TT49 decreases due to the relatively larger decrease in the fuel flow, which means the combustor mixes at a lower fuel-to-air ratio resulting in an overall colder fluid. The decrease in fuel flow results in less energy being extracted from the turbines decreasing the N2 value. The same arguments hold for the decrease in C_V, with differences in magnitude being attributed to the non-linearity of the turbo-fan.

6. Model enhancements using OD scaling functions

In order to fit the Genx-1b model in off-design, OD scaling factors are utilized. This chapter discusses the loss enhancement methodology. The first step of the methodology is to select a certain flight for fitting and establish a data filtering procedure as presented in Section 6.1. Then the model calibration at take-off is introduced and the results are discussed in Section 6.3. Then, the turbomachines OD functions corrections are discussed in Section 6.4. Then, an extension of the turbomachines corrections using quadratic splines is presented in Section 6.5. Nozzle corrections using OD function methodology and results are discussed in Section 6.6.

6.1. Flight selection and data filtering

The research objective is to investigate how low Reynolds numbers affect the performance of aero-engines and how it can be modeled in numerical gas turbine simulations. It is logical then that it follows that the data used for such investigation is based on a flight that undergoes large variations in Reynolds number. This was essentially the main basis for the specific flight choice given obviously that the data acquisition system and sensors on board are not faulty. Additionally, the availability of multiple flights with different trajectories was favored for validation purposes. Lastly, the data was based on an engine that had a recent maintenance shop visit to reduce the effects of performance deterioration.

The on-wing data used for the flight is based on the Continuous Engine Operating Data (CEOD) that is recorded during flight. The CEOD contains some gas path measurements of the GEnx-1b as well as secondary performance parameters. During a flight, the engine undergoes constant variations due to changes in atmospheric conditions and flight profiles. The CEOD data which captures measurements continuously is then expected to contain transient engine conditions. The aim of the project is to model the steady-state operation of the engine. Therefore, data filtering of the CEOD is very important, especially during take-off and climb where the engine undergoes highly transient conditions. The steady-state filtering procedure was established previously by Ramdin [40] and Rootliep [43]. This was data done by filtering for points with very low core spool speed variation. Moreover, filtering steady-state points for the climb phase in fact requires a stricter filter. This is because during the climb phase, the ambient conditions are continuously changing, assuming that the core speed variation is still below a threshold. Therefore, an additional filter for climb is used that removes fast altitude variation in time below a certain threshold. Finally, only the three main critical phases of the flight were considered for the modelling problem: take-off, climb, and cruise. During descent and taxing, the demand for high engine performance is considerably lower and therefore regarded as not critical phases.

The result of this filtering procedure still had an issue regarding the measurement of the fan spool speed. Compared to the climb phase, the corrected N1 speed undergoes a lot of variation in the cruise phase. This is shown in Figure 6.1. The reason for this difference is related to the flight scheduling procedures in airplanes. During the climb phase, the control system onboard sets a fixed fan speed schedule in order to achieve the climb at a certain profile. On the other hand, during the cruise phase usually the airplane velocity or Mach number is fixed and the fan speed is left in a "free state". The consequence from a modelling point of view is that the corrected N1 speed being an input in the model would result in a lot of variation in GSP's simulated output. Therefore, additional filtering to reduce this noise is needed. In the end, reverse engineering of models depends heavily on the input data.

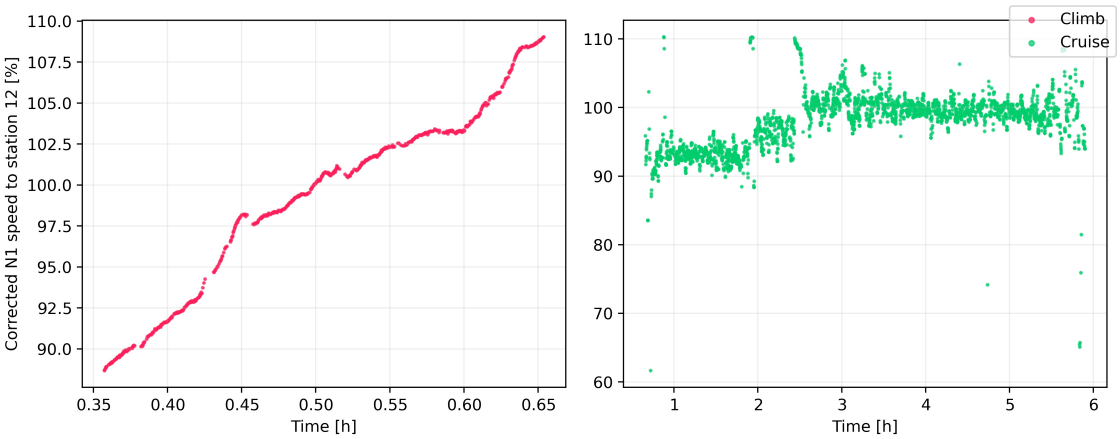

Figure 6.1: Corrected N1 speed variation over flight duration. Data points are filtered for near steady-state conditions.

In order to remove the aforementioned noise a special type of filtering based on removing points further away from the rolling median. The algorithm works by iterating through every point and filtering out points further away from the median given a certain threshold. The median is, however, not calculated for the entire set, but by considering only the neighboring points given a certain window size.

The end result is a smoother corrected fan spool speed variation over time as shown in the top graph of Figure 6.2. The bottom graph depicts the variation of corrected N1 speed with altitude. The reason for the 3 streaks in the cruise phase is due to the 3 cruise profiles of the flight. The flight altitude plotted against time is shown in Figure 6.3. It can be seen that during the cruise phase, 3 altitudes are maintained.

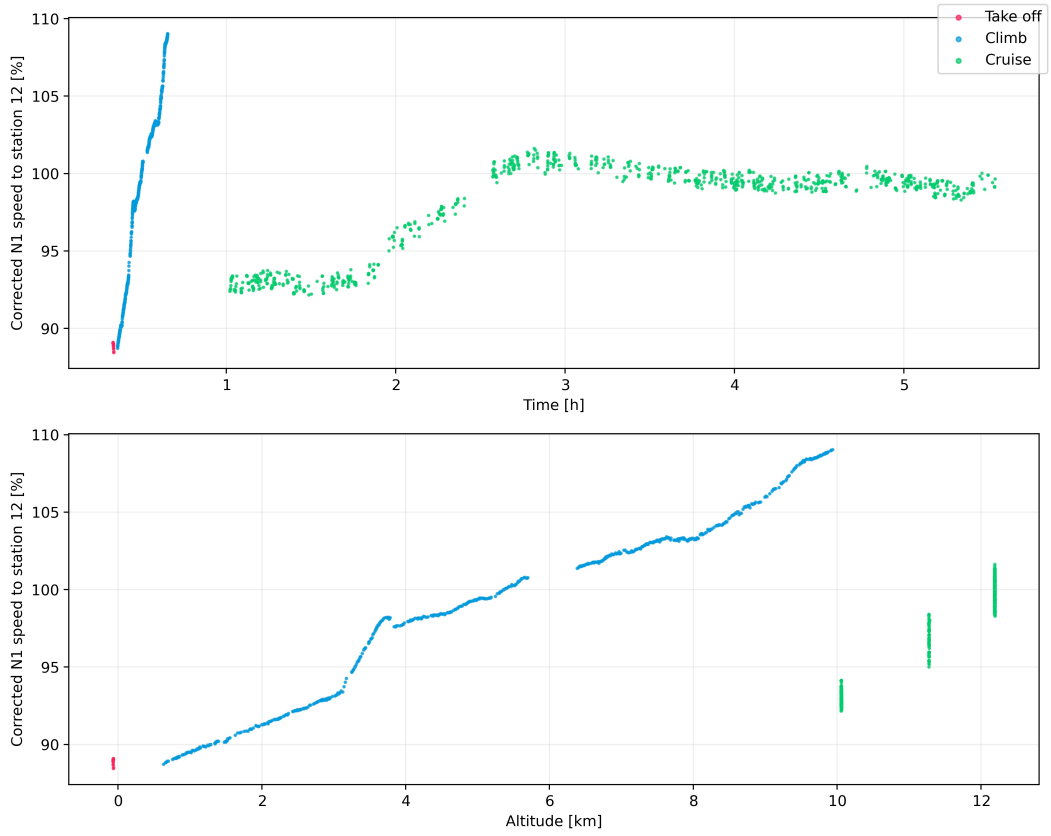

Figure 6.2: Corrected N1 speed variation over flight duration. Data points are filtered for near steady-state conditions with rolling median filtering applied.

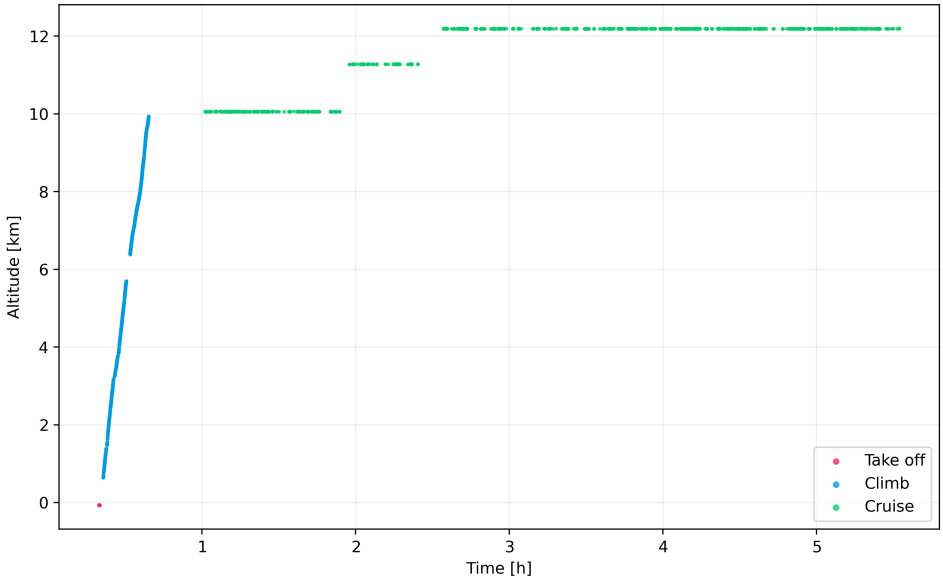

Figure 6.3: Flight overview of the selected flight.

6.2. Kmeans clustering-based approach

Data sampling on a single flight and further applying a reverse engineer model that is based on a fitting approach (next sections) runs the risk of creating a model that is not representative of all the flights. This is due to the potential over-fitting of the model to the selected flight. An alternative approach is to create a new dataset using Kmeans++ clustering [3]. A similar approach was employed by Kim [23] to reduce the number of points in transient operating conditions. The method is used to identify the points (clusters) where transient data is grouped and represent each cluster by a single point.

In this case, clustering can be performed to represent multiple flights by a set of data points. The hypothesis is that the newly obtained dataset is more representative of the remaining flights. First, a number of flights need to be selected. Then, these flights are all combined into one large dataset, where the Kmeans++ clustering algorithm can be utilized. The selection of the flight is based on a 50-50 split between training and validation sets for the available data of a single-engine.

The clusters are based on the input parameters shown in Section 4.2. Therefore, each clustered point is 5-dimensional (for each input parameter). In order to simplify visualization, the clusters shown in the following figures are based on a 2-dimensional representation of the total inlet temperature and the N1 corrected speed to inlet conditions. The clusters obtained for take-off, climb, and cruise are shown in Figure 6.4, Figure 6.5, and Figure 6.6, respectively. The flight points shown are based on half of a month of operational data (more on the validation set in Chapter 8). Moreover, the number of assigned clusters is 5. Having in total of 15 data points to represent an entire flight was found (by trial and error) to be a good balance in order to reduce the computational time (more on this in the next sections).

The analyses that are carried out throughout the report are all based on the former approach. The main aim of the research conducted is to attempt to capture the physical effects associated with losses that are correlated with the Reynolds number. The introduction of the clustering method is not part of the "proof-of-method", but rather a hypothesis that can be tested conveniently.

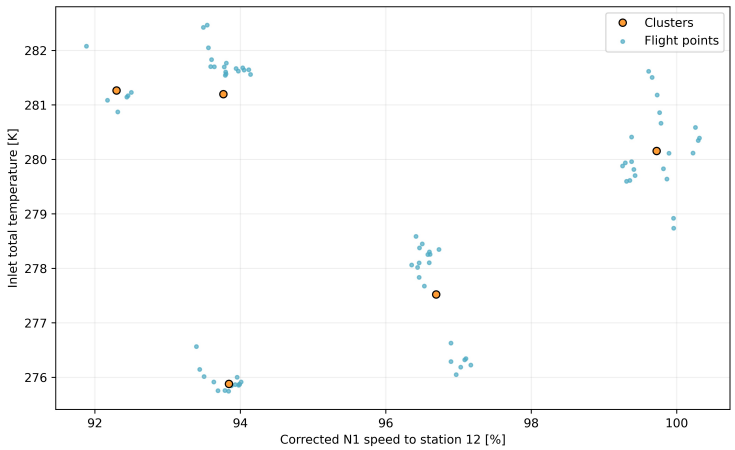

Figure 6.4: Clusters visualization for total inlet temperature vs N1 corrected speed to inlet conditions at take-off.

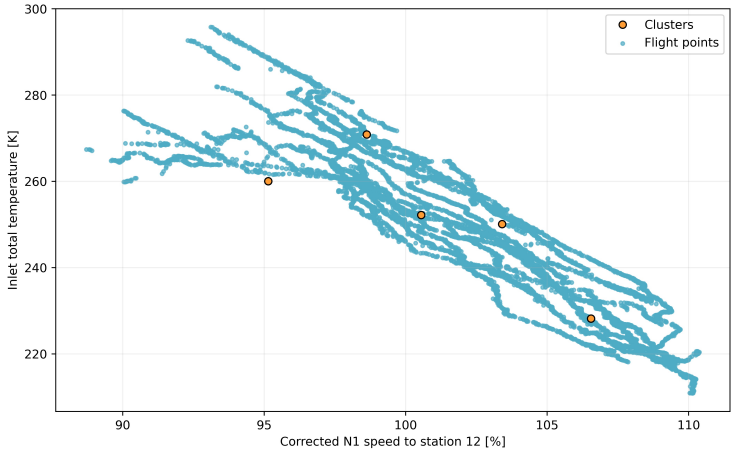

Figure 6.5: Clusters visualization for total inlet temperature vs N1 corrected speed to inlet conditions at climb.

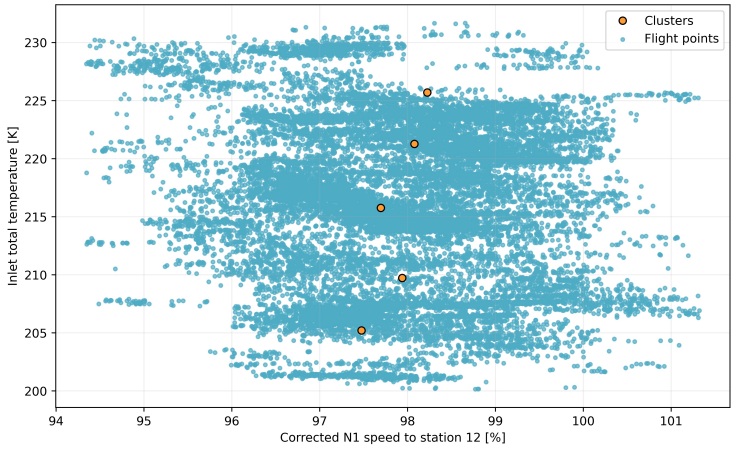

Figure 6.6: Clusters visualization for total inlet temperature vs N1 corrected speed to inlet conditions at cruise.

6.3. Model take-off calibration

In order to correct the model accuracy at take-off due to mounted- unmounted engines and engine-to-engine differences, a calibration step is needed. This section presents the calibration procedure and the resultant outcome.

6.3.1. Problem definition

The accuracy model developed by Ramdin at take-off is low as shown in Figure 4.2. This was due to the model's dependency on test-cell conditions. The major error difference is mainly attributed to installation effects and engine-to-engine differences. Roell [42] detailed the performance difference between test-cell and on-wing turbofans. To address the differences at take-off conditions a calibration step is needed. This is done by finding the OD scaling factors that improve accuracy in a minimization problem. Unlike the correction for the Reynolds effect where a series of scaling factors are needed to account for the variation in Reynolds numbers in the entire flight envelope, only a single set of scaling factors are needed for calibration. Additionally, the target parameters are based on a single point which is the median point. The conditions variations of steady-state points at take-off are not major and therefore, representing the entire phase by a single point is sufficient.

The defined scaling factors for calibrating the model were based on the same calibrating scaling factors used for the Reynolds effect correction to simplify the approach. The motivation for the chosen scaling factors is presented in ref Section 6.4. The bounds for the search space were set to be a maximum of 5% change in absolute terms. The choice is based on user trial and error until satisfactory results are achieved.

For the minimization problem, the optimizer used is the Genetic algorithm. GA solvers handle the non-linearity of gas turbines and the noise in data measurements well [28]. Moreover, Ramdin analyzed the use of different solvers and did a comparative study between Genetic algorithms and Bayesian Optimisation solvers. The conclusion was that GA solvers handle constraints better and are more suited for design vectors with a high number of variables.

Figure 6.7 depicts the calibration step in the minimization approach. First, the scaling factors are defined (Motivation in the next section). Then the scaling factors solver bounds are defined. With the flight parameters, that define the operating point of interest which is at take-off, the scaling factors are inputted into the simulation and the results are compared with the engine CEOD until satisfactory results are met.

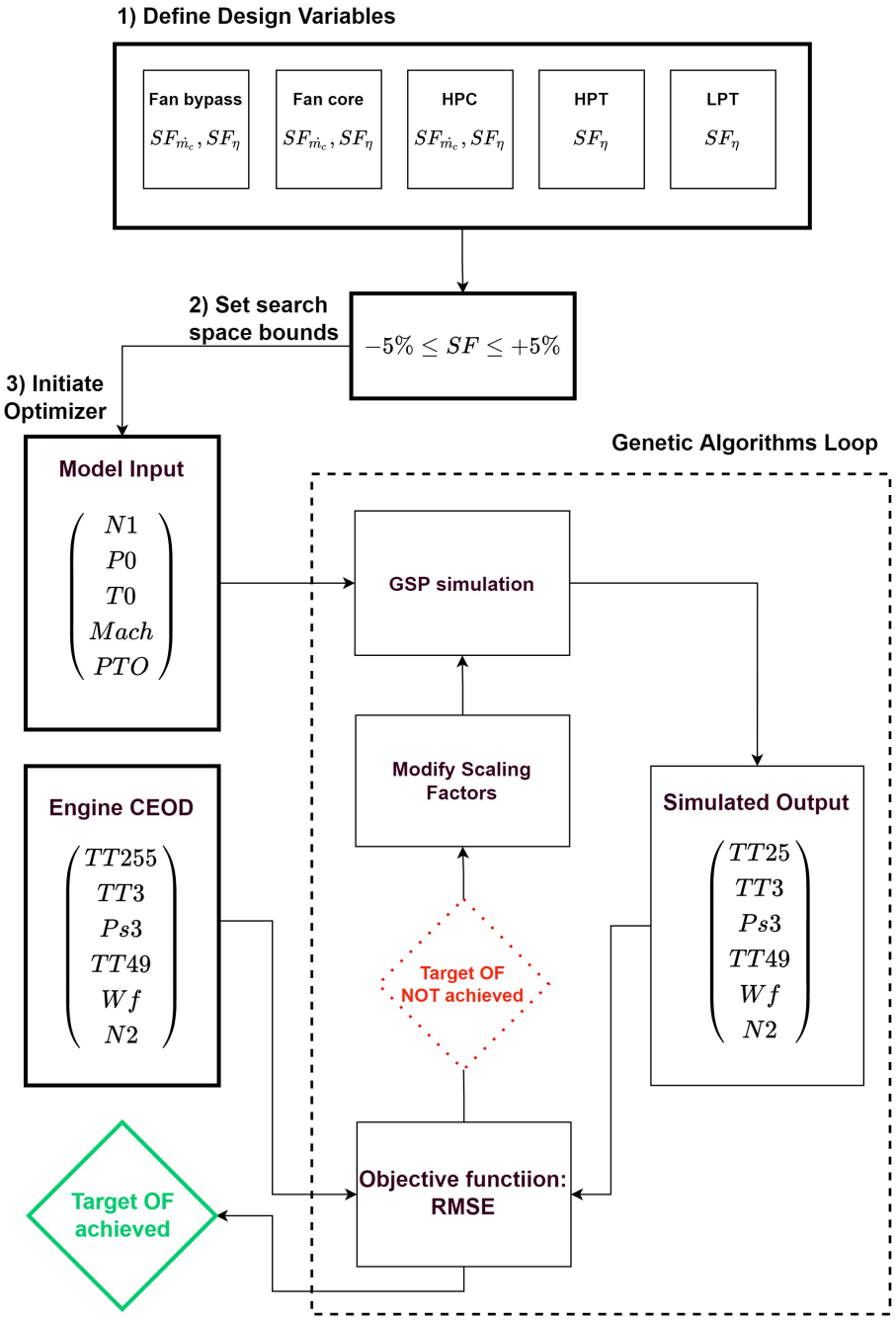

Figure 6.7: Take-off calibration flow diagram.

6.3.2. Take-off calibration results

The results of the calibration step using the optimization framework are shown in Table D.1. The scaling factor for fan core efficiency is set to the bound limit. This solver behavior was commonly reached with different initiation points. The solver simply caps the limit of a certain scaling factor, in this case, efficiency, and fine-tunes the other scaling factors to balance a solution that reduces the total RMSE. This is because altering the scaling factors changes the equilibrium condition of the entire gas turbine.

The simulated take-off output error before and after the calibration steps are shown in Figure 6.8 and Figure 6.9 respectively. It can be seen that the overall error with a maximum error of 1% at the maximum

corrected fan speed. This indicates that the model map itself requires further tuning if the error is to further decrease. Nonetheless, an error of 1% should be within acceptable limits of the problem due to the considerably higher errors in the climb and cruise phases.

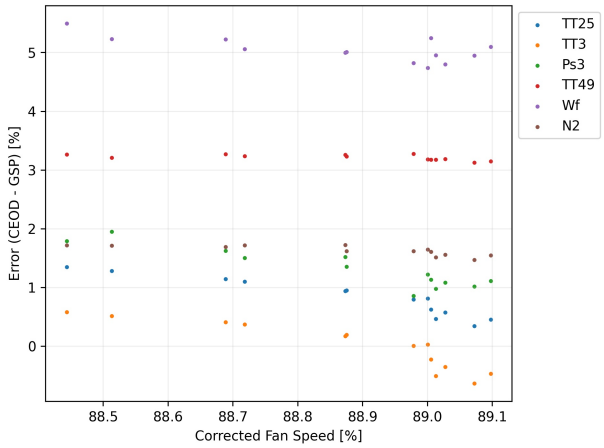

Figure 6.8: take-off output simulation error plotted at different corrected fan speeds with no DP calibration.

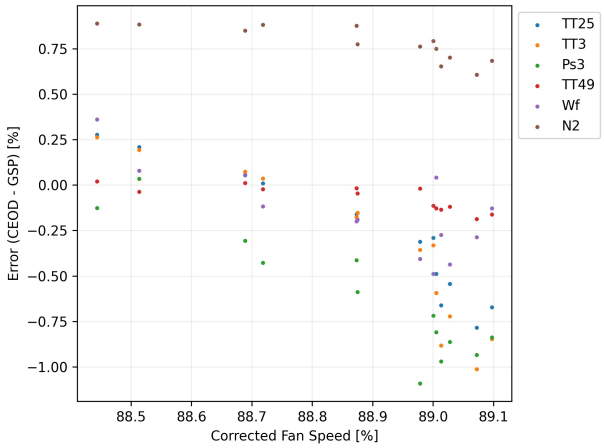

Figure 6.9: take-off output simulation error plotted at different corrected fan speeds with DP calibration.

6.4. Turbomachinery correction using OD scaling functions

The turbomachinery components maps need to be adapted in order to improve the model accuracy at off-design conditions especially, at the climb and cruise phases. This section provides the methodology of the correction procedure as well as the resultant outcomes.

6.4.1. Reynolds number correlation

As discussed in Chapter 3, the Reynolds number correlates directly with altitude, as was shown in the relation Equation 3.1. It was also shown how low Reynolds numbers decrease the performance of aero-engines. Since the GSP GEnx-1b model does not account for the Reynolds effects yet, part of the model error in Section 4.5 can be attributed to it. In Figure 6.10, the general trend of the Reynolds number at inlet stations of turbomachinery components is shown for the selected flight. It can generally be seen that the Reynolds number correlates negatively with altitude as expected. This is only not the case during a short duration of the flight in the climb between around 3 to 4 km altitude. The reason for the sudden increase in Reynolds number is attributed to the increase of the inlet fan speed due to the flight switch to a faster climb profile. This is well depicted in the bottom graph of Figure 6.2, where the slope of the corrected fan spool speed increases around the 3.5 km altitude mark. The increase in fan speed essentially increases the axial velocity in the gas path and consequently the Reynolds number.

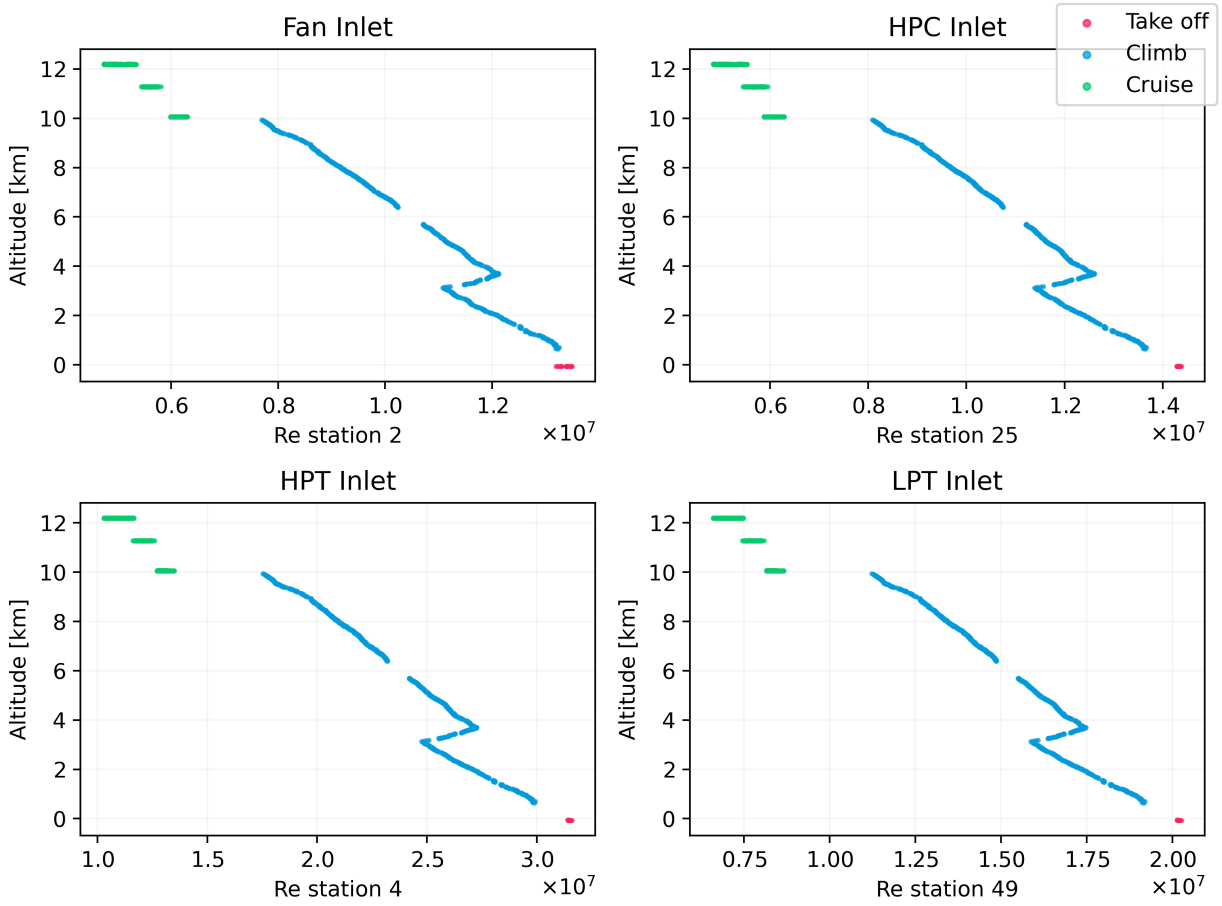

Figure 6.10: GSP simulation: Inlet Reynolds number of turbomachinery components vs altitude

This decrease in Reynolds number can be correlated with the increased error in climb and cruise. In the numerical model, the effects of the Reynolds number can be taken into account by directly altering the performance of the engine through its turbomachinery components. Then the problem becomes a model-matching procedure similar to the off-design test cell data matching methodologies applied by Ramdin. However, a clear distinction has to be made. Ramdin's method reversed engineered component maps using the corrected spool speed, that is the scaling factors (for pressure ratio, corrected mass flow, and efficiency) are functions of the corrected spools speeds (i.e. $SF_{\pi,\dot{m}_c,\eta} = f(N_c)3$) [1]. The use of corrected spool speed, in this case, makes sense as the aim was to reverse engineer the component maps themselves.

In the case of correlating the performance parameters of components with the Reynolds number reverse engineering the maps in the same fashion is not possible. This is because for a given corrected spool speed multiple Reynolds number values exist. Consider the graph shown in Figure 6.2, there exists a region where the corrected spool speed values in climb and cruise overlap, even though clearly from Figure 6.10, it can be seen that the components have different Reynolds numbers. This simply makes the traditional way of reverse engineering the maps inapplicable to perform the Reynolds correction.

6.4.2. OD scaling correction using components inlet Reynolds numbers

In order to correct using the Reynolds numbers, component performance parameters need to be controlled through the Reynolds numbers themselves. So in case the pressure ratio, corrected mass flow, or efficiency of a given component needs to change it shall be through a function that takes into account

[1] Spools here is used in the plural form to take into account the different components connected to either of the two shafts

the Reynolds number. Numerically, this can be done by altering the read-off values from the component maps. For example, the efficiency of the map depends on 2 states, the pressure ratio, and corrected spool speed ($\eta_{map} = F(PR, N_c)$). One could then alter the Pressure ratio value such that the read-off value from the component map would result in a different efficiency. Also, it is possible not to alter the pressure ratio but, to change the read-off value of the efficiency directly. In any case, the change in the performance values can be achieved by scaling them using a certain factor that is a function of the Reynolds number ($Factor = f(Re)$).

Alternatively, the change in performance parameters can be achieved indirectly by scaling the component maps themselves, which can be done through the use of the OD scaling functions. Then the pressure ratio, corrected mass flow, and efficiency are defined as a function of the Reynolds number ($\pi, \dot{m}_c, \eta = f(Re)$). Thus, every point in the flight envelope is corrected by reading off an independently defined map. In other words, the result of this procedure is a set of component maps that are a function of the Reynolds number, which are fed into the simulation continuously.

The issue, however, lies in finding those scaling factors. The general method, in this case, is to use an optimization framework to find the scaling factors that minimize the error of a series of target functions. In this case, the target functions are the CEOD parameters that measure the model's accuracy. Finding the scaling factors of each component for every steady-state point in the flight envelope is a near-impossible task if the scaling factors are directly the design vector parameters. Each flight CEOD can have steady-state points in the order of thousands. Given that there is a possibility of requiring more than scaling a singular dimension in a map and also having multiple turbomachinery components in the model, the problem becomes very computationally expensive.

To overcome this problem, the scaling factor can be defined as a polynomial that is a function of the Reynolds number. The generic polynomial parameters would then be fitted to achieve a performance that matches the target functions. The scaling factor is defined as shown in Equation 6.1. a, b, and c are the polynomial's coefficients. Re_{OD} is the Reynolds number at the point of interest, and Re_{DP} is a chosen Reynolds number where the scaling factor is equal to a.

$$SF_X = a + b\left(\left|\frac{Re_{\mathrm{OD}} - Re_{\mathrm{DP}}}{Re_{\mathrm{DP}}}\right|\right) + c\left(\left|\frac{Re_{\mathrm{OD}} - Re_{\mathrm{DP}}}{Re_{\mathrm{DP}}}\right|\right)^2 \tag{6.1}$$

In this case, the design variables of the minimization problem are the polynomial coefficients. In some cases, a can be defined as unity if no performance adaptation is required for the design point[2]. Due to low accuracy at the design point, which is at take-off (because performance deterioration due to the Reynolds number is expected at high altitude), a is the parameter that is used for calibration of the model.

6.4.3. Methodology

The problem is defined as a process that ultimately finds the optimal polynomial coefficients of Equation 6.1 for every scaling factor used such that the highest accuracy is achieved. The scaling factors employed are based on choices to correct for the off-design high altitude condition and take into account the type of turbomachine the correction is applied for.

As discussed in Chapter 3, the Reynolds number affects the pressure ratio, corrected mass flow, and efficiency of compressors and mainly only the efficiency of turbines. Therefore, the correction is component-type specific. The effect for compressors implies that the three performance criteria need to be corrected simultaneously. However, as discussed in the analysis of Section 5.1.4, the scaling factors do not sin-

[2]Design point here does not refer to the design point problem in the gas turbine simulation used to size the engine. The usage refers to an initial design value where the performance of the engine does not require scaling.

gularly affect the respected performance parameter that is being scaled (e.g. scaling the efficiency of the HPC affected the resultant pressure ratio, corrected mass flow, and efficiency. Check Appendix B). Moreover, a performance parameter is always implicitly a function of the other two parameters. As a result, for the Reynolds correction of compressors, only 2 parameters need to be chosen. Efficiency and the corrected mass flow will be the two parameters scaled in order to correct for compressors' performances. This includes the fan core, fan bypass, and the HPC maps. On the other hand, the turbine's efficiency will be scaled to correct for the HPT and LPT performances.

Figure 6.11 depicts the Reynolds correction using the minimization approach. First, the scaling factors are defined for each component as in Equation 6.1. The design variables in this case are the b and c coefficients of the scaling factor function. Therefore, the design vector length is 16 as opposed to 8 for the calibration step. The bounds are set to 15% change of the scaling factor function in absolute terms. The bounds for the optimizer were set based on trial and error until satisfactory results were met. The limiting factor tended to be the fan core component scaling factors. The optimizer attempts to impose the highest scaling factor for efficiency and then further balances the rest of the scaling factors down the gas path components. It is hard to pinpoint if the fan core component map itself is inaccurate solely or if the other components are also contributing to the error. This is because shifting the operation point of one component through scaling factors disturbs the equilibrium of the entire engine leading to the shift of all the components' operating points. The focus of the solver to numerically reach the bounds in order to blindly achieve the minimum objective function is an expected behavior of the under-determined system.

Since the Reynolds numbers for all three phases based on the output of the GSP simulation for the input flight points, before any corrections are applied, can be obtained, the bounds can also be computed as a function of the Reynolds numbers ($SF(Re)$) prior to any corrections. This means that setting the search space bounds is still an independent step. The polynomial coefficient combinations that achieve such bounds for the components inlet Reynolds numbers are shown in Table D.4. Once the scaling factors are defined and bounds are set within feasible physical limits, the optimization is initiated.

Note that the arrays for input and error computation are denoted by n, the number of data points in the flight envelope. This poses a computational cost issue. The flight simulation contains more than a thousand steady-state points. Using the data at this point in an optimization loop, where the entire flight needs to be simulated many times until convergence is met sufficiently, makes the problem impractical.

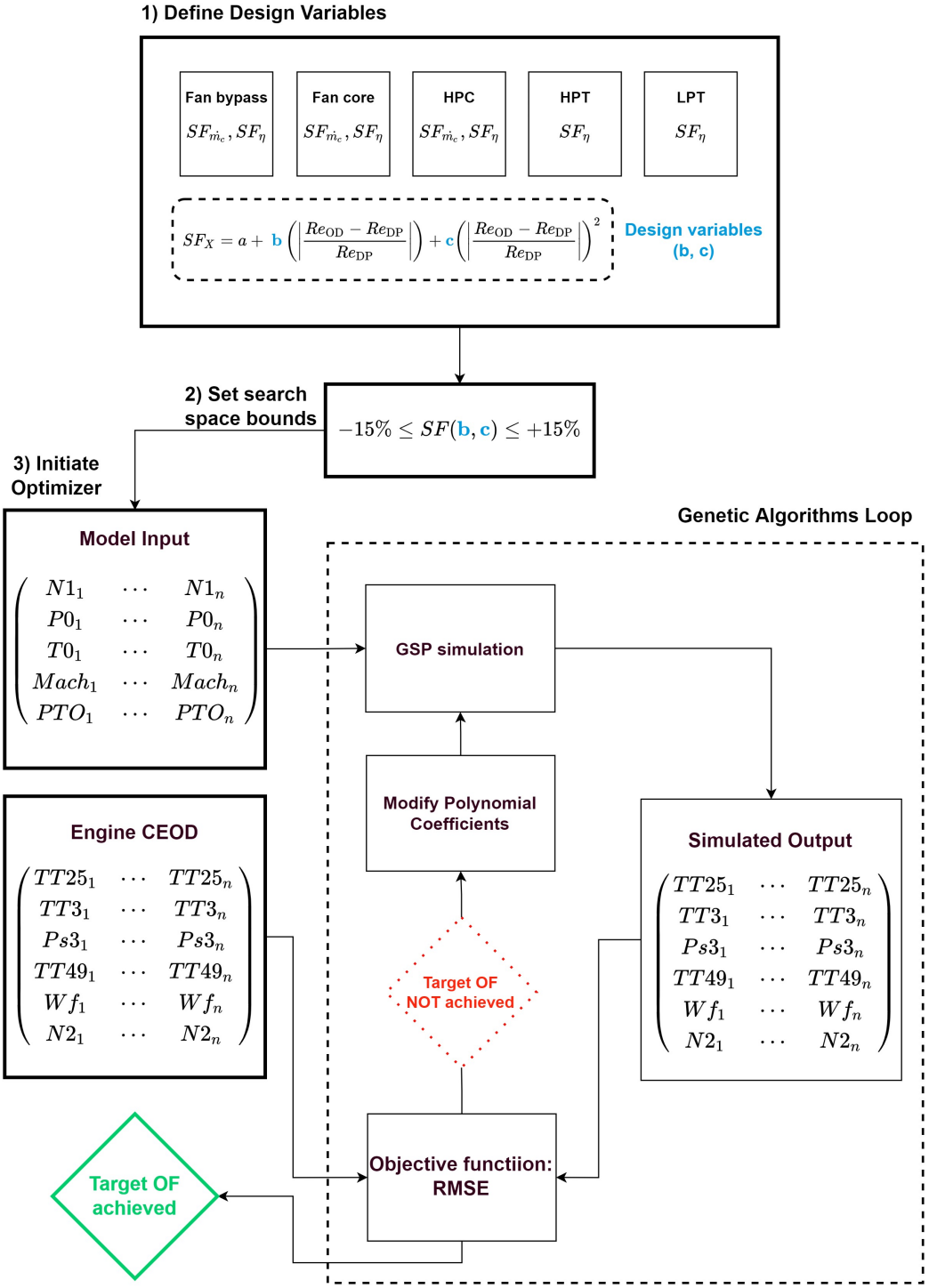

Figure 6.11: Reynolds correction flow diagram.

6.4.4. Data sampling - single flight

In order to have a feasible problem that is solvable within a reasonable time-frame, the number of points needs to decrease significantly. This can come at the cost of reducing the data accuracy if the points are not chosen carefully. The idea of the correction is to capture a certain pattern due to Reynolds numbers and correlate them to scaling factors. If point reduction is to be done, the same effect needs to be captured.

Reducing the number of points can be done by sampling certain points at each flight phase and assuming that they are sufficient to represent the entire flight. The sampling is then done on the basis of creating a sample set that captures the spread for the Reynolds numbers across all three phases.

The variation in the Reynolds number is due to the rapid change in altitude in the climb phase. For the cruise phase where certain altitudes are maintained most of the time, the Reynolds number therefore does not vary much due to altitude as compared to the change in fan speed. Therefore, points were uniformly sampled for the climb phase based on altitude, and for the cruise phase based on corrected fan speed. The final sampled flight version is shown in Figure 6.12 based on the original data shown in Figure 6.10.

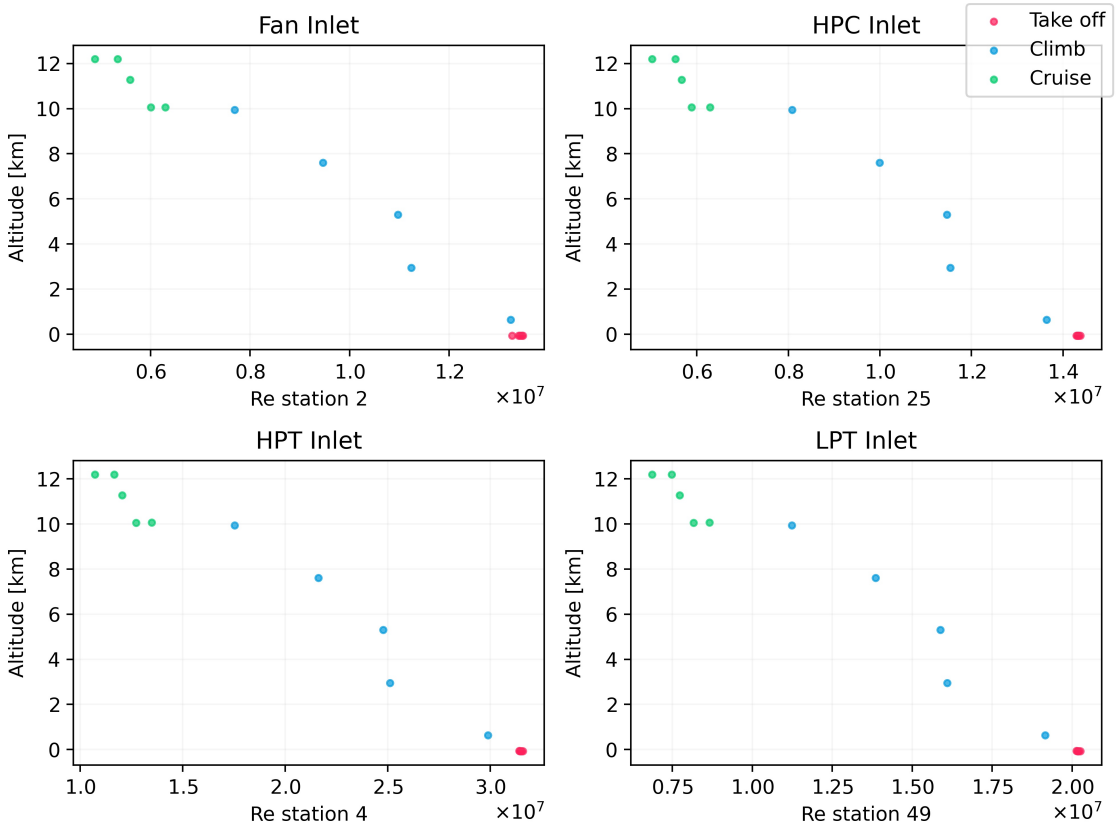

Figure 6.12: Sampled flight based on the GSP simulation: Inlet Reynolds number of turbomachinery components vs altitude.

6.4.5. Modelling assumptions

The following are the assumptions used in modelling the turbomachinery corrections using the OD scaling functions.

- The turbomachinery component maps with the chosen map design point do not need further pressure ratio scaling.
- Using the corrected mass flow and efficiency scaling factors for the compressors in OD fitting provides sufficient degrees of freedom for the optimizer to find a feasible solution.
- Using the efficiency scaling factors for the turbines in OD fitting provides sufficient degrees of freedom for the optimizer to find a feasible solution.
- The scaling factors solutions are applicable to model all flights with the same engine (same engine serial number).
- The bounds chosen are case-specific and are assumed to be correct for this modelling problem.

Determining the bounds is based on a trial-and-error approach and is heavily dependent on the modeler's judgment.

- All gas path simulated parameters outside of the on-wing measured ones are lacking. Improving the model beyond matching the target parameters is not possible. It is then assumed that the model user shall take this drawback into account (the model is expected to simulate the target parameters with a higher accuracy.).
- The data sampling approach is expected to capture the physical effect necessary to correct the component maps.
- The inlet guide vanes (IGV) and variable static vanes (VSV) are expected to affect the component maps. Their effect is, however, assumed to be captured within the component maps based on the scaling factor fitting. This assumption is mainly made for simplification. The main goal of the current modelling approach is a "proof of method". Further enhancements of the approach can be performed by data sampling for certain secondary performance parameter positions and performing the same fitting method. The model is then expected to be more accurate in modelling data points with the chosen secondary performance parameters.
- All other secondary performance parameters provided within the GEnx-1b CEOD are assumed to have negligible effects and are therefore neglected in the modelling approach. Additionally, those effects should be captured in the performance maps during the OD fitting.
- The employed OD scaling factors are expected to correct inherent errors within the model related to modeled components other than the respected component being scaled (e.g. the HPC map efficiency correction might be compensating for errors in the HPT map). This is a direct consequence of the under-determined system of equations.
- The on-wing sensor measurements are assumed to be true values. In reality measurement uncertainty, bias, and noise do exist. For simplification of the analysis done and focusing on the applied model enhancement methodology, the CEOD is considered sufficiently accurate.

6.4.6. Results and discussions

The Reynolds corrections results of the optimization are shown in Table D.3. Similar to the take-off calibration results, the optimizer opted for solutions that would maximize the scaling factor of the fan core efficiency. It still is not decisive whether the solver opting to improve the efficiency of the fan core is due to inaccuracies in the fan core map itself. The bounds defined in this problem are based on the scaling function that is defined as a polynomial. It is then more intuitive to look a the scaling factors results directly. This is shown in Section C.1.

The simulation error for the target parameters with the scaling factors applied is shown in Figure 6.13. It can be seen that the overall error has reduced significantly. It can also be seen that the cruise accuracy improves the highest compared to Figure 4.3. The cruise's accuracy is also better than the climb's. This is expected as the scaling factors affect scales with the Reynolds numbers deviation from take-off conditions. The highest improvement is therefore in the solutions that focus on cruise improvements rather than climb. From the solver's perspective, improving the cruise is also an "easier" task. This is because the Reynolds number variation in the cruise phase is much less than for the climb. Therefore, the optimal solution for the cruise lies in a region that is narrow. On the other hand, the solution for climb conditions requires taking into account all the Reynolds numbers from take-off to cruise. Satisfying all the steady-state points of the climb is a "harder" task for the solver.

The simulated climb error for different corrected fan speeds before and after Reynolds corrections are shown in Figure 6.14, and Figure 6.15. The correction effect is much more pronounced at higher corrected fan speed. This is because the fan speed increases during the climb, and therefore correlates with the Reynolds numbers. High Reynolds numbers exhibit the largest correction by the scaling function definition.

The simulated cruise error for different corrected fan speeds before and after Reynolds corrections are shown in Figure 6.16, and Figure 6.17. The parameter error prior to applying the correction is more constant per parameter. Once the correction is applied, the three different flight cruise altitudes can be noticed. This is because each of the three altitudes is associated with a different Reynolds number and subsequently, the scaling factors are different. It should be noted that even though the fan speeds at cruise have a higher spread than in climb, it is not the case for the Reynolds number spread. The Reynolds change due to the altitude gain during the climb is much larger as seen in Figure 6.10.

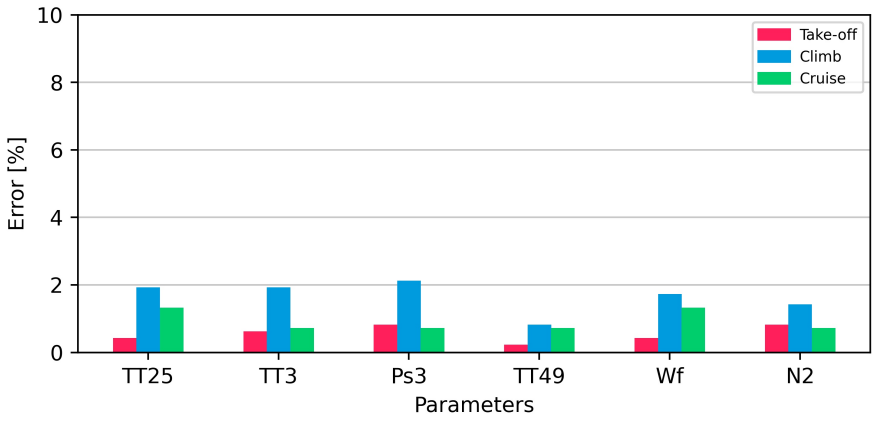

Figure 6.13: On-wing simulated flight error with Reynolds correction and take-off calibration.

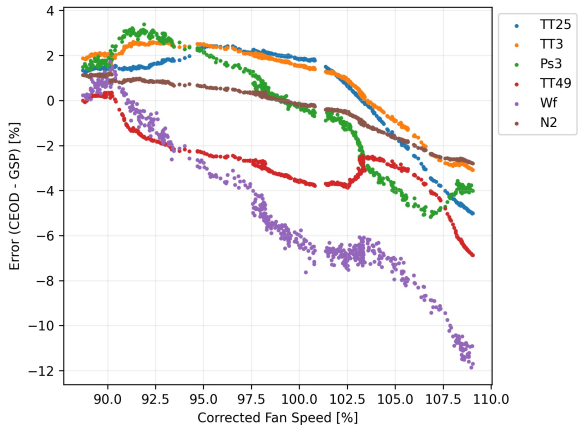

Figure 6.14: Climb output simulation error plotted at different corrected fan speeds with **no** Reynolds correction. Take-off calibration is applied.

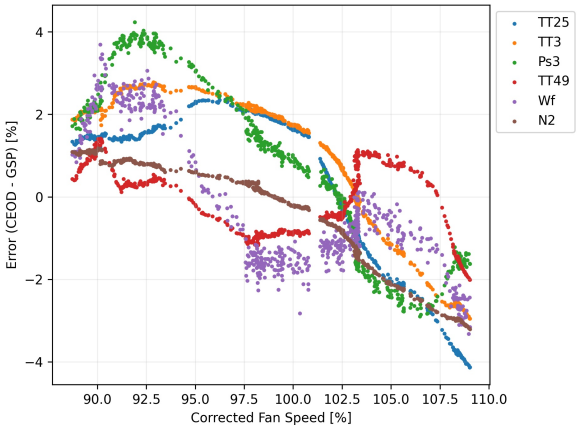

Figure 6.15: Climb output simulation error plotted at different corrected fan speeds with Reynolds correction. Take-off calibration is applied.

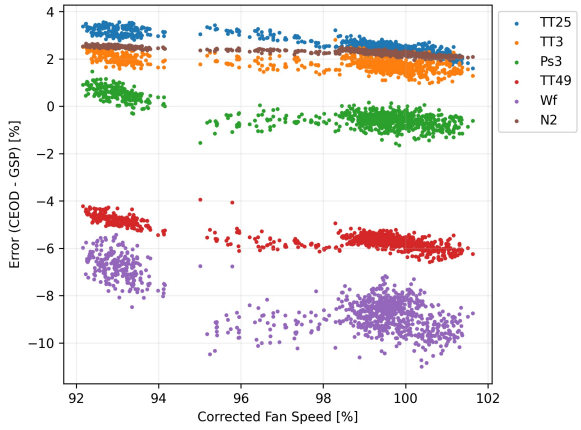

Figure 6.16: Cruise output simulation error plotted at different corrected fan speeds with **no** Reynolds correction. Take-off calibration is applied.

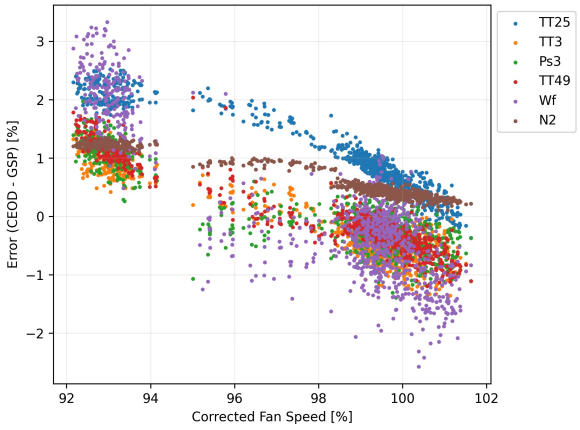

Figure 6.17: Cruise output simulation error plotted at different corrected fan speeds with Reynolds correction. Take-off calibration is applied.

6.5. Turbomachines quadratic splines approach

An extended approach to using the scaling factor as a polynomial to enhance accuracy is by utilizing splines. Splines are meant to improve fitting accuracy without increasing the order of the polynomial function. The latter in fact improves the accuracy of a fitting but comes at the cost of over-fitting and substantially increasing computational time. The idea of using splines that are quadratic, adds degrees of freedom to the scaling function in order to capture the Reynolds effect more accurately. As the method only aims at improving the model's accuracy through numerical means, the same assumptions hold from Section 6.4.5.

6.5.1. Methodology

The method is based on adding a number of breaking points (n) along the function which then the function is a number (n + 1) of quadratic polynomials that represent the scaling factor. The breaking points are then the connections between the quadratic polynomials. These polynomial functions should entail a degree of smoothness such that the final function is continuous. In the case of a quadratic polynomial, the smoothness constraint is the first-order derivative of the scaling function. Any higher orders smoothness constraint will result in the same quadratic polynomials (i.e. negating the usefulness of the splines).

Since the data is already split into take-off, climb, and cruise, it is convenient to place the breaking nodes between each phase. In the single equation scaling factors, the solution was heavily influenced by the cruise as the most error reduction is achievable there. The a priori assumption of using the splines is an added degree of freedom to further improve both the cruise and climb corrections (the solver will focus more on improving fitting for each phase without considering the other data points except for the smoothness constraints). Take-off conditions are "hard" to improve further beyond the calibration step as a function of the Reynolds numbers since the design point of the function (Re_{DP}) is at take-off.

If two breaking points are imposed, three different quadratic polynomial functions are required to represent a single scaling factor. A procedure is required in order to split the three problems chronologically. In the end, three polynomials should result in three optimization processes. The need for ordering the problems is mathematically due to smoothness constraints. Assuming that, the starting problem is the take-off, the solution shall not obey any constraint beyond the solver bounds. The climb and cruise solutions on the other hand need imposed constraints on the solver such that the solutions at the con-

nection points are smooth.

The most logical starting point for the splines optimization of the scaling factors is at the cruise phase because of its largest potential for improvement. The starting point is the least constrained as no requirement for smoothness is needed. Then, the constraints could be imposed on the solver as equality constraints [3]. The smoothness is imposed by equating the starting point of the cruise steady-state points and the last point of the climb steady-state points. Then, the optimization for the climb phase is initiated. Lastly, the process could be repeated for the take-off phase. The process flow is depicted in Figure 6.18. The last step for the take-off phase can be skipped without suffering much accuracy loss as the solution in that region is mainly affected by the calibration step. The last two terms of the polynomial function will always be very close to zero. The smoothness constraint is also not violated as the $Re_D P$ term for the climb is still at a take-off steady-state point (end of take-off point).

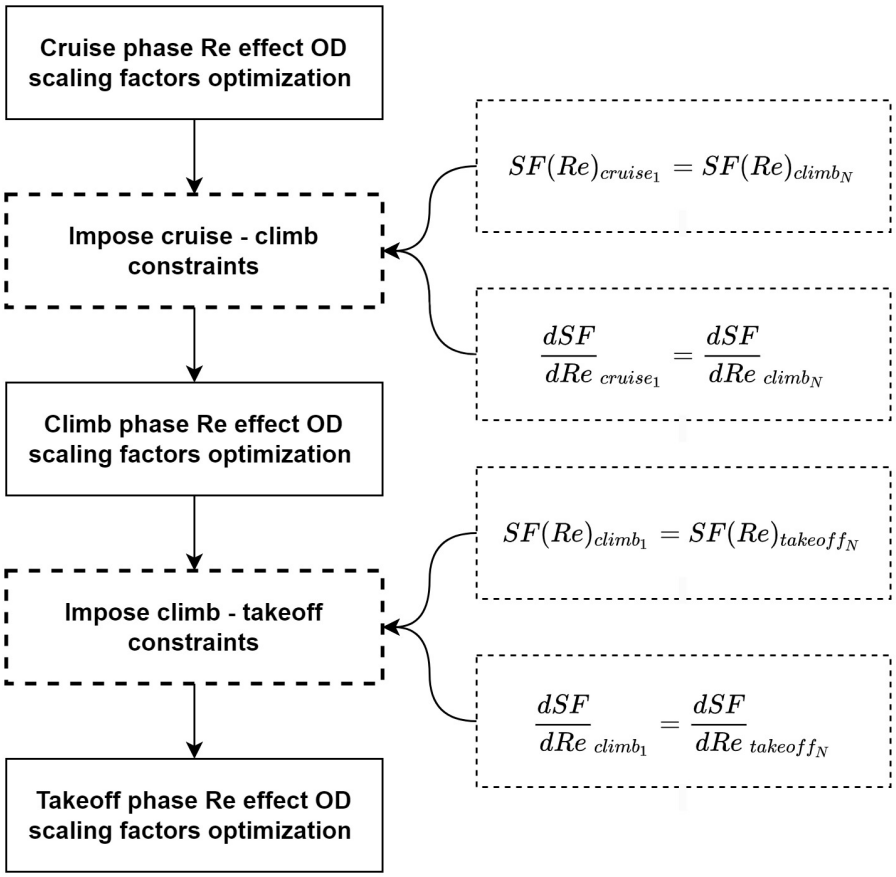

Figure 6.18: Reynolds corrections using OD quadratic splines procedure.

6.5.2. Results and discussions

The simulation error difference for the target parameters between using quadratic splines and single equation scaling factors are shown in Table 6.1 for climb and cruise. The take-off phase is out of the comparison as the change is negligible. It can be seen that the cruise error for all the parameters decreased. This indicates that in fact the single equation solution, even though mainly influenced by the cruise, was still limited by the climb. However, the average climb overall error has increased. In fact, the

[3] In practice this depends on the solver. Some types of solvers allow for hard constraints by violating them if needed to achieve a minimum. Other types require the use of inequality constraints with a tolerance.

Table 6.1: On-wing simulated flight error comparison of a single equation and quadratic splines corrections (quadratic Splines - single equation) for climb and cruise

Target parameter	Climb ΔE [%]	Cruise ΔE [%]
TT25	0.090	-0.618
TT3	-0.076	-0.259
Ps3	0.361	-0.261
TT49	0.675	-0.233
Wf	1.819	-0.329
N2	0.352	-0.445

global root mean square function for the objective function converges to a higher error value for using the splines solution as compared to the cruise.

These results at first may appear counter-intuitive as to why would the climb error increase if the solver had more freedom to fit each phase. The problem lies in the smoothness constraint. The solver achieved a high-accuracy model for the cruise. Finding a more accurate solution for the climb that smoothly matches the connection points to the high-accurate cruise solution was not possible. Due to the nature of the problem, the RMSE of phase does not affect the other. Therefore, the global RMSE could indeed decrease, which is what happened.

In order to overcome this issue, a possible solution is to employ the single equation OD scaling factor solution to the *cruise* splines solution. From that point, an attempt to decrease the climb solution could be started. The rationale is that the single equation solution balances the cruise and climb RMSE, but cannot improve one without impairing the other. Thus, the climb solution could be improved without changing the scaling factors for the cruise. This method maintains an overall same RMSE as for the single equation solution or lower.

The optimization results for the climb scaling factors splines polynomial is shown in Table D.5. The simulation error difference for the target parameters between using quadratic splines (cruise-based single equation solution) and single equation scaling factors are shown in Table 6.2 for the climb (the cruise difference is just zero). As a priori assumed, the climb error decreased by utilizing splines. The process can then be iterated once again by correcting for the cruise based on the new climb solution (in this case smoothness needs to be imposed for the cruise correction) until further improvement is reached. Care should be given to the number of iterations that could result in over-fitting to the selected flight. The results, based on the number of iterations reached at this point, which is one, are deemed satisfactory. The splines solution is visualized against the single equation solution in Section C.1.

Using the quadratic splines approach does in fact increase the model's accuracy. However, this comes at the cost of increased methodological complexity and increased computational time in order for the solver to find a solution. Additionally, the increased focus on matching the climb phase runs the risk of over-fitting. Therefore, the use of quadratic splines is deemed as a method to improve the model's accuracy based on user specifications. Based on this trade-off, further analyses and enhancements of the model will be carried out using the single equation OD scaling approach.

Table 6.2: On-wing simulated flight error comparison of a single equation and quadratic splines (cruise-based single equation solution) corrections (quadratic Splines - single equation) for climb and cruise

Target parameter	Climb ΔE [%]
TT25	-0.005
TT3	-0.099
Ps3	-0.238
TT49	0.042
Wf	-0.183
N2	-0.082

6.6. Nozzle performance correction using OD functions

As discussed in Section 3.5, nozzle losses are attributed to losses in the exhaust mass flow and velocity, which leads to a decrease in the total force. These losses are partly due to the viscous shear layer at the nozzle walls that leads to energy dissipation. Therefore, the nozzle losses do correlate with the decrease in the Reynolds numbers. The arguments presented in Section 6.4 hold for the nozzle corrections. The methodology presented here is an extension of the methodology presented for turbomachinery corrections using OD scaling functions. The data filtering and sampling procedure is thus unchanged.

6.6.1. Methodology

The methodology of correcting nozzle losses is based on utilizing the nozzle coefficients in off-design. These are the velocity and thrust coefficients in GSP. The physical consequence of the growth of the boundary layer in nozzles is a decrease in the average axial velocity through the nozzle and a decrease in the mass flow rate due to the blockage effect.

The use of the velocity coefficient directly alters the mass flow rate through the nozzle and consequently shifts the equilibrium of the entire engine to a different operating point. On the other hand, the thrust coefficient only modifies the thrust at the end of the calculations. Therefore, the engine operating point is not affected. The on-wing sensor measurement does not include any data on the thrust, which makes it not part of the target parameters. Using the thrust coefficient for model fitting, in this case, does not contribute to the accuracy of the model (at least per the definition of how accuracy is computed).

The velocity coefficient can then be presented by a generic polynomial as a function of the inlet Reynolds number as shown in Equation 6.2, respectively. The representation of the nozzle coefficients is applicable for both the core and bypass nozzles of the turbofan. Unlike the turbomachines representation of the scaling factors coefficients, which were based on the take-off calibration value, the value is based on the reverse engineering model by Ramdin [40]. In Ramdin's work, the coefficients were tuned to meet target parameters, of which the total thrust of the engine was one of them. Therefore, the model is expected to represent thrust at take-off accurately. Moreover, due to the lack of the thrust parameter in the CEOD, a calibration step is not feasible. Therefore, it is assumed that the thrust levels of the engines based on the mounted take-off conditions and unmounted test cell conditions are the same. The coefficients at take-off are shown in Table 6.3.

$$C_V = a + b\left(\left|\frac{Re_{\text{OD}} - Re_{\text{DP}}}{Re_{\text{DP}}}\right|\right) + c\left(\left|\frac{Re_{\text{OD}} - Re_{\text{DP}}}{Re_{\text{DP}}}\right|\right)^2 \tag{6.2}$$

Table 6.3: Nozzle coefficients values based on Ramdin's model matching.

Nozzle type	C_T	C_V
Bypass	0.93	1
Core	0.9376	1

The polynomial coefficients, *b*, and *c*, are now part of the problem definition. The optimal values need to be found in order to minimize the model error in matching the performance parameters. This can be done by extending the OD scaling approach established to account for turbomachinery losses. The resultant problem is one with an increased dimension of 4 design variables. This would directly increase the computational time for convergence (if possible), yet maintain the complexity of the application to a similar level.

The problem now becomes a series of scaling factors that optimally simulate the target parameters. This inherently creates an accumulation of errors within the model components. The high accuracy of sub-components would lead to an overall high-accuracy model, but a highly accurate model doesn't necessarily mean that the model components are highly accurate themselves. Therefore, because the optimizer is essentially fitting the model to simulate target parameters, errors in sub-components are practically present. For instance, the underperformance of a turbine in expanding the flow can be compensated for by the nozzle to meet the target parameters. The only tool left for enhancing the model is to attempt to keep the model as physically feasible as possible. This is done by bounding the optimizer to find solutions within specific regions.

It is essential to set bounds to the optimizer design variables for the nozzle coefficients within the ranges of the expected performance of a turbofan. The minimum reported value for the thrust coefficient by Kurzke [26] is around 0.8 but could be considered an outlier as the average is around 0.94 points. Also, Fletcher's [13] lowest reported value is 0.977. The values presented in the previous table are however lower. This is because, in Ramdin's approach [40], the optimizer was given more freedom to test thrust coefficients on a larger search space in order to obtain a more accurate model. It should be noted, however, that the model is numerical and carries assumptions to accomplish a target, that is to simulate the target parameters with high accuracy. Therefore, designers sometimes opt to go beyond correlations given that the results are still physical.

The bounds set is the model designer's choice. Allowing more freedom to the solver depends on the end goal (i.e. what parameters are needed to be simulated with high accuracy). If the optimal solution is outside the correlation bounds significantly, it is crucial to comprehend the extent to which the model can be used. For example, assuming that the optimal solution for the thrust coefficient is 0.5 (seriously off normal engine performance), one needs to be careful about the model's usage. Disregarding that the model is probably quite nonphysical, one can still use the model to simulate the target parameters with high accuracy (given that a good match was achieved). Pushing the model beyond this usage would be a blunder.

The bounds chosen for conducting the nozzle corrections for the velocity coefficients are shown in Section D.4. These bounds were set after trial and error as the optimizer usually opted for solutions very close to the upper bound. The extended design variables that include the nozzles losses coefficients are shown in Figure 6.19.

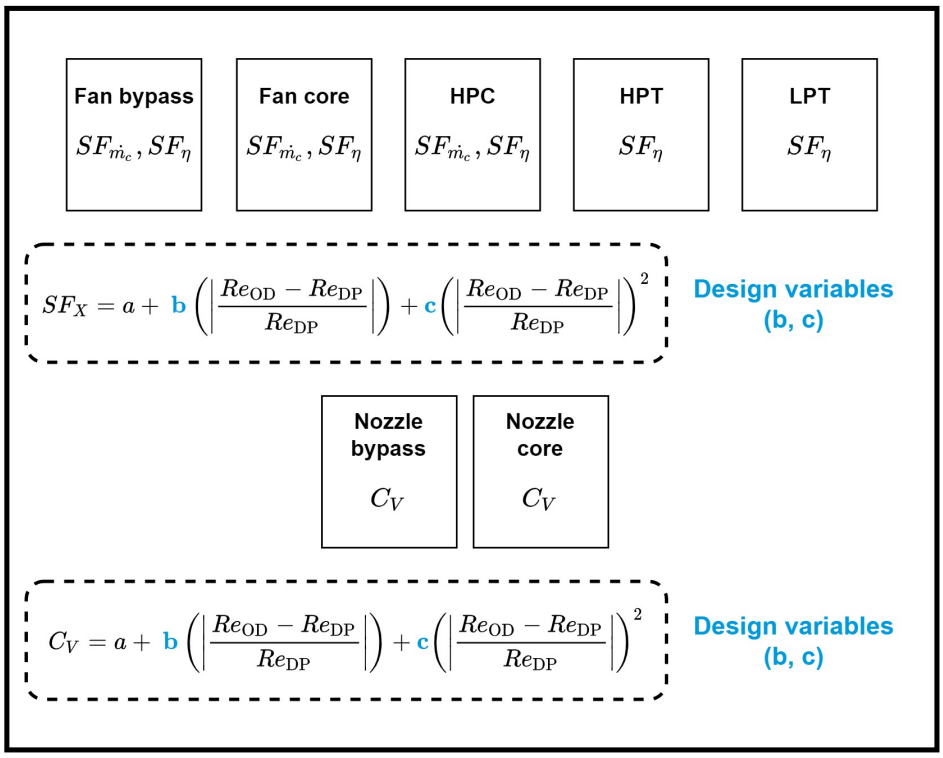

Figure 6.19: Extended design variables including nozzles losses coefficients.

6.6.2. Modelling assumptions

The following are the assumptions used in modelling the nozzle corrections using the OD scaling functions. These assumptions are complementary to the turbomachinery correction assumptions.

- Scaling the nozzles using the velocity coefficient is assumed to be sufficient to correct the nozzle performance.
- There is no direct quantification of the nozzle performance in the CEOD. It then assumed that the measured parameters were sufficient to correct the nozzle performance. The result is an added degree of freedom that enhances the fitting approach.
- The employed OD scaling factors are assumed to correct inherent errors within the model other than the nozzle performance. This is a direct consequence of the under-determined system of equations.
- The bounds chosen are case-specific and are assumed to be correct for this modelling problem. Determining the bounds is based on a trial-and-error approach and is heavily dependent on the modeler's judgment.

6.6.3. Results and discussions

The results of the extended approach with the scaling factors including nozzle corrections offer an overall improvement to the model's accuracy. The difference in error between the extended design vector with the nozzle velocity coefficient approach and the original design vector approach is shown in Table 6.4. The total RMSE error in fact drops. The nozzle coefficients and turbomachinery scaling factors variables optimized results are shown in Table D.7.

The results indicate that the added degree of freedom in modelling the nozzle through the velocity co-

efficients can, in fact, improve the accuracy of the model even though the nozzle performance is not within the CEOD and therefore not part of the optimization. As a direct consequence. the OD scaling factors compared with the previously obtained solution that neglected the nozzle performance is different. As the solver attempts to find a new optimal solution, all design variables change and all the scaling factor trends therefore also change. The new design vector solution set is visualized in Section C.2.

Including the velocity coefficients of the nozzles notably improved the Ps3 parameter in the climb. Typically, the climb improvements were not significant due to the higher Reynolds number associated with that flight phase. In this case, the added degree of freedom allowed the solver to improve the overall climb accuracy (note that TT25 error still increases) without decreasing the cruise accuracy. This result indicates that further improvements can be explored by correlating more parameters in the modelling approach.

Additionally, a solid improvement in cruise is gained amongst all parameters except for TT25. It can be concluded that including the velocity coefficients of the nozzles in the design vector does improve the overall results of the chosen flights. Further validation is still needed to prove that the model is applicable to different flights and the high accuracy is not an over-fitting case.

Table 6.4: On-wing simulated flight error change comparison (Extended design vector with nozzle coefficients method - original turbomachinery single equation design vector method)

Target parameter	Climb ΔE [%]	Cruise ΔE [%]
TT25	0.227	0.086
TT3	-0.135	-0.205
Ps3	-0.500	-0.321
TT49	-0.038	-0.276
Wf	-0.362	-0.522
N2	-0.072	-0.202

7. System performance simulation

To ensure that the scaling factors are well-defined and have tangible physical effects, a more detailed analysis of the gas path simulations is required. This chapter focuses on motivating changes in the gas path parameters through physical concepts and fundamental reasoning.

In most cases, the effects become apparent at high Reynolds numbers, which are determined by the scaling factors. These corrections depend on the inlet Reynolds numbers and primarily impact component performance parameters, the pressure ratio, efficiency, and corrected mass flow. The relationship between these parameters and the inlet Reynolds number is explored. For other cases, the gas path parameters are displayed over time.

Throughout this chapter, the spotlight is on understanding how corrections influence changes in Section 7.1 through Section 7.7. It then becomes evident that the target parameters play a pivotal role in driving any alterations. Lastly, general summarizing remarks are provided Section 7.8.

The figures and plots presented are based on GSP simulations using the input parameters of the CEOD. These are mentioned in Section 4.2. The additional input parameters in the corrected results are the scaling factors that modify the turbomachinery maps and nozzle coefficient's performance in order to achieve a higher model accuracy.

7.1. Components pressure ratios

The simulated turbomachinery components' pressure ratios before and after Re corrections are shown in Figure 7.1. The overall pressure ratio does not deviate except near the end of the climb. This change is due to pressure ratio changes in the fan core and HPC. The fan bypass pressure ratio change is negligible. Minor deviations are also present in the HPT and LPT.

The main deviation of the fan core and the HPC are due to the target parameters specifically, TT25 and TT3, due to their larger error deviation (shown in Figure 6.14 and Figure 6.16). Prior to applying Reynold's corrections, the model underestimates the TT25 and TT3 (Ps3 is relatively well predicted). Therefore, the optimizer will ultimately attempt to increase their values by manipulating the scaling factors. The increase in the fan core pressure ratio and then the decrease in the HPC results in the almost null effect in the OPR. This means that the change in pressure ratio mostly affects the gas path parameters at station 25. The TT25 value is then increased by the increase in the fan core pressure ratio.

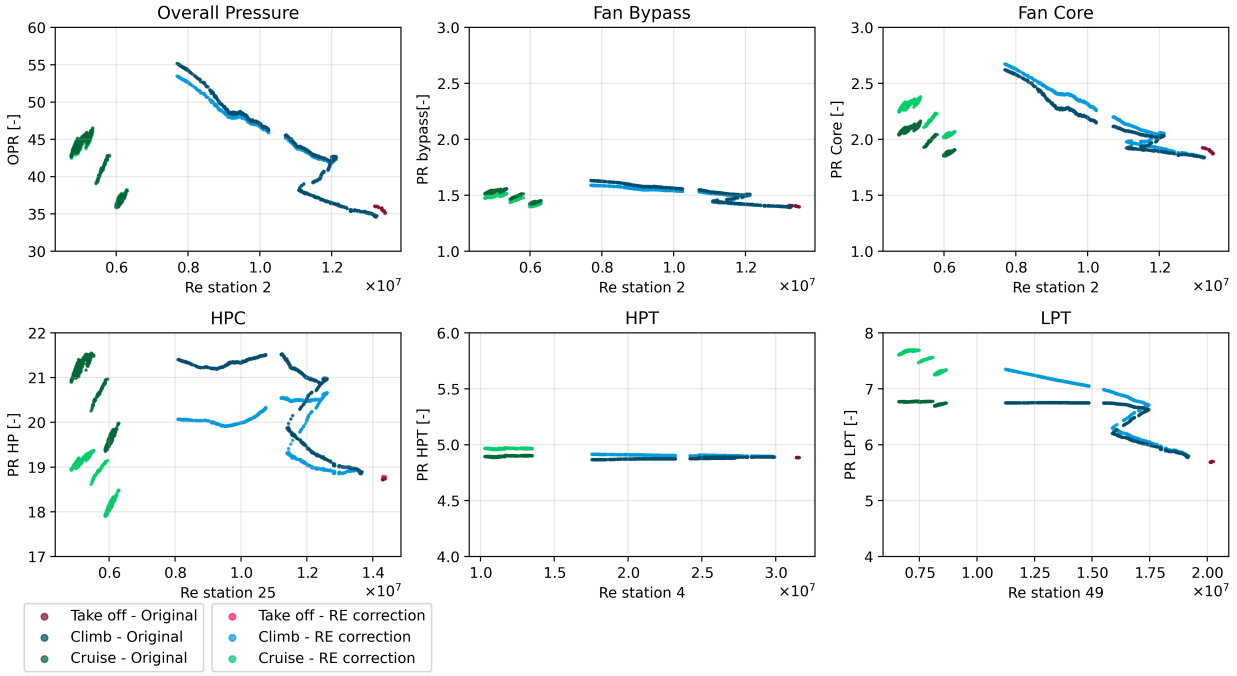

Figure 7.1: Corrected vs uncorrected simulated components pressure ratios.

7.2. Components efficiencies

The simulated turbomachinery components' efficiencies before and after Re corrections are shown in Figure 7.2. The general trend is an increase in the efficiency of all the components except for the HPC. The simulated fuel flow prior to correction is over-estimated. This means in order to obtain a more accurate model the simulated fuel flow value needs to decrease. In other words, the performance of the turbofan needs to increase. Therefore, the resultant trend is an increase in the overall efficiency of the system.

The HPC sharp decrease in efficiency is due to the TT3 target parameter. The TT3 value is underestimated. One way to increase the temperature at the end of the compression process is by decreasing the efficiency (i.e. the compressor requires more energy in order to obtain a certain pressure ratio).

Moreover, the increase in the HPT efficiency can be related to the shaft speed. The N2 estimated value prior to correction is underestimated. To increase the shaft speed the amount of energy extracted from the turbine needs to increase. Therefore improving the efficiency of the HPT results in an increase in the N2 speed value.

The largest efficiency gain is seen in the fan bypass. This is a direct result of the under-determined system that lacks the measurements at the bypass. None of the target parameters are in the bypass nozzle gas path. The result is a high level of freedom in the optimizer. Therefore, the optimizer attempts to improve the performance of the engine by directly largely attributing most of the error to the fan bypass component.

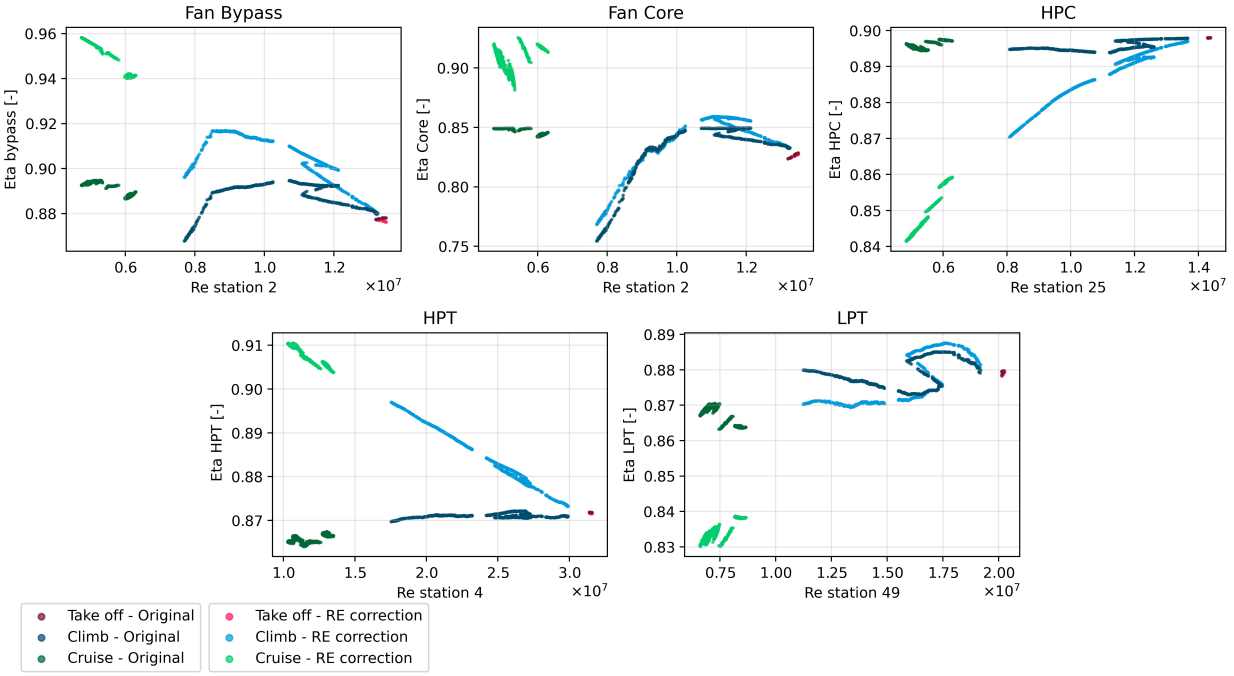

Figure 7.2: Corrected vs uncorrected simulated components efficiencies

7.3. Components corrected mass flow rate

The simulated turbomachinery components' corrected mass flow before and after Re corrections are shown in Figure 7.3. The main components that are affected are the compressors. This is a result of the problem definition where the corrected mass flow was not scaled. In the sensitivity analysis in Section 5.1.4, it was seen that the turbine-corrected mass flow was not affected by the scaling factors of the efficiency which is the only one used in this problem. It should be noted; however, the small differences seen in the turbine plots (note the scale!) are due to convergence (i.e. numerical truncation errors).

The increase seen in the fan bypass and fan core components is due to the speed-up of the N2 shaft. The corrected values with respect to inlet conditions, which include the N1 speed, are constant. The only other parameter that influences the total mass flow into the turbofan is the N2 speed. The N2 speed as mentioned is under-estimated prior to the correction.

The HPC corrected mass flow can be seen to be decreasing. Although the N2 speed is increasing and should correspond to higher mass flows, the inlet conditions are different and therefore affect the corrected values. The ratio of inlet pressure ratio increases to the inlet temperature ratio increase is higher; therefore, the corrected mass flow rate is lower [1].

[1] The corrected mass flow rate is defined as $W_c = \frac{W_{\text{map}}\sqrt{\frac{T_{\text{inlet}}}{288.15}}}{\sqrt{\frac{P_{\text{inlet}}}{1.01325}}}$

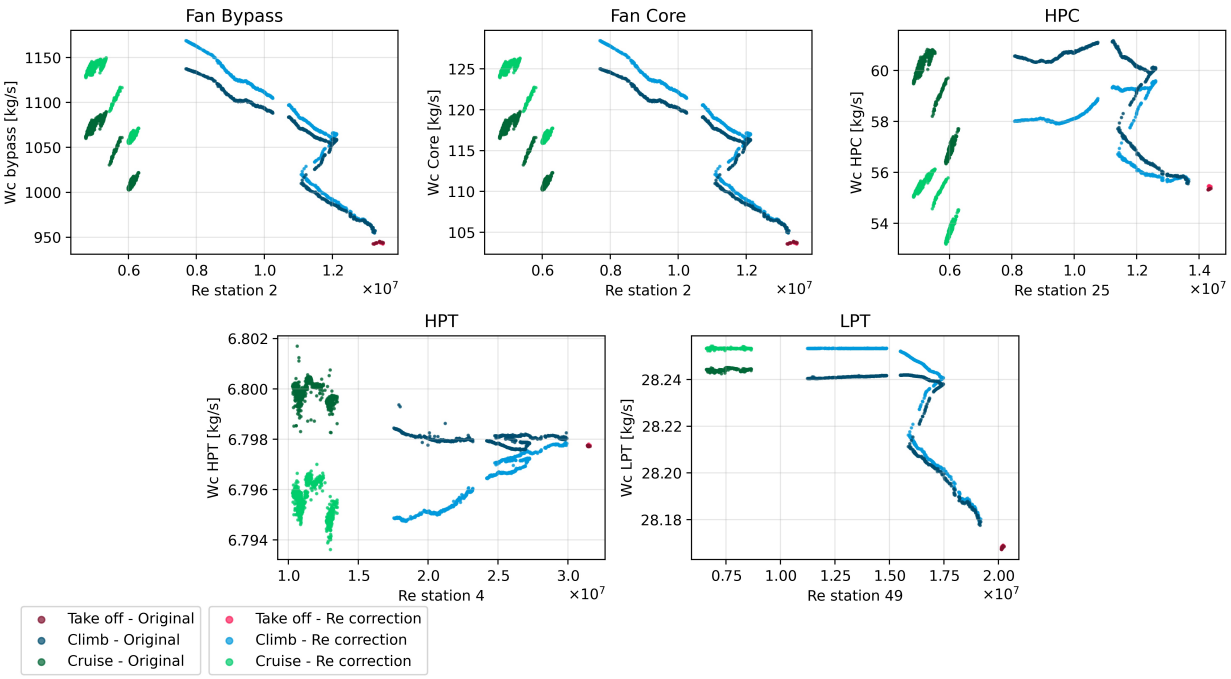

Figure 7.3: Corrected vs uncorrected simulated components corrected mass flows

7.4. Gas path mass flows

The simulated gas path mass flows before and after Re corrections are shown in Figure 7.4. In general, the mass flow rates are affected by altitude change, flight speed, and spool speeds. As the model input conditions, which include the ambient conditions the flight Mach number, and the fan speed, are constant (between corrected and uncorrected simulations) the only parameters that can alter the mass flow rate is the N2 shaft. The N2 shaft is increased due to the applied correction. The slight increase in the mass flow rates in the gas path is due to this core shaft speed increase.

The fuel flow can also be seen to decrease. This is because the model required a performance increase to improve the accuracy. The decrease in the fuel flow can be attributed to the overall increase of the engine efficiency which was achieved by increasing most of the component's efficiencies.

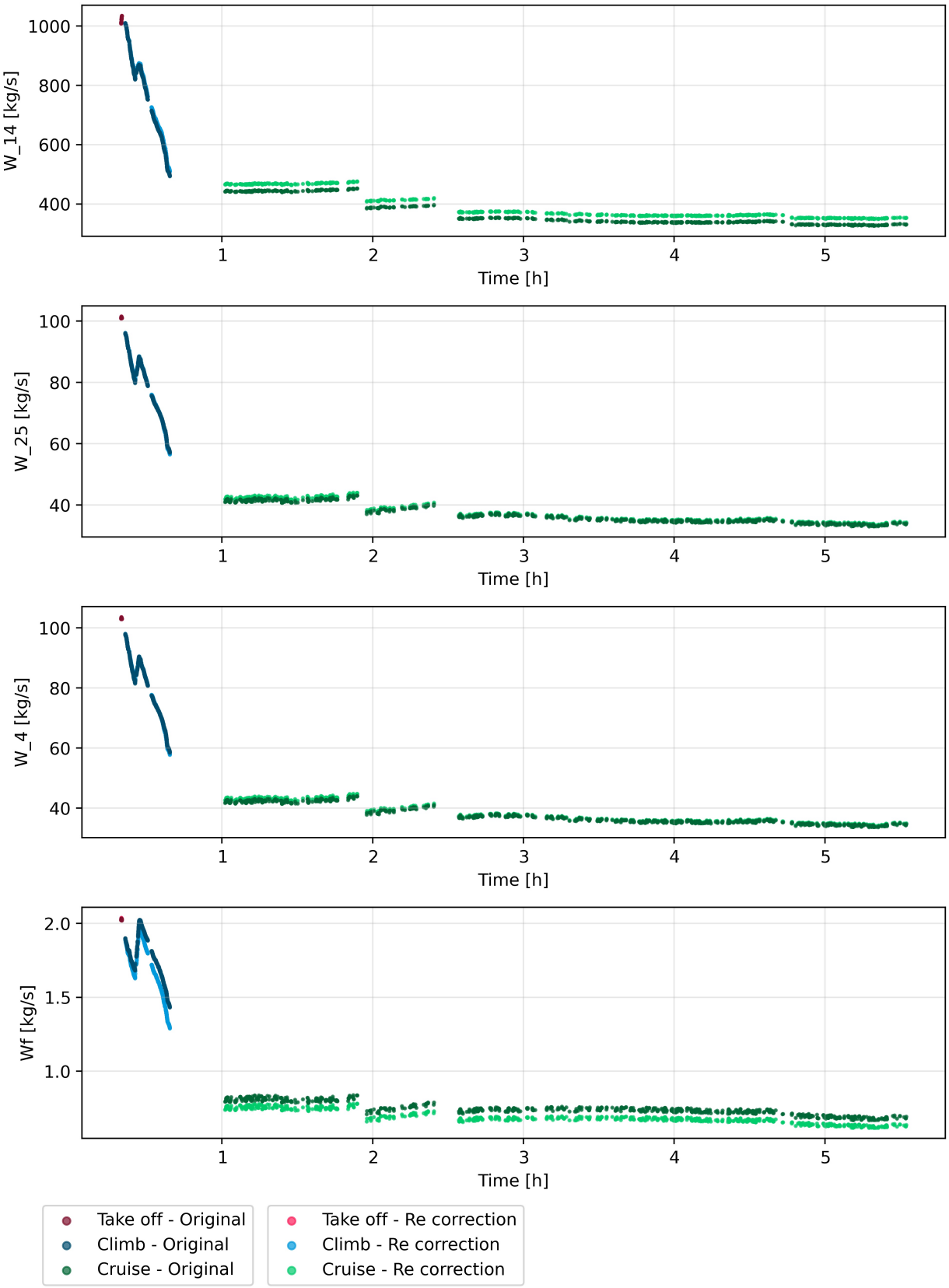

Figure 7.4: Corrected vs uncorrected simulated components gas path mass flows.

7.5. Gas path total pressures and temperatures

The simulated gas path total pressures and total temperatures before and after Re corrections are shown in Figure 7.5 and Figure 7.6, respectively. The deviations are due to the changes in the components' pressure ratios and efficiencies. In general, the main reason for the large differences seen is due to the lack of measurement sensors that allow the optimizer to obtain solutions with a higher degree of freedom.

The total pressures at the outlet of the turbomachinery components are not affected as was expected from the results of the pressure ratios. In the pressure ratios graphs, only the fan core was increased and then reduced back by the HPC. This is clear in the plots presented here. The reason the pressure ratio of the fan core is decreased as established is to match the TT25 value in the target parameters. The effect of the under-determined system due to the lack of all gas path measurements to be included in the target parameters is very pronounced in the total pressure plots. If multiple pressure sensors are recorded and provided in the CEOD, definitive deviations in the corrected results would be present.

The total temperature results on the other hand depict more deviation compared to the total pressures. The deviations are a result of the efficiency changes on top of the pressure ratio changes. The total temperature decrease in the fan bypass outlet is a result of the improved performance of the corrected model that requires lower fuel flow (note the negative effect of the reduced temperature on the bypass nozzle jet velocity and thrust).

The fan core, HPC, and HPT outlet total temperature changes are a direct result of the matching process of the target parameters (explicit definition). These changes can be seen as the means of changing the engine operating points. Essentially, the problem definition can be rewritten as a process where the optimizer attempts to find the best equilibrium points that match those target parameters.

The combustor outlet temperature decreases due to the decrease in the fuel flow, which results in a combustion process that is more lean (lower fuel-to-air ratio). Lastly, the LPT temperature decreases is a consequent result of the lower temperatures aft of the combustor (note the negative effect on the core nozzle jet velocity and thrust).

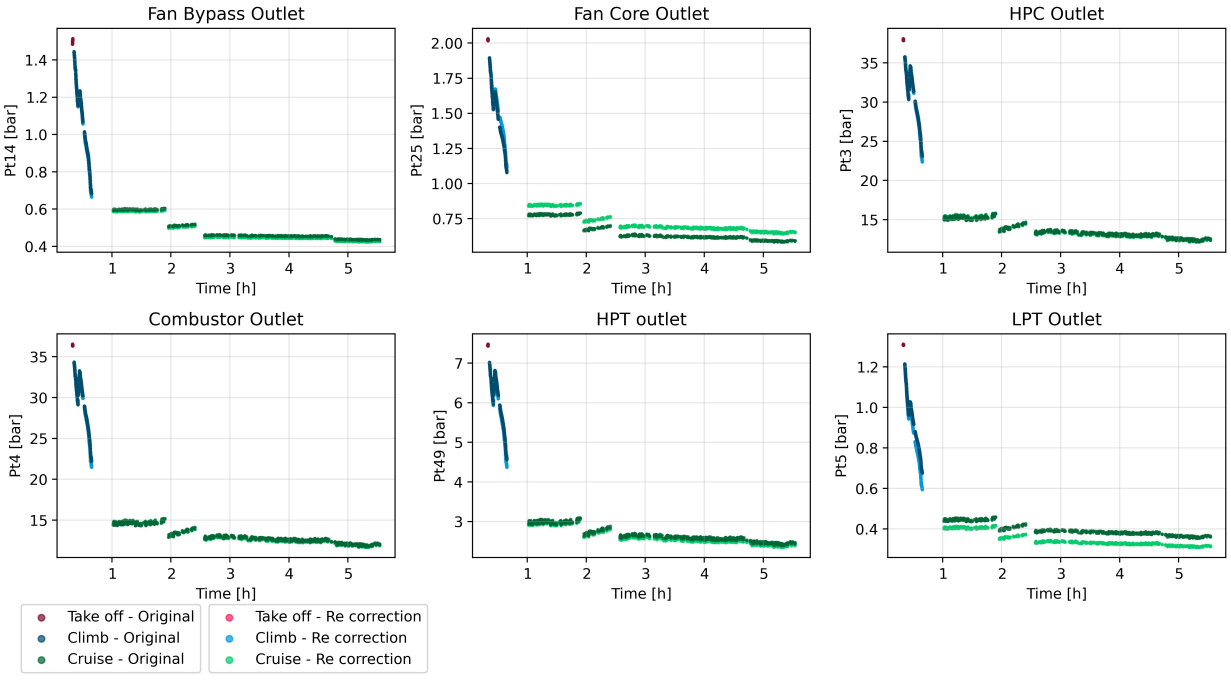

Figure 7.5: Corrected vs uncorrected gas path total pressures.

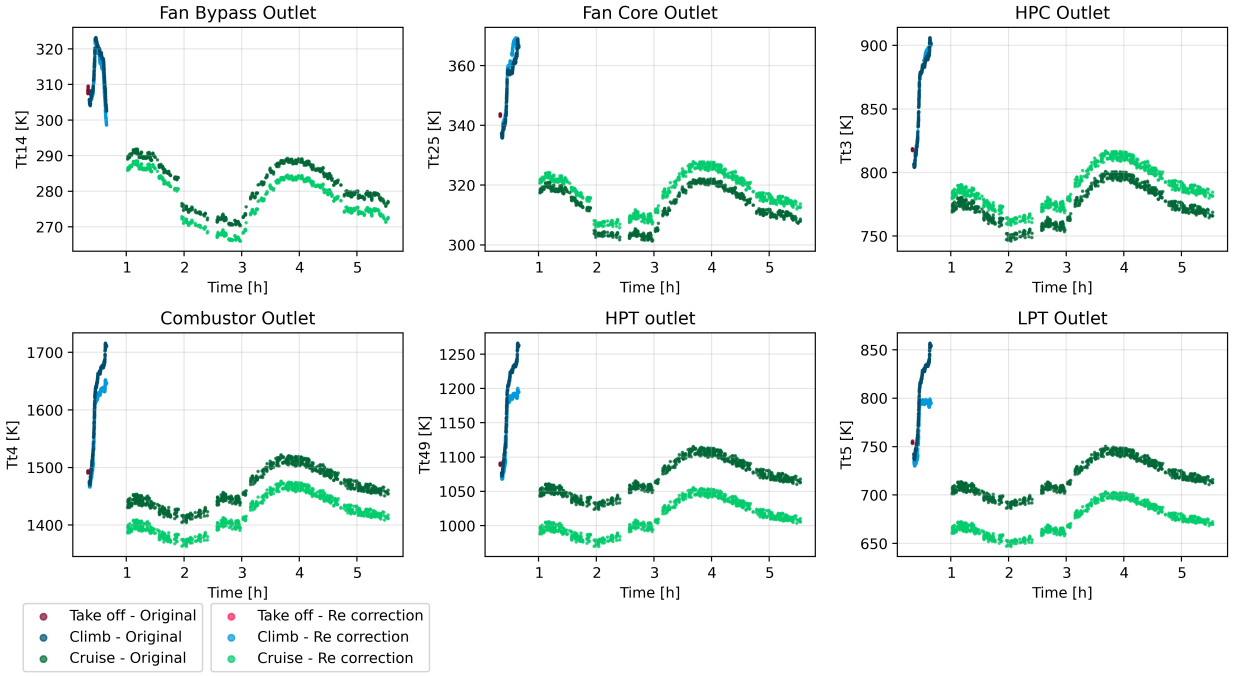

Figure 7.6: Corrected vs uncorrected gas path total temperatures.

7.6. Net force and thrust specific fuel consumption

The simulated net force and thrust-specific fuel consumption before and after Re corrections are shown in Figure 7.7. With the Reynolds corrections applied, the net thrust starts to mainly decrease at high altitudes. This could be counter-intuitive given that the mass flow rate increases, which increases the momentum term of the force equation. The force decrease is a result of the jet velocity which has a dependency on the nozzle inlet gas total temperature. The jet velocity in both cases of an unchoked and choked nozzle is a function of the gas properties and ambient conditions[2]. In Section 7.5, the total temperature was shown to drop. Therefore, the potential expansion of enthalpy into kinetic energy decreases. The resultant effect is an overall decrease, overcoming the mass flow rate gains, in the net thrust.

The thrust-specific consumption increases, as a direct consequence of the optimizer improving the turbofan performance at high altitudes. The effect is mainly due to the general improved efficiencies of most components that resulted in a lower fuel consumption.

[2] In case of an unchoked nozzle: $V_{\text{jet}} = \sqrt{2c_{p,g}(T_{0,6} - T_{\text{jet}})}$. In case of a choked nozzle: $V_{\text{jet}} = k_g \cdot R \cdot T_8$.

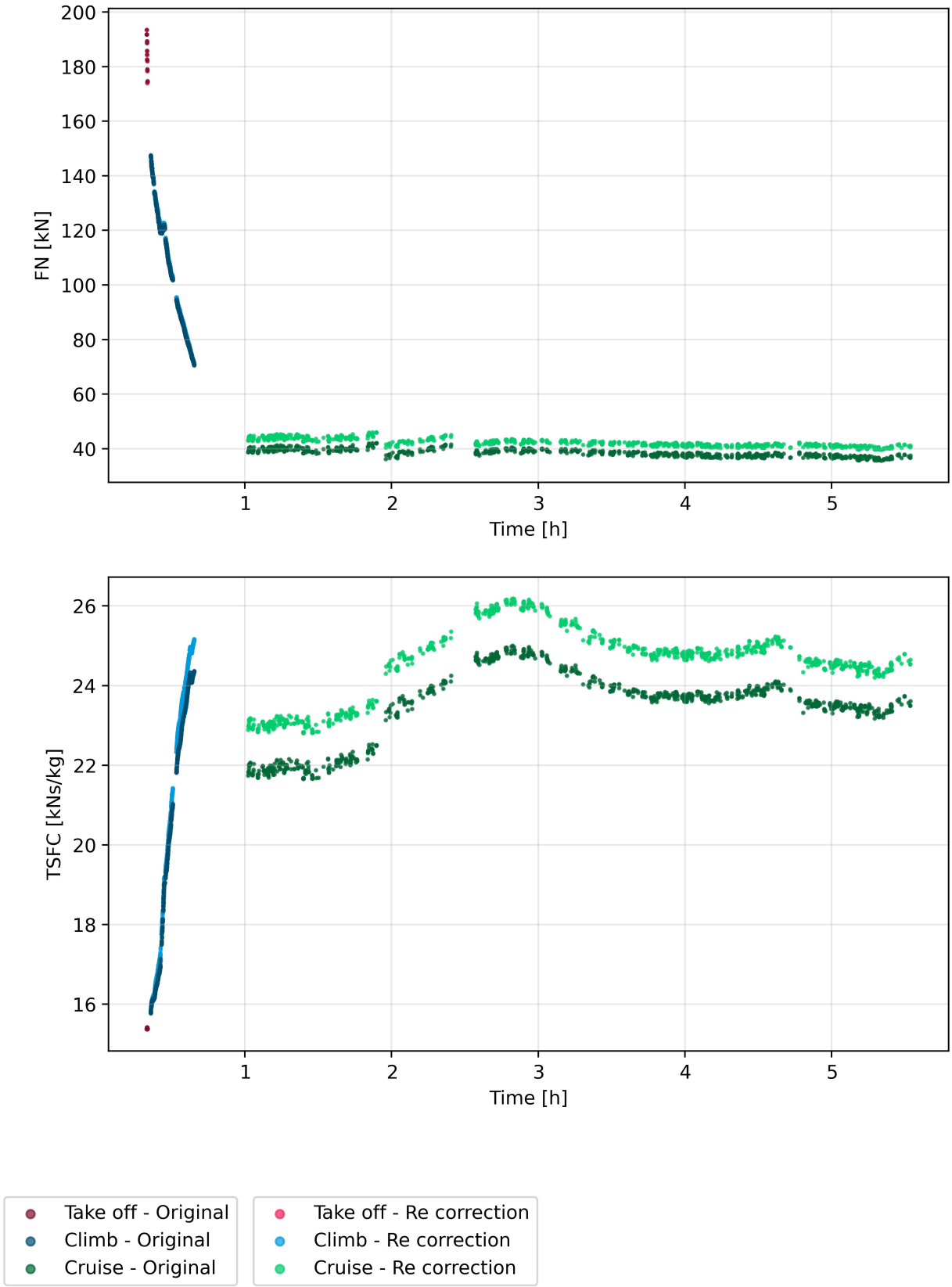

Figure 7.7: Corrected vs uncorrected simulated engine net force and thrust specific fuel consumption through the flight duration.

7.7. Turbomachinery components operating lines

This section depicts the components' operating lines on the component maps. Due to the nature of the problem, there is not a single component map as in a classical modelling problem. In this problem, there exist multiple operating points with a wide range of operational Reynolds numbers in the flight envelope. The result is a set of scaling factors for every operating point with unique inlet Reynolds numbers. Therefore, there exists multiple component maps. Visualizing the operating lines is consequently challenging, and the outcome is peculiar.

The operating lines plotted on the maps of the components are shown in Figure 7.8 to Figure 7.12. In the compressors plots, the speed lines are depicted for the scaled maps at the design point (this is the starting point at take-off with calibration scaling factors) and at the highest point in the flight envelope. The spool speed between both ends are then shown as a shaded region. One could interpret the shaded region as the areas where the map morphs in order to fit the model. It then should be clear that there exists multiple distinct maps throughout the shaded region. The shaded regions are connected and morph simultaneously.

On the other hand, the turbine maps do not depict the shaded region, due to the complexity of the plot (spool speed lines overlap). The speed lines at the design point and the highest point in the flight envelope are still depicted. In any case, the turbine operating lines do not vary as much as the compressors.

The operating lines shown are split into take-off, climb, and cruise. As the data points between the three flight phases are not continuous, several sudden changes are present between the phases. The sudden changes are a result of the scaling factors. Although the scaling functions themselves are continuous, the input data is not, especially between phases. The trends are directly a result of the application of the OD scaling factors. The following is a description of the operating lines trend per component.

- **Fan bypass** - The fan bypass operating line starts at take-off with the pressure ratio increasing throughout the climb. This is due to the increase in N1 speed and change in ambient parameters (pressure and temperature drop) that influence the increase in the corrected mass flow. The cruise point starts off at a lower pressure ratio compared to the climb end due to the decrease of the N1 speed and the requirement for a lower thrust level. Moreover, the efficiency is almost constant for the climb but starts to increase towards the end of the climb phase (top of climb). The efficiency then jumps to a higher value at cruise, where the effect of the scaling factors are very clear.
- **Fan core** - The fan core operating line starts at take-off with the pressure ratio increasing throughout the climb and cruise phases. The trend here is similar to the bypass with the exception of a decreasing efficiency towards top-of-climb. The efficiency increase in the bypass is due to the lack of sensor measurements there, which gives freedom to the solver to correct a large portion of the error using the bypass.
- **HPC** - The HPC operating line moves from take-off and the pressure ratio increases continuously in the climb. The cruise pressure ratios, however, start at a lower value due to the scaling down of the corrected mass flow. The efficiency decreases during the climb phase and the cruise phase reaching the lowest efficiency towards the end of the cruise. The reason for the large drop is to increase the TT3 target parameter.
- **HPT** - The HPT pressure ratio hardly changes throughout the entire flight envelope. This steadiness can be attributed to the general steadiness of the corrected core shaft speed compared to the corrected LPT shaft speed as shown in Figure 7.13. The efficiency of the HPT increases due to improving the performance of the turbine and reducing the fuel flow.
- **LPT** - Unlike the HPT, the LPT pressure ratio varies due to the variation of the corrected spool speed as shown in Figure 7.13. Efficiency of the LPT is generally constant with a small peak at the top-of-climb.

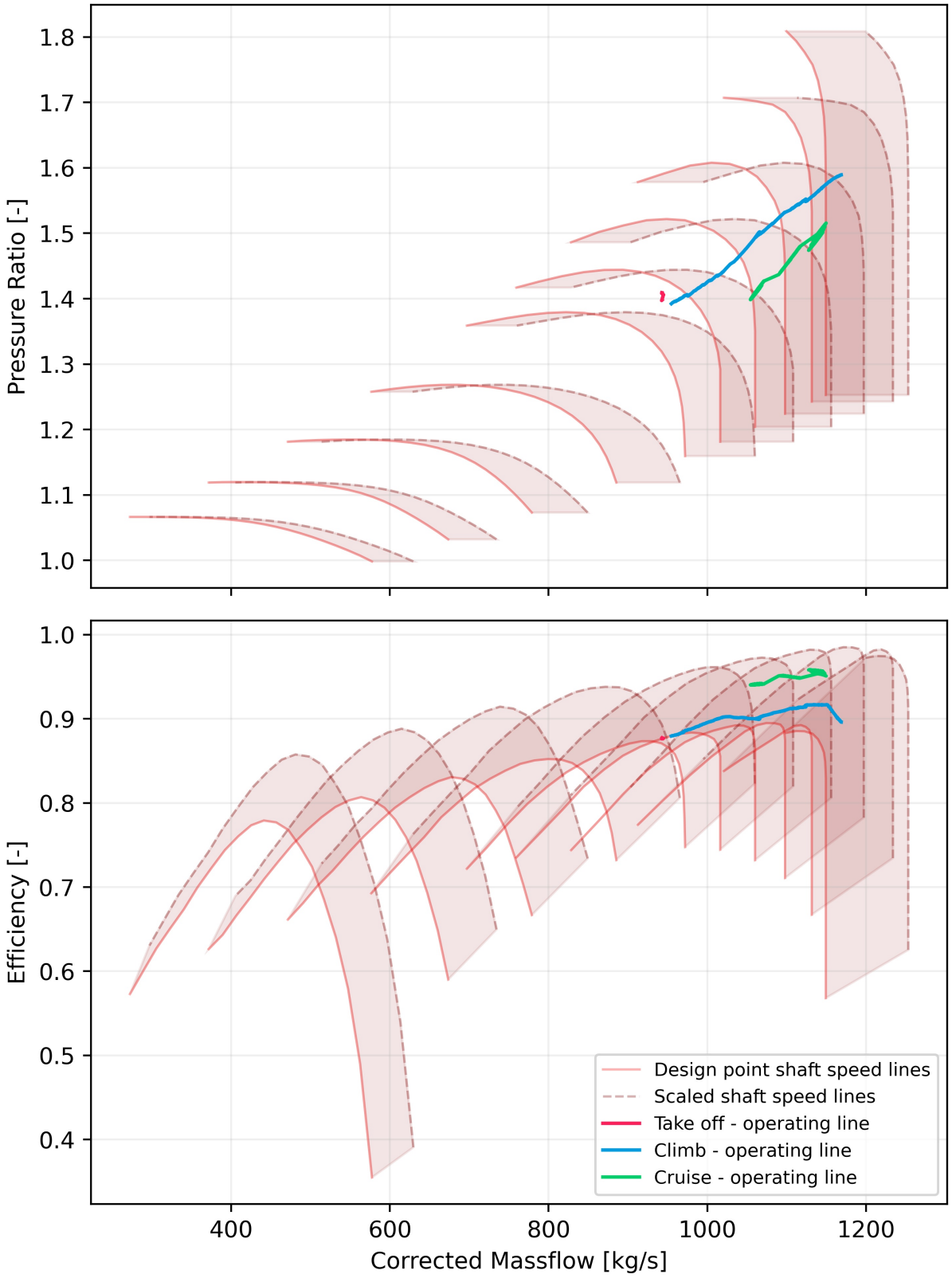

Figure 7.8: Fan bypass operating line plotted on the component map. Spool speed based on the map scaling are shown in shaded regions.

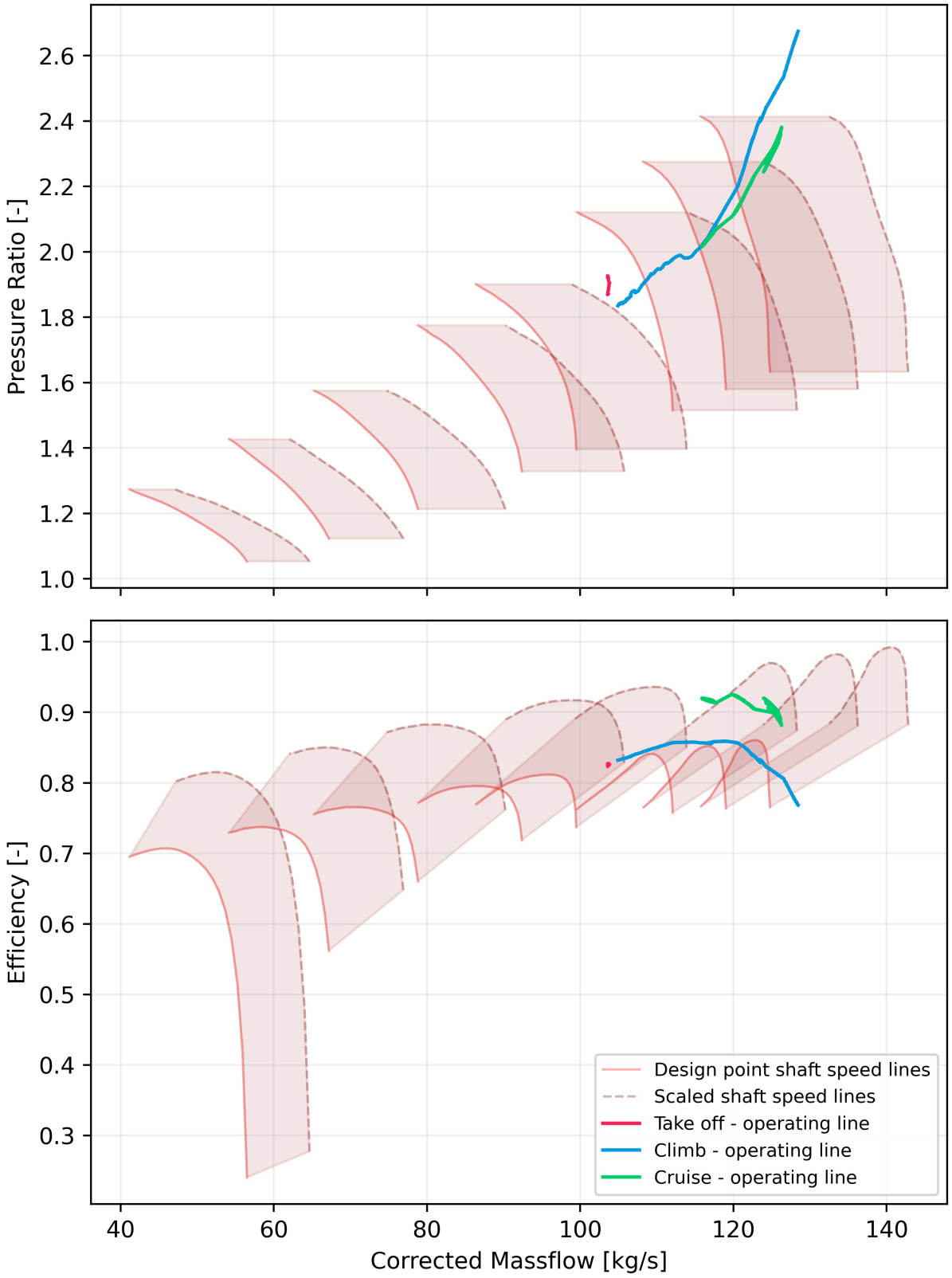

Figure 7.9: Fan core operating line plotted on the component map. Spool speed based on the map scaling are shown in shaded regions.

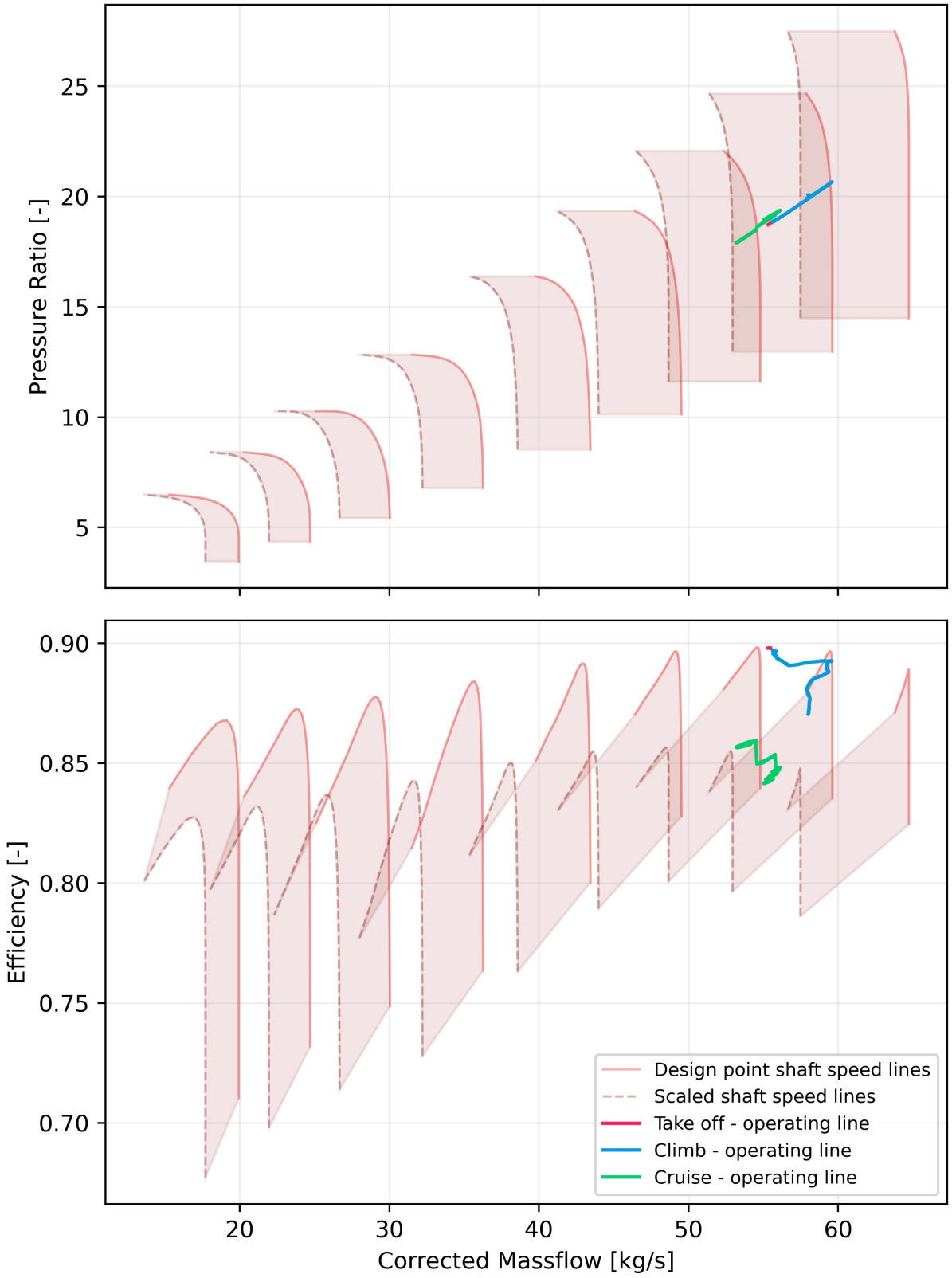

Figure 7.10: HPC operating line plotted on the component map. Spool speed based on the map scaling are shown in shaded regions.

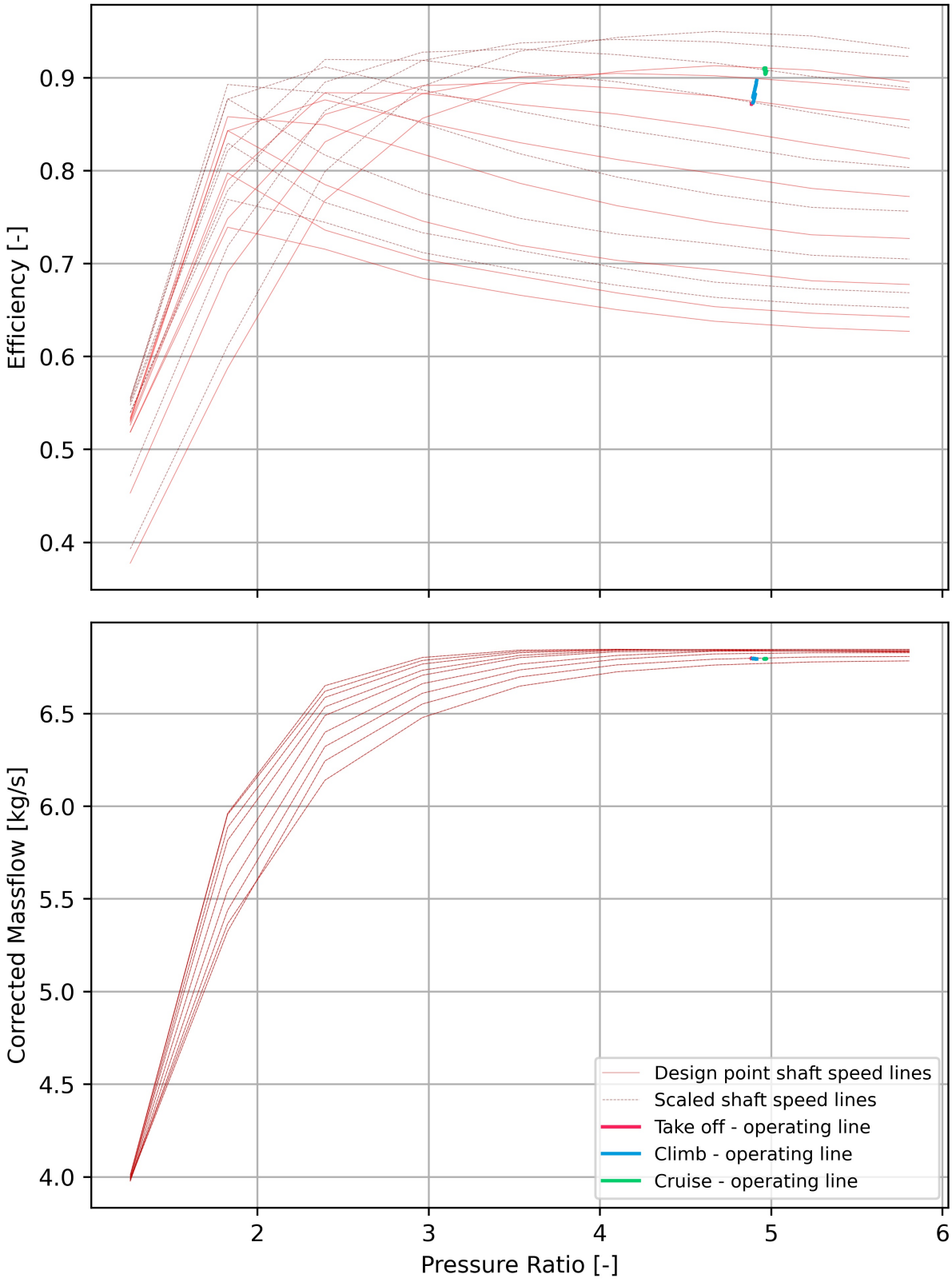

Figure 7.11: HPT operating line plotted on the component map. Spool speed based on the map scaling are shown for the smallest and largest scaled maps.

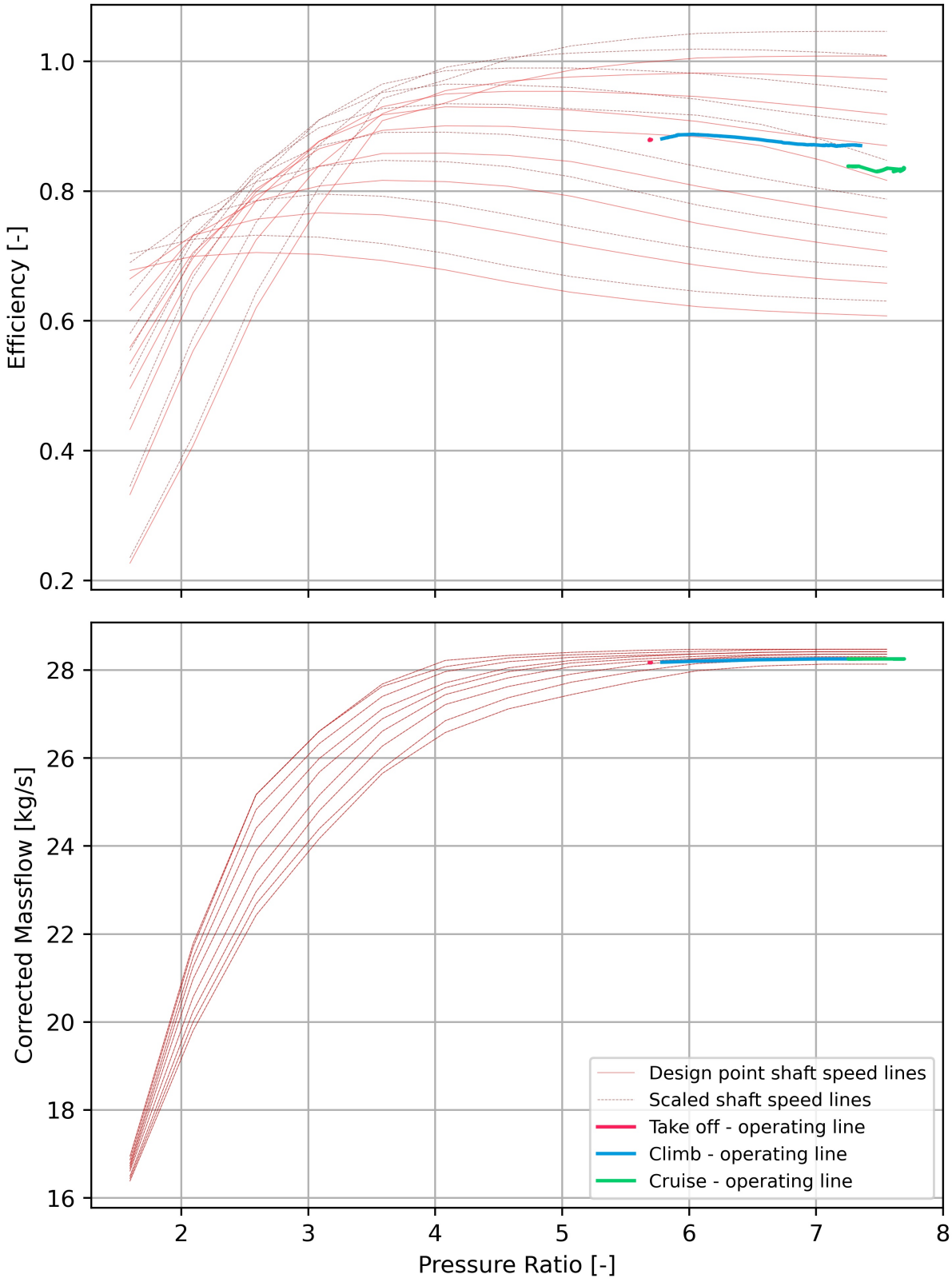

Figure 7.12: LPT operating line plotted on the component map. Spool speed based on the map scaling are shown for the smallest and largest scaled maps.

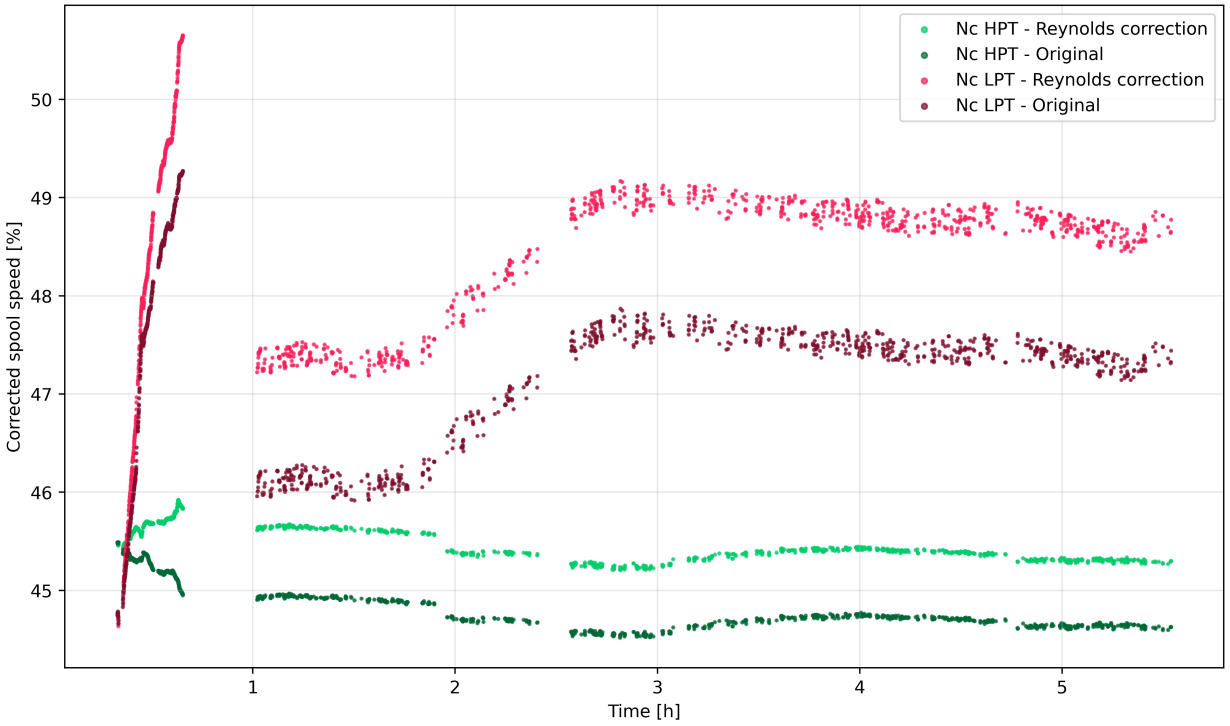

Figure 7.13: Re corrected vs uncorrected simulated HPT and LPT corrected spool speeds.

7.8. Correction comparison with on-wing sensor measurements

In general the behavior of the turbofan to changes due to the applied scaling factors correction can seem counter-intuitive. In this chapter, the underlying effects behind the behavior of the gas path parameters due to the applied corrections were emphasized. Most of the arguments were based on isolating each outcome (deviations due to correction) and breaking down in a systematic way the source/sources of the change. The model outcome deviations due to the applied corrections can all be traced back to the simulation input. This follows logically as what can cause deviations between two simulations based on the same exact turbofan model are the different inputs[3]. The different inputs in this case are the scaling factors that are trained to fit the target parameters. Therefore, the target parameters are the main causes of any deviation in the model (assuming the numerical error difference to be negligible). The difference between the simulated parameters prior to applying the Reynolds correction and the on-wing sensor measured parameters is shown in Figure 7.14. The same plots after applying the correction are shown in Figure 7.15. It can be seen that the simulation fits the target parameters with a higher accuracy due to the applied correction. The highest accuracy of the fit can be seen at the latest hours, which corresponds to the highest cruise altitude. This is due to the focus of the solver in gaining the largest accuracy increase which is achievable by focusing on the highest altitude. The list below provides descriptions of all simulation target parameters and explains how each one affects the gas path parameters in order to fit the model to the sensor-measured values.

[3]In this argument, the new model is still assumed to be the original model with the addition of the scaling factors as model inputs. The new model with correction applied is primarily based on a methodology

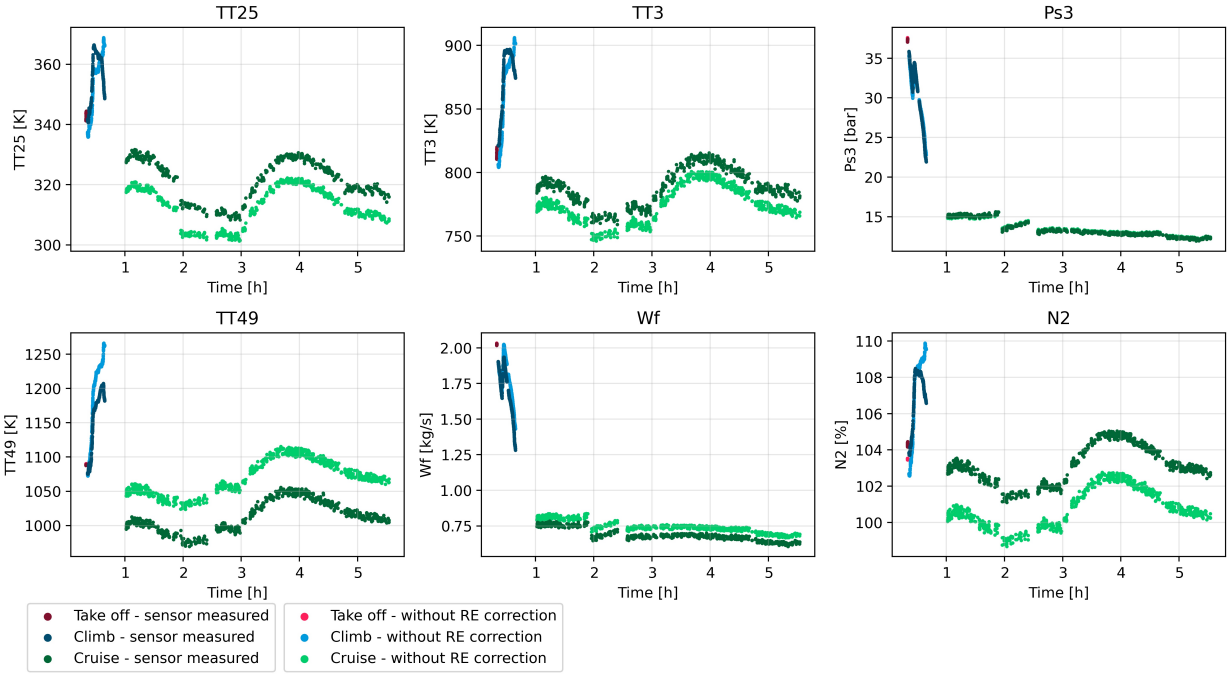

Figure 7.14: Uncorrected simulated vs measured sensor parameters throughout the flight duration

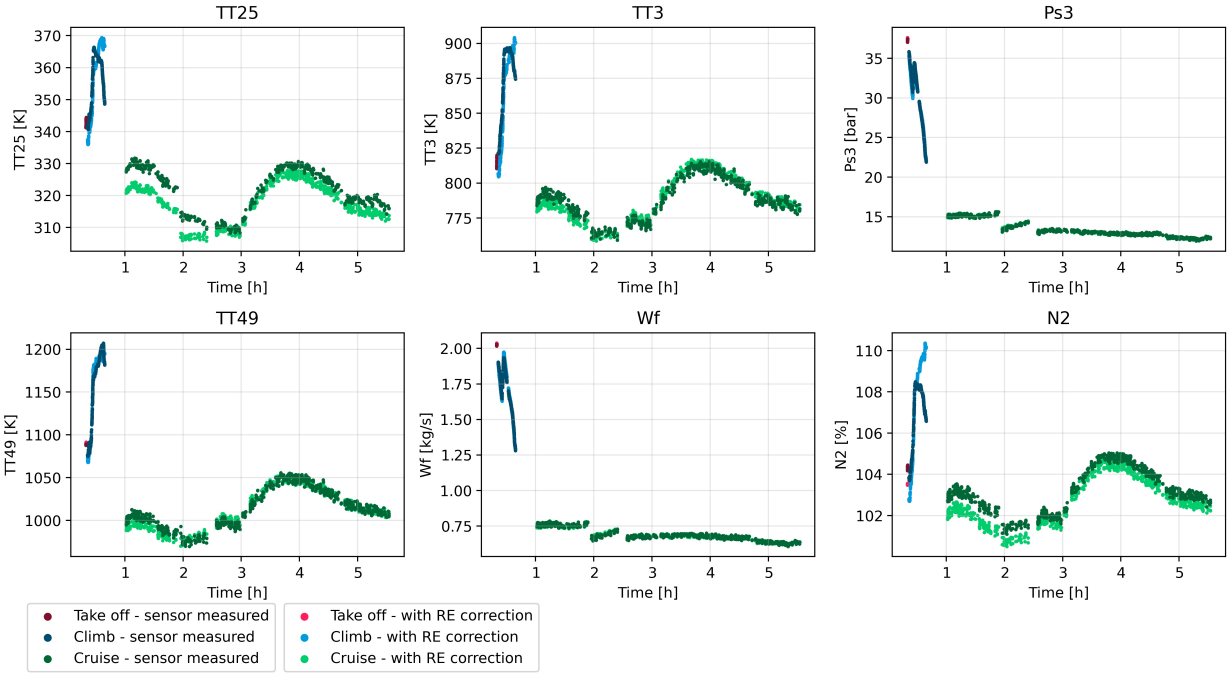

Figure 7.15: Corrected simulated vs measured sensor parameters throughout the flight duration

- **TT25** - The total temperature aft of the fan core is originally underestimated. The primary means of increasing the value is by increasing the fan core pressure ratio. This increases the energy supplied to the flow by the compressor and increases both the total pressure and temperature. Additionally, the fan core efficiency is increased which enhances the energy transfer from the compressor (less lost work). The effect is inverse to the required temperature increase; however, the pressure ratio increase is still dominant.
- **TT3** - The total temperature aft of the HPC is originally under estimated. Unlike the TT25, where the value was primarily changed by the fan core pressure ratio, the HPC pressure ratio is reduced

to maintain almost the same OPR. The means of change is due to the sharp decrease in HPC efficiency. Decreasing the efficiency diminishes the energy transfer, and induces dissipation, which results in a temperature increase.

- **Ps3** - The static pressure aft of the HPC is originally the most well-predicted. The predictions are partly under-estimated and partly over-estimated. Therefore, the optimizer approach for correction is least influenced by PS3. Moreover, the total pressure at station 3 does not deviate. This means the static pressure deviation is completely influenced by the dynamic term. The total temperature at station 3 is increased primarily in the cruise. This increase results in an increase in kinetic energy, the dynamic term, and therefore results in a decrease in static pressure.
- **Wf** - The fuel flow is originally over-estimated. This means that the fuel consumption needs to decrease or the performance of the turbofan needs to increase. The performance gain is obtained from the increase of the fan bypass, fan core, HPT, and LPT efficiencies. Essentially, that means for the same amount of compression, or energy extraction less fuel is needed.
- **TT49** - The total temperature aft of the HPT is originally over-estimated. The parameter is mainly affected by the decrease in fuel flow and the improved turbine efficiencies. The lower fuel flow results in a leaner combustion and consequently lower aft combustor temperatures. The high turbine efficiencies result in a higher energy extraction from the hot fluid decreasing its temperature.
- **N2** - The core spool speed is originally under-estimated. It follows from the decrease in fuel flow and combustor aft temperatures, that the total energy available for the turbine to extract is lower. Consequently, that results in a lower shaft speed. The effect is opposite to what is required. Therefore, the turbine efficiency values are increased to overcome the negative effect.

8. Model validation

Validating the enhanced model is a crucial step to guarantee correct usage in engine performance predictions. The model so far is corrected using a fitting approach. The method runs the risk of overfitting the training dataset (the chosen flight). Also, bias in the dataset is possible due to the data sampling methodology. Moreover, sensor data measurement errors in the training dataset could lead to a non-physical trained model. Therefore, the accuracy of the enhanced model needs to be tested in further predicting operational flights.

8.1. Single selected flight based modelling

The model performance on the fitted flight showcases improved accuracy. The flight used for training the dataset was chosen to include a vast spread of Reynolds numbers to capture the physical principles of the Reynolds effect over a wide range. The motivation for this choice was to ensure the feasibility of the model in predicting performance well within the majority of all flight points in take-off, climb, and cruise.

Model validation is conducted by testing the performance of the engine in predicting other flights based on the exact same physical engine. This way the engine-to-engine effects are dropped. Low model performance accuracy would then indicate drawbacks within the methodology itself. The validation was based on a dataset containing 25 flights within the same month of the training flight. The close proximity of recording the data limits the effects of deterioration. Therefore, the validation presented in this section assumes that no performance deterioration is present compared to the reference training flight. Moreover, the data underwent the same filtering procedure presented for the training flight.

The validation flights' average target parameters errors for the uncorrected and corrected models are presented in Figure 8.1 and Figure 8.2, respectively. In general, most of the improvement is gained at cruise due to the increased effect of the scaling factors. The take-off calibration proved to improve accuracy in some parameters, but not in others. However, an overall improvement is still present. The following is a list of remarks on each target parameter.

- **TT25** - The parameter accuracy generally increases. Additionally, the effect of the take-off calibration is present and does in fact reduce the error.
- **TT3** - The parameter accuracy is mainly improved in the cruise phase. The accuracy for climb and take-off on the other hand is negligibly affected.
- **PS3** - The accuracy at take-off is decreased; in fact, this is the only case where take-off calibration decreases the accuracy. The accuracy at climb and cruise are both increased.
- **TT49** - The accuracy in general is increased in all phases. The accuracy at take-off is particularly increased the most due to the take-off calibration. Yet, at take-off, the accuracy is still the lowest.
- **Wf** - In general, the accuracy increases in all the flight phases. Similar, to the TT49 parameter, the accuracy at take-off is the lowest.
- **N2** - The accuracy in take-off and climb are increased. However, the accuracy at climb is decreased

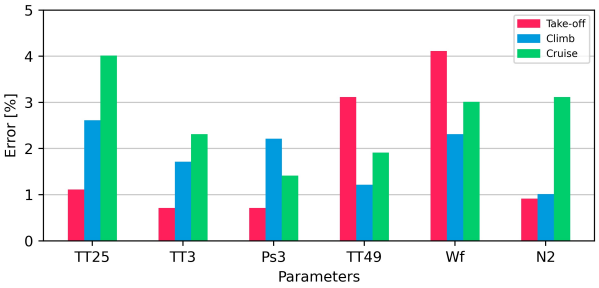

Figure 8.1: Validation flights average error per target parameter. (Uncorrected model).

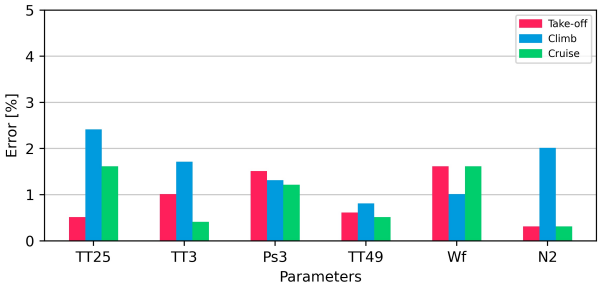

Figure 8.2: Validation flights average error per target parameter. (Corrected model based on a single selected flight).

In order to further analyze the applied correction on the validation dataset, the box-plot error distribution for the target parameters using the uncorrected and corrected models is presented.

Model take-off accuracy validation

The take-off accuracy is ultimately a measure of how well the take-off calibration step can be generalized. Looking at both the uncorrected and corrected model results in Figure 8.3 and Figure 8.4, respectively, the median error of the parameters is generally lower for the corrected model set except for the TT3 parameter. It can be seen that the chosen fitting flight data for the parameters TT3, Ps3, Wf, and N2 are either outside the interquartile range or are outliers. This is reflected in the higher error spread in the corrected results.

The effect of the calibration is a purely numerical one. The procedure was based on directly altering the scaling factors based on no physical correlations. Therefore, the model's high accuracy at the training flight and not the rest of the dataset is due to selection bias. Refinement by painstakingly selecting the training flight can further decrease the bias towards certain parameters. Nonetheless, the general prediction accuracy increases.

Looking at the fitting flight error between the corrected and the uncorrected model relative to the other flight error indicates the non-linearity of the engine. For example, looking at the TT49 data for the uncorrected model, it can be seen that the fitting point is very close to the median. However, the results of the corrected model indicate that the selected flight correction is outside the interquartile range.

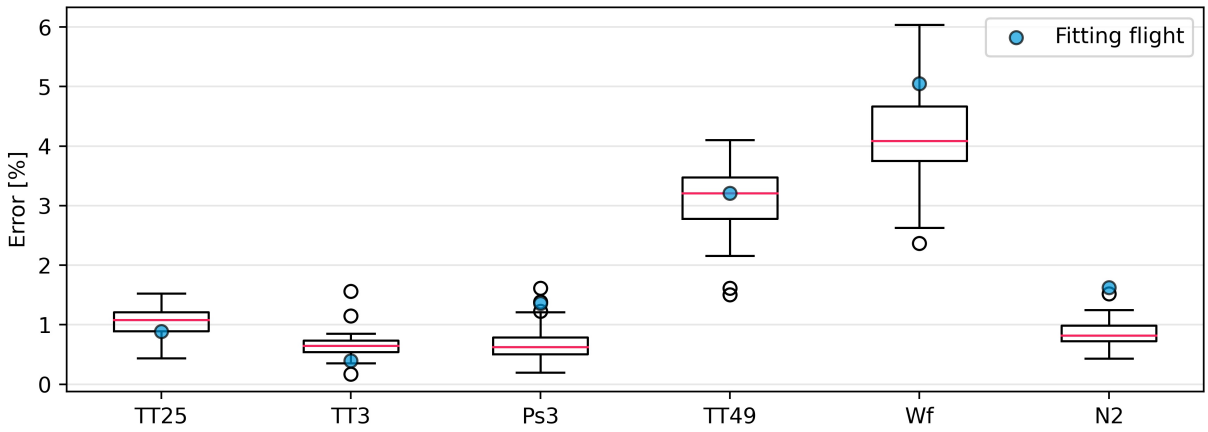

Figure 8.3: Boxplot for the take-off phase mean target parameters errors. (Uncorrected model).

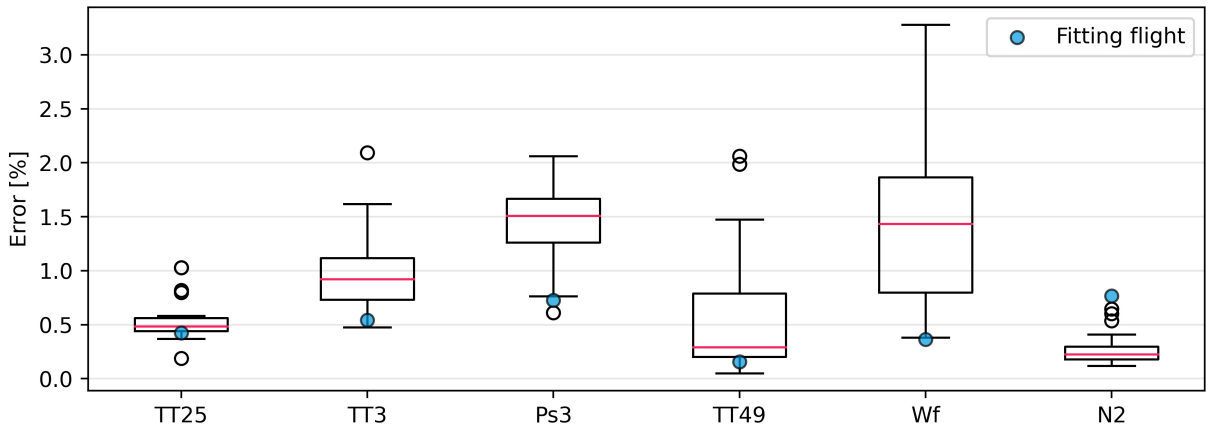

Figure 8.4: Boxplot for the take-off phase mean target parameters errors. (Corrected model based on a single selected flight)

Model climb accuracy validation

Looking at both the uncorrected and corrected model results in Figure 8.5 and Figure 8.6, respectively, the median error is lower for all the parameters in the corrected model figure except for the N2 parameters. This is true even though, a clear selection bias can be seen for TT25, TT3, PS3, and N2 parameters in the uncorrected model error. The result then indicates capturing a physical effect.

The scaling factors analyses showed that the solver's direction of correction was mainly focused on the cruise phase. Therefore, the climb corrections are not as large as the cruise. This is visible in the results presented as well, where the difference in results between the corrected and the uncorrected model medians is never more than 1%.

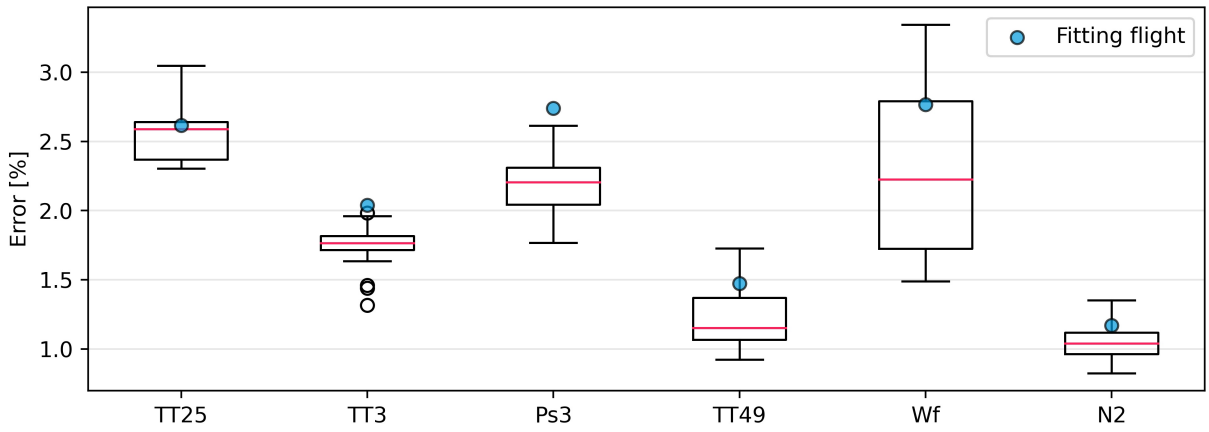

Figure 8.5: Boxplot for the climb phase mean target parameters errors. (Uncorrected model).

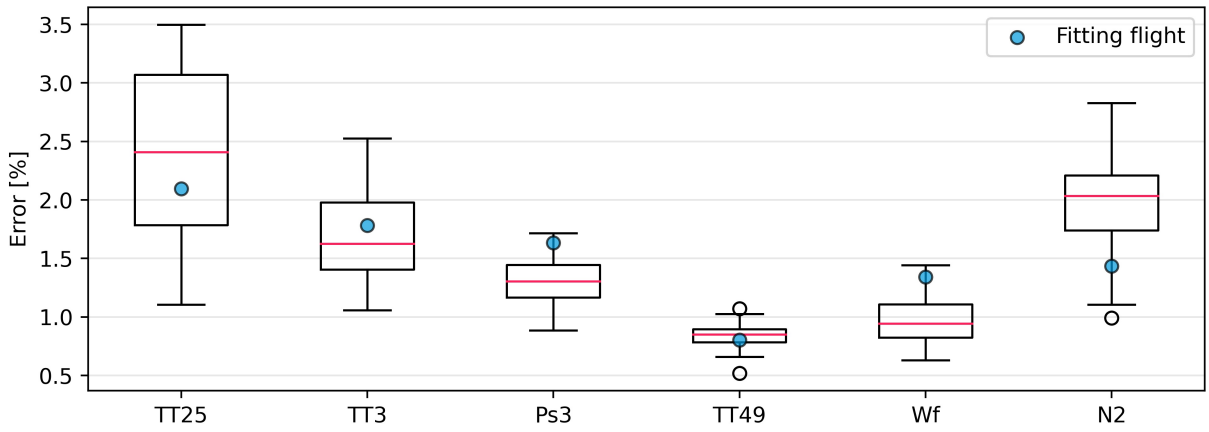

Figure 8.6: Boxplot for the climb phase mean target parameters errors. (Corrected model based on a single selected flight).

Model cruise accuracy validation

Looking at both the uncorrected and corrected model results in Figure 8.7 and Figure 8.8, respectively, the median error is lower for all the parameters in the corrected model figure. It can be observed that the medians for the corrected model figures are lower than 1% for TT3, PS3, TT49, and N2 parameters. In contrast, the climb corrected values are never below that figure. This clearly indicates the solver's prejudice to correct for the cruise error.

Moreover, it can be seen that the chosen flight points within the uncorrected figure are often outside the interquartile range, an indication of selection bias. Consequently, the corrected data spread is very large. This is also partially due to the non-linearity of the engine performance. Therefore, an argument could be made on whether the quadratic polynomial is sufficient to capture the error or not.

It should also be mentioned a bias in the validation flights dataset prior to applying any correction is affecting the results. For example, looking at the fuel flow in the uncorrected model figure, it can be seen that there exists an outlier. The result is a larger spread of the standard deviation in the corrected figure. The validation data assumes apriori that all flights are representable by the newly enhanced model. This is because the dataset is measured using the same engine sensors and data acquisition systems. Therefore, the assumption is that there exists no measurement bias across the flights.

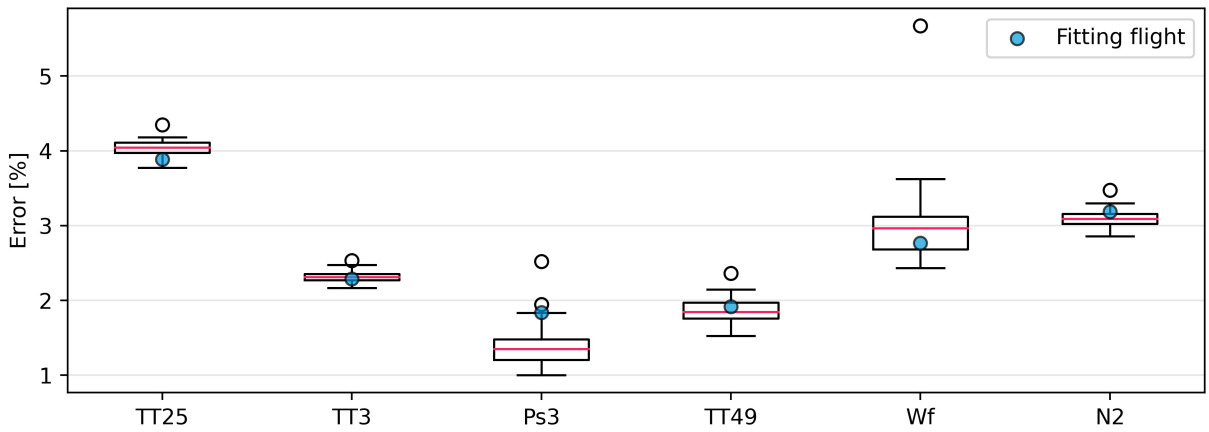

Figure 8.7: Boxplot for the cruise phase mean target parameters errors. (Uncorrected model).

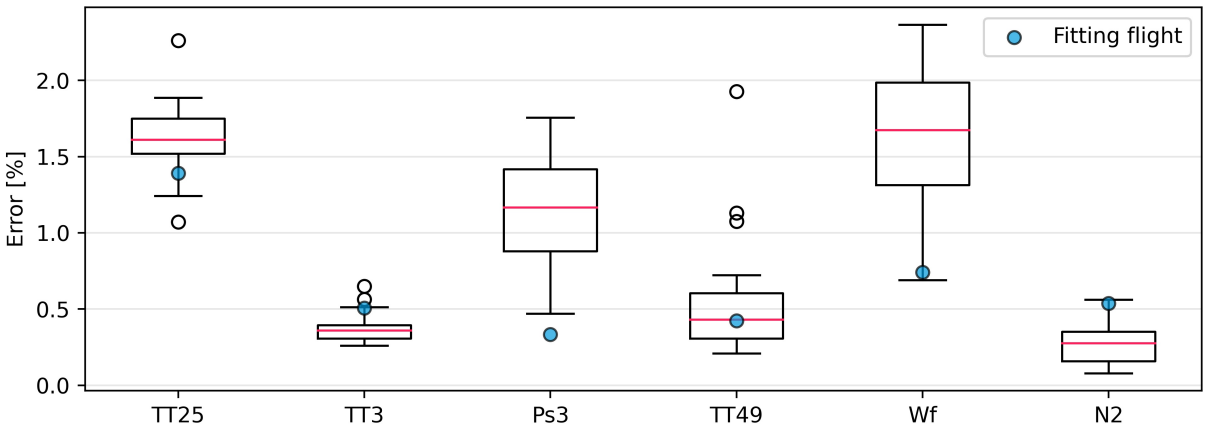

Figure 8.8: Boxplot for the cruise phase mean target parameters errors. (Corrected model based on a single selected flight).

8.2. Clustering based modelling

The model performance using the clustered dataset to fit the model in order to improve accuracy does not translate well to the validation set. The motivation behind using the clustering approach is to create a dataset that represents the larger pool of flights. Based on the 26 flights within a month, a 50-50 fitting and validation split was used. The split was used to test the hypothesis that 50 percent of the flights can be used to model the other 50 percent by utilizing the clustering-based approach.

The validation flights' average target parameters error for the clustering-based corrected model is shown in Figure 8.9. It can be seen from the results that on average the method simulates the target parameters with a larger error than that of the single selected flight modelling approach, shown in Figure 8.2, with the exception of the TT3 and PS3 parameters in take-off.

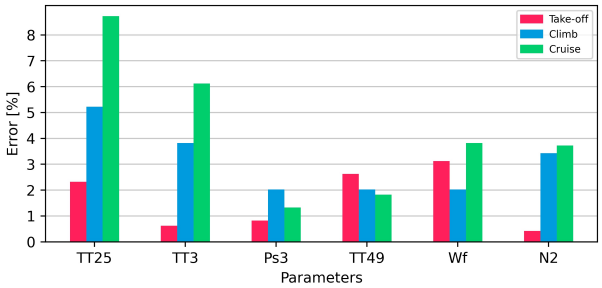

Figure 8.9: Validation flights average error per target parameter. (Corrected model based clustering).

The decrease in the accuracy level is due to the error associated with the clustering approach. Creating a dataset based on Kmeans++ clustering results in data points that are not real. The combination of the input parameters for a single point is not a physical point. The lack of this physical aspect in the modelling problem is what led to the poor accuracy in the validation set. Although the optimizer was able to obtain a set of OD scaling factors that minimizes the error for the clustered dataset, the solution performs badly in simulating the other flights. This argument also holds for the reason behind the slight improvement in TT3 and PS3 parameters in take-off. The take-off correction is based on a calibration step that is not physically correlated with any parameter. As K-means++ clustering is a mainly numerical method that doesn't consider the physical aspect of the engine cycle, the accuracy in simulating the take-off phase is not as low for the climb and cruise.

Due to the low accuracy of the clustering approach, further discussion is halted. The simulation error for the take-off, climb, and cruise phases are presented in Appendix E via boxplots for the fitting and validation flight sets.

8.3. Validation remarks

The validation analyses are presented to indicate how well the model correction methodology can hold for different flights outside the fitting one. In the case of the clustering-based modelling approach, it was seen that the model accuracy is not up to par. Therefore, the arguments made here are all referring to the single selected flight modelling approach.

The way the selected flight was chosen was based on data smoothness (low noise) and the Reynolds numbers range. The motivation was based on purely capturing a physical effect that can be applicable to any other model. This indicates a big assumption that no selection bias was introduced. However, the validation results show that the opposite is true. In many cases, the corrected selected flight was further away from the median. Even though a physical effect was captured, selection bias was present. The result is a model that is over-fitted to the selected training flight.

Moreover, the results reassure the prejudice of the solver towards mainly correcting for the cruise error. The cruise error was largely the one mostly improved across the validation set. Additionally, the fitted flight is outside the interquartile range for most of the parameters at the cruise. In an improved iteration of the model, the selected flight can be chosen to be close to the median. However, it can be challenging to simultaneously achieve that across all flight phases. Therefore, it becomes a model designer's choice on which flight phase is required to have the least spread. Based on such a concept, multiple models for each phase are then possible.

The outcomes of the validation step can be summarised in the following points:

- The root mean square error of all the parameters decreases in all flights due to the applied correction. This indicates an overall enhanced model that has an improved accuracy in predicting the selected engine in operation.
- Some of the parameters' mean errors are increased due to the applied correction at certain flight phases. The main reason for the increase is due to the selection bias and overfitting the model to the selected fitting flight. Most of the parameters on the other hand showcase accuracy improvements across the validation flights set.
- Model take-off validation results show the strongest effect of selection bias. This is because the take-off calibration procedure is a numerical factor and not based on physical correlations. Further improvements of this method are thus needed.
- Climb correction is the smallest across the entire validation set due to the lower effects of the scaling factors. This was already the case in the selected flight correction analyses in the previous chapters. The validation results are thus consistent.
- Selection bias is present in the dataset; however, the validation results indicate that an accuracy improvement is still achieved. This is an indication of capturing the physical effect of Reynolds corrections.
- Cruise correction is the most pronounced in the validation set due to the larger effects of the scaling factors. It was seen that the optimizer opted for solutions that targeted improving the cruise data points, the validation datasets therefore depict a high accuracy in cruise, which is the main driving factor of decreasing the root mean square error.

9. Conclusions

This thesis study is part of an aerospace engineering Masters degree at the Delft University of Technology in collaboration with KLM ES. The project aims to create an enhanced gas path model for condition monitoring at KLM ES. The model that is built in GSP is intended to be used in a gas path analyses tool (GPA) to conduct maintenance at KLM ES efficiently. The project is a continuation of several projects conducted at KLM ES.

The motivation behind enhancing gas path modelling is to achieve a model that has high accuracy in predicting measured sensor data. The modelling problem is a challenge due to the few numbers of sensors installed along the gas path of the engines. Moreover, the manufacturer keeps a lot of the data as proprietary. Therefore, a lot of the work done in this research is based on reverse engineering techniques. In this project, the GEnx-1b is the focus of the study. The GEnx-1b turbofan model was originally built in a previous project that matched the model to test cell conditions. This project aimed to extend the applicability of the model to predicting Continuous Engine Operating Data (CEOD). The key areas of improvement conducted in this project involved investigating altitude effects and nozzle losses present in the GEnx-1b model. Upon investigation, it was concluded that the Reynolds number in the gas path correlated with the error. The correction procedure was then based on first selecting a single CEOD flight data. This flight data would then serve as the basis of the analysis to capture the aforementioned effects. As the correlation was based on Reynolds number, the chosen flight was selected such that the variation of Reynolds numbers in the entire flight envelope is large enough to capture the effects in the most encompassing manner. The effects were then captured by employing quadratic scaling factors that alter the component's map and nozzle coefficients in off-design. The polynomial's coefficients served as the design variables where a minimization problem in an optimization framework was defined in order to meet the objective function, that is based on the measured sensor data. The final model showed a large accuracy gain across take-off, climb, and cruise. Moreover, the validation data generally indicated an overall improved model. The main conclusions drawn from the modelling approach and results are presented:

- **Take-off calibration**: The accuracy of the model prior to any corrections is very low at take-off. This is because the model was originally matched to test-cell data and not CEOD. Therefore, a calibration step is needed to correct for potential on-wing effects or engine-to-engine differences. The methodology was based on a stand-alone optimization problem using off-design scaling factors. The results showed a great match at take-off but a consequent accuracy decrease in climb and cruise.
- **Turbomachinery correction**: In order to capture the altitude effects in off-design, off-design scaling factors were employed. The scaling factors were defined as quadratic polynomials as a function of the inlet Reynolds number of each turbomachinery component. Then, the scaling factor polynomial coefficients were obtained through a minimization problem that aims to decrease the prediction vs measurement errors of the model. The scaling factors alter the component maps directly to shift the operating point of the component. In total, there were 8 scaling factors, with 16 design variables to minimize. The result results showed great improvements in accuracy especially at cruise, where the optimizer was able to reduce the error the most due to the high values of Reynolds numbers.
- **Nozzle losses correction**: Nozzle corrections were based on altering the performance thrust and velocity coefficients in off-design. The coefficients were based on quadratic polynomials and added on top of the turbomachinery scaling factors in the same optimization problem. The results indicated that the nozzle corrections were not useful. First, the thrust coefficient only modified the output thrust of the model and did not affect the operating point of the engine. Secondly, the bounds of the system only allowed for performance loss, meanwhile, in order to improve the accuracy of the model the performance had to increase.

- **System performance simulation**: A full system simulation of the model with and without the correction methodology applied was analyzed as verification of the underlying effects that resulted in matching the model in off-design. The changes in the gas path simulation due to the correction were discussed and all the alterations of the model were traced back to physical phenomena. The ultimate cause of the changes was due to the employed scaling factors. These scaling factors are a function of the measured parameters, that are now ultimately part of the system input that act as boundaries. The result is a deviation in the operating points of the turbofan model such that the sensor-measured parameters are predicted with high accuracy.
- **Model validation**: Model validation was conducted for the modelling approach using two types of datasets: single selected flight and clustering multiple flights. The validation results showed that the former is superior to the latter. For the single selected flight based modelling approach, validation was conducted using 25 flights within a month range of the fitting flight. The overall results indicate on average an increased model accuracy. In some cases the accuracy of some of the sensor-measured parameters was decreased; yet, the overall effect of each individual flight was an increase in accuracy (lower root mean square error). Moreover, the results indicate strong selection bias in the take-off dataset. In cruise and climb, selection bias is also present but the results indicate a consistent improvement in the accuracy. The interpretation of this is a valid capturing of the physical effects due to altitude changes.

The research undertaken indicates the feasibility of enhancing the modeling approach. This model improvement was informed by its correlation with a low Reynolds number phenomenon at high altitudes. It operates under the assumption that error reduction can be achieved through the correct application of methodological techniques. This project has yielded an improved model and a proof of concept, introducing a novel methodology for enhancing on-wing predictions. The procedures outlined are versatile and can be applied to various turbofan systems. Additionally, this procedure addresses the challenge of low sensor measurements and offers strategies to handle the under-determined systems of equations, that are the essence of the modelling challenge in this research field.

10. Recommendations

The results achieved in this research are promising. Further efforts and improvements can lead to new insights and valuable outcomes. Some of the recommendations to further build up on the enhanced modelling approach are provided in this chapter.

- In this study it was assumed that all the error is attributed to the Reynolds effect. In reality, this is never the case. It was convenient to make such a correlation as the model accuracy decreased with increasing altitude. It is certain that other factors might be contributing to the error, such as the component's corrected spool speeds. It is thus recommended that more investigation is pursued into the causes behind the model accuracy deviation.
- The model this study started with is not very accurate. This is due to the underperformance of the turbofan model at higher altitudes with no implementation of Reynolds effect losses within the model. A correct physical model should depict an opposite behavior. It is speculated that the cause of this issue is neglecting the Reynolds effect in the original model. It is therefore recommended, that the systematic approach created by Ramdin [40], is revised with the knowledge obtained in this study.
- The model take-off calibration step was created to match CEOD at take-off conditions. The process is a purely numerical one. It is recommended that further investigations be conducted to improve the method. The validation step especially showed a large selection bias at take-off which indicated the overfitting of the model at flight data. Alternatively, the take-off calibration process could then be done using a larger sample of data to reduce the bias towards a single flight.
- In the scaling factors functions, not all OD scaling factors were used (e.g. OD pressure ratio scaling factor). The motivation for this in turbines is that the pressure ratio hardly changes due to losses. In compressors, this is not the case. However, the pressure ratio was not included in the design variable to constrain the solver's freedom and improve the computational time to find a viable solution. It could still be useful to attempt to use the pressure ratio scaling factors in off-design to improve the model's overall accuracy. Using all scaling factors offers the possibility to enlarge the optimizer search space and potentially improve the model accuracy.
- It was seen in the scaling factor analyses that the optimizer opted for a solution that focused mainly on improving cruise accuracy. Consequently, the climb accuracy was not as improved. An attempt to tackle the issue was conducted using the quadratic splines approach. It was shown then that a more accurate model is possible but the improvements are not worth the increased complexity. However, there is still room for improving the overall results by enhancing the climb predictions.
- The analyses done for the validation indicate selection bias in some of the measured parameters. This is because the chosen flight for fitting was based purely on physical reasons. The modelling challenge, even though it relies on physical models, is still largely a numerical one. In the end, the few numbers of measurements along the turbofan call for such numerical approaches that employ AI methods, which provide freedom to a solver in order to find the best fit. The resultant model is then not fully physical and a lot of model deviations are treated by physical relations but rather by numerical ones. Therefore, the chosen dataset for fitting should be selected carefully. The extent to which the model can be used shall be then determined by the validation results.
- A main outcome of the validation results showed that the data used for the modelling problem is of utmost importance. The usage of the clustering approach indicated that the lack of the physical aspect in modelling resulted in a less accurate model. On the other hand, the use of a selected flight to capture the physical effect for correction proved to be superior. However, there still exists selection bias. It is therefore recommended a new data selection method is obtained that can strike a balance of treating the problem both from a data science and a physical engine cycle perspective.

- The research conducted neglected secondary performance effects. Including this in the modeling approach could further enhance the model as they are inputs that can be related to physical phenomena. For instance, the compressor variable stator vanes (VSV) are known to shift the operating point of the engine. These parameters are recorded in the CEOD and utilizing them might further improve the model's accuracy.
- The model fitting and validation conducted assumed no measurement errors are present in any of the sensor parameters. This simplifies the modelling problem but is not fully true. Sensor errors carry on in the model due to the fitting approach. Therefore, it is recommended that more scrutiny is applied in the usage of the measured sensor parameters.

References

[1] John J. Adamczyk et al. “Simulation of Three-Dimensional Viscous Flow Within a Multistage Turbine”. en. In: American Society of Mechanical Engineers Digital Collection, Mar. 2015. DOI: 10.1115/89-GT-152. URL: https://asmedigitalcollection.asme.org/GT/proceedings-abstract/GT1989/79139/239793 (visited on 05/09/2023).

[2] ANDERSON. *Fundamentals of aerodynamics*. Columbus, OH: McGraw-Hill Education, 2016. ISBN: 978-1-259-25134-4.

[3] David Arthur and Sergei Vassilvitskii. “k-means++: the advantages of careful seeding”. In: *Proceedings of the eighteenth annual ACM-SIAM symposium on Discrete algorithms*. SODA ’07. USA: Society for Industrial and Applied Mathematics, Jan. 2007, pp. 1027–1035. ISBN: 978-0-89871-624-5. (Visited on 05/02/2023).

[4] O. E. Baljeť. “A Study on Reynolds Number Effects in Turbomachines”. In: *Journal of Engineering for Power* 86.3 (July 1964), pp. 227–235. ISSN: 0022-0825. DOI: 10.1115/1.3677584. URL: https://doi.org/10.1115/1.3677584 (visited on 04/05/2023).

[5] A. D. S. Carter et al. “The effect of reynolds number on the performance of a single-stage compressor”. en. In: (1957). Accepted: 2014-10-21T15:55:01Z. URL: https://reports.aerade.cranfield.ac.uk/handle/1826.2/3752 (visited on 09/09/2023).

[6] N.A. Cumpsty. *Compressor aerodynamics*. Compressor aerodynamics. Issue: v. 10 tex.lccn: 2003069481. Krieger Pub., 2004. ISBN: 978-1-57524-247-7. URL: https://books.google.nl/books?id=AmM6PgAACAAJ.

[7] J. D. Denton. “The 1993 IGTI Scholar Lecture: Loss Mechanisms in Turbomachines”. In: *Journal of Turbomachinery* 115.4 (Oct. 1993), pp. 621–656. ISSN: 0889-504X. DOI: 10.1115/1.2929299. URL: https://doi.org/10.1115/1.2929299 (visited on 08/10/2023).

[8] Prajwal Deval. “Cylinder Drag Reduction Using Discrete Surface Roughness: An Experimental Investigation Into the Effect of Cylindrical Roughness Elements”. MA thesis. Delft University of Technology, Aug. 2023.

[9] Ihor S. Diakunchak. “Performance Deterioration in Industrial Gas Turbines”. en. In: American Society of Mechanical Engineers Digital Collection, Mar. 2015. DOI: 10.1115/91-GT-228. URL: https://asmedigitalcollection.asme.org/GT/proceedings-abstract/GT1991/79016/242056 (visited on 05/11/2023).

[10] Sydney Lawrence (viaf)54713015 Dixon and C. A. Hall. *Fluid mechanics and thermodynamics of turbomachinery*. eng. 7. ed. Amsterdam : Butterworth-Heinemann/Elsevier, 2014. ISBN: 978-0-12-415954-9. URL: http://lib.ugent.be/catalog/rug01:002520574.

[11] Daniel E. Eigenbrode and Erik A. Lindstrom. “Exhaust nozzle cooling scheme for gas turbine engine”. US5577381A. Nov. 1996. URL: https://patents.google.com/patent/US5577381A/en (visited on 05/20/2023).

[12] Said El Bouazzaoui. *Modeling of a GSP Diagnostic Tool for the CFM56-7B engines*. Tech. rep. Delft, The Netherlands: Delft University of Technology, 2008.

[13] Paul Fletcher and Philip P. Walsh. *Gas Turbine Performance*. en. Google-Books-ID: DtFml9BQkEIC. John Wiley & Sons, Apr. 2008. ISBN: 978-1-4051-5103-0.

[14] Robert Flitney. *Chapter Three. Rotary Seals | Elsevier Enhanced Reader*. en. DOI: 10.1016/B978-0-08-099416-1.00003-6. URL: https://reader.elsevier.com/reader/sd/pii/B9780080994161000036?token=EB59B3F1865C76775D1A79E3C073316763F35FECF8EBD3BC4B1206B7FC2E5FCE0B2ED2C9C1FA1B2594BE8864B3F719C3&originRegion=eu-west-1&originCreation=20230511160137 (visited on 05/11/2023).

[15] K. Ghorbanian and M. Gholamrezaei. “An artificial neural network approach to compressor performance prediction”. en. In: *Applied Energy* 86.7 (July 2009), pp. 1210–1221. ISSN: 0306-2619. DOI: 10.1016/j.apenergy.2008.06.006. URL: https://www.sciencedirect.com/science/article/pii/S0306261908001463 (visited on 04/06/2023).

[16] Ralph E. Grey and H. Dean Wilsted. *Performance of conical jet nozzles in terms of flow and velocity coefficients*. NTRS Author Affiliations: NTRS Report/Patent Number: NACA-TR-933 NTRS Document ID: 19930091998 NTRS Research Center: Legacy CDMS (CDMS). Jan. 1949. URL: https://ntrs.nasa.gov/citations/19930091998 (visited on 05/26/2023).

[17] D. den Haan. *GSP Gas Path Analysis on CF6-80 Engines at KLM Engine Services*. Tech. rep. Delft, The Netherlands: Delft University of Technology, 2010.

[18] Abdellah Hadjadj and Marcello Onofri. “Nozzle flow separation”. en. In: *Shock Waves* 19.3 (July 2009), pp. 163–169. ISSN: 1432-2153. DOI: 10.1007/s00193-009-0209-7. URL: https://doi.org/10.1007/s00193-009-0209-7 (visited on 05/20/2023).

[19] Awatef Hamed, W. Tabakoff, and D. Singh. “Modeling of Compressor Performance Deterioration Due to Erosion”. In: *International Journal of Rotating Machinery* 4 (Jan. 1998). DOI: 10.1155/S1023621X98000207.

[20] Shuxin Huang. “Reading the Moody chart with a linear interpolation method”. en. In: *Scientific Reports* 12.1 (Apr. 2022). Number: 1 Publisher: Nature Publishing Group, p. 6587. ISSN: 2045-2322. DOI: 10.1038/s41598-022-10552-x. URL: https://www.nature.com/articles/s41598-022-10552-x (visited on 05/18/2023).

[21] R. Hussin, N. Ismail, and S. Mustapa. “A study of foreign object damage (FOD) and prevention method at the airport and aircraft maintenance area”. en. In: *IOP Conference Series: Materials Science and Engineering* 152.1 (Oct. 2016). Publisher: IOP Publishing, p. 012038. ISSN: 1757-899X. DOI: 10.1088/1757-899X/152/1/012038. URL: https://dx.doi.org/10.1088/1757-899X/152/1/012038 (visited on 05/11/2023).

[22] Jean-Pierre Immarigeon et al. “Erosion Testing of Coatings for Aero Engine Compressor Components”. en. In: *Advanced Performance Materials* 4.4 (Oct. 1997), pp. 371–388. ISSN: 1572-8765. DOI: 10.1023/A:1008644527599. URL: https://doi.org/10.1023/A:1008644527599 (visited on 05/11/2023).

[23] Sangjo Kim. “A new performance adaptation method for aero gas turbine engines based on large amounts of measured data”. en. In: *Energy* 221 (Apr. 2021), p. 119863. ISSN: 0360-5442. DOI: 10.1016/j.energy.2021.119863. URL: https://www.sciencedirect.com/science/article/pii/S0360544221001122 (visited on 04/14/2023).

[24] Changduk Kong and Jayoung Ki. “Components Map Generation of Gas Turbine Engine Using Genetic Algorithms and Engine Performance Deck Data”. In: *Journal of Engineering for Gas Turbines and Power-transactions of The Asme - J ENG GAS TURB POWER-T ASME* 129 (Apr. 2007). DOI: 10.1115/1.2436561.

[25] Rainer Kurz and Klaus Brun. “Fouling Mechanisms in Axial Compressors”. In: *Journal of Engineering for Gas Turbines and Power* 134.3 (Jan. 2012). ISSN: 0742-4795. DOI: 10.1115/1.4004403. URL: https://doi.org/10.1115/1.4004403 (visited on 05/11/2023).

[26] Joachim Kurzke and Ian Halliwell. *Propulsion and Power An Exploration of Gas Turbine Performance Modeling*. eng. 1st ed. 2018. 2018. ISBN: 978-3-319-75979-1. URL: http://lib.ugent.be/catalog/ebk01:4100000004243679.

[27] Y. G. Li. “Gas Turbine Performance and Health Status Estimation Using Adaptive Gas Path Analysis”. In: *Journal of Engineering for Gas Turbines and Power* 132.4 (Jan. 2010). ISSN: 0742-4795. DOI: 10.1115/1.3159378. URL: https://doi.org/10.1115/1.3159378 (visited on 05/12/2023).

[28] Y. G. Li et al. “Improved Multiple Point Non-Linear Genetic Algorithm Based Performance Adaptation Using Least Square Method”. en. In: American Society of Mechanical Engineers Digital Collection, May 2012, pp. 49–60. DOI: 10.1115/GT2011-45289. URL: https://asmedigitalco

llection.asme.org/GT/proceedings-abstract/GT2011/54648/49/352085 (visited on 05/01/2023).

[29] Y. G. Li et al. "Nonlinear Multiple Points Gas Turbine Off-Design Performance Adaptation Using a Genetic Algorithm". In: *Journal of Engineering for Gas Turbines and Power* 133.7 (Mar. 2011). ISSN: 0742-4795. DOI: 10.1115/1.4002620. URL: https://doi.org/10.1115/1.4002620 (visited on 04/05/2023).

[30] Seymour Lieblein, Francis C. Schwenk, and R. Broderick. "Diffusion factor for estimating losses and limiting blade loadings in axial-flow-compressor blade elements". In: 1953. URL: https://api.semanticscholar.org/CorpusID:117788867.

[31] *LM2500 Engine | GE Aerospace*. URL: https://www.geaerospace.com/propulsion/marine/lm2500 (visited on 05/05/2023).

[32] A.B. McKenzie. *Axial flow fans and compressors: Aerodynamic design and performance*. Cranfield series in turbomachinery. tex.lccn: 97001249. Ashgate, 1997. ISBN: 978-0-291-39850-5. URL: https://books.google.nl/books?id=JdlSAAAAMAAJ.

[33] D. J. Mee et al. "An Examination of the Contributions to Loss on a Transonic Turbine Blade in Cascade". In: *Journal of Turbomachinery* 114.1 (Jan. 1992), pp. 155–162. ISSN: 0889-504X. DOI: 10.1115/1.2927979. URL: https://doi.org/10.1115/1.2927979 (visited on 08/14/2023).

[34] Gianluigi Misté and Ernesto Benini. "Turbojet Engine Performance Tuning With a New Map Adaptation Concept". In: *Journal of Engineering for Gas Turbines and Power* 136 (July 2014), p. 071202. DOI: 10.1115/1.4026548.

[35] Martijn van Moorselaar. "Gas Path Analysis on the GEnx-1B at KLM Engine Services". en. In: (2018). URL: https://repository.tudelft.nl/islandora/object/uuid%3A51b66a01-a485-4aac-a6e6-544f619b9aa1 (visited on 05/15/2023).

[36] Muaz Naeem, Radhev Singh, and D. Probert. "Implications of engine's deterioration upon an aero-engine HP turbine blade's thermal fatigue life". In: *International Journal of Fatigue* 22 (Feb. 2000), pp. 147–160. DOI: 10.1016/S0142-1123(99)00105-X.

[37] J. A. Nelder and R. Mead. "A Simplex Method for Function Minimization". In: *The Computer Journal* 7.4 (Jan. 1965), pp. 308–313. ISSN: 0010-4620. DOI: 10.1093/comjnl/7.4.308. URL: https://doi.org/10.1093/comjnl/7.4.308 (visited on 05/03/2023).

[38] Michiel Otten. "Development of a diagnostics model for the GEnx-1B turbofan engine using on-wing performance data". en. In: (2021). URL: https://repository.tudelft.nl/islandora/object/uuid%3A3269e573-31b7-4bf4-91f4-9cfd08166c63 (visited on 05/15/2023).

[39] *Overall and Stage Characteristics of Axial-flow Compressors*. en. DOI: 10.1243/PIME_PROC_1950_163_026_02. URL: https://journals.sagepub.com/doi/epdf/10.1243/PIME_PROC_1950_163_026_02 (visited on 05/09/2023).

[40] Shiv Ramdin. "A systematic approach for modelling modern turbofan engines". en. In: (2022). URL: https://repository.tudelft.nl/islandora/object/uuid%3Aaa5efca4-8f4a-44d6-8d15-0eeedd45b915 (visited on 05/09/2023).

[41] Narahari Rath, R. K. Mishra, and Abhijit Kushari. "Aero engine health monitoring, diagnostics and prognostics for condition-based maintenance: an overview". en. In: *International Journal of Turbo & Jet-Engines* (May 2022). Publisher: De Gruyter. ISSN: 2191-0332. DOI: 10.1515/tjeng-2022-0020. URL: https://www.degruyter.com/document/doi/10.1515/tjeng-2022-0020/html?lang=de&casa_token=aPzq5qZG-PwAAAAA%3AFUjZihnkogwVGSYccJpK-DtFL3vgL0zXF_itf0F7QAr_i82M1BooKK9osBgiK0JY-i3hYGT8-yg (visited on 05/10/2023).

[42] Bastiaan Röell. "Test-cell & On-wing Turbofan Performance Comparison at KLM Engine Services". en. In: (2019). URL: https://repository.tudelft.nl/islandora/object/uuid%3A8b882e0a-aa26-4785-90ce-27b5fed7b542 (visited on 05/15/2023).

[43] Tim Rootliep. “Turbofan Condition Monitoring using Evolutionary Algorithm based Gas Path Analysis: at KLM Engine Services”. en. In: (2020). URL: https://repository.tudelft.nl/islandora/object/uuid%3A7ff9b284-0b7b-4f70-8ed5-4d81f1eb113f (visited on 05/15/2023).

[44] Meinhard T. Schobeiri. “Losses In Turbine and Compressor Cascades”. en. In: *Gas Turbine Design, Components and System Design Integration: Second Revised and Enhanced Edition*. Ed. by Meinhard T. Schobeiri. Cham: Springer International Publishing, 2019, pp. 159–212. ISBN: 978-3-030-23973-2. DOI: 10.1007/978-3-030-23973-2_6. URL: https://doi.org/10.1007/978-3-030-23973-2_6 (visited on 08/10/2023).

[45] Michael Sielemann et al. “Introduction to Multi-Point Design Strategies for Aero Engines”. en. In: American Society of Mechanical Engineers Digital Collection, Jan. 2021. DOI: 10.1115/GT2020-14912. URL: https://asmedigitalcollection.asme.org/GT/proceedings-abstract/GT2020/84157/1094811 (visited on 04/05/2023).

[46] G. Sieros, A. Stamatis, and K. Mathioudakis. “Jet Engine Component Maps for Performance Modeling and Diagnosis”. In: *Journal of Propulsion and Power* 13.5 (Sept. 1997). Publisher: American Institute of Aeronautics and Astronautics, pp. 665–674. ISSN: 0748-4658. DOI: 10.2514/2.5218. URL: https://arc.aiaa.org/doi/10.2514/2.5218 (visited on 05/03/2023).

[47] A. G. Stamatis. “Evaluation of gas path analysis methods for gas turbine diagnosis”. In: *Journal of Mechanical Science and Technology* 25.2 (Feb. 2011), pp. 469–477. ISSN: 1976-3824. DOI: 10.1007/s12206-010-1207-5. URL: https://doi.org/10.1007/s12206-010-1207-5.

[48] Hai-Long Tang et al. “High altitude low Reynolds number effect on the matching performance of a turbofan engine”. In: *Proceedings of the Institution of Mechanical Engineers, Part G: Journal of Aerospace Engineering* 227 (Feb. 2012), pp. 455–466. DOI: 10.1177/0954410012437505.

[49] Ioannis Templalexis et al. “Development of a 2-D Compressor Streamline Curvature Code”. en. In: American Society of Mechanical Engineers Digital Collection, Sept. 2008, pp. 1005–1014. DOI: 10.1115/GT2006-90867. URL: https://asmedigitalcollection.asme.org/GT/proceedings-abstract/GT2006/42363/1005/314475 (visited on 05/09/2023).

[50] E. Tsoutsanis et al. “Part-Load Performance of Gas Turbines: Part I A Novel Compressor Map Generation Approach Suitable for Adaptive Simulation”. en. In: American Society of Mechanical Engineers Digital Collection, July 2013, pp. 733–742. DOI: 10.1115/GTINDIA2012-9580. URL: https://asmedigitalcollection.asme.org/GTINDIA/proceedings-abstract/GTINDIA2012/45165/733/242639 (visited on 05/02/2023).

[51] Elias Tsoutsanis et al. “A component map tuning method for performance prediction and diagnostics of gas turbine compressors”. en. In: *Applied Energy* 135 (Dec. 2014), pp. 572–585. ISSN: 0306-2619. DOI: 10.1016/j.apenergy.2014.08.115. URL: https://www.sciencedirect.com/science/article/pii/S0306261914009386 (visited on 04/05/2023).

[52] Elias Tsoutsanis et al. *Part-Load Performance of Gas Turbines Part I: A Novel Compressor Map Generation Approach Suitable for Adaptive Simulation*. Journal Abbreviation: ASME 2012 Gas Turbine India Conference, GTINDIA 2012 Publication Title: ASME 2012 Gas Turbine India Conference, GTINDIA 2012. Dec. 2012. DOI: 10.1115/GTINDIA2012-9580.

[53] Litvinov UA and Borovik VO. “Characters and using performance of jet engine”. Chinese. In: *Beijing: National Defensive Industry Press* (1986), p. 43.

[54] Louis A. Urban. “Gas Path Analysis Applied to Turbine Engine Condition Monitoring”. In: *Journal of Aircraft* 10.7 (1973). Publisher: American Institute of Aeronautics and Astronautics _eprint: https://doi.org/10.2514/3.60240, pp. 400–406. ISSN: 0021-8669. DOI: 10.2514/3.60240. URL: https://doi.org/10.2514/3.60240 (visited on 05/14/2023).

[55] M. L. Verbist. “Gas path analysis for enhanced aero-engine condition monitoring and maintenance”. en. In: (2017). DOI: 10.4233/uuid:e1079009-84c2-482d-afe4-e1f9fde0d137. URL: https://repository.tudelft.nl/islandora/object/uuid%3Ae1079009-84c2-482d-afe4-e1f9fde0d137 (visited on 05/13/2023).

[56] Michel L. Verbist et al. “Component Map Tuning Procedure Using Adaptive Modeling”. en. In: American Society of Mechanical Engineers Digital Collection, July 2013, pp. 371–379. DOI: 10.1115/GT2012-69688. URL: https://asmedigitalcollection.asme.org/GT/proceedings-abstract/GT2012/44670/371/289123 (visited on 04/05/2023).

[57] W. P. J. Visser. “Generic Analysis Methods for Gas Turbine Engine Performance: The development of the gas turbine simulation program GSP”. en. In: (2015). URL: https://repository.tudelft.nl/islandora/object/uuid%3Af95da308-e7ef-47de-abf2-aedbfa30cf63 (visited on 10/08/2023).

[58] Wilfried P. J. Visser and Michael J. Broomhead. “GSP, a Generic Object-Oriented Gas Turbine Simulation Environment”. en. In: American Society of Mechanical Engineers Digital Collection, Aug. 2014. DOI: 10.1115/2000-GT-0002. URL: https://asmedigitalcollection.asme.org/GT/proceedings-abstract/GT2000/78545/239142 (visited on 05/13/2023).

[59] Ming-Yang Wang et al. “Effects of Reynolds number and loading distribution on the aerodynamic performance of a high subsonic compressor airfoil”. In: *Proceedings of the Institution of Mechanical Engineers, Part A: Journal of Power and Energy* 234.8 (Dec. 2020). Publisher: IMECHE, pp. 1069–1083. ISSN: 0957-6509. DOI: 10.1177/0957650919899541. URL: https://doi.org/10.1177/0957650919899541 (visited on 05/16/2023).

[60] A. B. Wassell. “Reynolds Number Effects in Axial Compressors”. In: *Journal of Engineering for Power* 90.2 (Apr. 1968), pp. 149–156. ISSN: 0022-0825. DOI: 10.1115/1.3609154. URL: https://doi.org/10.1115/1.3609154 (visited on 05/16/2023).

[61] Mohamed Yaakoub. “Enhanced Gas Path Modelling for Condition Monitoring”. Master’s Thesis Literature Study. Delft Universtiy of Technology, 2023.

[62] Binbin Yan et al. “A tuning scheme of cycle reference point for gas turbine adaptive performance simulation with field data”. en. In: *Journal of Mechanical Science and Technology* 34.12 (Dec. 2020), pp. 5279–5294. ISSN: 1976-3824. DOI: 10.1007/s12206-020-1129-9. URL: https://doi.org/10.1007/s12206-020-1129-9 (visited on 04/14/2023).

[63] Binbin Yan et al. “Enhanced Component Analytical Solution for Performance Adaptation and Diagnostics of Gas Turbines”. en. In: *Energies* 14.14 (Jan. 2021). Number: 14 Publisher: Multidisciplinary Digital Publishing Institute, p. 4356. ISSN: 1996-1073. DOI: 10.3390/en14144356. URL: https://www.mdpi.com/1996-1073/14/14/4356 (visited on 04/12/2023).

[64] Qingcai Yang, Shuying Li, and Yunpeng Cao. “A new component map generation method for gas turbine adaptation performance simulation”. en. In: *Journal of Mechanical Science and Technology* 31.4 (Apr. 2017), pp. 1947–1957. ISSN: 1976-3824. DOI: 10.1007/s12206-017-0344-5. URL: https://doi.org/10.1007/s12206-017-0344-5 (visited on 04/05/2023).

[65] Yulong Ying et al. “Study on gas turbine engine fault diagnostic approach with a hybrid of gray relation theory and gas-path analysis”. In: *Advances in Mechanical Engineering* 8 (Jan. 2016). DOI: 10.1177/1687814015627769.

[66] Youhong Yu et al. “Neural-network based analysis and prediction of a compressors characteristic performance map”. en. In: *Applied Energy* 84.1 (Jan. 2007), pp. 48–55. ISSN: 03062619. DOI: 10.1016/j.apenergy.2006.04.005. URL: https://linkinghub.elsevier.com/retrieve/pii/S030626190600047X (visited on 05/03/2023).

[67] Li Yuan et al. “Research on Fault Prognosis Methods Based on Data-driven:A Survey”. In: *IOP Conference Series: Materials Science and Engineering* 1043 (Jan. 2021), p. 042008. DOI: 10.1088/1757-899X/1043/4/042008.

[68] By T. A. Zaki, Paul A. Durbin, and X. Wu. “Separation and transition to turbulence in a compressor passage”. In: URL: https://api.semanticscholar.org/CorpusID:18856011.

[69] Na Zhang and Ruixian Cai. “Analytical solutions and typical characteristics of part-load performances of single shaft gas turbine and its cogeneration”. en. In: *Energy Conversion and Management* 43.9 (June 2002), pp. 1323–1337. ISSN: 0196-8904. DOI: 10.1016/S0196-8904(02)00018-3.

URL: https://www.sciencedirect.com/science/article/pii/S0196890402000183 (visited on 05/04/2023).

[70] Hongyu Zhou et al. “Long-short term memory and gas path analysis based gas turbine fault diagnosis and prognosis”. In: *Advances in Mechanical Engineering* 13 (Aug. 2021), p. 168781402110377. DOI: 10.1177/16878140211037767.

[71] Wenxiang Zhou et al. “A Novel Data-Driven-Based Component Map Generation Method for Transient Aero-Engine Performance Adaptation”. In: *Aerospace* 9.8 (2022). ISSN: 2226-4310. DOI: 10.3390/aerospace9080442.

A. Reynolds number correlations

A.1. Wassel's correlation

The Wassel performance correction for the Reynolds number first presented in the author's paper [60], is based on correlations of 20 compressors. The correlations are only reported for values above the critical Reynolds number; however, it is indicated to be a low value ($0.25 * 10^5$). In this section, the correlation's important parameters are briefly presented for application purposes. One should refer to the original paper for a more fundamental understanding of the correlation approach. Moreover, in the book [32], A. B. Mckenzie dedicates an entire chapter for Reynolds correction featuring the Wassel correlations. The author presents the method using an example approach.

Efficiency correction

The correlation assumes efficiency in the form

$$\left(1-\eta\right) = k\mathrm{Re}^{-n} \tag{A.1}$$

with n, the number index as

$$n = p \cdot q \tag{A.2}$$

p and q are parameters that are based on Mach number and geometry variations as presented in Figure A.1.

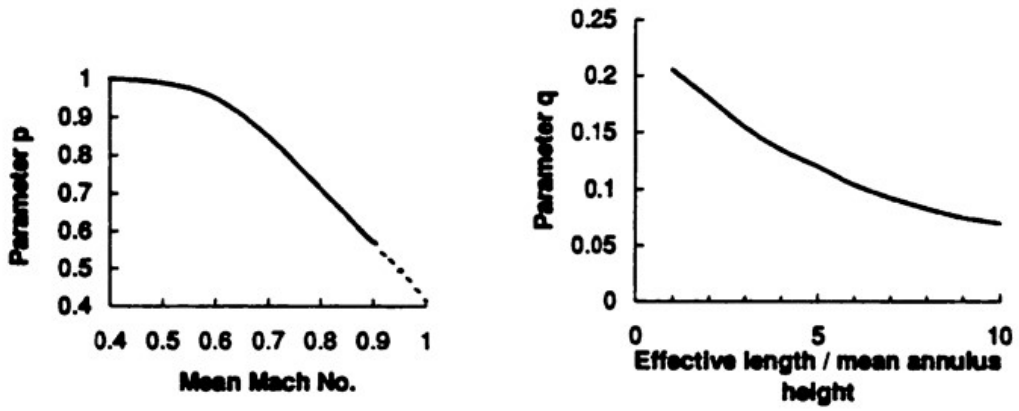

Figure A.1: Wassel efficiency correction parameters. Image from the adaptation of [32] based on the original paper.

Mass flow correction

For mass flow correction, the correlation takes into account the geometry of the blades in the compressor cascade. The correlation takes the form

$$(O/x)(Q_A/Q_A^* - 1) = f(Re_2) \tag{A.3}$$

The geometry variables and Re_2 are defined in Figure A.2. Q_A is defined as the mass flow with the asterisk denoting the uncorrected term.

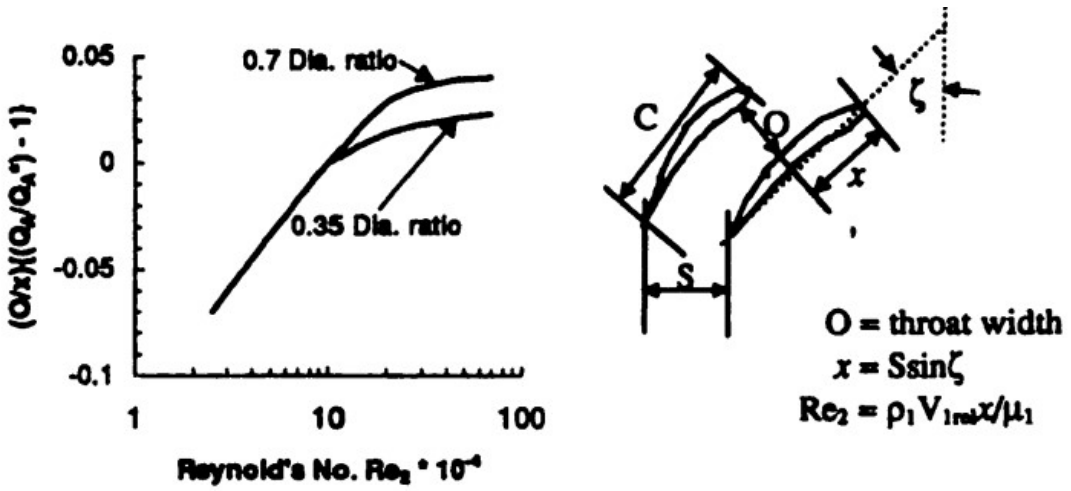

Figure A.2: Wassel mass flow correction parameters for different blade length to diameter ratios. Image from the adaptation of [32] based on the original paper.

Surge pressure ratio correction

For surge pressure ratio correction another Reynolds number, Re_3 is defined as

$$Re_3 = \rho_1 * V_a * H/\mu_1 \tag{A.4}$$

where ρ is inlet density, V_a the axial velocity, H the annulus height at the inlet, and μ is the inlet viscosity. The correlation is presented in Figure A.3. Rs is the surge pressure ratio and the asterisk denotes the uncorrected term.

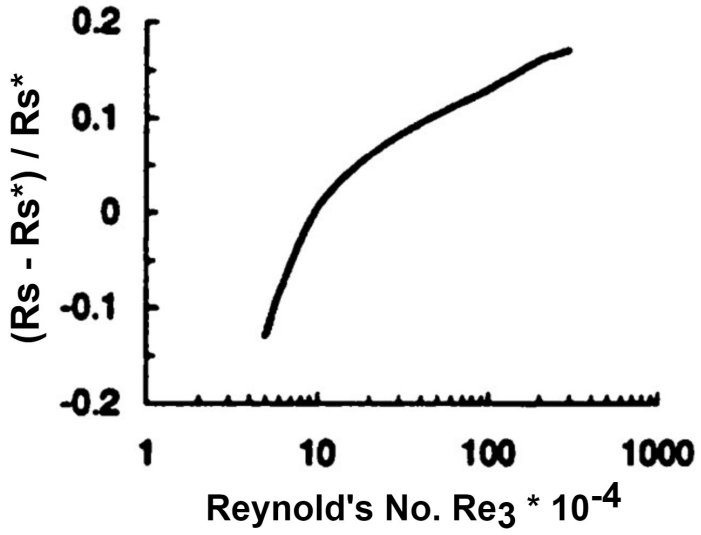

Figure A.3: Wassel surge pressure ratio correction parameters. Image adapted for readability based from the adaptation of [32] based on the original paper.

A.2. Litvinov correlations

The Litvinov [53] is a semi-empirical method that is based on a series of experimental results of turbomachinery. The model was presented in the paper by Tang et al. [48] for comparison against their

presented method that utilizes CFD methods for quantifying the Reynolds effect.

In the Litvinov method, Equation A.5 presents the defined Reynolds number for compressors. V_c is the incidence relative velocity, B_c is the chord length at the middle span, ρ_c is the flow density at the inlet, and μ_c is the viscosity at the inlet.

$$\mathrm{Re}_c = \frac{V_c B_c \rho_c}{\mu_c} \tag{A.5}$$

The Reynolds effect directly impacts the component's performance and as a result, could be represented by changes in the component maps. Equation A.6 and Equation A.7 represent the normalized mass flow capacity and efficiency of the compressor, respectively, for corrected rotation speed N_{cor} $\left((N/N_{ds})/\sqrt{T/T_{ds}}\right)$ higher than 1. The subscript 0 used for the normalization parameter in Equation A.6 and Equation A.7 represents the parameter's value at the critical Reynolds number 3.5×10^5 defined by the authors. For corrected rotating speeds below 0.8, Equation A.8 and Equation A.9 can be used to calculate the normalized mass flow capacity and efficiency respectively. For corrected speed above 0.8 and below 1 a linear interpolation between methods is suggested.

$$\frac{Q_c}{Q_{c0}} = 0.799 + 0.208\left(\mathrm{Re}_c/10^5\right) - 0.784\left(\mathrm{Re}_c/10^5\right)^2 + 0.0104\left(\mathrm{Re}_c/10^5\right)^3 \tag{A.6}$$

$$\frac{\eta_c}{\eta_{c0}} = 0.8997 + 0.208\left(\mathrm{Re}_c/10^5\right) - 0.0287\left(\mathrm{Re}_c/10^5\right)^2 + 0.0034\left(\mathrm{Re}_c/10^5\right)^3 \tag{A.7}$$

$$\frac{Q_c}{Q_{c0}} = 0.66 + 0.288\left(\mathrm{Re}_c/10^5\right) - 0.0836\left(\mathrm{Re}_c/10^5\right)^2 + 0.0083\left(\mathrm{Re}_c/10^5\right)^3 \tag{A.8}$$

$$\frac{\eta_c}{\eta_{c0}} = 0.8539 + 0.1165\left(\mathrm{Re}_c/10^5\right) - 0.034\left(\mathrm{Re}_c/10^5\right)^2 + 0.0036\left(\mathrm{Re}_c/10^5\right)^3 \tag{A.9}$$

For turbines, Equation A.10 represents the defined Reynolds number. W_t is the mass flow of the gas, B_t is the chord length at the middle span, A_{th} is the throat area and μ_t is the viscosity at the inlet. Equation A.11 and Equation A.12 represent the normalized mass flow capacity and efficiency of the turbine, respectively. The authors do not extend on the corrected rotational speed region the equations are supposedly applicable in. It is assumed that they hold for all the turbine's operational points as they are usually choked in operation. The subscript 0 used for the normalization parameter in Equation A.11 and Equation A.12 represents the parameter's value at the critical Reynolds number 2.5×10^5 defined by the authors.

$$\mathrm{Re}_t = \frac{W_t B_t}{A_{th}\mu_t} \tag{A.10}$$

$$\frac{Q_t}{Q_{t0}} = 0.905 + 0.146\left(\mathrm{Re}_t/10^5\right) - 0.0917\left(\mathrm{Re}_t/10^5\right)^2 + 0.0206\left(\mathrm{Re}_t/10^5\right)^3 \tag{A.11}$$

$$\frac{\eta_t}{\eta_{t0}} = 0.907 + 0.1548\left(\mathrm{Re}_t/10^5\right) - 0.088\left(\mathrm{Re}_t/10^5\right)^2 + 0.01645\left(\mathrm{Re}_t/10^5\right)^3 \tag{A.12}$$

Finally, to obtain the pressure ratios Equation A.13 can be used. k in these equations is not explicitly defined. It is assumed to be the specific heat ratio. It is not clear in the paper how this formula is

obtained. Additionally, as the pressure ratio is implicitly defined through mass flow and efficiency, it is assumed through logical reasoning that Equation A.13 is not a pressure ratio correction, but rather a sure pressure ratio correction.

$$\frac{\pi^{(k-1)/k}-1}{\eta} = \frac{\pi_0^{(k-1)/k}-1}{\eta_0} \tag{A.13}$$

B. OD scaling factors sensitivity

In order to interpret the results of deploying OD scaling factors for performance matching, their effects need to be analyzed. Therefore a sensitivity test was conducted to establish all turbomachinery components' behaviour based on altering each OD scaling factor individually. The results presented are therefore for the fan bypass, fan core, HPC, HPT, and LPT. The scaling factors were altered by a 5% change both positive and negative. The chosen point for the analysis is a steady-state take-off point, and all the simulations are based on individual steady-state simulations with the chosen takeoff condition. The results shown in the following figures present the pressure ratio, corrected mass flow, efficiency, corrected spool speed, and beta map value of each respective component. Fan bypass, fan core, HPC, HPT, LPT results are shown in Figure B.1, Figure B.2, Figure B.3, Figure B.4, and Figure B.5, respectively.

Fan bypass

First scaling the pressure ratio simply affects the pressure ratio values mainly and the other performance parameters negligibly. Scaling the corrected mass flow affects the mass flow mainly. The pressure ratio is also affected due to the shift in the beta values. Note the Nc values are constant as they are input boundary parameters to the system of equations. The shift in beta value can be interpreted as increased error in the conservation of mass which leads to triggering the state variables update loop. Finally, scaling the efficiency affects the efficiency mainly. The pressure ratio also changes a slightly due to the shift in the beta value.

Fan core

Scaling the pressure ratio mainly affects the pressure ratio and slightly affects the mass flow. Scaling the mass flow on the other hand affects all three performance parameters due to the shift in the the original convergence point, which is triggered by violating the conservation laws. Finally, scaling efficiency mainly affect the efficiency and slightly affects the mass flow.

HPC

Scaling the pressure ratio affects the pressure ratio mainly. Similarly, scaling the corrected mass flow affects the mass flow mainly. However, scaling the efficiency does change all three performance parameters greatly. It is particular to see the pressure ratio, mass flow, and efficiency all correlate positively to a change. This in fact can only be achieved if the spool speed is increased. Note that the input boundary Nc is the fan spool, therefore the N2 spool is a free state in the numerical solver. On the other hand, the beta value decreases as the Nc value increases. Looking at Figure 5.1 and Figure 5.3, a decrease in the beta value should reduce the pressure ratio and the efficiency. However, the increase change in the corrected spool speed is larger.

HPT

Scaling the pressure ratio affects the pressure ratio insignificantly, at least compared to the changes seen for compressors. This is because the beta value reverses the effects. The solver is generally able to do so in turbines easily because the $\dot{m}_c$ vs β and the η vs β maps shown in Figure 5.5 and Figure 5.6, respectively, have a lot of horizontal line regions for the same corrected spool speed. Essentially the turbine is reverting back to the original stable equilibrium position. Scaling the corrected mass flow changes mainly the mass flow. Scaling efficiency changes the efficiency mainly.

LPT

Similar to the HPT scaling the pressure ratio does not affect the pressure ratio of the component. Scaling the mass flow only affects the mass flow significantly. Scaling the efficiency also only significantly affects the efficiency.

General Remarks

In general, it was noticed that the change in flight point did not affect the outcome of the results in the way that it would change how they should be generally interpreted. The scaling factors that triggered the convergence iteration loop to find different state variables due to conservation laws errors were the same. However, the performance change (increase and decrease) sometimes was noticed to be different. It is difficult to provide a general physical cause for the Newton-raphson solver behaviour. Ultimately, it is objectively trying to minimize the error functions. Additionally, when a single scaling factor was employed other component's performances were also affected. Therefore, when multiple scaling factors are employed at the same time it becomes difficult to isolate trends. Manual iteration to achieve a certain overall performance could be possible in simple engine model configurations. For the GEnx1-b and similar models, it is only logical then to make use of artificial intelligence methods to aid in performance matching

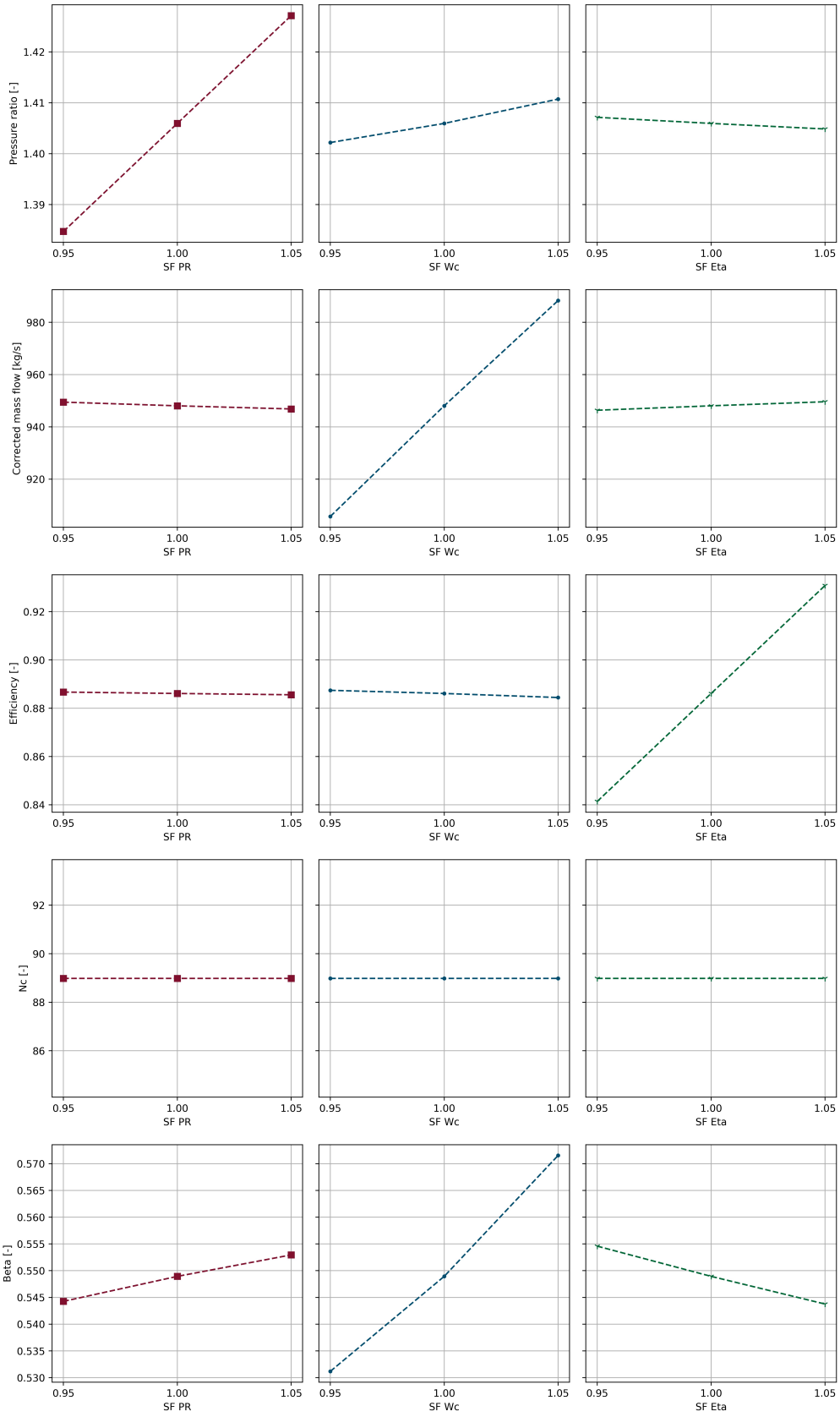

Figure B.1: Effect of varying pressure ratio, corrected mass flow, and efficiency OD scaling factors of the fan bypass per column, respectively, using values of [0.95, 1, 1.05] on map parameters.

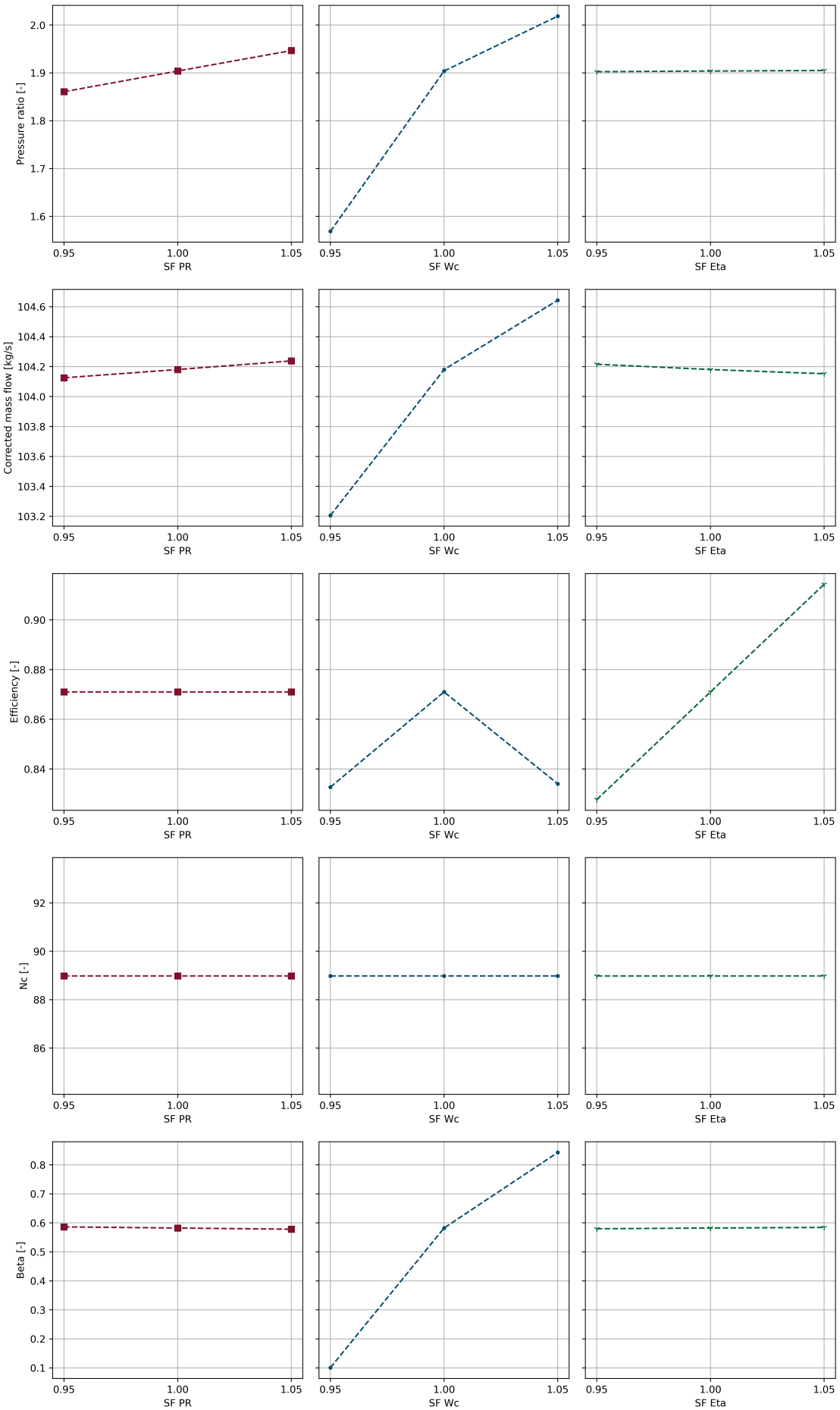

Figure B.2: Effect of varying pressure ratio, corrected mass flow, and efficiency OD scaling factors of the fan core per column, respectively, using values of [0.95, 1, 1.05] on map parameters.

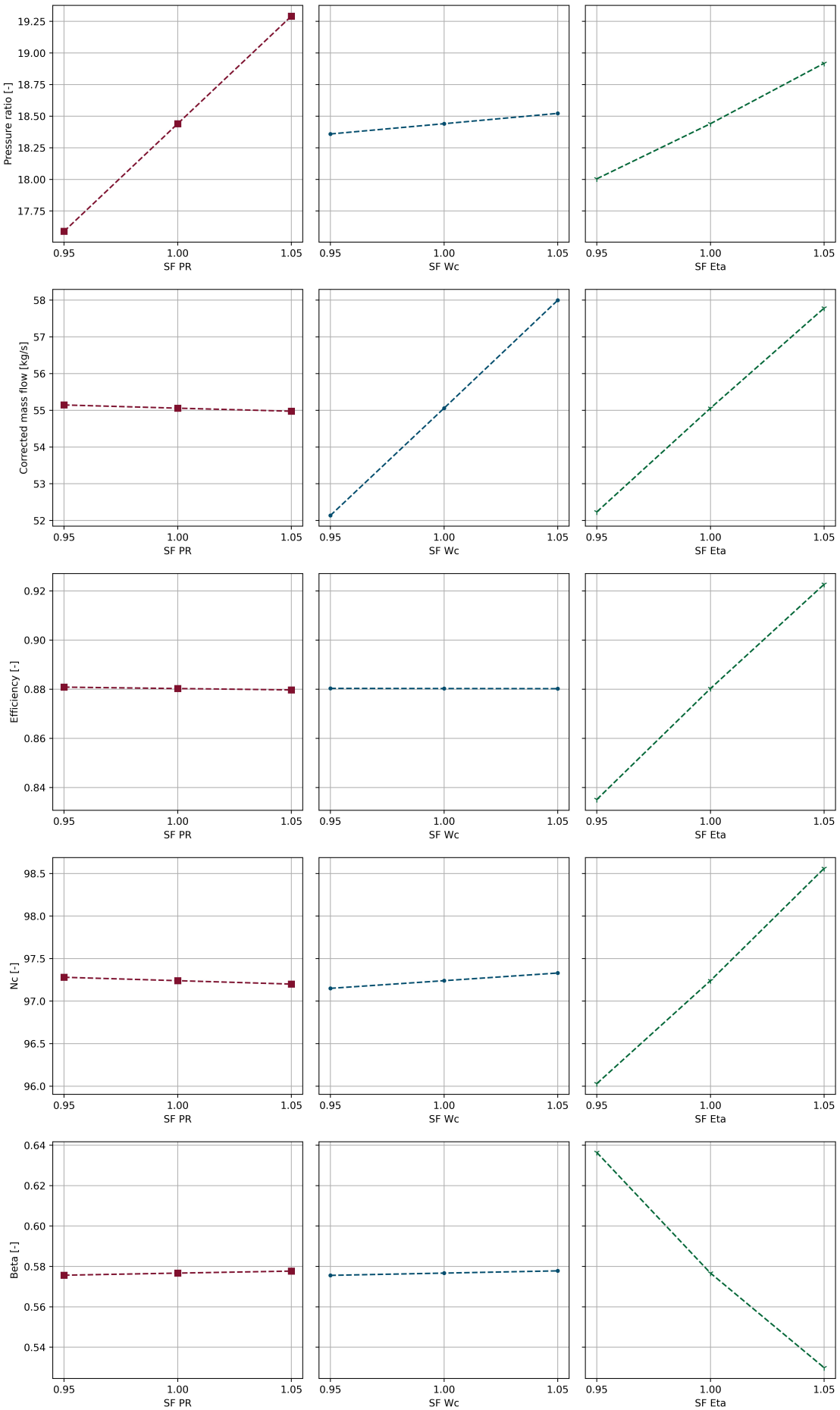

Figure B.3: Effect of varying pressure ratio, corrected mass flow, and efficiency OD scaling factors of the HPC per column, respectively, using values of [0.95, 1, 1.05] on map parameters.

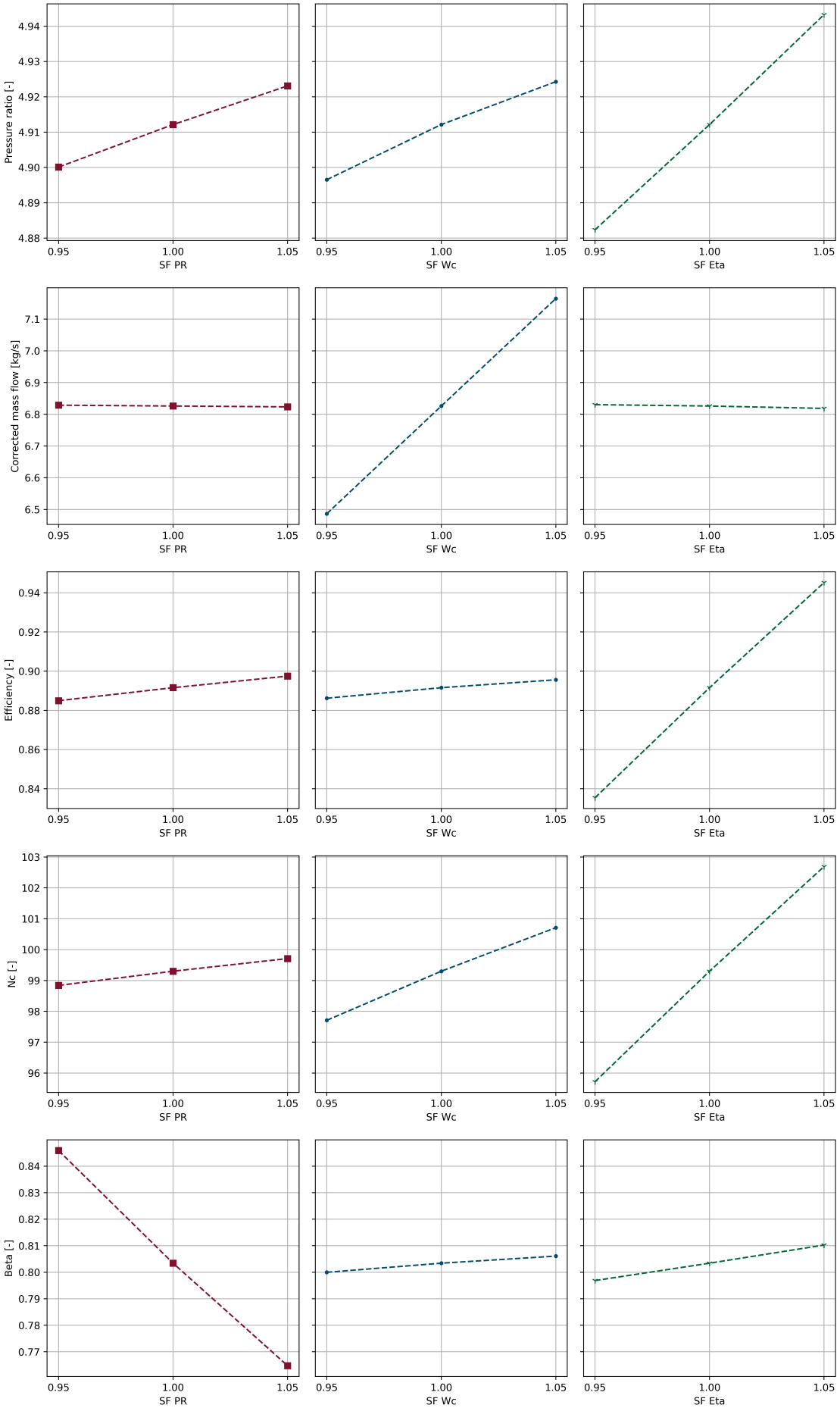

Figure B.4: Effect of varying pressure ratio, corrected mass flow, and efficiency OD scaling factors of the HPT per column, respectively, using values of [0.95, 1, 1.05] on map parameters.

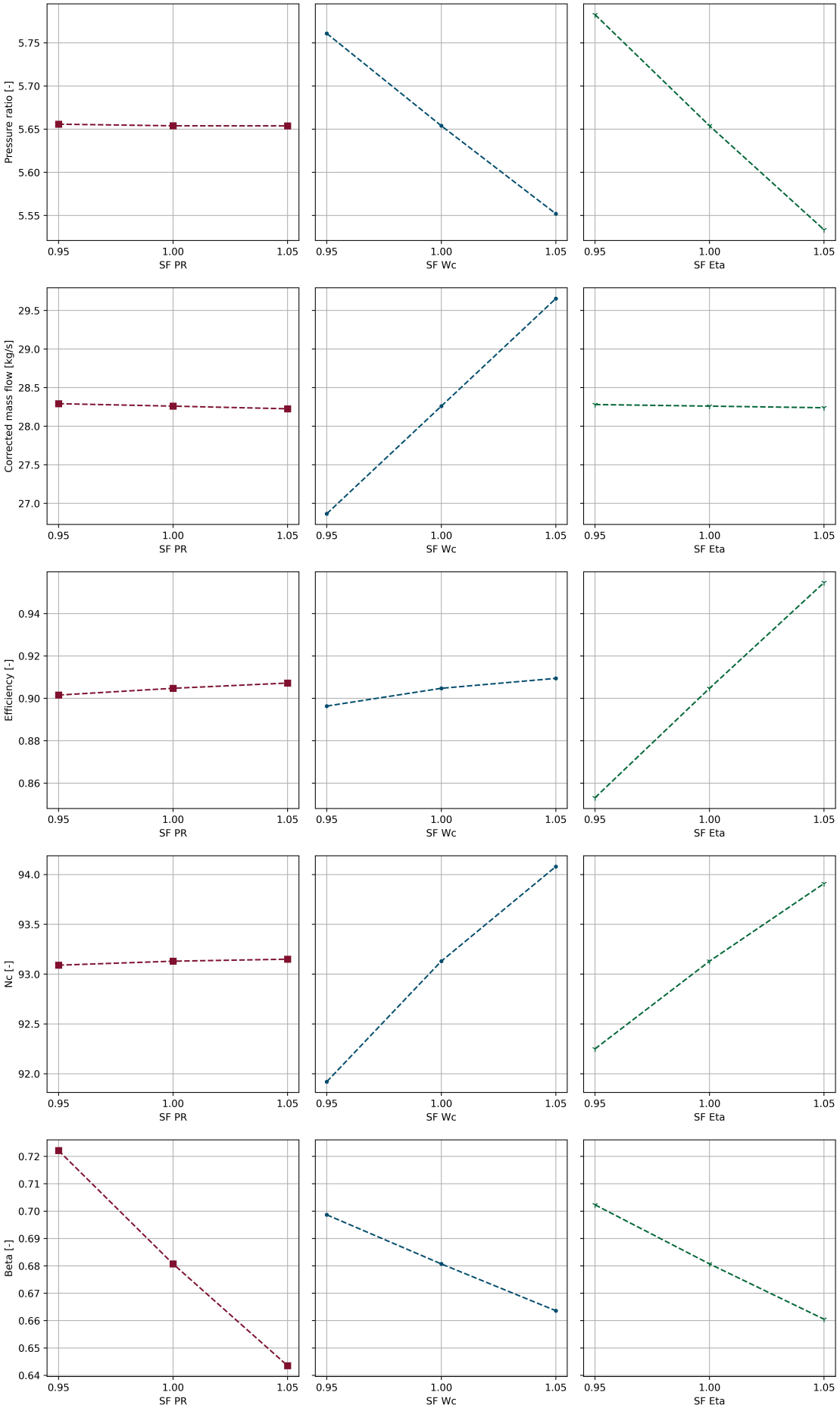

Figure B.5: Effect of varying pressure ratio, corrected mass flow, and efficiency OD scaling factors of the LPT per column, respectively, using values of [0.95, 1, 1.05] on map parameters.

C. OD scaling factors trends

The final result of the optimization process is a set of scaling factors that increase the model's accuracy. This appendix provides a visual representation of the turbomachinery OD scaling factors and the nozzle coefficient functions for the different optimization runs.

C.1. Turbomachinery single equation and splines approach optimizer solve

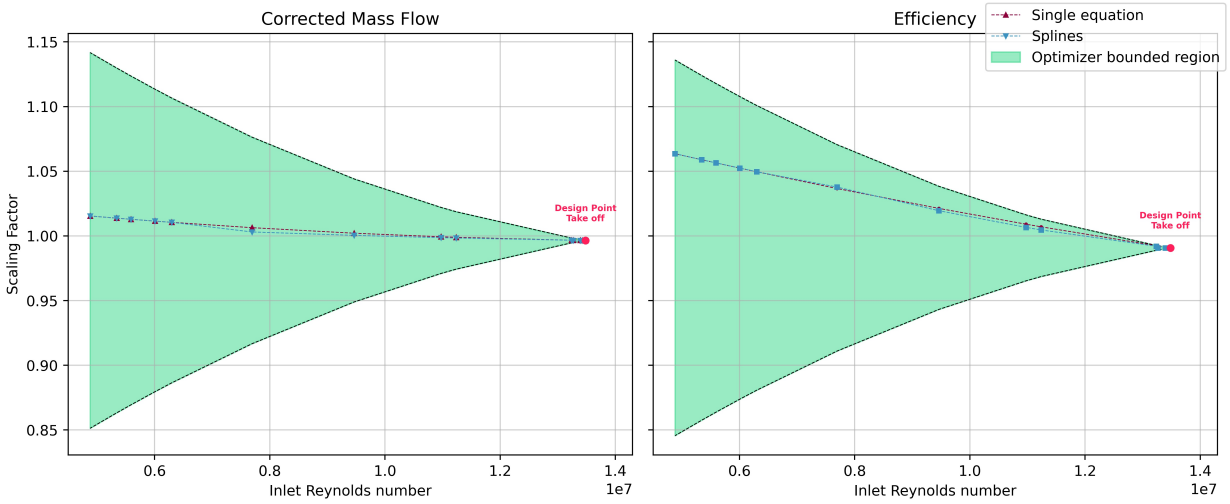

Figure C.1: Fan Bypass scaling factors.

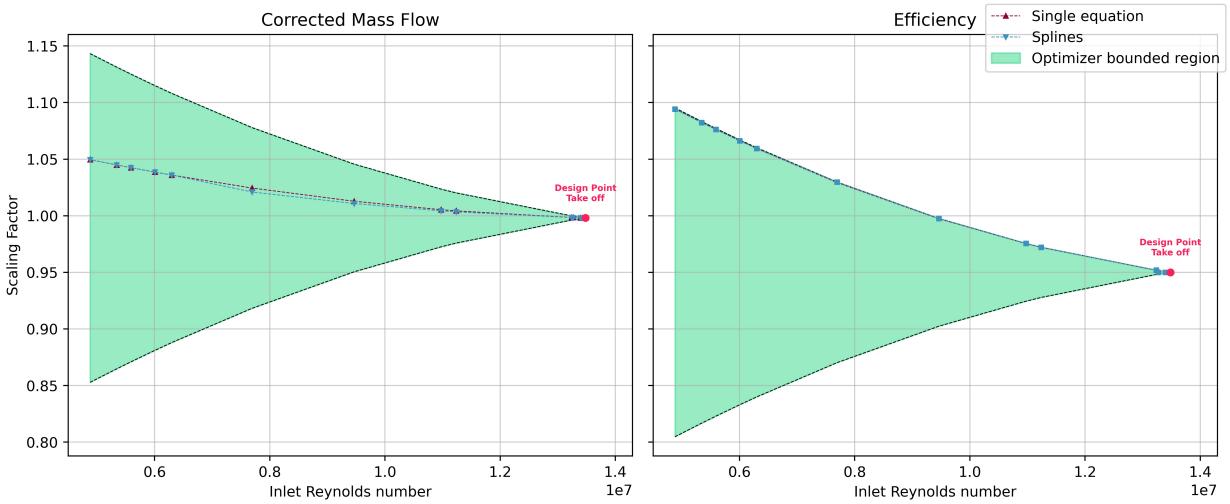

Figure C.2: Fan Core scaling factors.

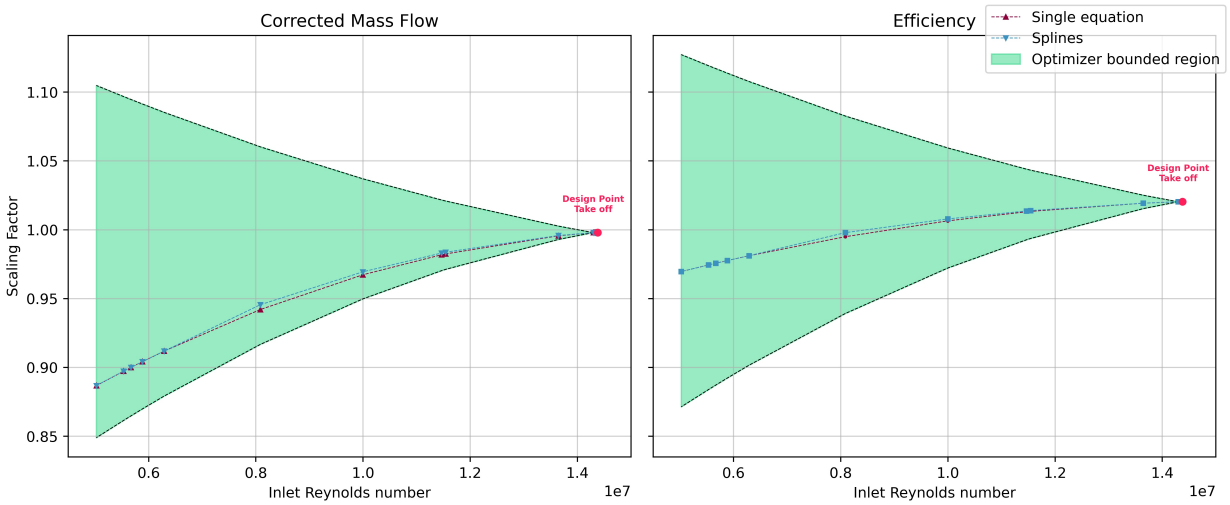

Figure C.3: HPC scaling factors.

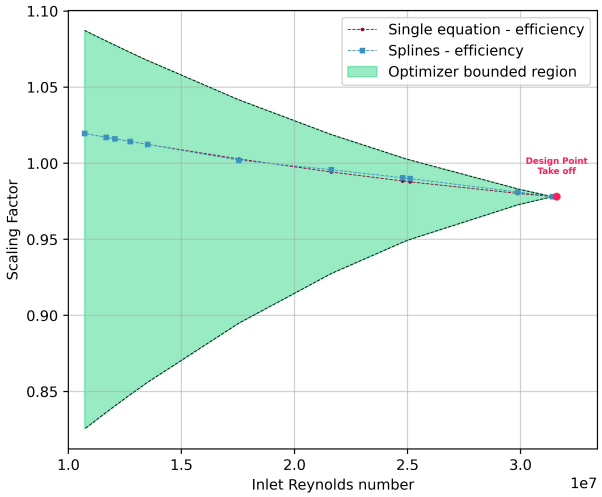

Figure C.4: HPT scaling factors.

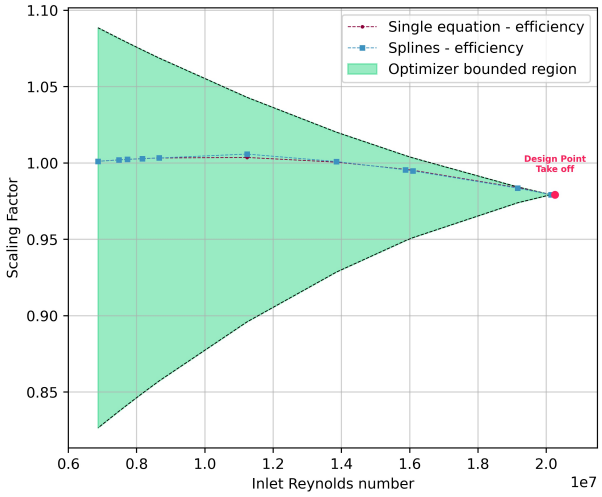

Figure C.5: LPT scaling factors.

C.2. Turbomachinery single equation with nozzle correction optimizer solve

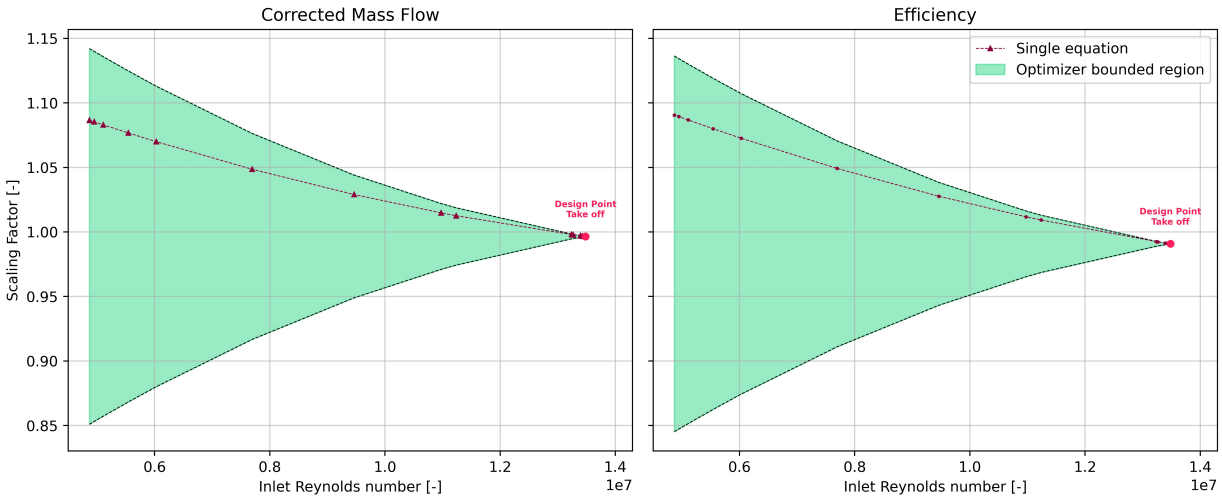

Figure C.6: Fan Bypass scaling factors.

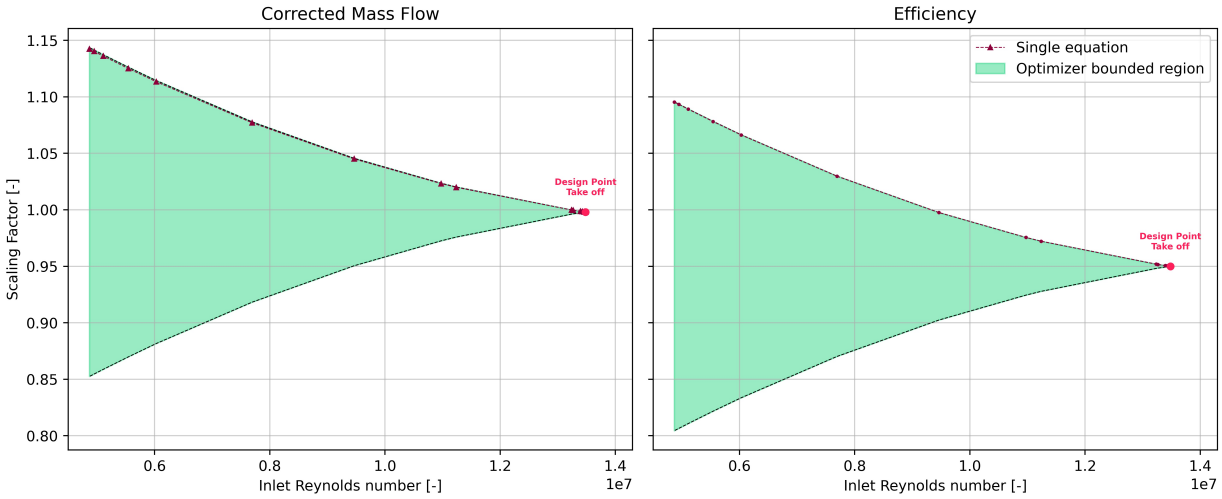

Figure C.7: Fan Core scaling factors.

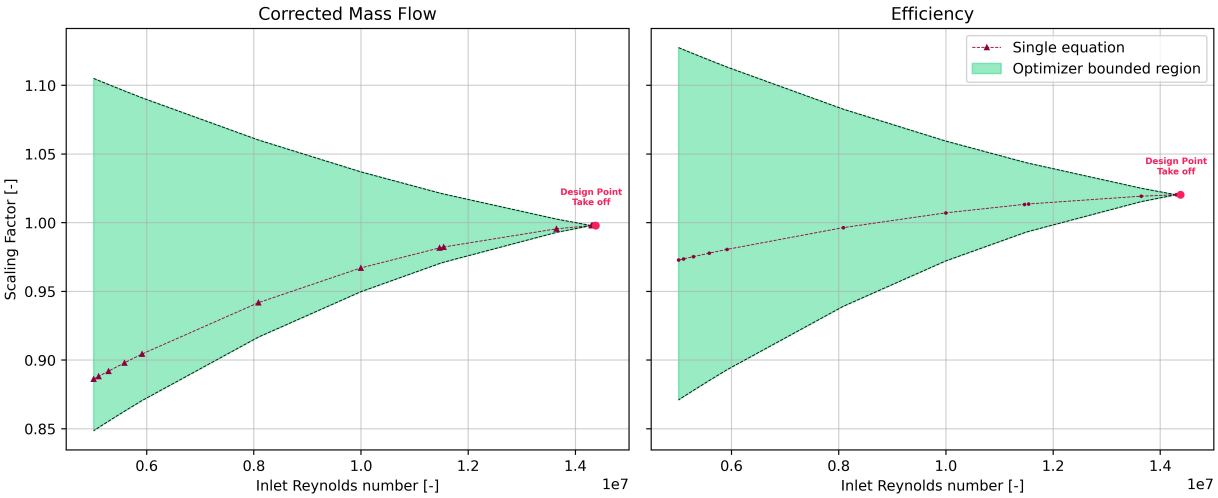

Figure C.8: HPC scaling factors.

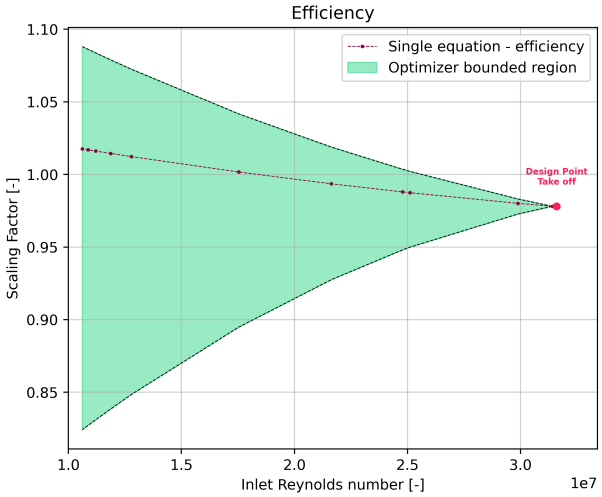

Figure C.9: HPT scaling factors.

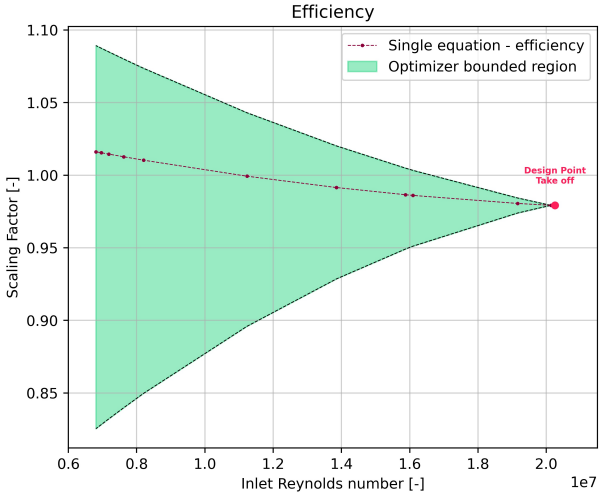

Figure C.10: LPT scaling factors.

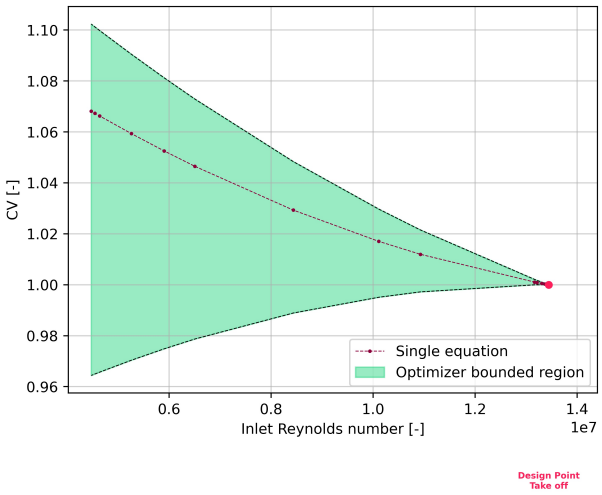

Figure C.11: Bypass nozzle velocity coefficient.

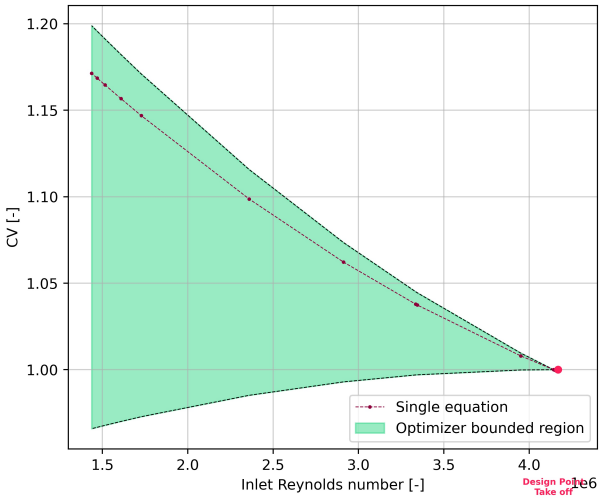

Figure C.12: Core nozzle velocity coefficient.

C.3. Clustering-based modelling approach

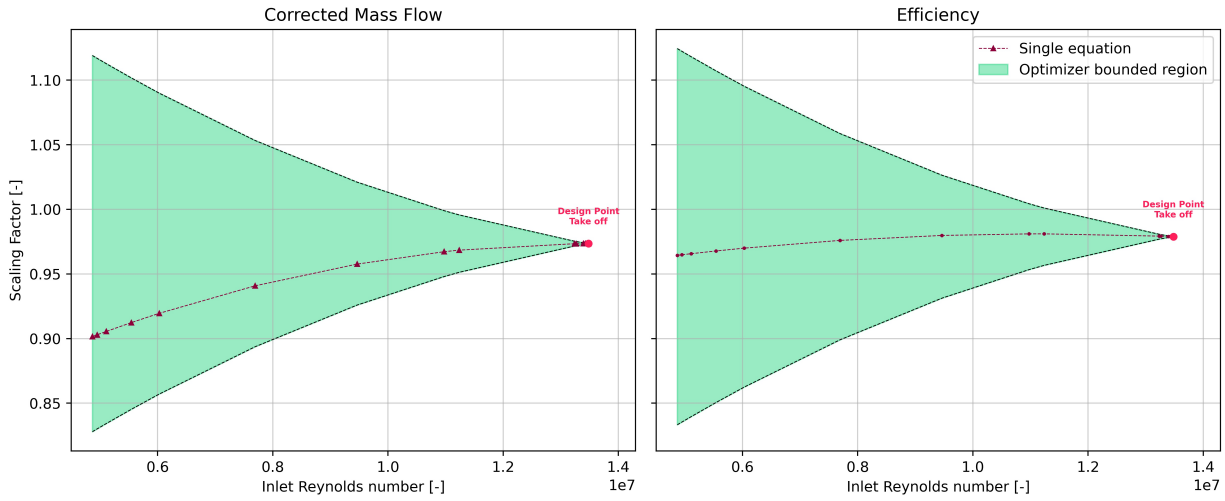

Figure C.13: Fan Bypass scaling factors.

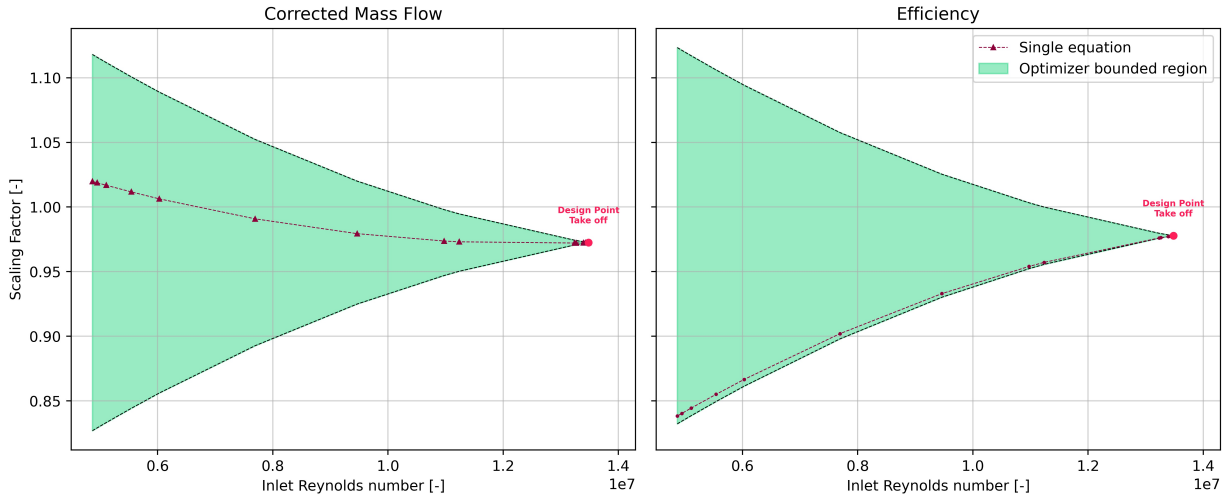

Figure C.14: Fan Core scaling factors.

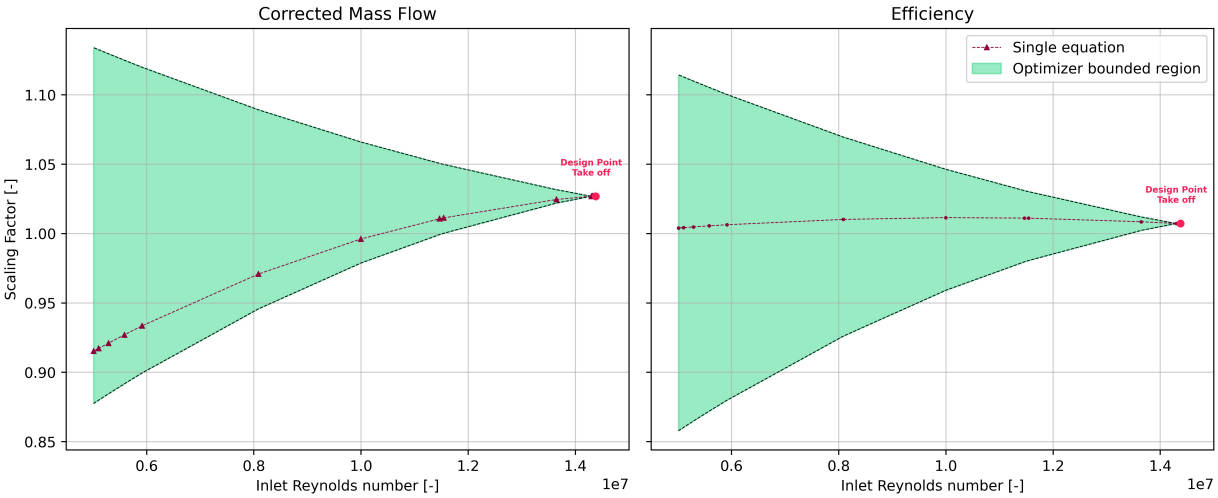

Figure C.15: HPC scaling factors.

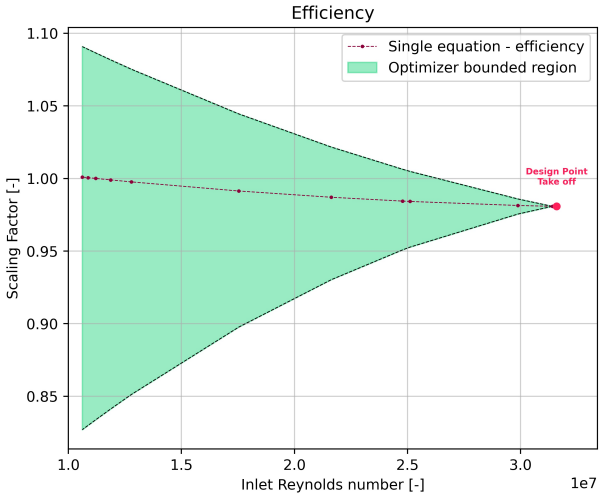

Figure C.16: HPT scaling factors.

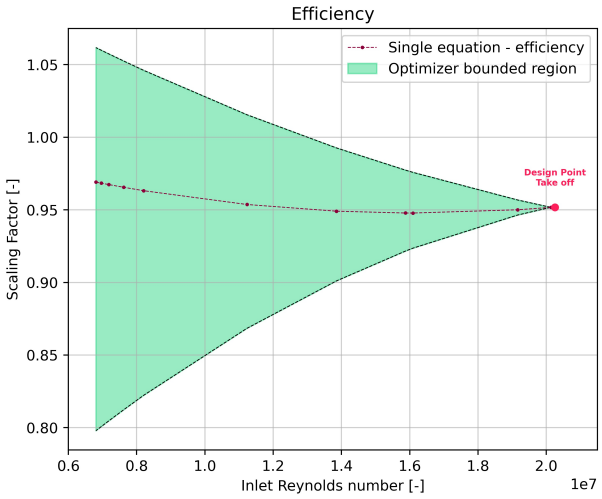

Figure C.17: LPT scaling factors.

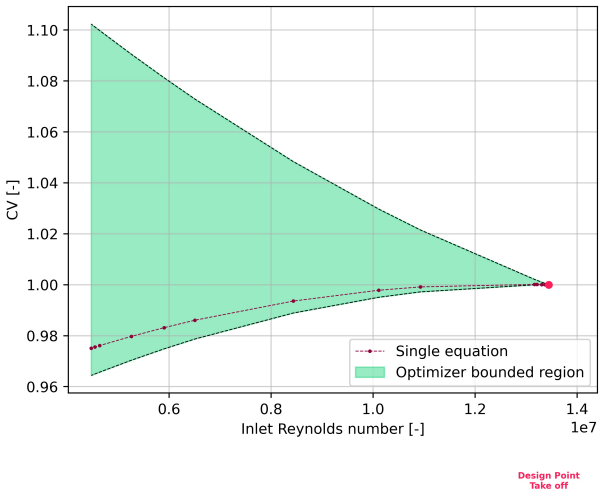

Figure C.18: Bypass nozzle velocity coefficient.

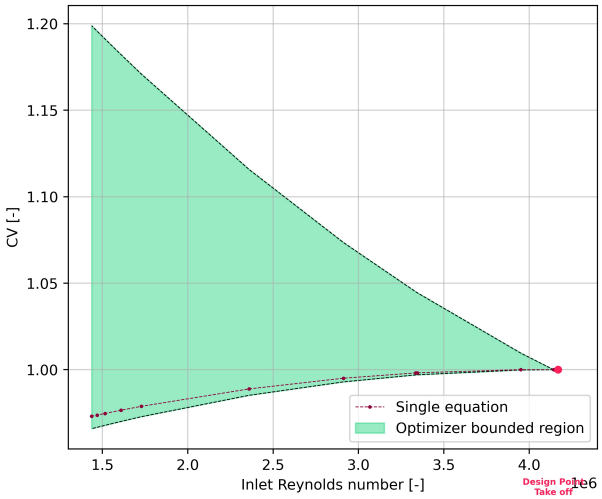

Figure C.19: Core nozzle velocity coefficient.

D. Optimizer solutions

The solutions for the individual optimizer runs are presented. Additionally, the scaling factors coefficients optimizer bounds are shown.

D.1. Take-off calibration

Table D.1: Take-off calibration optimization results.

Components	Design variable	Value
Fan bypass	$SF_{\dot{m}_c}$	**0.996**
	SF_η	**0.991**
Fan core	$SF_{\dot{m}_c}$	**0.998**
	SF_η	**0.950**
HPC	$SF_{\dot{m}_c}$	**0.998**
	SF_η	**1.02**
HPT	SF_η	**0.978**
LPT	SF_η	**0.979**

Table D.2: Scaling factors polynomials bounds.

Components	Scaling factor	bounds
Fan bypass	$SF_{\dot{m}_c}$	**(0.95, 1.05)**
	SF_η	**(0.95, 1.05)**
Fan core	$SF_{\dot{m}_c}$	**((0.95, 1.05)**
	SF_η	**(0.95, 1.05)**
HPC	$SF_{\dot{m}_c}$	**(0.95, 1.05)**
	SF_η	**(0.95, 1.05)**
HPT	SF_η	**(0.95, 1.05)**
LPT	SF_η	**(0.95, 1.05)**

D.2. Turbomachinery OD scaling approach - single equation

Table D.3: OD correction optimization results based on Reynolds number correlation.

Components	Scaling factor	Value (b)	Value (c)
Fan bypass	$SF_{\dot{m}_c}$	**-0.009**	**0.032**
	SF_η	**-0.092**	**0.035**
Fan core	$SF_{\dot{m}_c}$	**-0.022**	**0.092**
	SF_η	**-0.1**	**0.198**
HPC	$SF_{\dot{m}_c}$	**0.042**	**-0.2**
	SF_η	**0.019**	**-0.092**
HPT	SF_η	**- 0.042**	**0.032**
LPT	SF_η	**-0.1**	**-0.101**

Table D.4: Scaling factors polynomials bounds (single equation).

Components	Scaling factor	bounds (b)	bounds (c)
Fan bypass	$SF_{\dot{m}_c}$	**(-0.1, 0.1)**	**(-0.2, 0.2)**
	SF_{η}	**(-0.1, 0.1)**	**(-0.2, 0.2)**
Fan core	$SF_{\dot{m}_c}$	**(-0.1, 0.1)**	**(-0.2, 0.2)**
	SF_{η}	**(-0.1, 0.1)**	**(-0.2, 0.2)**
HPC	$SF_{\dot{m}_c}$	**(-0.1, 0.1)**	**(-0.2, 0.1)**
	SF_{η}	**(-0.1, 0.1)**	**(-0.2, 0.1)**
HPT	SF_{η}	**(-0.1, 0.1)**	**(-0.2, 0.1)**
LPT	SF_{η}	**(-0.1, 0.1)**	**(-0.2, 0.1)**

D.3. Turbomachinery OD scaling approach - splines

The results shown are for the climb phase. The solution for the cruise is based on the solution from the Section D.2.

Table D.5: OD correction optimization results based on Reynolds number correlation (climb splines solution).

Components	Scaling factor	Value (b)	Value (c)
Fan bypass	$SF_{\dot{m}_c}$	**-0.009**	**0.016**
	SF_{η}	**-0.067**	**0.100**
Fan core	$SF_{\dot{m}_c}$	**-0.019**	**0.080**
	SF_{η}	**-0.100**	**0.200**
HPC	$SF_{\dot{m}_c}$	**0.037**	**-0.193**
	SF_{η}	**0.019**	**-0.076**
HPT	SF_{η}	**-0.063**	**-0.021**
LPT	SF_{η}	**-0.092**	**-0.072**

Table D.6: Scaling factors polynomials bounds (Splines).

Components	Scaling factor	bounds (b)	bounds (c)
Fan bypass	$SF_{\dot{m}_c}$	**(-0.1, 0.1)**	**(-0.2, 0.2)**
	SF_{η}	**(-0.1, 0.1)**	**(-0.2, 0.2)**
Fan core	$SF_{\dot{m}_c}$	**(-0.1, 0.1)**	**(-0.2, 0.2)**
	SF_{η}	**(-0.1, 0.1)**	**(-0.2, 0.2)**
HPC	$SF_{\dot{m}_c}$	**(-0.1, 0.1)**	**(-0.2, 0.1)**
	SF_{η}	**(-0.1, 0.1)**	**(-0.2, 0.1)**
HPT	SF_{η}	**(-0.1, 0.1)**	**(-0.2, 0.1)**
LPT	SF_{η}	**(-0.1, 0.1)**	**(-0.2, 0.1)**

D.4. Combined turbomachinery and nozzle OD scaling approach - single equation

Table D.7: Combined turbomachinery and nozzle OD scaling approach optimization results.

Components	Scaling factor	Value (b)	Value (c)
Fan bypass	$SF_{\dot{m}_c}$	**-0.081**	**0.094**
	SF_η	**-0.095**	**0.096**
Fan core	$SF_{\dot{m}_c}$	**-0.098**	**0.200**
	SF_η	**-0.100**	**0.200**
HPC	$SF_{\dot{m}_c}$	**0.043**	**-0.200**
	SF_η	**0.018**	**-0.084**
HPT	SF_η	**-0.041**	**0.028**
LPT	SF_η	**-0.024**	**0.047**
Nozzle bypass	C_V	**-0.049**	**0.047**
Nozzle core	C_V	**-0.166**	**0.800**

Table D.8: Scaling factors polynomials bounds (Extended design vector).

Components	Scaling factor	bounds (b)	bounds (c)
Fan bypass	$SF_{\dot{m}_c}$	**(-0.1, 0.1)**	**(-0.2, 0.2)**
	SF_η	**(-0.1, 0.1)**	**(-0.2, 0.2)**
Fan core	$SF_{\dot{m}_c}$	**(-0.1, 0.1)**	**(-0.2, 0.2)**
	SF_η	**(-0.1, 0.1)**	**(-0.2, 0.2)**
HPC	$SF_{\dot{m}_c}$	**(-0.1, 0.1)**	**(-0.2, 0.1)**
	SF_η	**(-0.1, 0.1)**	**(-0.2, 0.1)**
HPT	SF_η	**(-0.1, 0.1)**	**(-0.2, 0.1)**
LPT	SF_η	**(-0.1, 0.1)**	**(-0.2, 0.1)**
Nozzle bypass	C_V	**(-0.1, 0.0))**	**(-0.08, 0.08)**
Nozzle core	C_V	**(-0.1, 0.0))**	**(-0.08, 0.08)**

D.5. Clustering-based modelling approach

Table D.9: Take-off calibration optimization results. (Clustering-based modelling).

Components	Design variable	Value
Fan bypass	$SF_{\dot{m}_c}$	**0.93**
	SF_η	**0.98**
Fan core	$SF_{\dot{m}_c}$	**0.97**
	SF_η	**0.98**
HPC	$SF_{\dot{m}_c}$	**1.03**
	SF_η	**1.01**
HPT	SF_η	**0.98**
LPT	SF_η	**0.95**

Table D.10: Combined turbomachinery and nozzle OD scaling approach optimization results. (Clustering-based modelling)

Components	Scaling factor	Value (b)	Value (c)
Fan bypass	$SF_{\dot{m}_c}$	**0.001**	**-0.174**
	SF_η	**-0.025**	**-0.076**
Fan core	$SF_{\dot{m}_c}$	**0.021**	**0.149**
	SF_η	**0.091**	**-0.200**
HPC	$SF_{\dot{m}_c}$	**0.043**	**-0.200**
	SF_η	**-0.03**	**-0.055**
HPT	SF_η	**-0.011**	**0.03**
LPT	SF_η	**0.04**	**0.1**
Nozzle bypass	C_V	**-0.004**	**-0.07**
Nozzle core	C_V	**-0.008**	**-0.068**

Table D.11: Scaling factors polynomials bounds. (Extended design vector). (Clustering-based modelling).

Components	Scaling factor	bounds (b)	bounds (c)
Fan bypass	$SF_{\dot{m}_c}$	**(-0.1, 0.1)**	**(-0.2, 0.2)**
	SF_η	**(-0.1, 0.1)**	**(-0.2, 0.2)**
Fan core	$SF_{\dot{m}_c}$	**(-0.1, 0.1)**	**(-0.2, 0.2)**
	SF_η	**(-0.1, 0.1)**	**(-0.2, 0.2)**
HPC	$SF_{\dot{m}_c}$	**(-0.1, 0.1)**	**(-0.2, 0.1)**
	SF_η	**(-0.1, 0.1)**	**(-0.2, 0.1)**
HPT	SF_η	**(-0.1, 0.1)**	**(-0.2, 0.1)**
LPT	SF_η	**(-0.1, 0.1)**	**(-0.2, 0.1)**
Nozzle bypass	C_V	**(-0.1, 0.0))**	**(-0.08, 0.08)**
Nozzle core	C_V	**(-0.1, 0.0))**	**(-0.08, 0.08)**

E. Clustering-based modelling simulated error

The accuracy of the clustering-based modelling approach on the fitting and validation sets is presented.

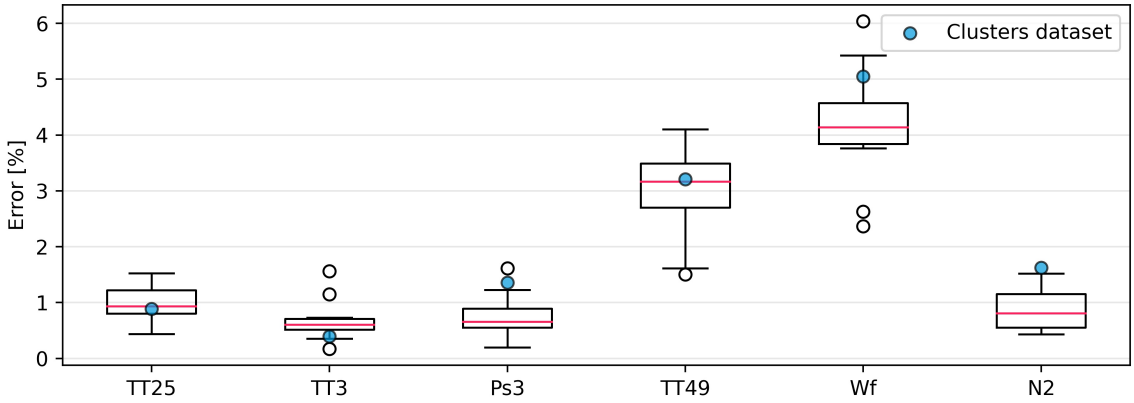

Figure E.1: Boxplot for the take-off phase mean target parameters errors. (Fitting dataset).

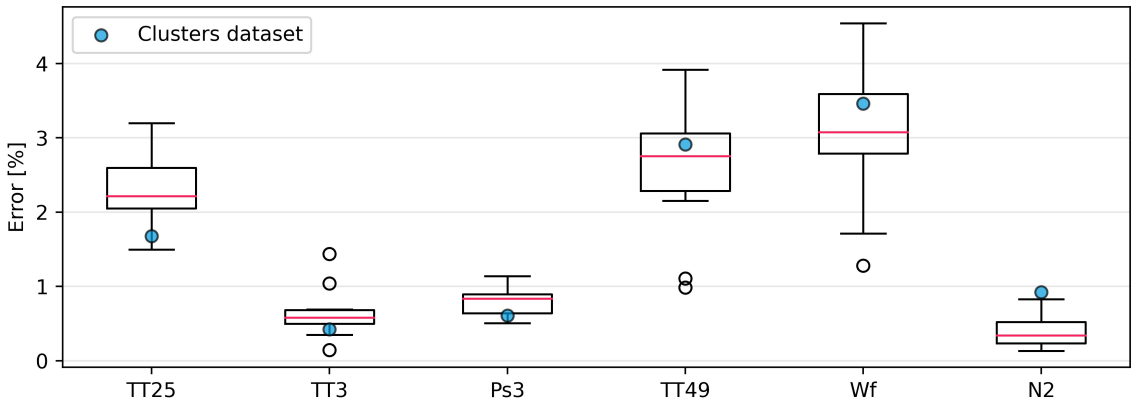

Figure E.2: Boxplot for the take-off phase mean target parameters errors. (Validation dataset)

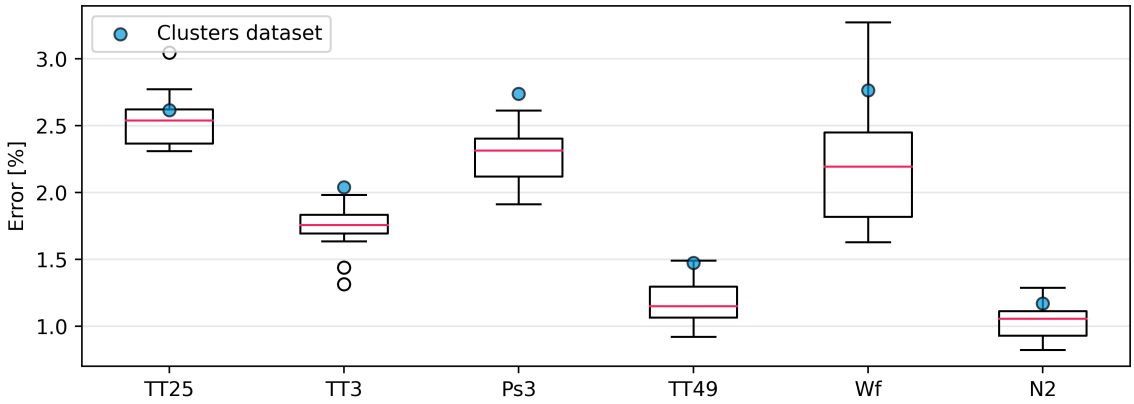

Figure E.3: Boxplot for the climb phase mean target parameters errors. (Fitting dataset).

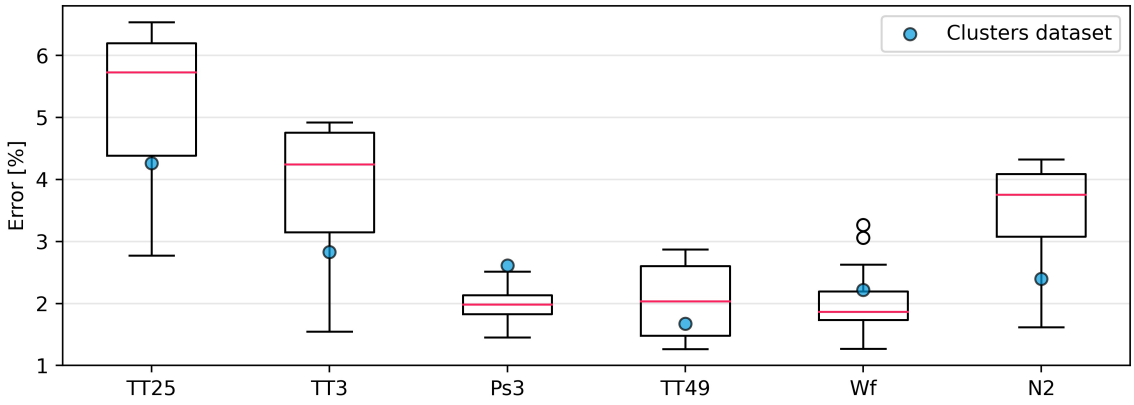

Figure E.4: Boxplot for the climb phase mean target parameters errors. (Validation dataset)

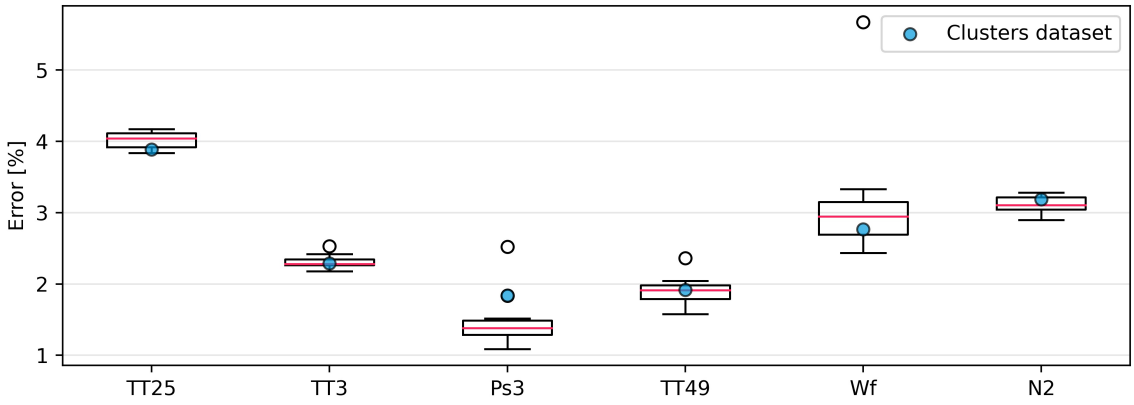

Figure E.5: Boxplot for the cruise phase mean target parameters errors. (Fitting dataset).

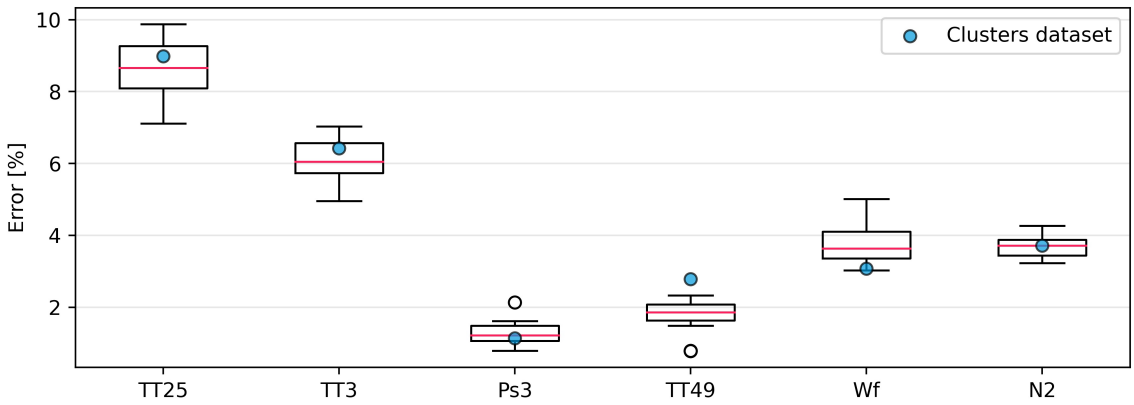

Figure E.6: Boxplot for the cruise phase mean target parameters errors. (Validation dataset)